Australian National University

Using multi-platform LiDAR to assess vegetation structure for woodland forest fauna

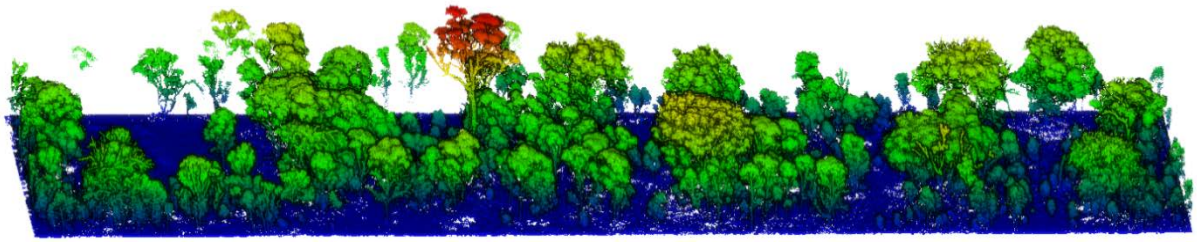

Shukhrat Shokirov

A thesis submitted for the degree of Doctor of Philosophy
The Australian National University

Declaration

I declare that the research presented in this thesis is my own original work unless otherwise referenced or acknowledged. This thesis contains published manuscripts and manuscripts prepared for publication in collaboration with my supervisors and co-authors. The author contributions are provided below. No part of this thesis has been submitted for any previous degree.

Chapter 1. Comparison of TLS and ULS data for wildlife habitat assessments in temperate woodlands

S. Shokirov, S. R. Levick, T. Jucker, P. Yeoh and K. Youngentob, "Comparison of TLS and ULS Data for Wildlife Habitat Assessments in Temperate Woodlands," *IGARSS 2020 - 2020 IEEE International Geoscience and Remote Sensing Symposium*, Waikoloa, HI, USA, 2020, pp. 6097-6100, doi: 10.1109/IGARSS39084.2020.9323451.

S. Shokirov conducted field work, collected TLS data, designed and conducted the pilot study, analysed the data and drafted the manuscript. K. Youngentob and S. R Levick proposed the sampling design and assisted with data analyses and supervision. T. Jucker and P. Yeoh collected ULS data and contributed to post-data processing. All authors edited and improved subsequent versions of the manuscript.

Chapter 2. Habitat highs and lows: Comparing terrestrial and UAV LiDAR for modelling avian species richness and abundance in a restored woodland.

S. Shokirov, T. Jucker, S. R. Levick, A. D. Manning, T. Bonnet, M. Yebra, J. Borevitz, K. Youngentob, (In preparation) “Habitat highs and lows: Comparing terrestrial and UAV LiDAR for modelling avian species richness and abundance in a restored woodland.” *Remote Sensing of Ecology and Conservation.*

S. Shokirov conducted fieldwork, collected TLS data, undertook data analysis and drafted the manuscript. A. Manning provided animal population data. T. Jucker collected ULS data and contributed to data post-processing and analyses with S. R. Levick. T. Bonnet also made substantial contributions to statistical modelling. S. R. Levick. T. Jucker, M. Yebra, J. Borevitz, K. Youngentob, and A. Manning contributed to the design of the study and data interpretation. K. Youngentob provided funding and project supervision. All authors edited and improved the manuscript.

Chapter 3. Multi-sensor approach for detecting coarse woody debris in a landscape with varied ground cover.

S. Shokirov, M. Schaefer, S. R. Levick, J. Borevitz, T. Jucker, I. Abdurahmanov, K. Youngentob, (In preparation) "Multi-sensor approach for detecting coarse woody debris in a landscape with varied ground cover." *International Journal of Remote Sensing.*

S. Shokirov collected TLS and field validation data, conducted data analysis, and drafted the manuscript. M. Schaefer and S. R Levick proposed data processing methods and assisted with data analyses. J. Borevitz and I. Abdurahmanov provided advice on machine learning methods and supervised this work. T. Jucker collected ULS data and assisted with post-processing. K. Youngentob contributed to data analysis, interpretation and project funding. All authors edited and improved the manuscript.

Chapter 4. Using multiplatform LiDAR to identify relationships between vegetation structure and the abundance and diversity of woodland reptiles and amphibians.

S. Shokirov, S. R. Levick, T. Jucker, A. D. Manning, K. Youngentob, (In preparation) "Using multiplatform LiDAR to identify relationships between vegetation structure and the abundance and diversity of woodland reptiles and amphibians." *Remote Sensing.*

S. Shokirov conducted fieldwork, collected TLS data, undertook data analysis and drafted the manuscript. A. D. Manning provided animal population data. T. Jucker collected ULS data and assisted with post-processing. S. R Levick and T. Jucker proposed methods for data analyses and modelling. K. Youngentob assisted with data interpretation and project supervision. All authors edited and improved the manuscript.

Shukhrat Shokirov

April 2021

Acknowledgements

I would like to express my sincere gratitude to all the people who have supported, motivated and encouraged me through this academic journey.

First of all, I thank my parents for bringing me to this life and taking care of me. I thank them for sacrificing an enormous part of their life to meet my needs, which cannot be repaid. I love you both!

I am deeply grateful to my primary supervisor Dr Kara Youngentob for her invaluable advice and continuous support, and patience during my PhD study. Your immense knowledge and plentiful experience have encouraged me in all the time of my academic research and daily life. You taught me how to conduct successful research, build a network and collaborate with interdisciplinary teams.

Big thanks to my co-supervisor Dr Tommaso Jucker for being incredibly supportive. His discussion, ideas and modelling skills have been absolutely invaluable.

Special thanks to my co-supervisor Associate Professor Shaun Levick for his extremely helpful advices throughout the years. I spent a valuable month in Darwin and learned new remote sensing skills from him which helped me to successfully conduct my research.

My heartfelt gratitude goes to my other co-supervisors Professor Adrian D. Manning, Professor Justin Borevitz, Dr Michael Schaefer and Professor William Foley for their support, insightful comments and suggestions which greatly shaped my work.

I am thankful to Dr Kristen Williams, Associate Professor Marta Yebra, and Professor Patricia Backwell for their collaboration, support and encouragement.

I would like to give a special thanks to Dr Timothee Bonnet who offered his statistical skills and Dr Sue McIntyre and Dr Melissa Snape for invaluable advice. Thanks to Jennifer Newport for providing access to animal data and all the researchers and volunteers who contributed to bird and reptile data collection.

I would also like to take the opportunity to thank the Foley lab staff, Karen, Hannah, Pip, David, Carsten, Jessie, Sarah, Murraya, Kim, Laura and James for their friendly working environment.

Numerous amazing people helped me for field data collection. I cannot thank enough to my volunteers, Louise McGibbon, Evelyn Wu, Renee Stainer, Phoebe Hopkins, Katie Spooner, Wenjuan Wang, Molly Folkard, Zenia Xie, Karen, Prasanna, Wenjuan Wang, Divya Muthiah, Bartlett Candice, Mark

Jenkins, Nicole Butcher, Shiyao Zong. Thank you all for your dedication and hard work during the fieldwork.

I also want to thank Kimberley Schiphof for her diligent proofreading of some of the chapters.

I thank to Professor Scott Keogh, Professor Michael Jennions, Jack Egerton, Wes Keys, Audra Johnstone and Ben Durant for running friendly and supportive environment at the department of Ecology and Evolution.

I would like to thank all people in Ecology and Evolution for warm and friendly atmosphere. Special thanks to Kalya, Carlos, Hee-Jin, Arild, Alex C, Rocco, Alex S, Weliton, Buddhie, Fonti, Fitria, Putter, Lauren, Chaminda, Upama, Shawan, Damien, Connie, Jessica, Leo, Regina, Mahbie, Cassandra, Ian, Zoe, Oliver, Dani, Rita, Claire, Darren, Mel, Piet, Octavia, Rasel, Josef, Rose, Richard, Truc and Tobias. Big thanks to Coast who always supported and encouraged during hard times. I am very grateful to Professor Rob Magrath for friendly neighbourship and offering his family house to live with my family during the last months of my PhD.

Finally, I am very grateful for my family, relatives and friends in Uzbekistan for inspiring, encouraging and believing in me. Many thanks to my brothers, Shavkat, Ilhom, Rustam and Mukhtor for their love and care. Special appreciation to my wife Kamola for her love, patience and taking care of me all the time. We are blessed to have Ulugbek (son) and Asila (daughter). Thank you for being such great children. I love you all!

Unfortunately, my PhD study period didn't go smoothly. In addition to a global pandemic in my final year and wildfires of unprecedented scale and severity near my home in south-eastern Australia, I lost my younger brother and two of my uncles during this time. My uncles were highly educated, intelligent and caring people. I remember their invaluable advices which helped me to become who I am. My brother Shavkat was the best brother ever, who was young, energetic, generous, kind, positive and caring person. He was a devoted son, brother, father, uncle, husband, friend and colleague. We spent wonderful times of our childhood together in a family house in a small village of Uzbekistan. He was always next to me, ready to fight for me to protect me from bully kids on streets or at school. I remember him making our family laugh by telling jokes during our family events or during our garden works. Shavkat helped our family to stand on our feet during difficult times by working hard despite the fact that he was still a student at school. He was one of the top students at school and university, and he was passionate to learn new things. His co-workers remember him as a punctual, dedicated and supportive person with a great sense of humour who was constantly getting promotions… You are

always in my heart, in my thoughts, in my life, always and forever! We all love and miss you beyond words. *Alloh joyingni jannatda qilsin ukajonim!*

This work is for your memory, my brother!

This project was supported by The Australian National University and The Commonwealth Scientific and Industrial Research Organization. I gratefully acknowledge their financial support.

Contents

Abstract

Vegetation structure can support biodiversity by creating a variety of microclimates and microhabitats that contribute to food and shelter for different species. For this reason, biodiversity and wildlife habitat assessments often require measurements of vegetation structure. Traditional methods for measuring the structure and distribution of vegetation are time-consuming and often limited to small areas or a subset of the landscape. Light detection and ranging (LiDAR) is an alternative remote sensing method for collecting three dimensional information on vegetation structure and other landscape features across wide areas. For the first time, we used multi-platform LiDAR data from a terrestrial sensor (TLS) and an unmanned aerial vehicle (ULS) to investigate the relationship between vegetation structure and the diversity and abundance of birds, reptiles and amphibians in a critically endangered grassy woodland ecosystem.

The first Chapter of this thesis involves TLS and ULS data collection methods, post-processing steps and exploratory data analysis. I calculated a number of variables to characterise the three-dimensional structure of vegetation across four structurally different, one hectare sites and compared the values of the TLS and ULS derived variables. The different sites type included; 1) high-tree, high-shrub, 2) high-tree, low-shrub, 3) low-tree, high-shrub, and 4) low-tree, low-shrub. Generally, ULS had better overall coverage but TLS outperformed ULS by producing higher volumetric and height diversity indices within our landscape. I discuss the factors that may have influenced these observations and implications for using this data for wildlife habitat assessments.

In the Second Chapter, the relationship between TLS and ULS derived vegetation structural variables and overall bird abundance, species richness and diversity were investigated using mixed effects regression models. Models showed strong significant associations between vegetation structural variables including canopy roughness, vegetation volume, vertical complexity and the abundance of individual species and guilds. The best performing models were for individual bird species and guilds, whereas overall diversity and abundance showed less association to LiDAR-derived vegetation structural metrics. TLS and ULS based models performed similarly when identifying vegetation structural associations with bird abundance and species richness.

In the Third Chapter, coarse woody debris (CWD) from TLS, ULS and the combination of both datasets (Fusion) was extracted. Several topographic variables were calculated as raster imagery from LiDAR point clouds and Random Forest (RF) machine learning algorithms were then utilised to classify CWD. Noise reduction algorithms were applied to reduce noise from the classified imagery.

Digital height model (DHM), surface roughness and topographic position index were important variables in classifying CWD with RF. Classification accuracy varied depending on the amount of ground vegetation cover. The impacts of ground vegetation cover on CWD accuracy in a grassy woodland were quantified and discussed.

The Fourth Chapter explores the relationship between LiDAR derived vegetation structural metrics and the presence and abundance of reptiles and amphibians. Models found significant associations between woodland reptile and amphibian populations and a number of vegetation structural characteristics from the selected variables, the most common of which were mean canopy height, canopy skewedness, vertical complexity, volume of vegetation and CWD. Notable relationships between herpetofauna population data and vegetation structural metrics are discussed with reference to existing literature on habitat associations for these animals. I also explore reasons why significant associations between LiDAR derived vegetation structural metrics and animal population data were not consistent across sensors and suggest directions for future research.

Introduction

Vegetation structure is the three-dimensional spatial arrangement of vegetation, which is an important aspect of habitat quality for many animals (Verschuyl et al., 2008, Jung et al., 2012)). Vegetation structure is widely used by animals for foraging, nesting, reproduction, hibernation and protection from predation (McElhinny et al., 2006). Therefore, animal habitat assessments often require accurate measurement of vegetation structure (Lahoz-Monfort et al., 2010, Davies and Asner, 2014). To date, a number of traditional field-inventory methods have been developed to measure vegetation structure (MacArthur, 1961, Peet et al., 1998). However, data collection using these methods is usually labour intensive, time-consuming and limited to small spatial extents (Lahoz-Monfort et al., 2010, Wood et al., 2012, Davies and Asner, 2014).

Light detection and ranging (LiDAR) is a rapidly developing technology that has opened the door to wide-scale mapping of landscape and vegetation structure with a high degree of accuracy and detail. LiDAR emits a laser light from a sensor and records light reflected back from earth objects, calculating the distance to generate a three-dimensional representation of structural features (Lefsky et al., 2002, Goetz et al., 2007). LiDAR sensors can be attached to spaceborne, airborne (ALS), unmanned aerial vehicle (ULS), terrestrial (TLS) and mobile platforms to collect three-dimensional data (Vierling et al., 2008). Most of the research and applications involving LiDAR are focused on vegetation mapping for estimating above ground biomass, canopy volume and three-dimensional distributions of forest

structure (Lim et al., 2003, Hackenberg et al., 2015, Puletti et al., 2020). More recently, however, LiDAR has captured the attention of ecologists looking for tools to improve wildlife habitat assessments and/or investigate plant-animal interactions across landscapes (Davies and Asner, 2014, Bakx et al., 2019).

The majority of wildlife habitat research with LiDAR data has come from sensors on airplanes, which have shown great promise for identifying and quantifying many vegetation and landscape features across wide areas, but typically have much lower resolution than ULS or TLS sensors (Bakx et al., 2019). The main limitation of ALS in forests and woodlands is that structural information from the sub-canopy and ground layer is often occluded by upper canopy vegetation (Bakx et al., 2019, Levick et al., 2021). As a result, below canopy structural information has been largely excluded from studies of animal-habitat associations with LiDAR data (Shun Li, 2019). However, below canopy vegetation structure can also be important for explaining landscape use by many different species (Cody, 1981b, Fischer et al., 2004, Bakx et al., 2019) and these features can be captured by terrestrial (Maas et al., 2008, Blakey et al., 2017) and even airborne ULS sensors (Chisholm et al., 2013).

High resolution LiDAR (TLS and ULS) datasets can provide a nearly complete representation of the three-dimensional structure of vegetation, which is not possible using traditional field-inventory methods (Levick et al., 2021). Highly detailed and accurate information on canopy, sub-canopy and ground layer structures collected from these sensors have been used for forest inventory (Moskal and Zheng, 2012, Brede et al., 2019), vegetation biomass (Hackenberg et al., 2015, Wang et al., 2017) and fuel hazard assessments (Hillman et al., 2021). Despite its great potential for capturing important habitat structural elements of canopy and sub-canopy dependent species, TLS datasets have been used in only a few animal habitat modelling studies (Vogeler and Cohen, 2016); including bird nesting habitat selection (Michel et al., 2008), butterfly populations estimates (Hristov et al., 2019), bat habitat preferences and flight behaviour (Yang et al., 2013, Blakey et al., 2017) and modelling the functional properties of cover for prey animals (Olsoy et al., 2015). Even fewer studies have utilized ULS to investigate animal-habitat associations (for an exception see, (Wilson et al., 2020). Compared to airplane sensors, ULS and TLS typically offer higher resolution data but require longer survey times for large areas, and this is particularly true for stationary terrestrial sensors that must be manually repositioned throughout a landscape. However, higher resolution data and below canopy detail may be important for capturing structural elements at scales relevant to landscape use by many animals and particularly those that depend on sub-canopy vegetation features (Vogeler and Cohen, 2016).

For the first time, I utilized high resolution TLS and ULS data for investigating relationships between vegetation structure and the abundance and diversity of birds, reptiles and amphibians in a woodland landscape. The general aim of this study was twofold: 1) to investigate relationship between LiDAR derived vegetation structural metrics and animal population data and, 2) to examine the performance of TLS, ULS and the combined datasets (Fusion) for modelling habitat structures that may be important to woodland fauna.

Over the course of the research presented in my thesis chapters, I focused on the following questions: 1) Can TLS and ULS capture vegetation structural metrics that help explain the presence and abundance of woodland bird and reptile species? 2) Which sensor and platform provides the most accurate measurements of these vegetation structural metrics, TLS or ULS? 3) Can we accurately detect coarse woody debris from ULS, TLS? 4) Does the fusion of TLS and ULS data improve the performance of models for detecting coarse woody debris and measuring structural attributes that help explain animal - habitat associations?

Although this research was conducted in south-eastern Australia, the developed methods and applications are relevant to many species and communities across the globe.

Thesis Outline

The chapters of this thesis, are intended for publication in academic journals. The target peer-reviewed journal is included on the Declarations page along with co-author contributions to the manuscript. To keep a consistent style throughout the thesis, tables and figure formats, abbreviations and reference styles have been standardised. References for each chapter are provided directly after each chapter.

As the primary author of each chapter/journal article, I was responsible for the majority of the work involved in every manuscript, including field data collection, data analysis, literature review and writing. My supervisors, advisors and several other colleagues added significant contributions to various aspects of my research (e.g., research design, data analysis, and manuscript editing). Where applicable, I have recognized their contributions by including them as co-authors in the journal articles.

References

BAKX, T. R. M., KOMA, Z., SEIJMONSBERGEN, A. C., KISSLING, W. D. & ZURELL, D. 2019. Use and categorization of Light Detection and Ranging vegetation metrics in avian diversity and species distribution research. *Diversity and Distributions,* 25**,** 1045-1059.

BLAKEY, R. V., LAW, B. S., KINGSFORD, R. T. & STOKLOSA, J. 2017. Terrestrial laser scanning reveals below-canopy bat trait relationships with forest structure. *Remote Sensing of Environment,* 198**,** 40-51.

BREDE, B., CALDERS, K., LAU, A., RAUMONEN, P., BARTHOLOMEUS, H. M., HEROLD, M. & KOOISTRA, L. 2019. Non-destructive tree volume estimation through quantitative structure modelling: Comparing UAV laser scanning with terrestrial LIDAR. *Remote Sensing of Environment,* 233.

CHISHOLM, R. A., CUI, J., LUM, S. K. Y. & CHEN, B. M. 2013. UAV LiDAR for below-canopy forest surveys. *Journal of Unmanned Vehicle Systems,* 01**,** 61-68.

CODY, M. L. 1981. Habitat Selection in Birds: The Roles of Vegetation Structure, Competitors, and Productivity. *BioScience,* 31**,** 107-113.

DAVIES, A. B. & ASNER, G. P. 2014. Advances in animal ecology from 3D-LiDAR ecosystem mapping. *Trends Ecol Evol,* 29**,** 681-91.

FISCHER, J., LINDENMAYER, D. B. & COWLING, A. 2004. The challenge of managing multiple species at multiple scales: reptiles in an Australian grazing landscape. *Journal of Applied Ecology,* 41**,** 32-44.

GOETZ, S., STEINBERG, D., DUBAYAH, R. & BLAIR, B. 2007. Laser remote sensing of canopy habitat heterogeneity as a predictor of bird species richness in an eastern temperate forest, USA. *Remote Sensing of Environment,* 108**,** 254-263.

HACKENBERG, J., WASSENBERG, M., SPIECKER, H. & SUN, D. 2015. Non Destructive Method for Biomass Prediction Combining TLS Derived Tree Volume and Wood Density. *Forests,* 6**,** 1274-1300.

HILLMAN, S., WALLACE, L., LUCIEER, A., REINKE, K., TURNER, D. & JONES, S. 2021. A comparison of terrestrial and UAS sensors for measuring fuel hazard in a dry sclerophyll forest. *International Journal of Applied Earth Observation and Geoinformation,* 95.

HRISTOV, N. I., NIKOLAIDIS, D., HUBEL, T. Y. & ALLEN, L. C. 2019. Estimating Overwintering Monarch Butterfly Populations Using Terrestrial LiDAR Scanning. *Frontiers in Ecology and Evolution,* 7**,** 266.

JUNG, K., KAISER, S., BÖHM, S., NIESCHULZE, J. & KALKO, E. K. V. 2012. Moving in three dimensions: effects of structural complexity on occurrence and activity of insectivorous bats in managed forest stands. *Journal of Applied Ecology,* 49**,** 523-531.

LAHOZ-MONFORT, J. J., GUILLERA-ARROITA, G., MILNER-GULLAND, E. J., YOUNG, R. P. & NICHOLSON, E. 2010. Satellite imagery as a single source of predictor variables for habitat suitability modelling: how Landsat can inform the conservation of a critically endangered lemur. *Journal of Applied Ecology,* 47**,** 1094-1102.

LEFSKY, M. A., COHEN, W. B., PARKER, G. G. & HARDING, D. J. 2002. Lidar Remote Sensing for Ecosystem Studies. *BioScience,* 52**,** 19-30.

LEVICK, S. R., WHITESIDE, T., LOEWENSTEINER, D. A., RUDGE, M. & BARTOLO, R. 2021. Leveraging TLS as a Calibration and Validation Tool for MLS and ULS Mapping of Savanna Structure and Biomass at Landscape-Scales. *Remote Sensing,* 13.

LIM, K., TREITZ, P., WULDER, M., ST-ONGE, B. & FLOOD, M. 2003. LiDAR remote sensing of forest structure. *Progress in Physical Geography,* 27**,** 88-106.

MAAS, H. G., BIENERT, A., SCHELLER, S. & KEANE, E. 2008. Automatic forest inventory parameter determination from terrestrial laser scanner data. *International Journal of Remote Sensing,* 29**,** 1579-1593.

MACARTHUR, R., and J. MacArthur 1961. On bird species diversity. *Ecology,* 42**,** 594-598.

MCELHINNY, C., GIBBONS, P., BRACK, C. & BAUHUS, J. 2006. Fauna-habitat relationships: a basis for identifying key stand structural attributes in temperate Australian eucalypt forests and woodlands. *Pacific Conservation Biology,* 12**,** 89-110.

MICHEL, P., JENKINS, J., MASON, N., DICKINSON, K. J. M. & JAMIESON, I. G. 2008. Assessing the ecological application of lasergrammetric techniques to measure fine-scale vegetation structure. *Ecological Informatics,* 3**,** 309-320.

MOSKAL, L. M. & ZHENG, G. 2012. Retrieving Forest Inventory Variables with Terrestrial Laser Scanning (TLS) in Urban Heterogeneous Forest. *Remote Sensing,* 4**,** 1.

OLSOY, P. J., FORBEY, J. S., RACHLOW, J. L., NOBLER, J. D., GLENN, N. F. & SHIPLEY, L. A. 2015. Fearscapes: Mapping Functional Properties of Cover for Prey with Terrestrial LiDAR. *BioScience,* 65**,** 74-80.

PEET, R. K., WENTWORTH, T. R. & WHITE, P. S. 1998. A Flexible, Multipurpose Method for Recording Vegetation Composition and Structure. *Castanea,* 63**,** 262-274.

PULETTI, N., GROTTI, M., FERRARA, C. & CHIANUCCI, F. 2020. Lidar-based estimates of aboveground biomass through ground, aerial, and satellite observation: a case study in a Mediterranean forest. *Journal of Applied Remote Sensing,* 14**,** 044501.

SHUN LI, L. Z. Y. G. H. Y. T. W. L. F. J. G. 2019. Advances in LiDAR technology in the field of animal ecology. *Biodiversity Science,* 27**,** 1021-1031.

VERSCHUYL, J. P., HANSEN, A. J., MCWETHY, D. B., SALLABANKS, R. & HUTTO, R. L. 2008. Is the effect of forest structure on bird diversity modified by forest productivity? *Ecol Appl,* 18**,** 1155-70.

VIERLING, K. T., VIERLING, L. A., GOULD, W. A., MARTINUZZI, S. & CLAWGES, R. M. 2008. Lidar: shedding new light on habitat characterization and modeling. *Frontiers in Ecology and the Environment,* 6**,** 90-98.

VOGELER, J. C. & COHEN, W. B. 2016. A review of the role of active remote sensing and data fusion for characterizing forest in wildlife habitat models. *Revista de Teledetección*.

WANG, D., XIN, X., SHAO, Q., BROLLY, M., ZHU, Z. & CHEN, J. 2017. Modeling Aboveground Biomass in Hulunber Grassland Ecosystem by Using Unmanned Aerial Vehicle Discrete Lidar. *Sensors (Basel),* 17.

WILSON, S. J., HEDLEY, R. W., RAHMAN, M. M. & BAYNE, E. M. 2020. Use of an unmanned aerial vehicle and sound localization to determine bird microhabitat. *Journal of Unmanned Vehicle Systems,* 9**,** 59-66.

WOOD, E. M., PIDGEON, A. M., RADELOFF, V. C. & KEULER, N. S. 2012. Image texture as a remotely sensed measure of vegetation structure. *Remote Sensing of Environment,* 121**,** 516-526.

YANG, X., SCHAAF, C., STRAHLER, A., KUNZ, T., FULLER, N., BETKE, M., WU, Z., WANG, Z., THERIAULT, D., CULVENOR, D., JUPP, D., NEWNHAM, G. & LOVELL, J. 2013. Study of bat flight behavior by combining thermal image analysis with a LiDAR forest reconstruction. *Canadian Journal of Remote Sensing,* 39**,** S112-S125.

Chapter 1. Comparison of TLS and ULS Data for Wildlife Habitat Assessments in Temperate Woodlands

Authors: Shukhrat Shokirov[1,2], Shaun R Levick[2], Tommaso Jucker[3], Paul Yeo[4], Kara Youngentob[1]

[1]Research School of Biology, Australian National University, Australia

[2]CSIRO Land and Water, Australia

[3]School of Biological Sciences, University of Bristol, England

[4]CSIRO Health and Biosecurity, Australia

Keywords: UAV, LiDAR, terrestrial vegetation, structure, wildlife conservation

Abstract

This study employs LiDAR technology to calculate vegetation structural metrics that may be useful for assessing habitat quality and predicting the presence and abundance of structurally sensitive animal species. We compare outputs from two LiDAR platforms, an Unmanned Aerial Vehicle (RIEGL miniVUX-1UAV LiDAR; ULS) and a Terrestrial Laser Scanner (Topcon GLS2000; TLS) that we used to collect structural data from a critically endangered woodland ecosystem in SE Australia. This is also the site of a long-term restoration study and ongoing wildlife population monitoring. Despite better overall coverage by the ULS, the TLS provided considerably higher values for ground layer vegetation complexity and higher vegetation volume for the mid-story and canopy strata. We discuss the factors that may influence these observations and implications for using these sensors for habitat assessments.

Introduction

Models that predict the presence and abundance of species are important tools in wildlife management and applied ecology (De Wan et al., 2009). Vegetation structure is an aspect of habitat quality that can influence the presence and abundance of many animals (Davies and Asner, 2014). However, the collection of accurate vegetation structural data over whole landscapes is limited by time and resources.

Remote sensing methods provide alternative means for collecting vegetation and landscape structural data over wide areas. Light Detection and Ranging (LiDAR) is the most direct tool for capturing variation in structural elements at high spatial resolution for parameterizing organism-habitat models (Graf et al., 2009, Tattoni et al., 2012). LiDAR point clouds allow analysts to calculate landscape structural variables including terrain models, vegetation height, density and biomass, volume, and spatial distributions of landscape features (van Leeuwen et al., 2006, Jupp and Lovell, 2007). This information may be useful for identifying important, structure-specific habitat elements that can influence the presence and abundance of particular species (Bradbury et al., 2005, Davies and Asner, 2014) .

Despite the fact that the application of LiDAR to habitat mapping is relatively new, many studies already have been undertaken to assess its utility for habitat assessment for a range of different animals, but with considerable focus on birds (Bradbury et al., 2005, Lesak et al., 2011, Sillero and Gonçalves-Seco, 2014). For example, (Clawges et al., 2008) found a relationship between bird species diversity and LiDAR based vegetation volume, foliage diversity and shrub density. Although canopy height

metrics have been used to predict the distribution, breeding success and diversity of some bird species (Bradbury et al., 2005, Lesak et al., 2011), a thorough review found that vegetation heterogeneity and complexity is often more influential than simple canopy cover or vegetation height for animal diversity (Davies and Asner, 2014). Estimates of landscape surface heterogeneity with LiDAR point clouds have also been used to identify habitat preferences of lizards (Sillero and Gonçalves-Seco, 2014).

Airborne LiDAR (ALS) sensors are commonly used in these studies because they allow information to be collected across wide areas in a relatively short period of time (Clawges et al., 2008, Sillero and Gonçalves-Seco, 2014). For canopy dwelling wildlife, ALS and LiDAR data from unmanned aerial vehicles (ULS) can be particularly useful because most of the returns from these sensors are from the upper vegetation layers. However, a limitation of ALS and ULS is their ability to see landscape features in detail that may be wholly or partially occluded by tree canopies (Jupp and Lovell, 2007). This can be especially problematic for measuring important structural habitat elements for those species that are understory specialists (Cody, 1981a). Although terrestrial laser scanning (TLS) data allow for better coverage of landscape structure below forest canopies, data collection is almost always more time consuming and the understory of some forest landscapes can be difficult to access and capture with TLS in the desired detail due to dense vegetation (Jupp and Lovell, 2007).

In Australia, temperate woodlands are a critically endangered ecosystem due to anthropogenic landscape and climate change (Lindenmayer et al., 2010). Despite once being widespread throughout southern Australia and Tasmania, less than 3% of the original extent of these ecological communities still exist (Hobbs and Yates, 2000, Lindenmayer et al., 2010). The remaining temperate woodlands are critical habitat for multiple endangered bird, reptile and mammal species (Lindenmayer et al., 2010, Manning et al., 2011). These landscapes are also ideal to investigate the utility of ULS and TLS data for wildlife habitat assessments owing to the unique structural composition of these environments and the need to identify appropriate methods to assess, protect, and restore habitat for the threatened species and ecological communities there.

Woodlands differ from dense forests in that the growth of trees is more widely spaced, which can facilitate better penetration into the understory by ULS. In these landscapes, ULS may provide sufficient detail to capture understory structure to assess habitat for ground and shrub dwelling animals. Widely spaced trees and low, grassy understories also make it easier to collect TLS data and cover a wider area with less occlusion. For the first time, we compare the ability of data collected with a common, commercially available TLS (Topcon GLS2000) and ULS data (RIEGL miniVUX-1UAV LiDAR) to provide key structural metrics of vegetation that may be useful for habitat assessments for

temperate woodland bird and reptile species based on earlier research into relationships between habitat quality/site occupancy and landscape structure (Cody, 1981a, Manning et al., 2011, Davies and Asner, 2014, Howland et al., 2014).

Methods

Study Area

The study area is located in Mulligan's Flat-Goorooyarroo long-term Woodland Experiment in the Australian Capital Territory (ACT), Australia (35°09' S - 149°09', elevation 650-700m; Fig. 1). This temperate woodland is dominated by Blakely's Red Gum (*Eucalyptus blakelyi*) and Yellow Box (*E. melliodora*) in the canopy, *Acacia spp.* in the mid-story, and a ground-layer of native grasses that include *Joycea pallida*, *Austrodanthonia spp.*, *Themeda australis* and *Aristida ramose* (McIntyre et al., 2010).

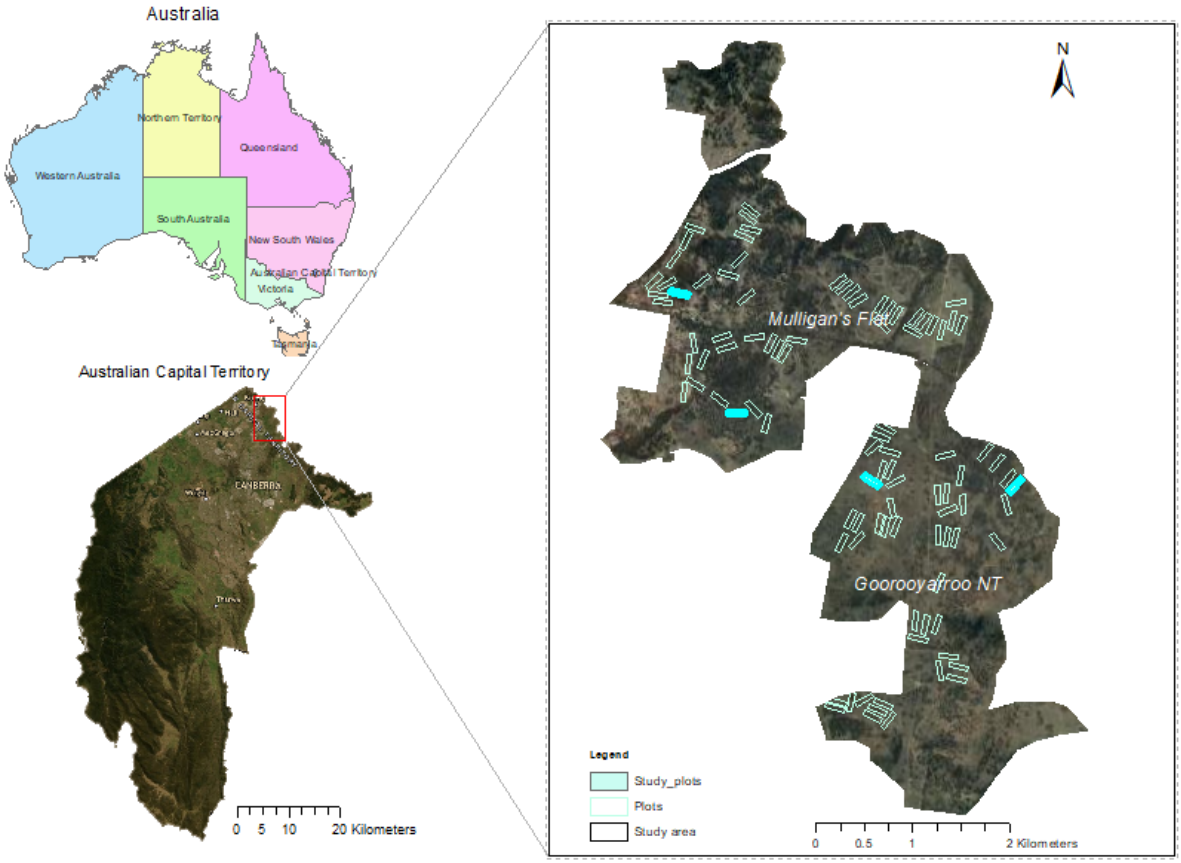

Figure 1: The study area, Mulligan's Flat-Goorooyarroo Woodland Experiment, in Canberra Australia. The four plots selected for this study are highlighted in blue.

The aim of the Mulligan's Flat-Goorooyarroo Woodland Experiment is to restore the structure and function of a temperate woodland and to increase its native biodiversity (Manning et al., 2011). The area includes 96, 1 ha plots (200 m x 50 m) where surveys for birds, reptiles and small mammals have been undertaken bi-annually for the past decade. Various restoration activities have also been conducted throughout the landscape and additional information about the ongoing research and restoration in this area can be found here: http://www.mfgowoodlandexperiment.org.au/. Mean average daily temperatures range from 6.5° C to 19.7° C, and mean annual rainfall is 615.9 mm (Bureau of Meteorology, 2019).

TLS data collection and post-processing

We used a Topcon GLS2000 (Tokyo, Japan) for TLS data collection in the previously established 96, 1 ha plots (Manning et al., 2011). Data was only collected during daylight hours and fine weather (no rain or strong wind) between October 1st and 31st in 2018. The Topcon GLS2000 is a high-density laser scanner that emits near-infrared light (1064 nm) pulses at up to 120,000 per second. The field-of-view is 360° and 270° in the horizontal and vertical direction, respectively. The beam diameter of a single pulse is 4 mm at 60 m. TLS data were collected from 7 stations in each 1 ha plot in zigzag formation, with approximately 30 m between scanning stations (1.7 m scanner height) and a scanning resolution of 6 mm at 10 m. The position of each scan was measured with a differential GPS (Trimble Geoexplorer 6000). In total, 672 scans were collected across the 96 plots.

The full 96 plot dataset was used for a separate study to investigate relationships between LiDAR derived structural metrics and the presence and abundance of birds and reptiles. For this comparative study, we selected four plots (Fig. 1) that represent the four woodland vegetation types within the study area: 1. High tree cover, high shrub cover (HH). 2. Low tree cover, high shrub cover (LH). 3. High tree cover, low shrub cover (HL). 4. Low tree cover, low shrub cover (LL) (Manning et al., 2011).

Coordinates of scan stations were post-processed to improve the location accuracy using Stromolo base station data, 20 km from the study area. In each plot, point clouds from the 7 individual scan stations were merged using the Multi-Station Adjustment (MSA) plugin in RiScan Pro software (RIEGL Laser Measurement Systems GmbH). MSA searches for planar surfaces in the point clouds and aligns common points on overlapping planes from different stations. Next, the point clouds from each plot were georeferenced using GPS locations of each scan position measured in the field, clipped with corresponding 96 plot polygons and subsampled into 10 mm spacing using Cloud Compare (CloudCompare 2.10.2). Datasets were cleaned of noise and classified into ground and non-ground

classes and normalized by converting elevation values to height above ground values using LAStools software scripts (Isenburg, 2012) (Fig. 2).

ULS data collection and post-processing

The ULS LiDAR platform consists of a quadcopter integrated with RIEGL miniVUX-1UAV LiDAR sensor and APX INS/GNSS systems. ULS LiDAR data were collected between the 7th and 14th of November, 2018, in fine weather, during daylight hours, with a 100 kHz pulse repetition rate and up to 100,000 measurements/second. The flight was performed at 80 m above the take off point, flying at approximately 25.2 km/h, with up to 5 returns per pulse. We used DJI ground station pro V2 to plan the flights (SZ DJI TECHNOLOGY CO., 2018).

ULS data from the 96 plots were clipped to create separate point clouds for each plot and noise points were removed using *lasnoise* (Isenburg, 2012). Point clouds were classified into ground and non-ground points using *lasground* (Isenburg, 2012). We normalized point clouds by converting elevation values to height above ground values (Fig. 2) with *lasheight* (Isenburg, 2012). The same four plots for the TLS data analyses were also used for the ULS analyses.

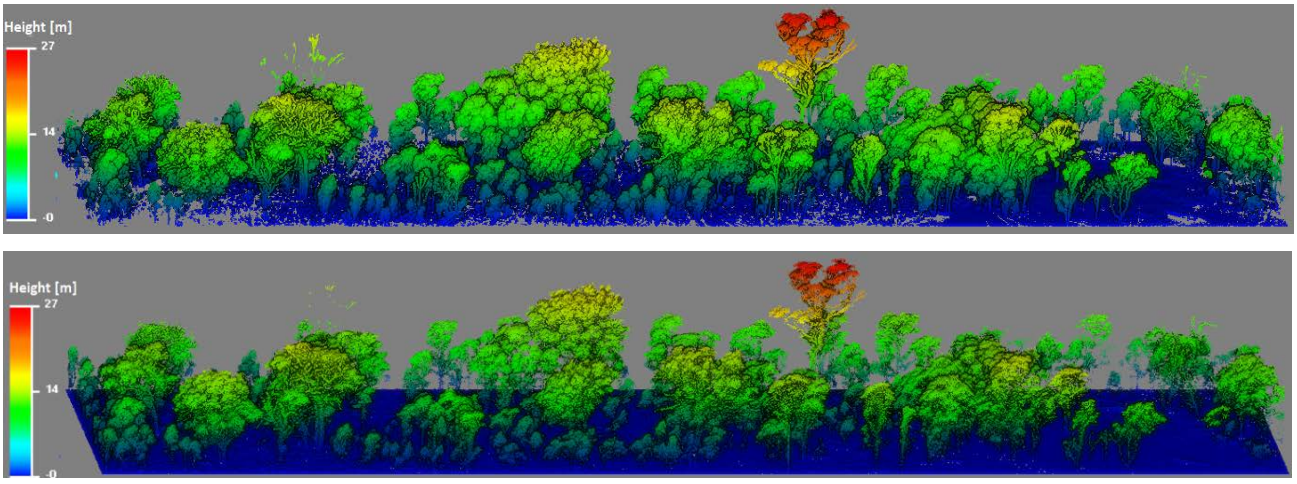

Figure 2: Normalized TLS (top) and ULS (bottom) point clouds from plot HH colored by height.

Calculating LiDAR landscape structural metrics

We calculated a number of structural variables from TLS and ULS normalized height point clouds. Canopy height metrics and canopy structural indices were calculated from points above 1.3 m using the *lascanopy* function in LAStools (Isenburg, 2012). We then stratified the image into three vegetation layers, ground (<= 1m), mid-story (>1 m – <10 m), and canopy (>10 m), based on established descriptions of vegetation strata for eucalypt grassy woodlands (Department of Environment, 2013). For each layer, we calculated mean and standard deviation of height and Shannon Diversity Index

using lidR package (Roussel, 2017). In addition, volumetric data for each layer were computed by excluding ground points and constructing 0.5 m voxels (volumetric pixels) from point clouds, with each voxel made of one or more points.

Results and discussion

As expected, there were a number of observed differences in the performance and coverage of the ULS and TLS sensors. Figure 3 depicts the cloud-to-cloud (C2C), absolute distance between returns from the two point clouds. Despite the fact that the point cloud from the TLS was denser than the ULS data (Fig. 2), the ULS provided more complete coverage due in part to its multiple returns, compared to the single return of the TLS scanner and occlusion issues experienced by the ground-based TLS (Fig. 3). More scanning stations would have increased the coverage of the TLS but also substantially increased the data collection and processing time. A multiple return TLS could also improve coverage from the same number of stations.

Despite the occluded areas, the merged TLS data created detailed point clouds that generally outperformed the ULS data in their ability to detect vegetation structural information across most layers and vegetation types. However, the ULS reported higher vegetation volume than the TLS in the ground-layer of the LL plot and no difference in the ground-layer of the HH plot. Visual inspection revealed that LL plot had a lot of coarse woody debris (e.g., fallen logs) that caused occlusion errors (laser pulses were blocked) in the TLS point cloud (Table 1). Since LL also had relatively few trees and shrubs, the ULS could better detect the ground-layer vegetation volume. Vegetation volume was higher with TLS than ULS for all other plot types and vegetation strata.

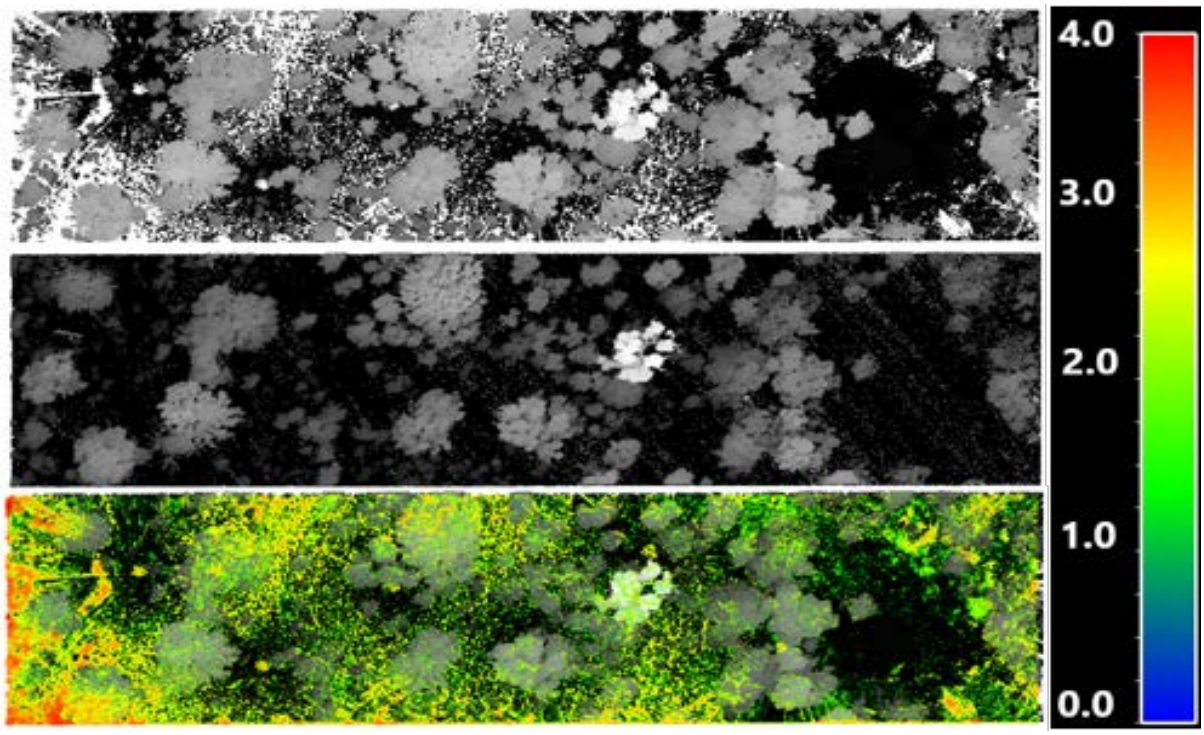

Figure 3: Normalized TLS (top) and ULS (middle) point clouds from plot HH shaded by height. The bottom image shows the cloud to cloud absolute distance between returns from the two point clouds using a colour scale.

The TLS captured more variation than the ULS in the ground-layer vegetation of all plot types and the mid-story of the LL plot according to the Shannon Diversity Index (Table 1). This is probably due to the higher point cloud density of the TLS sensor, which performs particularly well in more open landscape conditions. Diversity index performance for the remaining mid-story and canopy vegetation layers was similar across sensors.

Table 1. LiDAR structural metrics calculated from the ground-layer, mid-story, and canopy vegetation strata. ULS data is on the left and TLS data on the right of each column.

Plot	Volume (m^3)		Mean Height		Standard Deviation of Height		Shannon Diversity Index	
	ULS	TLS	ULS	TLS	ULS	TLS	ULS	TLS
HH	4960.88	4968.50	0.03	0.11	0.07	0.16	0.03	0.19
LH	4701.13	5383.13	0.02	0.05	0.06	0.14	0.02	0.17
HL	5245.50	5783.75	0.04	0.09	0.08	0.17	0.05	0.28
LL	5097.38	4367.88	0.05	0.03	0.07	0.11	0.04	0.11
Ground-layer (≤1m)								
HH	9609.00	14796.13	6.54	6.02	2.28	2.36	0.93	0.95
LH	6640.13	12991.88	6.13	5.78	2.52	2.50	0.95	0.96
HL	5979.38	9678.13	5.98	5.56	2.60	2.63	0.96	0.96
LL	153.88	575.50	5.01	6.41	3.14	2.60	0.86	0.93
Mid-story (>1m - < 10m)								
HH	5215.63	6375.00	13.20	12.97	3.10	3.22	0.64	0.62
LH	3723.25	5235.75	12.84	12.40	2.00	1.94	0.60	0.58
HL	6511.38	9162.88	14.67	14.05	2.75	2.62	0.69	0.67
LL	458.63	978.75	14.94	13.42	2.01	2.11	0.62	0.62
Canopy (>10m)								

Vegetation height was consistently higher in ULS than TLS data owing to the position of airborne vs terrestrial sensors (Tables 1 and 2). Since airborne sensors have a clear line of sight to the upper canopy, max height is more accurately recorded by the ULS (Table 2). However, height percentile values below the top layer of vegetation are typically lower for TLS due to its ability to detect more structural information under the canopy compared to the ULS (Table 2). Canopy cover was also captured more completely with the TLS than the ULS data for the same reason (Table 2).

Table 2. LiDAR canopy metrics calculated from >1.3 m.

Plot	Max Height		Standard Deviation of Height		5 th Percentile Height		50 th Percentile Height		90 th Percentile Height		Skewness		Kurtoses		Canopy Cover %	
	ULS	TLS	ULS	TLS	ULS	TLS	ULS	TLS	ULS	TLS	ULS	TLS	ULS	TLS	ULS	TLS
HH	27.77	27.73	4.23	4.00	3.13	2.32	9.37	7.50	14.51	12.86	0.76	1.09	4.57	5.58	38.40	58.80
LH	19.34	19.31	4.04	3.66	2.54	1.96	9.56	7.34	14.40	12.49	-0.07	0.36	2.18	2.59	30.20	50.10
HL	22.02	22.07	4.99	4.88	2.57	2.07	11.43	9.21	17.69	16.29	-0.18	0.17	2.00	2.01	27.20	49.60
LL	18.45	18.49	3.92	3.98	4.52	3.61	14.59	10.95	17.31	15.78	-1.46	-0.31	4.73	2.36	2.20	17.00

Conclusion

This research compared the performance of ULS and TLS data for estimating vegetation structural metrics that may be useful for habitat assessments for temperate woodland bird and reptile species. TLS detected more variation in vegetation structure in the ground-layer than the ULS. Despite voxelization, TLS also outperformed ULS in estimating the volume of vegetation across all layers except the ground layer of woodlands with low tree and shrub cover due to low-lying occlusions. This is worth noting for reptile habitat assessments that may focus on ground-layer metrics. Overall, based on existing studies that have linked measures of vegetation structural diversity and volume to animal species richness and abundance, the TLS sensor is likely to perform better than the ULS for this purpose. However, the TLS is more time consuming in data collection and processing so this must be weighed against the faster but potentially more limited coverage of ULS across wide areas.

References

BRADBURY, R. B., HILL, R. A., MASON, D. C., HINSLEY, S. A., WILSON, J. D., BALZTER, H., ANDERSON, G. Q. A., MARK J. WHITTINGHAM, M. J., DAVENPORT, I. J. & BELLAMY, P. E. 2005. Modelling relationships between birds and vegetation structure using airborne LiDAR data a review with case studies from agricultural and woodland environments. British Ornithologists' Union, IBIS, 147, 443–452.

BUREAU OF METEOROLOGY, A. 2019. Climate summaries archive [Online]. Available: http://www.bom.gov.au/climate/current/annual/act/archive/2018.summary.shtml [Accessed 08/08/2020 2020].

CLAWGES, R., VIERLING, K., VIERLING, L. & ROWELL, E. 2008. The use of airborne lidar to assess avian species diversity, density, and occurrence in a pine/aspen forest. Remote Sensing of Environment, 112, 2064-2073.

CODY, M., L. 1981. Habitat Selection in Birds: The Roles of Vegetation Structure, Competitors, and Productivity. BioScience, 31, 107-113.

DAVIES, A. B. & ASNER, G. P. 2014. Advances in animal ecology from 3D-LiDAR ecosystem mapping. Trends Ecol Evol, 29, 681-91.

DE WAN, A. A., SULLIVAN, P. J., LEMBO, A. J., SMITH, C. R., MAERZ, J. C., LASSOIE, J. P. & RICHMOND, M. E. 2009. Using occupancy models of forest breeding birds to prioritize conservation planning. Biological Conservation, 142, 982-991.

DEPARTMENT OF ENVIRONMENT, G. o. A. 2013. Vegetation Assessment Guide.

GRAF, R. F., MATHYS, L. & BOLLMANN, K. 2009. Habitat assessment for forest dwelling species using LiDAR remote sensing: Capercaillie in the Alps. Forest Ecology and Management, 257, 160-167.

HOBBS, R. J. & YATES, C. J. 2000. Temperate eucalypt woodlands in Australia: Biology, conservation, management and restoration, Surrey Beatty & Sons Pty., Ltd.

HOWLAND, B., STOJANOVIC, D., GORDON, I. J., MANNING, A. D., FLETCHER, D. & LINDENMAYER, D. B. 2014. Eaten out of house and home: impacts of grazing on ground-dwelling reptiles in Australian grasslands and grassy woodlands. PLoS One, 9, e105966.

ISENBURG, M. 2012. LAStools-efficient tools for LiDAR processing. Available at: http: http://www. cs. unc. edu/~ isenburg/lastools/[Accessed October 9, 2012].

JUPP, D. L. B. & L, L. J. 2007. Airborne and Ground-Based Lidar Systems for Forest Measurement: Background and Principles. Australia: CSIRO.

LESAK, A. A., RADELOFF, V. C., HAWBAKER, T. J., PIDGEON, A. M., GOBAKKEN, T. & CONTRUCCI, K. 2011. Modeling forest songbird species richness using LiDAR-derived measures of forest structure. Remote Sensing of Environment, 115, 2823-2835.

LINDENMAYER, D., BENNETT, A. F. & HOBBS, R. 2010. An overview of the ecology, management and conservation of Australia's temperate woodlands. Ecological Management & Restoration, 11, 201-209.

MANNING, A. D., WOOD, J. T., GUNNINGHAM, R. B., MCINTYRE, S., SHORTHOUSE, D. J., GORDON, I. J. & LINDENMAYER, D. B. 2011. Integrating research and restoration: the establishment of a long-term woodland experiment in south-eastern Australia. Zoologist, 35, 633-648.

MCINTYRE, S., STOL, J., HARVEY, J., NICHOLLS, A. O., CAMPBELL, A., REID, A., MANNING, A. D., LINDENMAYER, D. B. & 2010. Biomass and floristic patterns in the ground layer vegetation of box-gum grassy eucalypt woodland in Goorooyarroo and Mulligans Flat Nature Reserves, Australian Capital Territory. Cunninghamia: a journal of plant ecology for eastern Australia, 11, 319-357.

ROUSSEL, J. 2017. Auty, D. lidR: Airborne LiDAR Data Manipulation and Visualization for Forestry Applications. R package version, 1.

SILLERO, N. & GONÇALVES-SECO, L. 2014. Spatial structure analysis of a reptile community with airborne LiDAR data. International Journal of Geographical Information Science, 28, 1709-1722.

SZ DJI TECHNOLOGY CO., L. 2018. DJI GS Pro User Manual.

TATTONI, C., RIZZOLLI, F. & PEDRINI, P. 2012. Can LiDAR data improve bird habitat suitability models? Ecological Modelling, 245, 103-110.

VAN LEEUWEN, W. J. D., ORR, B. J., MARSH, S. E. & HERRMANN, S. M. 2006. Multi-sensor NDVI data continuity: Uncertainties and implications for vegetation monitoring applications. Remote Sensing of Environment, 100, 67-81.

Chapter 2. Habitat highs and lows: Comparing terrestrial and UAV LiDAR for modelling avian species richness and abundance in a restored woodland**.**

Authors: Shukhrat Shokirov[1,2], Tommaso Jucker[3], Shaun R Levick[2], Adrian D. Manning[4], Timothee Bonnet[1], Marta Yebra[4], Justin Borevitz[1], Kara Youngentob[1]

[1]Research School of Biology, Australian National University, Australia

[2]Commonwealth Scientific and Industrial Research Organization, Land and Water, Australia

[3]School of Biological Sciences, University of Bristol, Bristol, UK

[4]Fenner School of Environment & Society Australian National University, Australia

Abstract

Vegetation structure influences landscape use and habitat quality for many bird species. Owing to the difficulties associated with collecting structural data from traditional field measurements, numerous studies have investigated the utility of Light detection and ranging (LiDAR) for providing landscape-scale structural information that may be useful for wildlife habitat assessments and to explore plant-animal interactions. Notably, almost all of these studies have involved the use of LiDAR from airborne rather than terrestrial platforms. Many LiDAR structural metrics that have been shown to be important for explaining bird species occurrence and diversity, such as vegetation complexity in the understory and ground-layer and overall vegetation volume, may be partially obscured from airborne sensors by tree canopy cover. For the first time, we collected terrestrial LiDAR (TLS) and unmanned aerial vehicle (UAV) LiDAR (ULS) data in a woodland landscape to compare the ability of both sensors to identify relationships among vegetation structural metrics and bird species richness and abundance. Individual species abundance models provided better prediction power (mean R^2 = 0.311 (TLS), R^2 = 0.305 (ULS)) than bird community abundance by functional guilds (mean R^2 = 0.226 (TLS), R^2 = 0.235 (ULS)), overall bird abundance (R^2 = 0.097 (TLS), R^2 = 0.164 (ULS)), species richness (R^2 = 0.139 (TLS), R^2 = 0.141 (ULS)) and diversity (R^2 = 0.171 (TLS), R^2 = 0.161 (ULS). Canopy roughness, vertical complexity of the first vegetation layer, total vegetation volume and canopy height were among the most common significant variables in explaining avian biodiversity and individual species abundance. Our study revealed that several vulnerable bird species are strongly associated with LiDAR structural variables, which may assist with habitat assessment and conservation management. Overall, TLS and ULS models provided similar results. However, contrary to our initial expectations, ground layer vegetation complexity, which typically showed a strong positive relationship to ground foraging species, was detected better by ULS than TLS in this open woodland landscape due to low-lying occlusions, like coarse woody debris and shrubs, in the TLS field of view.

Introduction

Vegetation structure as important habitat elements for avifauna

Vegetation structure is the horizontal and vertical arrangement of plants across the landscape (Verschuyl et al., 2008, Davies and Asner, 2014) . Vegetation structural complexity and heterogeneity have been shown to have a positive relationship to biodiversity because they create a greater variety of microclimate and microhabitats that produce more food and cover for a range of species (Verschuyl

et al., 2008). MacArthur et al. (1961) first identified the importance of the vertical distribution of foliage density for bird species diversity. They found a strong relationship between bird species diversity and the height profile of foliage density that was structure driven, since it was not related to vegetation species diversity. Notably, they also found that foliage density at ground (<2 m), midstory (2-25 m) and canopy (>25 m) layers appeared to contribute equally to bird diversity. Subsequent studies have also identified strong relationships between bird biodiversity and abundance and vegetation structure. For example, bird species abundance was found to be strongly associated to canopy, sub-canopy and understory biomass (Stanley and Herman, 1974). Kikkawa (1982) identified a strong relationship between bird abundance and various forest structural attributes including foliage height diversity and canopy cover. Research by Sekercioglu et al. (2002) identified significant relationships between the horizontal heterogeneity of trees and forest dependent bird abundance and species richness.

Remote sensing of vegetation structure

Several metrics of forest structural complexity have been developed to estimate vertical and horizontal vegetation height, volume, variation, canopy cover, coarse woody debris and dead standing wood (James and Shugart Jr, 1970, Verschuyl et al., 2008). Traditional methods to derive these metrics typically involve plot level measurement that are very time consuming, can be particularly difficult in rough terrain or dense understories, and assess only a fraction of the available vegetation that is then extrapolated to wider areas (James and Shugart Jr, 1970, Zehm et al., 2003, David et al., 2010). The development of aerial photography and satellite-based multispectral imagery (e.g. Landsat) from the early 1970s offered spectral reflectance measurements of vegetation attributes that could be collected much more rapidly over wide areas, such as biomass, plant canopy cover and leaf area index (Rouse et al., 1974, Tucker, 1979). While useful for looking at relationships between habitat heterogeneity and bird species richness (Turner et al., 2003, Leyequien et al., 2007), these sensors were only capable of providing imagery data in two-dimensions (i.e., XY coordinates). They were unable to provide three-dimensional (Z coordinates) measurements such as canopy height variability and vegetation complexity in different forest layers, which are necessary for assessing various aspects of vegetation structure (Lefsky et al., 2002, Turner et al., 2003), which also may be important habitat criteria for many animals (MacArthur, 1961, Goetz et al., 2007, Vierling et al., 2008).

The introduction of Light Detection and Ranging (LiDAR) remote sensing technology provided high-resolution topographic maps and information on vegetation height, cover, volume and vegetation complexity with a high level of detail and accuracy (Lefsky et al., 2002, Goetz et al., 2007, Levick et al., 2019). Unlike passive sensors like, Landsat, IKONOS, Sentinel or aerial photography that depends

on sun light reflected from objects, LiDAR is based on the use of a laser pulse emitted from a sensor and reflected back from objects. Reflected light is detected and digitized by the sensor creating a record of returns that are a function of the distance between the sensor and the reflected object (Lefsky et al., 2002, Goetz et al., 2007, Anderson et al., 2016).

Discrete return LiDAR sensors measure one or more returns from each emitted laser pulse (Lefsky et al., 2002, Anderson et al., 2016). Multiple return sensors may provide more detailed information than single return sensors, since each light pulse may return from a different object depth in the field of view (Anderson et al., 2016, Jucker et al., 2018). Full-waveform sensors record the time-varying intensity of the returned energy from each laser light pulse, which provides a record of height distribution of the surface features. The major difference between discrete and waveform is that the discrete return sensors measure major peaks on the vegetation surface; however, waveform return sensors capture the entire signal trace on the surface for later processing (Lefsky et al., 2002, Anderson et al., 2016). LiDAR sensor platforms can be terrestrial (Terrestrial Laser Scanner - TLS), mobile, UAV (Unmanned Aerial Vehicle - ULS), airborne (Airborne Laser Scanner - ALS) or satellite based (Vierling et al., 2008, Sumnall et al., 2016).

LiDAR derived vegetation structure and bird species richness and abundance

Vegetation structural metrics derived from LiDAR data have been widely used to investigate animal - habitat relationships, with a particular focus on birds (Bradbury et al., 2005, Goetz et al., 2007, Müller et al., 2010, Eldegard et al., 2014). In one of the first comparisons between passive and active sensor capabilities for this purpose, Goetz et al. (2007) found that LiDAR derived canopy height distribution variables proved to be a stronger predictor of bird species richness in temperate forest ecosystems than a commonly used Normalized Difference Vegetation Index (NDVI) derived from Landsat imagery. Another study identified relationships between bird presence and canopy height percentiles, standard deviation of laser returns and canopy density metrics calculated from LiDAR data from a boreal forest (Eldegard et al., 2014). LiDAR derived vegetation structure, such as foliage height diversity, vegetation volume and shrub density were also found to be significantly correlated to bird species diversity and density in forest environments (Clawges et al., 2008). Moreover, forest songbird species richness and species richness by different functional guilds have been predicted from LiDAR-derived canopy and mid-story height and mid-story density in mixed hardwood forest (Lesak et al., 2011). Researchers also investigated the usefulness of LiDAR-based structural metrics for predicting bird species diversity and richness in broad-leaved forest (Sasaki et al., 2016). They found that total vegetation volume was the strongest predictor of species richness whereas forest canopy gap had a strong correlation with species diversity. Another study found that bird species richness increased with

canopy horizontal heterogeneity calculated from LiDAR data; however, vertical heterogeneity had a negative effect on species richness (Carrasco et al., 2019). A review by Davies and Asner revealed that 23 avian studies found a positive relationship between species richness and abundance and canopy structural diversity and vertical distribution of vegetation. In particular, vegetation structural heterogeneity appeared to have a stronger relationship to bird observations than canopy cover alone (Davies and Asner, 2014).

Notably, almost all of the studies that used LiDAR to investigate relationships between vegetation structure and habitat quality for birds have used airborne or UAV LiDAR data (Eldegard et al., 2014, Sasaki et al., 2016, Carrasco et al., 2019). While airborne platforms provide accurate information on upper strata vertical structure and volume of vegetation, they may be limited in their ability to measure vegetation metrics in the ground and mid layers because of weak penetration of ALS pulses through the upper canopy (Bakx et al., 2019, LaRue et al., 2020, Crespo-Peremarch et al., 2020). A recent review analyzed 50 papers on bird species distributions and species richness in relation to LiDAR-based vegetation variables (Bakx et al., 2019). It was found that most of the studies used low density ALS data, usually 10 points/m^2, which have limited penetration below the canopy, especially to ground layer vegetation. Authors recommended that future studies should focus on higher density point clouds that can capture more detail below the canopy, as the lower strata of vegetation is also important for many bird species (Bakx et al., 2019). They also suggested that, in addition to the widely used horizontal and height diversity vegetation metrics, future research should also consider vegetation volume in different strata, which can be calculated from voxelized point cloud. Voxelized point cloud means creating three-dimensional grids or so called “voxels” from one or more LiDAR points (Sasaki et al., 2016).

Terrestrial LiDAR can generally provide more detailed information on vegetation below the canopy of forests and woodlands because it measures the vegetation from the ground level and typically with higher resolution (LaRue et al., 2020). However, depending on the vegetation height and density, TLS can also suffer from occlusions, particularly in the canopy but also in other strata where vegetation or other landscape structural features block the field of view, resulting in gaps of information (LaRue et al., 2020, Crespo-Peremarch et al., 2020). Several studies have investigated the best placement of terrestrial LiDAR sensors in the landscape depending on the density of trees and area of measurement to provide the most complete coverage (Trochta et al., 2017, Muir et al., 2018). There is always a trade-off between the amount of time required to repeatedly position the scanners to collect the data and the completeness of the data coverage. The automatic registration of ALS and TLS point clouds allows data to be combined from multiple perspectives and this can help resolve some occlusion issues; however, this is time-consuming as well (Dai et al., 2019). Data collection with TLS can also be

impaired by the difficulties associated with traditional field data collection in inaccessible areas with dense understories. Even in relatively open landscapes, TLS data collection is usually slow and is typically only applied to smaller areas (< 1 ha) (Liang et al., 2016a). However, in open woodlands in particular, TLS may offer some advantages for measuring vegetation structural metrics that are known to be important predictors of bird habitat quality and the occurrence and diversity of bird species (Michel et al., 2008).

For the first time, we compare the performance of high density TLS and ULS LiDAR derived landscape structural variables for modelling community, functional trait and species level bird abundance in an Australian woodland landscape which can also be applicable to various forest environment across the globe. We used the data from both sensors to test the following hypotheses:

(1) TLS and ULS data can be used to accurately classify field-measured vegetation classes;

(2) high density TLS LiDAR point clouds will perform better for modelling overall bird abundance, species richness and diversity than lower density ULS point clouds, and;

(3) the relationship between landscape structural data and particular bird species and groups will be modelled more accurately from the TLS platform for bird species and guilds that are most associated with ground and mid-story vegetation layers and ULS for those that primarily use the canopy strata.

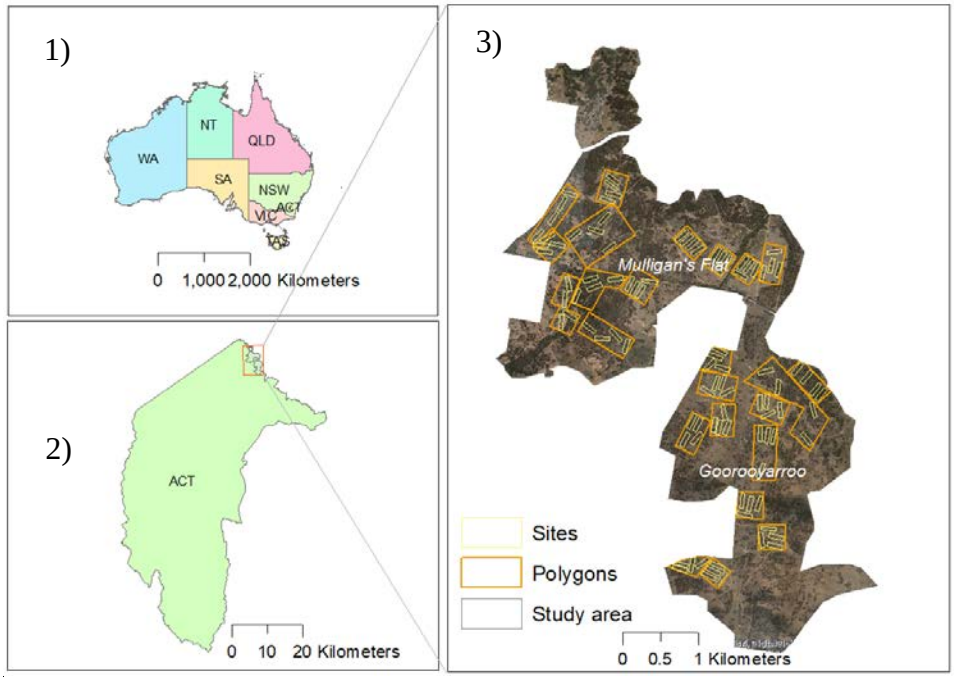

Figure 1. Map of study area. 1) Australia, 2) Australian Capital Territory (ACT), 3) Mulligan's Flat-Goorooyarroo Woodland Sanctuaries: Yellow color show 96, 1 ha sites, orange color show 24 polygons with four vegetation types.

Methods

Study area

The study area comprises Mulligan's Flat (683 ha) and Goorooyarroo (702 ha) nature reserves (MFGO) in the north-eastern corner of the Australian Capital Territory (ACT), Australia (35°09' S - 149°09' E; Fig. 1). These two adjacent reserves were established in 1994 and 2006 respectively to conserve and restore a critically endangered grassy woodland ecosystem (Manning et al., 2011). Locally common tree species include Blakely's Red Gum (*Eucalyptus blakelyi*) and Yellow Box (*E. melliodora*) with a relatively open midstory of primarily *acacia spp*. The grassy ground-layer vegetation is dominated by *Joycea pallida, Austrodanthonia spp*., *Themeda australis* and *Aristida ramose* (McIntyre et al., 2010, Shorthouse et al., 2012, McIntyre et al., 2014). Prior to becoming reserves, MFGO was leasehold grazing land with some areas of past cropping and pasture improvement (Manning et al., 2011, Shorthouse et al., 2012). The topography is gently undulating with a few hills and the elevation ranges from 650 m to 700 m. Average daily temperature in 2018 ranged from a minimum of 6.9˚C to a maximum of 22.0 ˚C, and mean annual rainfall was 472.0 mm (Bureau of Meteorology, 2019).

Restoration activities have been undertaken in an attempt to restore the function and biodiversity of the areas, and feral predators and grazers have been excluded with purpose built fencing around the reserves (Manning et al., 2013). To monitor ecosystem recovery over time, animal and vegetation surveys are periodically conducted across 96, 1 ha plots (200m x 50 m). These plots are stratified across the reserves in 24 clusters that include four different vegetation types: 1) high tree cover, high shrub cover (HTHS), 2) high tree cover, low shrub cover (HTLS), 3) low tree cover, low shrub cover (LTLS), and 4) low tree cover, high shrub cover (LTHS). Each plot is marked in the field along the long axis by plastic pegs at the 0 m and 200 m points, and with star pickets (A and B) at the 50 m and 150 m points (Manning et al., 2011). Bird surveys have been conducted twice a year since 2005 at each plot using an acoustic and visual point count method (Manning et al., 2011).

Bird data collection

As part of long-term monitoring at MFGO, annual bird surveys are conducted during two separate visits by different, experienced bird observers in October using an acoustic and visual point count method (Manning et al., 2011). For this study, we used bird data collected within a year of LiDAR data collection (i.e., survey periods from 2017 to 2019), because it is unlikely that the vegetation

structure would have changed substantially in the period between LiDAR data acquisition and bird counts. During the surveys, observers stand at the A and B star picket at the 50 m and 150 m position along the long axes of each plot. The presence and abundance of birds in concentric bands (0 – 25 m, 25 – 50 m, 50 – 100 m and over 100 m and overhead) are recorded for ten minutes. Detailed information about bird survey methods are provided in (Manning et al., 2011).

TLS data collection and post - processing

Terrestrial LiDAR data was collected with a Topcon GLS2000 (Topcon Corporation, Japan). The Topcon GLS2000 is a high-density laser scanner that emits near-infrared light (1064 nm) laser pulses at up to 120,000 laser pulses per second. The field-of-view of the scanner is 360° and 270° (horizontal and vertical direction, respectively). The beam diameter of the single pulse is 4 mm at 60 m. We conducted a pilot study in March 2018 to determine the best method to characterize the 96 X 1 ha (50 m X 200 m) experimental sites with TLS data to achieve the most complete coverage within a timeframe that would allow us to scan all of the sites within a month.

We collected TLS data at 1.7m scanner height with 6 mm point spacing at 10 m distance from the scanner. Data were collected from 5, 6 and 7 scanning stations in a test site (Fig 2). These stations were established in a zigzag formation with approximately equal spacing between the stations to cover the 200 m x 50 m site. Data collection was performed with and without co-registering the scanning stations to determine whether co-registration during collection was more efficient than later co-registration during post-processing. Co-registration allows a surveyor to tie multiple scans in the same plot together using targets directly in the field. However, this method requires more time to place and scan targets and could reduce the number of scan points within a site in a given timeframe (Liang et al., 2016b, Blakey et al., 2017). We found that data could be co-registered effectively during post-processing, and that allowed us to maximize the number of scans collected in the field. From 1th to 31th October 2018, we collected seven individual scans without co-registration in all 96, 1 ha sites for a total of 672 scans with 6 mm at 10 m scanning resolution. The position of each scan was measured with a differential GPS (Trimble Geoexplorer 6000 series) and post-processing was performed using local base station data to improve the point location accuracy to approximately 50 cm.

Point clouds from seven individual scan stations were co-registered using Multi-station Adjustment (MSA) plugin in RiScan Pro software (RIEGL Laser Measurement Systems GmbH). Co-registering point clouds with MSA consists of two steps: manual and automatic registration. First, point clouds from two scans have been manually coarsely aligned by using the overlapping objects (trunks, trees and shrubs) in both scans. Then, automatic registration was implemented which uses at least four identical points from overlapping areas of two scans. The MSA uses the iterative closest points (ICP)

algorithm that minimizes the 3D distance between the identical points by translating and rotating the entire point cloud along X, Y, Z axes until the least minimum distance between the identical points from two dataset is achieved (Šašak et al., 2019). Following, the position and orientation of the first and second scan was locked and the same procedure was performed to register the third scan to the initial two scans.

Next, the point cloud from each site was georeferenced using DGPS locations of each scan position measured in the field and clipped to the spatial extent of each 96 site. Point clouds were then subsampled into 1 cm spacing to homogenize the point distributions and duplicate points have been removed using Cloud Compare (CloudCompare 2.10.2).

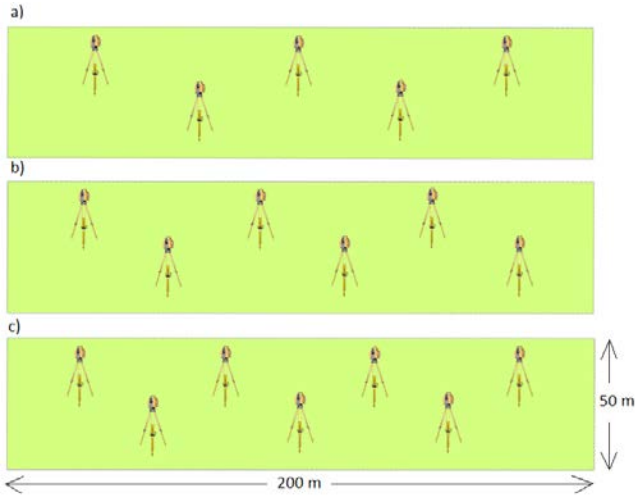

Figure 2. Test scan positions: a) 5 scans, b) 6 scans and c) 7 scans for 200 m by 50 m size sites.

ULS data collection and post-processing

We collected ULS LiDAR data across all of the 96, 1 ha sites in fine weather conditions from November 7th – 14th, 2018. The ULS LiDAR platform consisted of a quadcopter integrated with RIEGL miniVUX-1UAV LiDAR sensor (RIEGL Laser Measurement Systems GmbH, Austria) and APX INS/GNSS system (Trimble, USA). The flights were performed at approximately 90 m above the take off point with approximately 25.2 km/h speed, up to 5 returns per pulse, 100 kHz pulse repetition rate, and up to 100,000 measurements/second. Maximum scan angle of the LiDAR sensor was approximately ±60º with swath width about 100 m. On average the four adjacent plots were covered by 500×500m flight area which was covered by around 11 parallel lines and one diagonal flight line on the return to landing. However, it is difficult to know what the average number of flight lines per plot as it was depended on where they were in the area we flew and their orientation. We used DJI ground station pro V2 to plan the flight missions (SZ DJI TECHNOLOGY CO., 2018). The ULS

LiDAR sensor failed to collect data on two sites, which were excluded from further analysis of ULS and TLS data. Data processing was done in RiPROCESS software suite by RIEGL which allowed to bring in the trajectory data of the drone flight, align the flight paths, georeference the point cloud and then export it in LAS format. The trajectory data of the UAV LiDAR that was feed into RiPROCESS was generated using POSPAC UAV (Applanix) using the IMU/GNSS data from the drone and RINEX data from the base station which was obtained from Gungahlin location of Smartnet global network. The ULS LiDAR data collected over the 94 sites were clipped by corresponding polygons to create separate point cloud for each site. Point spacing in ULS data across 94 sites ranged from 5 cm to 17 cm with an average of 10 cm. For this reason, we homogenized the point cloud with 10 cm spacing and removed duplicate points using Cloud Compare (CloudCompare 2.10.2).

Canopy height model

Point clouds were cleaned from noise points and classified into ground and non-ground points using *LAStools* (Isenburg, 2012). We normalized point clouds by converting elevation values to height above ground values with *LAStools* (Isenburg, 2012) (Fig. 3).

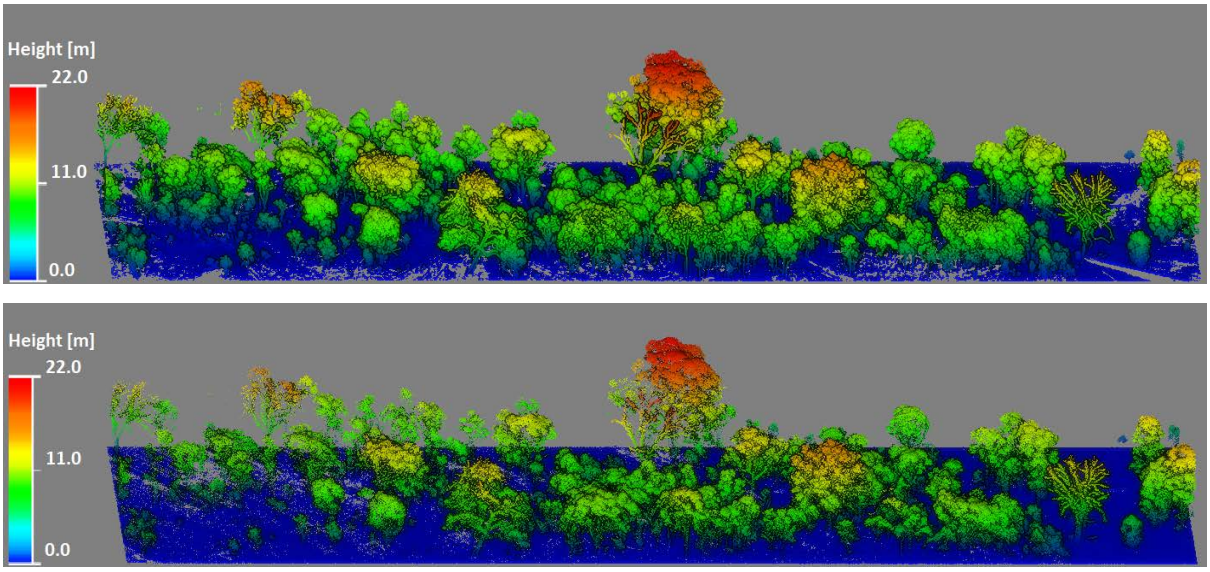

Figure 3. Normalized TLS point cloud of site GO72A-3 colored by height (top) and normalized ULS point cloud of plot GO72A-3 colored by height (bottom).

Calculating landscape variables from the LiDAR dataset

Canopy metrics were calculated from points above 1.3 m (Table 1). Based on existing vegetation layer descriptions for eucalypt grassy woodlands (Department of Environment, 2013), we divided the point cloud into three layers representing the ground layer (≤1m), the mid-story (> 1m to 10m) and the

upper story (> 10m) (Fig. 4) and calculated additional vegetation metrics for each layer (Table 1). Vegetation volume was estimated by excluding ground points and constructing 0.5 m voxels (volumetric pixels) from point clouds, with each voxel made of one or more points. A fraction of woody canopy cover for each site was calculated by creating 0.25m grids from points above 1.3m and dividing the sum of the areas of all pixels by the size of the total area of the site (200m×50m). A total of 37 metrics were computed with lidR package (Roussel, 2017). List of LiDAR –derived landscape variables and descriptions are provided in Table 1.

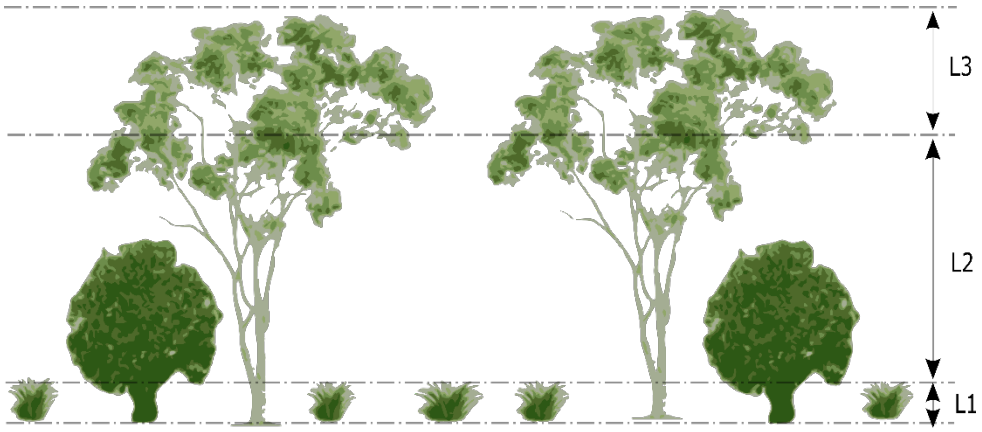

Figure 4. Vegetation layers: L1 - ground layer (L1 > 1m), L2 - mid-story layer (1m < L2 < 10m), L3 - upper story layer (L3 > 10m).

Table 1. Description of calculated landscape structural variables from LiDAR dataset

Name of variable	**Description**
maxH	Maximum height of canopy (points > 1.3m). High maximum value means there are big trees in the site.
meanH	Mean height of canopy (points > 1.3m). If the value is higher, the site has more big trees, if the value is lower, more shrubs and regeneration trees abundant in the site.
stdH	Standard deviation of canopy height (points > 1.3m). It describes the variation in the canopy height.
skewH	Skewness of canopy height. Negative skewness – the distribution dominated by higher points (upper canopy is dominant) but a few extreme lower points, positive skewness - the distribution dominated by lower points (lower canopy is dominant) but a few extreme higher points, (points > 1.3m).
kurH	Kurtosis of canopy height. Negative kurtosis – the distribution centered on mean values (mid-canopy is dominant), without much

	higher or lower canopy, positive kurtosis – the distribution heavy on tails, with more at the high and low ends and less in the center (lower and upper canopy is dominant), (points > 1.3m).
p_05, p_10, p_25, p_50, p_75, p_90, p_95, p_99	Canopy height percentiles. Canopy height percentile here was defined as the height below which a specified percentage of total point clouds were located, (points > 1.3m). For example, p_05 = 2.0 m means that 5% of vegetation points found below 2 m. Vegetation density is higher at p_05 = 2.0 m than p_05 = 3.0 m.
vci_2m, vci_5m, vci_10m, vci_15m, vci_20m	Vertical complexity indexes (VCI) at 2m, 5m, 10m, 15m, 20m height bins, (points > 1.3m). Vertical complexity indexes (VCI) at 2m, 5m, 10m, 15m, 20m height bins, (points > 1.3m). $$VCI = (-\sum_{i=1}^{HB}[(p_i \ln(p_i)]))/\ln(HB)$$ Where *VCI* in a vertical complexity index, *HB* is the total number of height bins, and p_i is the proportional abundance of LiDAR returns in height bin *i*. A VCI value close to one indicates that most height bins have equal amount of vegetation. VCI value decreases if the distribution of canopy in the height bin becomes more uneven (van Ewijk et al., 2011).
cov	Fraction of canopy cover, (points > 1.3m).
height_cv	Coefficient of variation of height, (points > 1.3m). Indicates the canopy height variation.
canopy_roughness	Canopy roughness describes complexity/variability of canopy height (Herrero-Huerta et al., 2020) (points > 1.3 m). Higher variability in the canopy height provides higher roughness index and vice versa.
canopy_shannon	Normalized Shannon diversity index of canopy (Pretzsch, 2009), (points > 1.3m). Indicates canopy height diversity.
tvolume	Total vegetation volume (m^3) – number of 0.5 m^3 voxels divided by 8 (ground points excluded).
vlayer_L1	Vegetation volume (m^3) in 1st layer (points 0-1m¸ ground points excluded).

vlayer_L2	Vegetation volume (m^3) in 2^{st} layer (points 1m-10m).
vlayer_L3	Vegetation volume (m^3) in 3^{st} layer (points 10m and above).
meanH_L1, meanH_L2, meanH_L3	Mean height of 1^{st}, 2^{nd}, 3^{rd} layer.
sdH_L1, sdH_L2, sdH_L3	Standard deviation of vegetation height in 1^{st}, 2^{nd}, 3^{rd} layer.
roughness_L1, roughness_L2, roughness_L3	Roughness indexes of 1^{st}, 2^{nd}, 3^{rd} layer (Jenness, 2004). Horizontal distribution of vegetation across different layers.
vci_L1, vci_L2, vci_L3	Vertical complexity indexes of 1^{st}, 2^{nd}, 3^{rd} layer (van Ewijk et al., 2011). Vertical distribution of vegetation across different layers.

Statistical analysis

Bird data

We calculated bird abundance (maximum number of individual birds counted), species richness (cumulative total number of species), Shannon diversity index using "vegan" R package (Jari Oksanen, 2019) and functional diversity indices including functional richness, functional evenness, functional divergence, functional dispersion and Rao's quadratic entropy for each site using "FD" package (Laliberté and Legendre, 2010) in R language (R Team, 2019). Shannon diversity index is used to characterize species diversity in a community (Morris et al., 2014). Functional richness defined as the amount of niche space occupied by the species within a community. Functional evenness measures the regularity of the distribution of species abundances and dissimilarities in a functional space. Functional divergence is the degree to which abundance distribution in niche space maximizes divergence in functional characters within the community (Mason et al., 2005). Functional diversity indices quantify the trait diversity and act as a surrogate for the diverse ecological functions performed in the community. Rao's quadratic entropy measures the diversity of ecological communities and is based on the proportion of the abundance of species in a community and a measure of dissimilarity between the species (Ricotta and Szeidl, 2009). The diversity of trait values within a community is therefore referred as either trait diversity or functional diversity (FD) (Karadimou et al., 2016).

Bird guilds were assigned based on different functional traits (i.e., grassland specialist, water bird, woodland generalist, woodland specialist), nesting substrate (i.e., arboreal, ground, hollow,

opportunistic, understory), foraging substrate (i.e., air, aquatic, arboreal, ground, opportunistic), and dispersion (low, partial, high).

Model selection process

A key stratifying unit of the plots established in our study area were the clusters, which were comprised of four vegetation types (HTHS, HTLS, LTLS, LTHS) (Manning et al., 2011). We first explored the ability of ULS and TLS data to correctly classify plots according to these vegetation categories. We used a multinomial regression model using "multinom" function in "nnet" R package (Venables and Ripley, 2003) for this analysis. We tested two models, one based on the first four principle components calculated from all the TLS and ULS LiDAR variables and a model based on selected TLS and ULS LiDAR variables.

To select the variables for the selected-variable model, we first used a correlation matrix based Principal Component Analysis (PCA) (Kassambara, 2017) to visualize the data and plotted the contribution of each variables to first two principal axes using *factoextra* R package (Mundt, 2020) (Fig. 5). To avoid strong collinearity between 37 LiDAR variables, we then selected variables that were not highly correlated (0.7 maximum threshold) in keeping with other studies (Dormann et al., 2013) (Sasaki et al., 2016). Pearson correlation matrices of TLS and ULS variables are provided in Appendix 1 and Appendix 2 respectively. When selecting between two highly correlated variables, we attempted to select for the most ecologically meaningful variable (e.g. average height (*meanH*) and 75th percentile height (*p_75*) resulted in a selection for average height"). We also selected at least one variable from each layer and several canopy metrics to cover all strata of vegetation in the landscape. Our assumption was that bird communities and trait groups rely on different layers of vegetation volume or structural complexity and we wanted to capture that range in the selected variables. All explanatory variables were standardized so that they have a mean of zero ("centering") and standard deviation of one ("scaling") (Becker et al., 1988). This ensures that the estimated coefficients are all on the same scale, making it easier to compare effect sizes.

We tested the performance of both the 12 selected variables and the first four PCA variables to investigate relationships between the LiDAR metrics and overall bird abundance, species richness and diversity. For the remainder of our analyses, we used the model type that most accurately classified the plots into their appropriate landscape class.

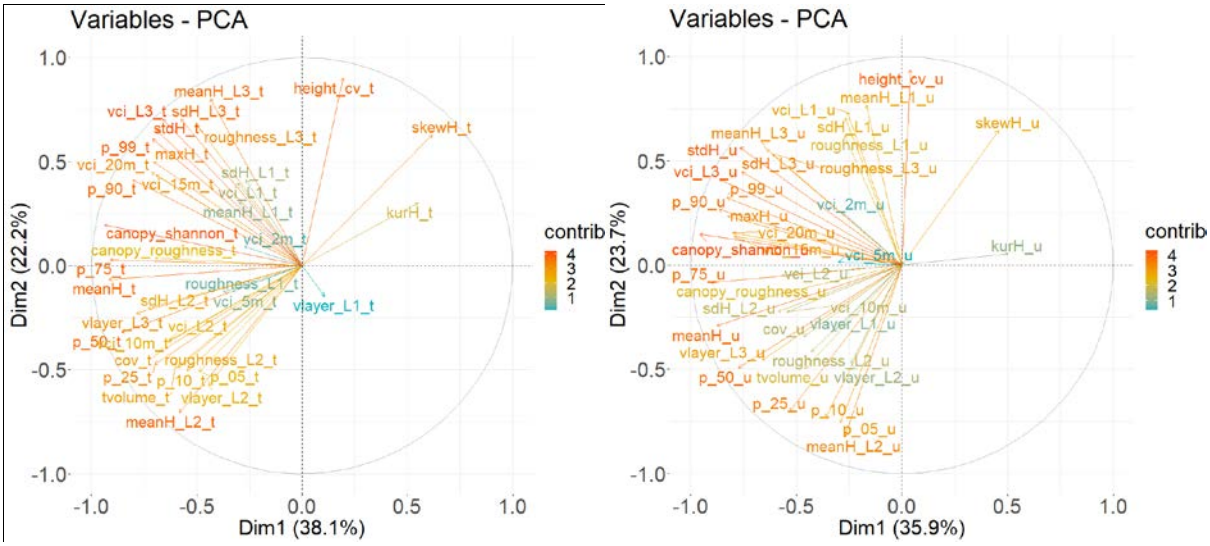

Figure 5. Contribution of TLS (left) and ULS (right) LiDAR variables for the first and the second PCA axis

Overall bird abundance, species richness and diversity

To evaluate which LiDAR based vegetation structural variables had the strongest relationship to bird abundance, species richness, species diversity, and functional diversity of birds across plots, we fitted linear mixed effects models with lmer function in lme4 package in R (Bates et al., 2015). Mixed models extend the basic linear model such that they recognize grouped or nested structures in data by random effects (Melin et al., 2018). In these models, predictor variables were the selected vegetation structural metrics (fixed effects) and 24 polygons by four vegetation classes (random effects). Response variables were bird abundance, species richness, species diversity and functional diversity indexes. We also tested the performance of the first four principle components (PCA1, PCA2, PCA3, PCA4) calculated from all LiDAR metrics as explanatory variables in these model to see how it preformed compared to the selected variables model that we used for all analyses.

Bird abundance within functional guilds

Correlations between bird abundance within functional traits and vegetation structural metrics were evaluated using Poisson distribution Generalized Linear Mixed Effects Models (GLMM) with glmer function in lme4 R package (Bates et al., 2015). Explanatory variables for these models were selected vegetation structural variables (fixed effects) and 24 clusters by four vegetation classes (random effects), where abundance within functional guilds were response variables.

Individual bird species abundance

The relationship between individual bird species abundance and LiDAR structural metrics were also examined using GLMMs. In these models, explanatory variables were the selected TLS and ULS

LiDAR variables (fixed effects) and 24 clusters by four vegetation classes (random effects), and response variables were the abundance of each different bird species in our dataset. An overview of variable selection and modelling is provided in Fig. 6.

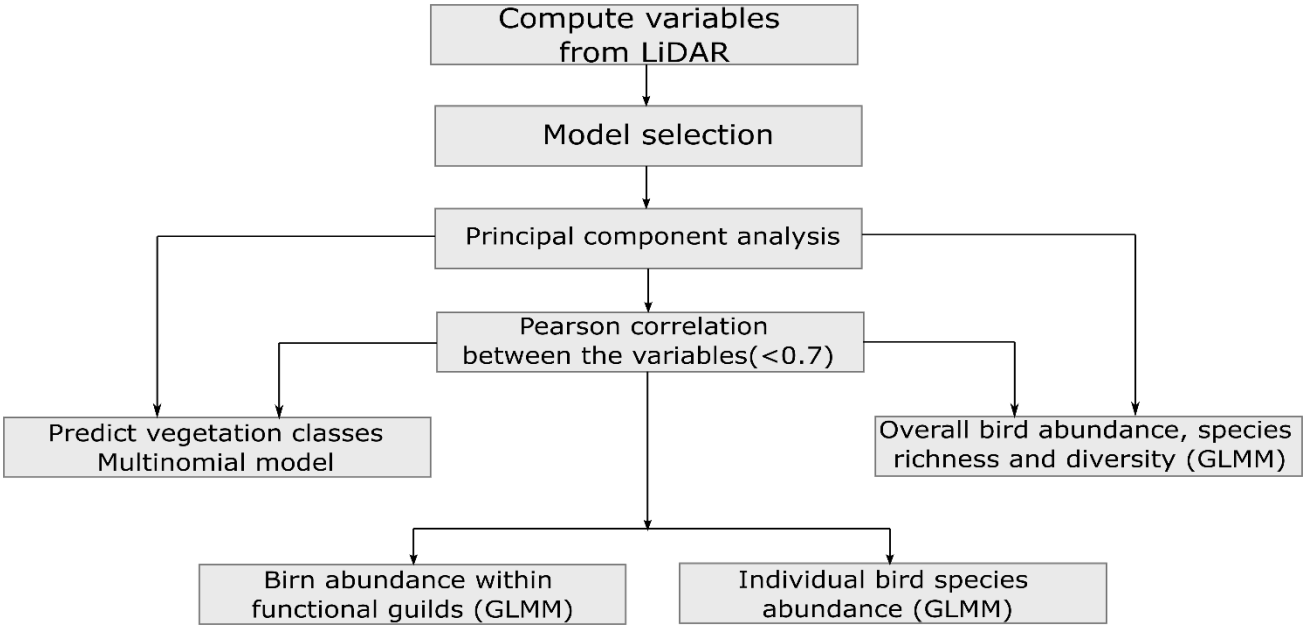

Figure 6. Variable selection and modelling workflow

Examination of model fit

We used Residual Diagnostics for HierARchical Models (DHARMa) package (Hartig, 2017) for examining the model fit, dispersion, zero-inflation, residual spatial and temporal autocorrelation problems. Marginal and conditional R^2 were calculated to evaluate proportion of variance explained by fixed and mixed effects for models by species and guilds (Nakagawa et al., 2013).

Examination of each model revealed that some models did not converge. By further evaluating these models, we found that those models had very few count data in species abundance or functional traits. To solve this, we retained the species or guilds that had at least 10% count data across the sites. This means that each species or guild should have counts at 10 or more sites to be valid for modelling. Of an original 84 individual bird species, 51 species across 16 functional guilds occurred in at least 10 sites for modelling. If the model convergence issue persisted, which happened in five individual species abundance models, we were able to resolve this by decreasing the number of fixed effects by removing those with the lowest explanatory values.

Significance of predictor variables for each model were demonstrated by z score with significance threshold of $z = 1.96$ (equal to $p < 0.05$).

Results

Statistical analysis produced several interesting outcomes including number of birds and species richness, relationship between TLS and ULS derived vegetation structural variables, power of TLS and ULS data for predicting different vegetation classes and more importantly association between LiDAR variables and avian species in community and individual species level. Details have been provided in following subsections.

Bird data

A total of 12117 birds observations (5540 in Mulligan's Flat and 6577 in Goorooyarroo nature reserves) from 84 bird species were observed from the double surveys each year across the three year period from 2017 to 2019. A maximum of 238 birds and 36 species and a minimum of 42 birds and 10 species were counted in any one site (Table 2).

Table 2. Basic statistics from bird data across plots. Abundance - bird abundance, SR - species richness, Bird_shannon - shannon diversity, FRic – functional richness, FEve – functional evenness, FDiv – functional diversity, FDis – functional dispersion, RaoQ - Rao's quadratic entropy

Statistics	Abundance	SR	Bird_shannon	FRic	FEve	FDiv	FDis	RaoQ
Maximum	238.00	36.00	3.22	0.09	0.82	0.96	0.29	0.09
Mean	126.22	21.97	2.63	0.01	0.67	0.87	0.24	0.07
Stdev	42.60	5.91	0.35	0.02	0.07	0.04	0.02	0.01
Median	121.50	22.00	2.69	0.01	0.67	0.87	0.24	0.07
Minimum	42.00	10.00	1.68	0.00	0.50	0.78	0.17	0.04

Variable selection

The Pearson correlation matrix showed that most of the TLS and ULS variables are strongly correlated to each other ($r > 0.7$) (Fig. 7). Only the L1 metrics and lower strata canopy metrics showed a weak correlation ($r < 0.3$) .

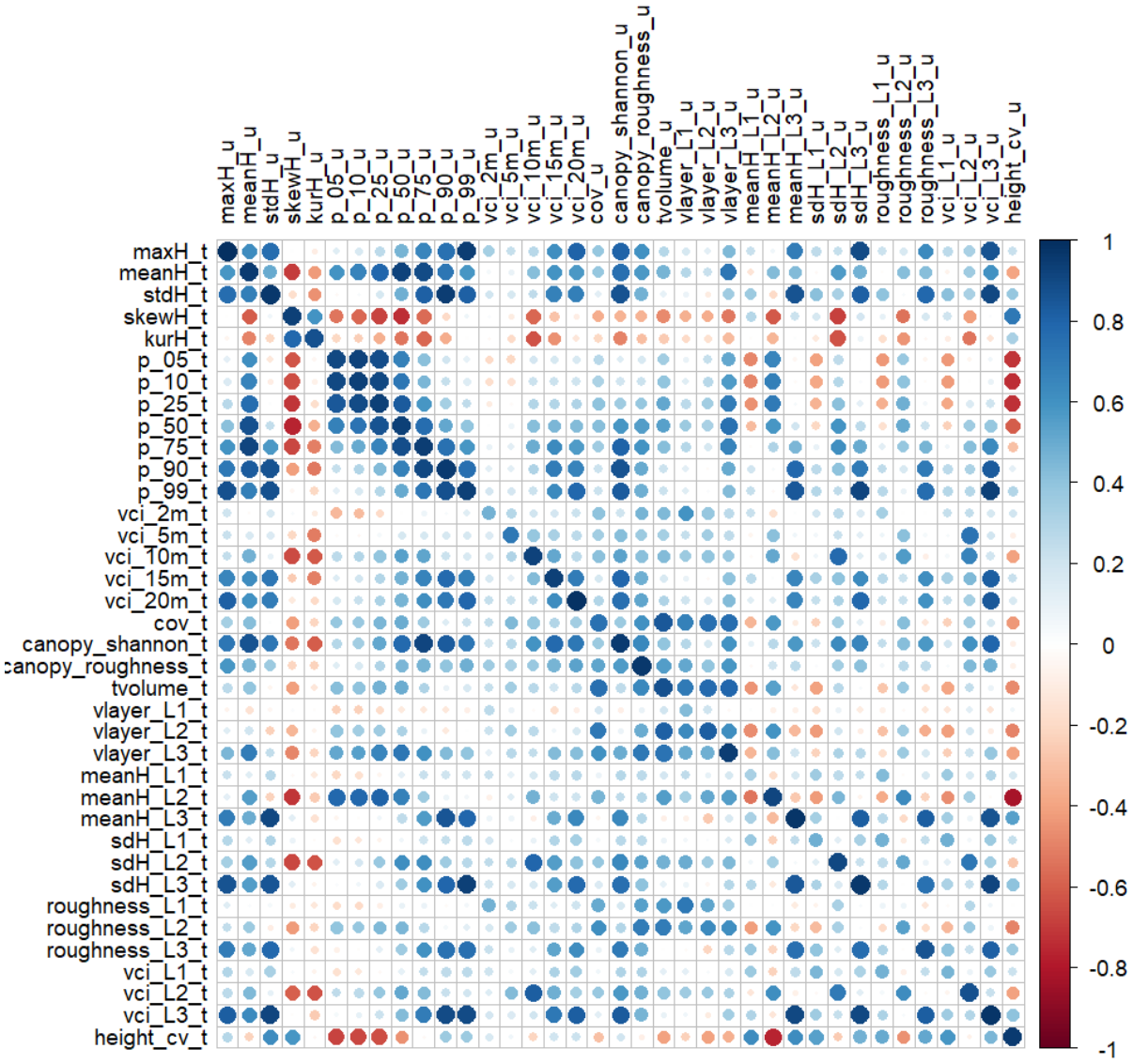

Figure 7. Correlation matrix of TLS (Y axis) and ULS (X axis) variables

Our variable selection method resulted 12 out of 37 LiDAR metrics being selected for the models. Basic statistics for these TLS and ULS variables are provided in Figure 8.

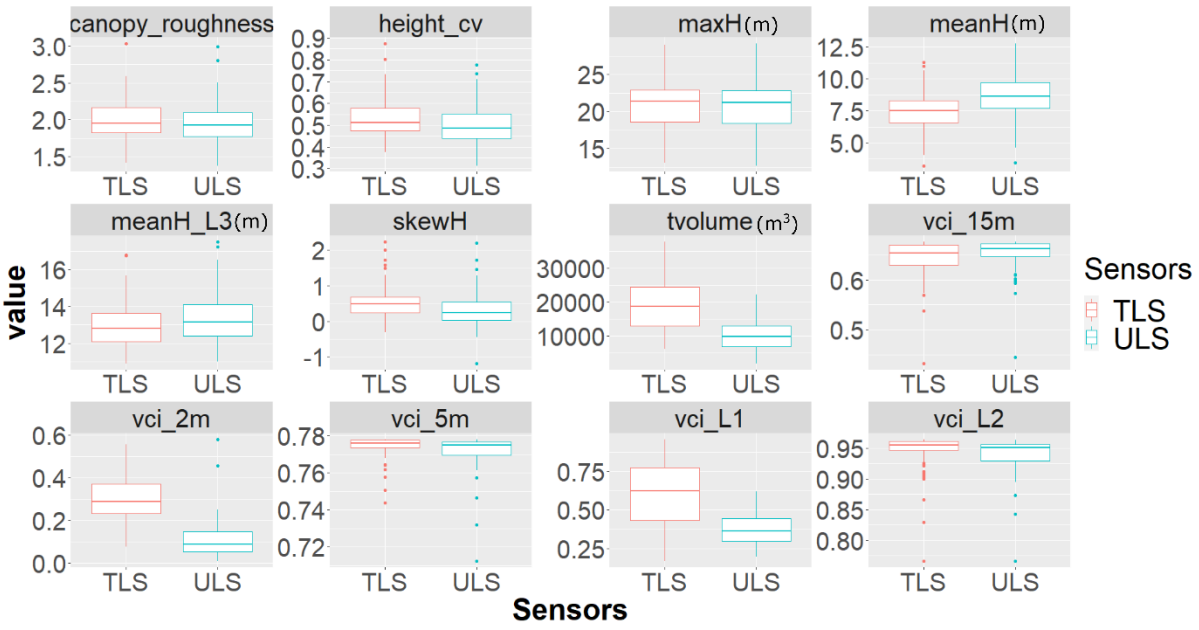

Figure 8. Boxplots represent a basic statistics of selected TLS and ULS variables

Predicting vegetation classes from the LiDAR dataset

Multinomial regression models showed that selected LiDAR variables provided better accuracy in predicting vegetation classes than the first four PCA variables for both TLS and ULS data. Moreover, selected ULS variables provided better results in vegetation type classification than the TLS variables with 71.3% and 67.0%, respectively (Table 3 and Table 4). For both TLS and ULS datasets, models were better at classifying HTHS and LTLS vegetation classes than HTLS and LTHS vegetation classes. Overall, the results of multinomial model shows that some of the predefined vegetation types could be accurately classified with LiDAR. In addition, ULS LiDAR data classified vegetation classes with slightly higher accuracy overall than the TLS data in this woodland landscape.

Table 3. Confusion matrix for vegetation classes prediction modelling using TLS LiDAR variables

Vegetation classes were predicted from the first four PCA variables calculated from all TLS LiDAR variables					User's accuracy (%)	Vegetation classes were predicted from 12 selected TLS LiDAR variables				User's accuracy (%)
	HTHS	HTLS	LTHS	LTLS		HTHS	HTLS	LTHS	LTLS	
HTHS	21	5	6	4	58.3	26	5	6	3	65.0
HTLS	3	3	1	0	42.9	2	6	0	0	75.0
LTHS	6	5	9	0	45.0	1	3	9	3	56.3
LTLS	0	3	4	24	77.4	1	2	5	22	73.3
Producer's accuracy (%)	70.0	18.8	45.0	85.7		86.7	37.5	45.0	78.6	
Classification accuracy (%)	60.6					67.0				

Table 4. Confusion matrix of vegetation classes prediction modelling using ULS LiDAR variables

Vegetation classes were predicted from the first four PCA variables calculated from ULS LiDAR variables					User's accuracy (%)	Vegetation classes were predicted from 12 selected ULS LiDAR variables				User's accuracy (%)
	HTHS	HTLS	LTHS	LTLS		HTHS	HTLS	LTHS	LTLS	
HTHS	24	4	13	3	54.5	25	3	4	1	75.8
HTLS	3	5	1	2	45.5	3	8	2	1	57.1
LTHS	3	3	1	0	14.3	1	4	11	3	57.9
LTLS	0	4	5	23	71.9	1	1	3	23	82.1
Producer's accuracy (%)	80.0	31.3	5.0	82.1		83.3	50.0	55.0	82.1	
Classification accuracy (%)	56.4					71.3				

Overall bird abundance, species richness and diversity

Models from selected LiDAR variables performed better than PCA models from all LiDAR variables in predicting overall bird abundance, species richness and diversity. The variance explained by fixed effects for overall bird abundance, species richness and diversity models was higher (mean $R^2 = 0.158$) for the models built from selected LiDAR variables than the PCA variables (mean $R^2 = 0.056$) (Appendix 3, 4). Because of this and also considering that selected LiDAR variables predicted vegetation classes better than the PCA model from all LiDAR variables (Table 3 and Table 4), we decided to use the selected variable models for the remainder of our analyses.

The linear mixed effects model for the overall bird abundance did not find a significant relationship to any of the 12 selected variables from the ULS or TLS data (Appendix 4, "Abundance", Fig. 9). Bird species richness (*SR*) was positively related to several TLS-derived variables including mean height (*meanH. P < 0.01*), and skewness (*skewH, P < 0.05*) and variation of canopy height (*height_cv, P < 0.01*) and negatively correlated to mean height of third layer (*meanH_L3, P < 0.01*). However, total vegetation volume (*tvolume*) was the only significant predictor ($P < 0.05$) among the ULS selected variables for predicting bird species richness (SR). Bird diversity (*Bird_shannon*) was positively significantly influenced by TLS and ULS mean canopy height (*meanH, P < 0.01 (TLS), P < 0.05 (ULS)*) and total volume (*tvolume, P < 0.05 (TLS), P < 0.05 (ULS)*), and negatively influenced by mean height of third layer (*meanH_L3, P < 0.01 (TLS), P < 0.05 (ULS)*) (Appendix 4, "Bird_shannon, Fig. 9). Among the functional diversity indexes, functional evenness (*FEve*) was negatively correlated to only TLS-based vegetation complexity between 10 and 15 meter canopy height (*vci_15m, P < 0.05 (TLS)*). However, *vci_15m* derived from TLS (*P < 0.01)* and ULS (*P < 0.05*) data was significantly negatively related to functional divergence. Functional dispersion (*FDis*) and Rao's quadratic entropy (*RaoQ*) were negatively influenced by TLS and UAV – derived vegetation complexity between 1.3 m

and 2 m (*vci_2m, P < 0.05*) and 10 m and 15 m (*vci_15m, P < 0.05*), and positively related to ULS – based vegetation complexity in the first layer of vegetation (*vci_L1, P < 0.01*) (Appendix 4, Fig. 9).

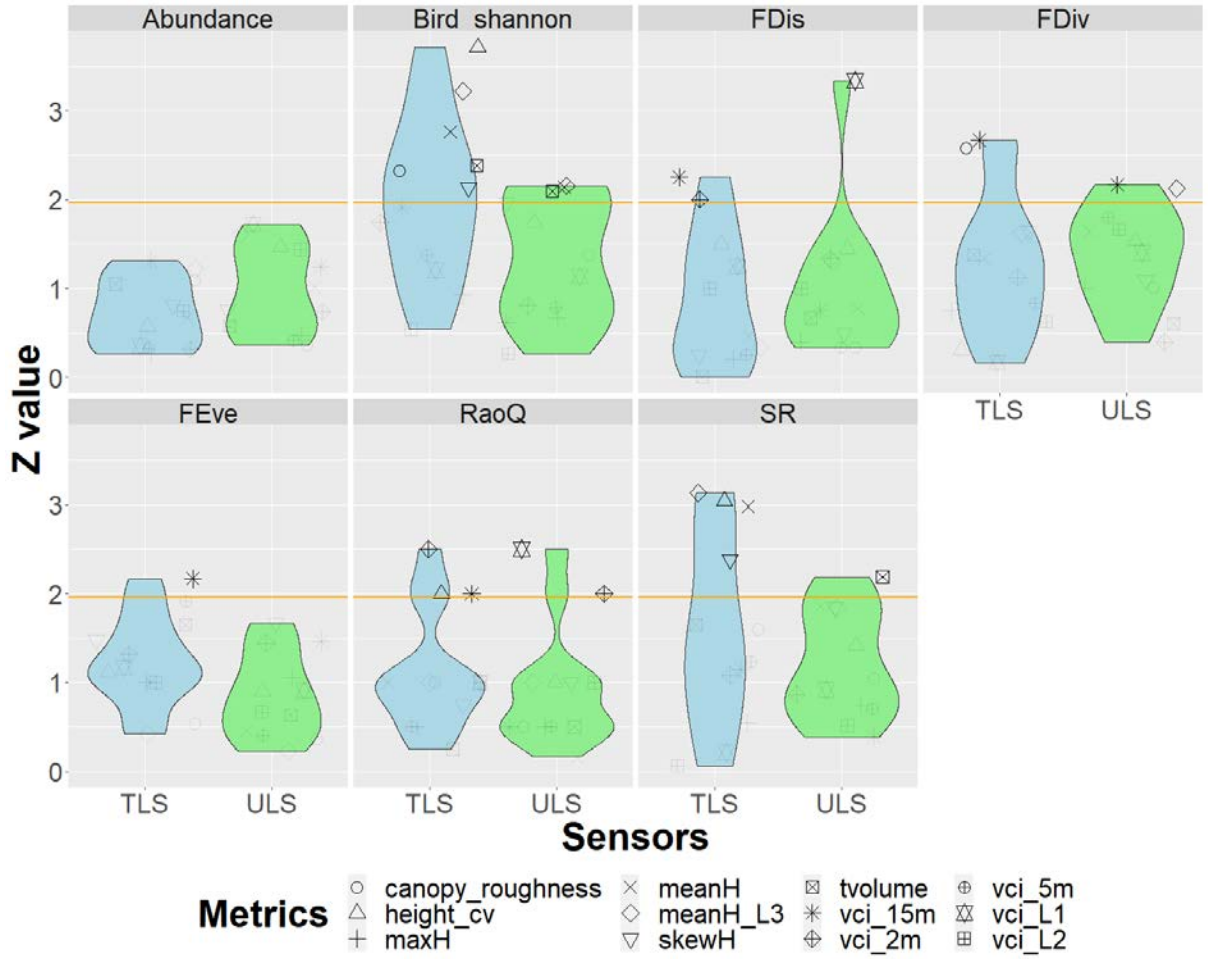

Figure 9. Plot illustrates the significance of predictor variables (by z value) for predicting overall bird abundance, species richness and diversity. Point symbols represent predictor variables. Horizontal orange line shows the significance threshold ($z = 1.96$, or $p < 0.05$) of predictors.

Bird abundance within functional guilds

Table 5 describes basic statistics about bird abundance within functional guilds. Most of the surveyed birds belong to the woodland specialists habitat class (WS.HC, n = 8725), nested in hollows (Hol.Nest, n = 4668), foraged in the trees (Arb.Forage, n = 6649) and displayed low dispersal (Low.Disp, n =8187).

Table 5. Basic statistics about bird abundance within functional traits across plots

Statistics	GS. HC	WB. HC	WG. HC	WS. HC	Arb. Nest	Grnd. Nest	Hol. Nest	Opp. Nest	Usty. Nest	Air. Forage	Aqu. Forage	Arb. Forage	Grnd. Forage	Opp. Forage	Low. Disp	Partial. Disp
Sum	238	83	2868	8725	6174	44	4668	749	279	165	83	6649	2879	2138	8187	3722
Maximum	17	14	106	200	148	11	159	31	24	28	14	141	98	71	210	118
Mean	2.53	0.88	30.51	92.82	65.68	0.47	49.66	7.97	2.97	1.76	0.88	70.73	30.63	22.75	87.10	39.60
Stdev	3.14	2.35	20.33	34.72	28.19	1.59	32.00	7.93	4.81	4.08	2.35	27.53	18.98	13.64	34.44	23.14
Median	1.50	0.00	26.50	86.00	62.50	0.00	40.00	6.00	1.00	0.00	0.00	65.00	25.00	19.50	84.50	37.50
Minimum	0	0	2	28	11	0	5	0	0	0	0	19	5	1	29	3

All of the 16 guilds were significantly correlated to one or more LiDAR variables, and some guilds showed a stronger response to landscape structure than others (Appendix 5, Fig. 10). Models from TLS data explained between 8.5% and 39.9% (mean of 22.6%) variability, and ULS models explained between 6.8% and 40.8% (mean of 23.5%) variability in abundance of birds across functional guilds. The most robust TLS-based explanatory models were the water bird habitat class (R^2=0.399) and aquatic foragers abundance (R^2=0.399), which were positively correlated to *meanH* (*P < 0.05*), *skewH* (*P < 0.05*) and *vci_5m* (*P < 0.01*), and negatively correlated to *maxH* (*P < 0.05*) *and meanH_L3* (*P < 0.05*). The ground nesting guild model from TLS data explained substantial variance (R^2 = 0.338), and was negatively influenced by *maxH* (*P < 0.01*) and positively influenced by *skewH* (*P < 0.05*), *tvolume* (*P < 0.05*) and *vci_L2* (*P < 0.01*). The TLS-based opportunistic foraging model was the third best at explaining variance in the data (R^2 = 0.310). That model was negatively correlated to *maxH* (*P < 0.05*), *meanH* (*P < 0.05*), *skewH* (*P < 0.05*) and *height_cv* (*P < 0.001*) and strongly positively correlated to *canopy_roughness* (*P < 0.001*) and *meanH_L3* (*P < 0.001*) (Appendix 5, Fig. 10).

The ULS-based models also performed best for aquatic foraging and water bird habitat guilds (R^2 = 0.408), which were positively related to *vci_5m* (*P < 0.001*), *vci_15m* (*P < 0.001*) and *vci_L1* (*P < 0.05*). The next best performing ULS guild model was for woodland generalist abundance (R^2 = 0.370) and was positively associated with *maxH* (*P < 0.01*) and *vci_L1* (*P < 0.001*). The ULS model also explained substantial variance in abundance of ground nesting birds (R^2=0.355), which were positively influenced by *meanH* (*P < 0.05*) and *skewH* (*P < 0.05*), but negatively related to *maxH* (*P < 0.05*) (Appendix 5, Fig. 10).

The contribution of explanatory variables to the functional guilds models

Canopy roughness (*canopy_roughness*) was the best predictor variable for the TLS- based models with a significant correlation to 10 functional guilds followed by *skewH, maxH* and *meanH* height of canopy and *meanH_L3* (Fig. 10). The best predictor variables for ULS-based models were *vci_5m* – significantly correlated to 9 guilds, *maxH, canopy_roughness* and *vci_L1* (Fig. 10).

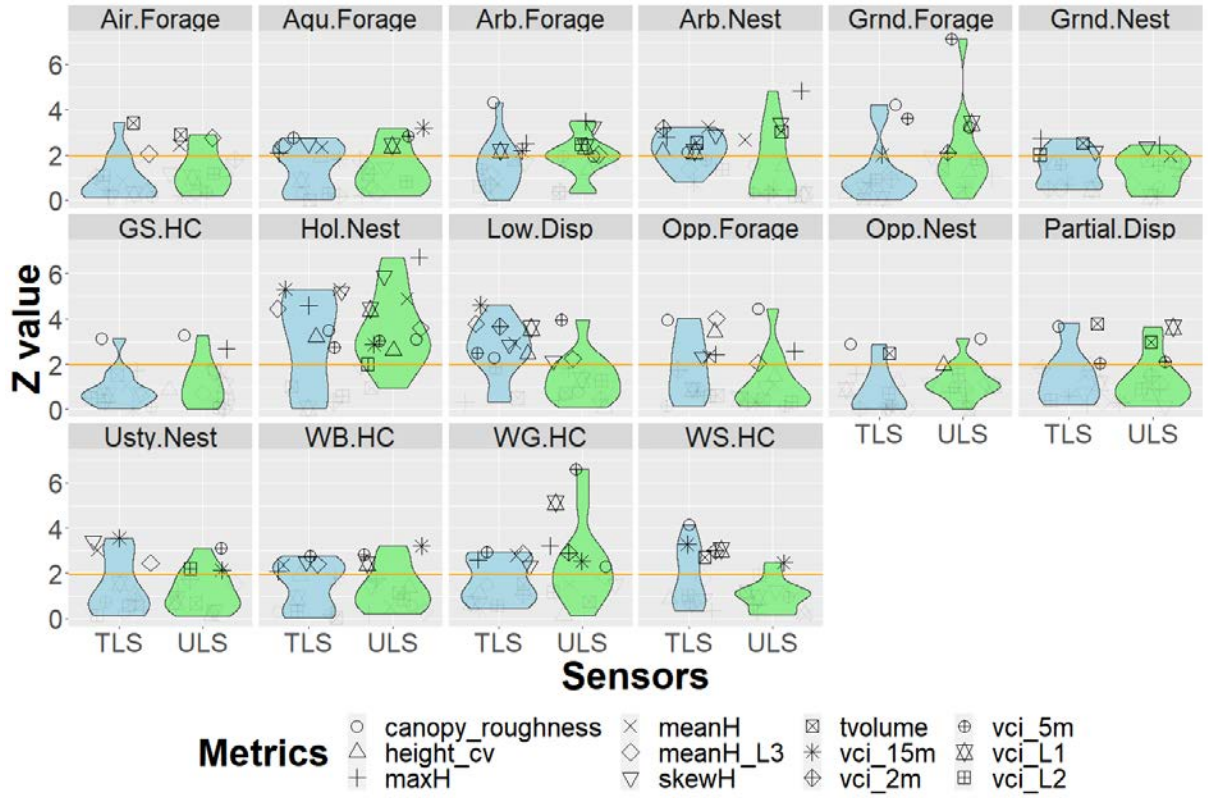

Figure 10. Plot illustrates the significance of predictor variables (by z value) for predicting bird abundance by functional guilds. Point symbols represent predictor variables. Horizontal orange line shows the significance threshold (z = 1.96, or p < 0.05) of predictors. Habitat class (grassland specialist, water bird, woodland generalist, woodland specialist), nesting substrate (arboreal, ground, hollow, opportunistic, understory), foraging substrate (air, aquatic, arboreal, ground, opportunistic), and dispersion (low, partial, high) groups.

Individual bird species abundance

Mixed – effects Poisson regression models showed that the abundance of forty-nine out of fifty one bird species responded to TLS and ULS – derived vegetation structural variables (Appendix 6). Only Grey Shrike Thrush and Pallid Cuckoo abundance showed no relationship to any TLS or ULS LiDAR structural variables. For the TLS-based models, *canopy_roughness* was significantly related to the abundance of 16 bird species, followed by *tvolume*, which was related to the abundance of 15 bird species (Fig. 11). In the ULS models, *vci_L1* related to bird species abundance more than any other variable (22 bird species), followed by *canopy_roughness* (17 bird species) (Fig. 11). The explained variance of TLS models ranged from 4.2% to 81.7% with an average of 31.1%. Similarly, ULS-models explained 4.9% to 83.4% (mean = 30.5%) of variation in bird species abundance.

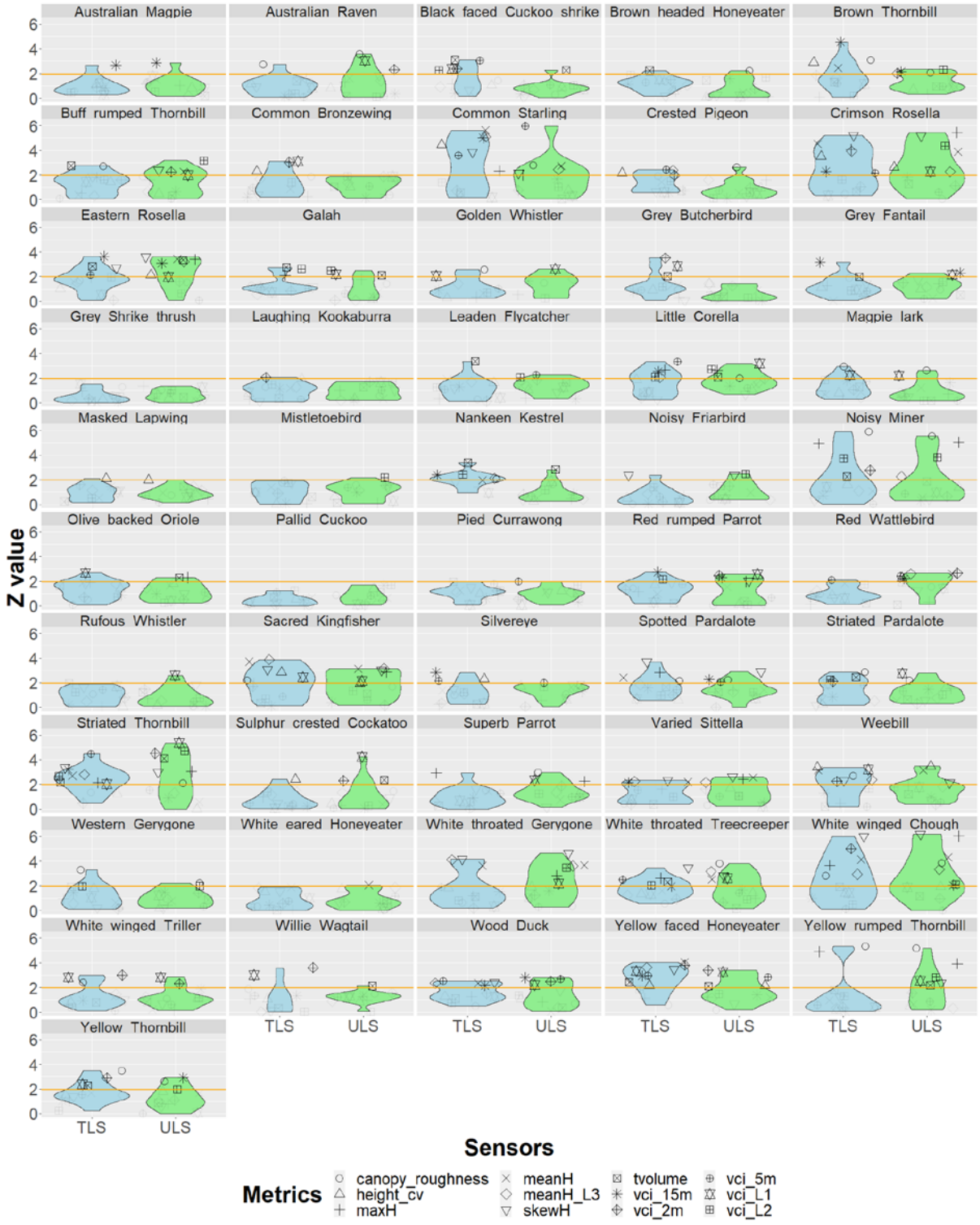

Figure 11. Plot illustrates the significance of predictor variables (by z value) for predicting individual bird species abundance. Point symbols represent predictor variables. Horizontal orange line shows the significance threshold ($z = 1.96$, or $p < 0.05$) of predictors.

The model for Nankeen Kestrel abundance was the best performing TLS model (R^2 = 0.817), and was strongly correlated to *vci_15m* (*P < 0.05*), *canopy_roughness* (*P < 0.05*), *meanH_L3* (*P < 0.05*) and *vci_L2* (*P < 0.05*) and negatively related to *meanH* (*P < 0.05*) and *tvolume* (*P < 0.001*) (Appendix 6, Fig 11). The second best TLS model was Spotted Pardalote abundance (R^2 = 0.772) which was correlated to *maxH* (*P < 0.01*), *meanH* (*P < 0.05*), *skewH* (*P < 0.001*) and *tvolume* (*P < 0.05*). White Throated Treecreeper abundance was also strongly related to TLS LiDAR-derived vegetation structure (R^2 = 0.739) and had a positive relationship to *skewH* (*P < 0.05*), *vci_15m* (*P < 0.05*), *tvolume* (*P < 0.05*) and *vci_L2* (*P < 0.05*), and a negative relationship with *maxH* (*P < 0.05*) and *vci_5m* (*P < 0.05*) (Appendix 6, Fig 11).

The best performing ULS model was for Varied Sittela abundance (R^2 = 0.834), which was explained by *maxH* (*P < 0.05*), *meanH* (*P < 0.05*), *skewH* (*P < 0.01*) and *meanH_L3* (*P < 0.05*). The White Throated Treecreeper abundance model (R^2 = 0.777) showed significant correlation with *meanH* (*P < 0.05*), *skewH* (*P < 0.01*), *canopy_roughness* (*P < 0.001*), *meanH_L3* (*P < 0.01*) and *vci_L1* (*P < 0.05*). Likewise, the Sacred Kingfisher abundance model explained 76.2% variance and was related to *maxH* (*P < 0.01*), *meanH* (*P < 0.01*), *skewH* (*P < 0.01*), *meanH_L3* (*P < 0.01*), *vci_L1* (*P < 0.05*) and *height_cv* (*P < 0.05*) (Appendix 6, Fig. 11).

Overall, TLS and ULS data produced very similar results in predicting individual bird species abundance, and this was demonstrated by the linear relationship between the explained variances of TLS and ULS models (Fig. 12).

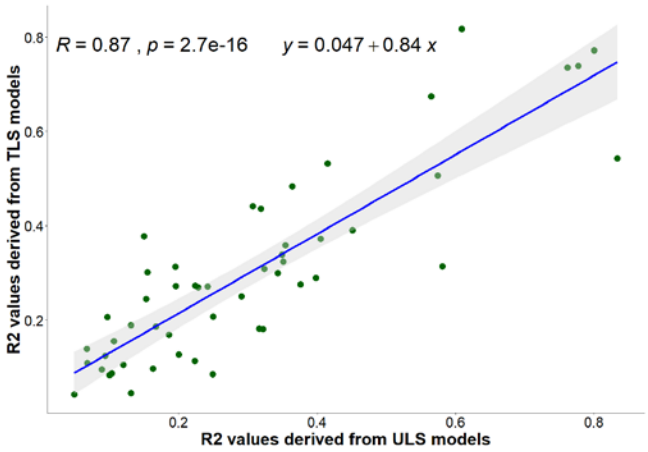

Figure 4. The relationship between explained variance (R2) calculated from TLS and ULS based Poisson distribution mixed model for predicting individual bird species abundance.

Discussion

For the first time, we used high resolution LiDAR imagery from ULS and TLS platforms in a woodland landscape to investigate relationships between LiDAR-derived structural metrics and overall bird

abundance, bird abundance within guilds, species richness and other biodiversity metrics. Although both approach produced promising results, multinomial regression models from 12 selected variables were better at classifying sites according to their four vegetation types than the PCA models. Hence, our first hypothesis on TLS and ULS data can be used to accurately classify field-estimated vegetation classes was strongly supported. Overall, bird abundance was not significantly related to any TLS or ULS LiDAR-derived variables and this may be due to the number of different bird species that occupied a wide variety of structural niches in the landscape (Lesak et al., 2011). Models for predicting bird species richness, biodiversity and abundance within functional guilds performed better than overall bird abundance. However, the scale at which bird species richness and biodiversity metrics respond to structure, due to the presence of multiple species that use multiple spatial scales, may not be accurately reflected in site-level LiDAR metrics (Seavy et al., 2009). Some individual bird species abundance models were able to explain a very large amount of variability in abundance, which is promising for using this data for habitat assessments and improving our understanding of habitat requirements for threatened species in particular. Canopy roughness, vertical complexity of the first layer, total vegetation volume and canopy height were the variables that were most strongly associated with bird community and individual species abundance. Our assumption that higher density LiDAR point clouds from the TLS platform would create better models than the lower density, airborne ULS data was not supported by our data. This was likely influenced by low-lying occlusions in the data that were more substantial for the TLS than the ULS owing to the positing of the sensors and the characteristics of the woodland landscape (Olschofsky et al., 2016). As a result, the ULS generally provided better results for predicting the abundance of individual bird species and guilds that forage on the ground than the TLS based on our methodology. We discuss the overall finding in more detail below and provide recommendations for future research.

Overall bird abundance, species richness and diversity

Despite some variation in bird abundance being explained by TLS and ULS structural metrics, abundance was not significantly related to any of the predictors (Appendix 4). This may be due to contrasting habitat requirement across the large suite of different species included in the total abundance tally (Wiens and Rotenberry, 1981). Models for predicting bird species richness did find significant relationships to some variables but these were dependent on the data source (TLS or ULS). Species richness was significantly positively related to TLS canopy height diversity and upper canopy height. The only ULS predictor that was significantly positively related to bird species richness was the total volume of vegetation. The TLS sensor may be able to capture more meaningful canopy height variation for birds than the ULS data owing to the position of the sensor under the canopy, which

allows it to detect more detail from vegetation below the canopy. Species diversity prediction models from TLS and ULS data provided similar results. Overall, canopy height and total volume showed the strongest relationship to the bird diversity indices (Appendix 4), but canopy height variation (*height_cv*) was only significant in TLS-based metrics. This further supports the idea that the TLS sensor was able to capture canopy height variation in a more meaningful way for bird habitat quality, probably owing to the positioning of the sensor (Ashcroft et al., 2014, Blakey et al., 2017). Nonetheless, the higher density TLS data did not perform better than the ULS data in terms of overall ability to explain variance in this data. Therefore, our first hypothesis that high density TLS LiDAR point clouds will perform better for modelling overall bird abundance, species richness and diversity than lower density ULS point clouds was not supported.

Generally, our results from species richness and diversity models agree with relationships identified in previous studies (Clawges et al., 2008, Lesak et al., 2011, Sasaki et al., 2016). Earlier study by Clawges et al. (2008) found a significant correlation between ALS LiDAR-derived canopy height diversity and bird species diversity. Similarly, ALS LiDAR – derived canopy height and mid-story density and height has been associated with song bird species richness (Lesak et al., 2011). Notably, these studies reported relatively low overall explained variance (R^2 <= 0.2), which is also in keeping with our findings. The typically low explained variance for community level data (e.g., bird species richness and diversity) in these models may be due to a mismatch in scale, since some of the bird species frequently use landscape areas beyond the plot level that have different overall structural characteristics. Bird occurrence and habitat relationships can be scale-dependent (Seavy et al., 2009, Weisberg et al., 2014). Weisberg et al. (2014) investigated multiscale habitat heterogeneity and bird occurrence using LiDAR data, and they found the strongest associations at a 200 m (4 ha) scale and the weakest associations at a 50 m (0.25 ha) scale. A similar study on multiscale analysis using LiDAR derived canopy height measurements (Seavy et al., 2009) found that specific bird species responded differently to vegetation structure at different spatial scales. Future studies should revisit this dataset at a variety of scales.

Modelling bird abundance within functional guilds

All of the functional guilds that we analyzed were significantly related to LiDAR derived vegetation structural metrics. Generally, TLS and ULS data achieved similar results in predicting functional guild abundance (mean R^2 = 0.235 and mean R^2 = 0.226, respectively). A few earlier studies have also used remote sensing to investigate relationships between bird functional guilds and vegetation structure, but they used species richness within guilds, rather than species abundance within guilds (Lesak et al., 2011, Lee et al., 2017). For example, ALS - derived vegetation measures have been used for estimating

songbird species richness by nesting, foraging and edge preferring guilds (Lesak et al., 2011). In that study, models using structural metrics from ALS data explained between 7.0% and 16.1% of the variance in species richness in nesting guilds, whereas our study explained between 8.5% and 33.7% (TLS) and 6.8% and 35.5% (ULS) variance in the abundance of birds from various nesting guilds. Another study also found significant relationships between canopy height and density variables and foraging guilds (Lesak et al., 2011). Our models showed that bird abundance by functional guilds are significantly influenced by canopy height variables, canopy roughness and vertical complexity of vegetation in the ground layer. Notably, the ULS models found strong correlations between ground foraging guilds and ground-layer vegetation structure, but the TLS models did not show this relationship. The ULS may capture more structural heterogeneity due to less occlusion in the ground-layer in an open woodland than the TLS. As a result, a portion of our second hypothesis that overall, TLS data will perform better than ULS data in predicting avian functional guild abundance is rejected, despite the higher point density of TLS.

Modelling individual bird species abundance

The relationship between specific vegetation structural metrics and the abundance of certain bird species may be useful for future management and conservation efforts, particularly for vulnerable species. In many cases, the link between the structural metrics and specific bird species can be easily explained by their habitat preference, lending more weight to this relationship. For example, we found that the abundance of the vulnerable Superb Parrot (*Polytelis swainsonii*, Nature Conservation Act 2014) is positively influenced by TLS-derived maximum height of trees and ULS-derived maximum height of trees and the complexity of the first layer vegetation and negatively influenced by horizontal distribution of canopy (*canopy roughness*). Separate studies have found that Superb Parrots use large trees for nesting and breeding and ground vegetation for foraging (Manning et al., 2004a). In addition to the Superb Parrot, our LiDAR-derived structural models also performed very well in predicting the abundance of two other threatened species, the White-winged Triller (*Lalage tricolor*, Nature Conservation Act 2014), and the Varied Sittella (*Daphoenositta chrysoptera*, Nature Conservation Act 2014).

Some woodland sensitive birds also responded to the LiDAR derived vegetation structural metrics. For example, Brown Thornbill (*Acanthiza pusilla*) species found in sparse eucalypt woodlands (Stagoll et al., 2010) was negatively correlated to canopy roughness and mean height of canopy (Appendix 6, Fig 10). Noisy Miners (*Manorina melanocephala*) are less likely to occur in areas with high shrub cover (Crates et al., 2018), and our noisy miner model also found a significant negative relationship to shrub layer vegetation (Appendix 6).

On the other end of the extreme, we found no relationship between our site-level structural variables and the abundance of the Grey Shrike-thrush (*Colluricincla harmonica*) or Pallid Cuckoo (*Cacomantis pallidus*). These common species are widely distributed across Australia and use habitat at large spatial scales and across a wide range of landscape types. If relationships between these species and specific structural variables are to be found, then it is more likely to be at larger spatial scales than our 1 ha site-level metrics. Overall though, the individual bird species models from both TLS and ULS performed better than the community based models and that's notable because habitat is a species specific concept (Manning et al., 2004b, Betts et al., 2014). In trying to understand the structural requirements of wildlife using LiDAR data, it may be best to focus on individual species rather than overall abundance or diversity (Manning et al., 2004b). Contrasting requirements from multiple species may frustrate attempts to model relationships to structural vegetation data (Halstead et al., 2019).

Overall, ULS models generally outperformed TLS models in predicting the abundance of birds from species that were positively or negatively influenced by ground-layer vegetation complexity. Out of 51 bird species, ULS ground-layer vegetation structure was important for 22 species, compared to 13 species for the TLS models (Appendix 6, Fig. 10). The abundance of ground foraging birds such as Yellow-rumped Thornbill, Yellow-faced Honeyeater, Sulphur-crested Cockatoo, Superb Parrot, Red-rumped Parrot, Little Corella were significantly influenced by ground layer vegetation complexity for ULS but not TLS data (Appendix 6, Fig 10). This might be related to the occlusion of TLS laser pulses by ground vegetation (LaRue et al., 2020) and the ability of ULS to capture ground vegetation structure in an open woodland due to the open canopy architecture of this landscape (Yebra et al., 2015). As expected though, we did find that some species that depend on canopy strata such as Buff-rumped Thornbill, Eastern Rosella, Red-rumped Parrot and Red Wattlebird were significantly associated with more ULS canopy variables than TLS. For these reasons, our hypothesis that the relationship between landscape structural data and particular bird species will be modelled more accurately from the TLS data for bird species that are most associated with ground and mid-story vegetation layers and the ULS data for species that primarily use the canopy strata is only partially supported.

Limitations of this study

Although we attempted to compare the performance of TLS and ULS data in modelling bird habitat, this study has some limitations that should be mentioned. To start with, we collected 7 scans of TLS data over 1 ha sites, and this is a relatively low number of scans compared to the recent studies that used more than 16 scans in 1 ha sites (Wilkes et al., 2017, Levick et al., 2021). However, most of those studies used only a few hectares of study areas which makes more scans of data collection and post-

processing feasible. As we had 96 × 1 ha sites, collecting and processing more TLS scans would take a lot more time which would have a negative impact on completing the bigger study at the right time. On the other hand, more TLS scans would decrease incident angle (angle between the incoming laser pulse and surface normal) which would allow to capture dense vegetation and ground more accurately, and this would significantly reduce occlusion (Soudarissanane et al., 2009). Unlike TLS scans, ULS is able to send laser beams with small incident angles and therefore captures ground layers more accurately.

Furthermore, Topcon GLS2000 is a single return LiDAR sensor, and this is also an important constraint of this sensor as a multiple return TLS sensor might have penetrated occluding dense vegetation (Wilkes et al., 2017). Ability of the ULS sensor to record multiple returns provided another advantage over the TLS sensor. We acknowledge that these factors are important and might have a significant influence on the results.

Conclusion

Our models showed strong relationships between the abundance of many individual bird species and TLS and ULS LiDAR derived vegetation structural metrics. This type of data can be useful for identifying habitat requirements for a variety of bird species (Graf et al., 2009). Understanding the landscape-scale that species use and matching this to the scale of LiDAR structural metrics may improve our ability to identify relationships between remotely sensed vegetation structure and wildlife (Seavy et al., 2009). This is the first study that uses both ULS and TLS data for investigating relationships between a wide range of bird population data and vegetation structure in a woodland landscape. According to Bakx et al. (2019) there hasn’t been any study in Australia to model avian abundance and species richness using LiDAR data before.

This study revealed several landscape structural metrics from LiDAR dataset including vegetation volume, canopy height variability and vegetation complexity that are related to bird abundance and species richness. We also found that some bird species use the different layers of vegetation while others depend on the landscape scale.

ULS is faster, and can easily capture structural metrics across wide areas, whereas TLS can provide highly detailed point-clouds, but requires more time to collect. Our findings show that ULS, in most cases, performed as well or better than TLS in this landscape type and based on our methodologies. However, TLS models may be improved by using more scan stations to reduce occlusions. Ability of our ULS sensor to record multiple returns per laser beam might be a significant advantage over the TLS sensor as it helped to penetrate the upper canopy and capture structural details on the ground and mid-story. Higher point density TLS LiDAR data in itself does not offer an advantage over lower point

density ULS data if the coverage is less complete and the landscape type allows a ULS sensor to view lower strata vegetation to successfully model structural associations between plants and animals.

Acknowledgement

We thank all of our volunteers; L. McGibbon, E. Wu, R. Stainer, P. Hopkins, K. Spooner, Jackie, K. Subasinghe, M. Folkard, Z. Xie, Karen, Prasanna, W. Wang, D. Muthiah, B. Candice, M. Jenkins, N. Butcher, and S. Zong for their hard work during data collection. Thanks to Dr M. Welvaert for additional statistical support and consultation.

"Thanks to Canberra Ornithologists Group (COG) and the many volunteers who have undertaken bird surveys for us since 2005; special thanks to J. Bounds and B. Lindenmayer for assistance in organizing volunteer support. Special thanks to S. Holliday who has conducted surveys for us since the inception of the Experiment. Thank you to S. Rapley for extra assistance with recent surveys and a special thanks to J. Newport for organizing bird surveys since 2010. We thank all the ACT Government staff and Woodlands and Wetlands Trust staff and volunteers that have assisted in all aspects of this project. Bird surveys were covered by ANU ethics Protocols C.RE.44.05, C.RE.59.09, F.ES.10.10, A2011/017, A2014/35, A2017/33 and A2020/40; and ACT project licenses LT2005201, LT2007279, LT2009347, LT2010417, LT2014769, LT2015834, LT2016905 and LT2017959. Funding and in-kind logistic support for this project was provided by the ACT Government as part of an Australian Research Council Linkage Grant (LP0561817; LP110100126, LP140100209). ADM was supported by an Australian Research Council Future Fellowship for part of the study (FT100100358)."

References

ANDERSON, K., HANCOCK, S., DISNEY, M., GASTON, K. J., ROCCHINI, D. & BOYD, D. 2016. Is waveform worth it? A comparison of LiDAR approaches for vegetation and landscape characterization. *Remote Sensing in Ecology and Conservation,* 2**,** 5-15.

ASHCROFT, M. B., GOLLAN, J. R. & RAMP, D. 2014. Creating vegetation density profiles for a diverse range of ecological habitats using terrestrial laser scanning. *Methods in Ecology and Evolution,* 5**,** 263-272.

BAKX, T. R. M., KOMA, Z., SEIJMONSBERGEN, A. C., KISSLING, W. D. & ZURELL, D. 2019. Use and categorization of Light Detection and Ranging vegetation metrics in avian diversity and species distribution research. *Diversity and Distributions,* 25**,** 1045-1059.

BATES, D., MÄCHLER, M., BOLKER, B. & WALKER, S. 2015. Fitting Linear Mixed-Effects Models Using lme4. *Journal of Statistical Software,* 67**,** 48.

BECKER, R., CHAMBERS, M. & WILKS, A. R. 1988. *The New S Language: A Programming Environment for Data Analysis and Graphics*, Wadsworth & Brooks/Cole Advanced Books & Software.

BETTS, M. G., FAHRIG, L., HADLEY, A. S., HALSTEAD, K. E., BOWMAN, J., ROBINSON, W. D., WIENS, J. A. & LINDENMAYER, D. B. 2014. A species-centered approach for uncovering generalities in organism responses to habitat loss and fragmentation. *Ecography,* 37**,** 517-527.

BLAKEY, R. V., LAW, B. S., KINGSFORD, R. T. & STOKLOSA, J. 2017. Terrestrial laser scanning reveals below-canopy bat trait relationships with forest structure. *Remote Sensing of Environment,* 198**,** 40-51.

BRADBURY, R. B., HILL, R. A., MASON, D. C., HINSLEY, S. A., WILSON, J. D., BALZTER, H., ANDERSON, G. Q. A., MARK J. WHITTINGHAM, M. J., DAVENPORT, I. J. & BELLAMY, P. E. 2005. Modelling relationships between birds and vegetation structure using airborne LiDAR data a review with case studies from agricultural and woodland environments. *British Ornithologists' Union, IBIS,* 147**,** 443–452.

BUREAU OF METEOROLOGY, A. 2019. *Climate summaries archive* [Online]. Available: http://www.bom.gov.au/climate/current/annual/act/archive/2018.summary.shtml [Accessed 08/08/2020 2020].

CARRASCO, L., GIAM, X., PAPEŞ, M. & SHELDON, K. 2019. Metrics of Lidar-Derived 3D Vegetation Structure Reveal Contrasting Effects of Horizontal and Vertical Forest Heterogeneity on Bird Species Richness. *Remote Sensing,* 11**,** 743-762.

CLAWGES, R., VIERLING, K., VIERLING, L. & ROWELL, E. 2008. The use of airborne lidar to assess avian species diversity, density, and occurrence in a pine/aspen forest. *Remote Sensing of Environment,* 112**,** 2064-2073.

CRATES, R., TERAUDS, A., RAYNER, L., STOJANOVIC, D., HEINSOHN, R., WILKIE, C. & WEBB, M. 2018. Spatially and temporally targeted suppression of despotic noisy miners has conservation benefits for highly mobile and threatened woodland birds. *Biological Conservation,* 227**,** 343-351.

CRESPO-PEREMARCH, P., FOURNIER, R. A., NGUYEN, V.-T., VAN LIER, O. R. & RUIZ, L. Á. 2020. A comparative assessment of the vertical distribution of forest components using full-waveform airborne, discrete airborne and discrete terrestrial laser scanning data. *Forest Ecology and Management,* 473**,** 118268-118283.

DAI, W., YANG, B., LIANG, X., DONG, Z., HUANG, R., WANG, Y. & LI, W. 2019. Automated fusion of forest airborne and terrestrial point clouds through canopy density analysis. *ISPRS Journal of Photogrammetry and Remote Sensing,* 156**,** 94-107.

DAVID, T. P., HERRICK, J. E. & ABBOTT, L. B. 2010. A comparison of cover pole with standard vegetation monitoring methods. *The Journal of Wildlife Management,* 74**,** 600-604.

DAVIES, A. B. & ASNER, G. P. 2014. Advances in animal ecology from 3D-LiDAR ecosystem mapping. *Trends Ecol Evol,* 29**,** 681-91.

DEPARTMENT OF ENVIRONMENT, G. o. A. 2013. Vegetation Assessment Guide.

DORMANN, C. F., ELITH, J., BACHER, S., BUCHMANN, C., CARL, G., CARRÉ, G., MARQUÉZ, J. R. G., GRUBER, B., LAFOURCADE, B., LEITÃO, P. J., MÜNKEMÜLLER, T., MCCLEAN, C., OSBORNE, P. E., REINEKING, B., SCHRÖDER, B., SKIDMORE, A. K., ZURELL, D. & LAUTENBACH, S. 2013.

Collinearity: a review of methods to deal with it and a simulation study evaluating their performance. *Ecography,* 36**,** 27-46.

ELDEGARD, K., DIRKSEN, J. W., ØRKA, H. O., HALVORSEN, R., NÆSSET, E., GOBAKKEN, T. & OHLSON, M. 2014. Modelling bird richness and bird species presence in a boreal forest reserve using airborne laser-scanning and aerial images. *Bird Study,* 61**,** 204-219.

GOETZ, S., STEINBERG, D., DUBAYAH, R. & BLAIR, B. 2007. Laser remote sensing of canopy habitat heterogeneity as a predictor of bird species richness in an eastern temperate forest, USA. *Remote Sensing of Environment,* 108**,** 254-263.

GRAF, R. F., MATHYS, L. & BOLLMANN, K. 2009. Habitat assessment for forest dwelling species using LiDAR remote sensing: Capercaillie in the Alps. *Forest Ecology and Management,* 257**,** 160-167.

HALSTEAD, K. E., ALEXANDER, J. D., HADLEY, A. S., STEPHENS, J. L., YANG, Z. & BETTS, M. G. 2019. Using a species-centered approach to predict bird community responses to habitat fragmentation. *Landscape Ecology,* 34**,** 1919-1935.

HARTIG, F. 2017. DHARMa: residual diagnostics for hierarchical (multi-level/mixed) regression models. *R package version 0.1,* 5.

HERRERO-HUERTA, M., BUCKSCH, A., PUTTONEN, E. & RAINEY, K. M. 2020. Canopy Roughness: A New Phenotypic Trait to Estimate Aboveground Biomass from Unmanned Aerial System. *Plant Phenomics,* 2020**,** 6735967.

ISENBURG, M. 2012. LAStools-efficient tools for LiDAR processing. *Available at: http: http://www.cs.unc.edu/~isenburg/lastools/*.

JAMES, F. C. & SHUGART JR, H. H. 1970. A quantitative method of habitat description. *Audubon Field Notes,* 24**,** 727-736.

JARI OKSANEN, F. G. B., Michael Friendly, Roeland Kindt, Pierre Legendre, Dan McGlinn, Peter R. Minchin, R. B. O'Hara, Gavin L. Simpson, Peter Solymos, M. Henry H. Stevens, Eduard Szoecs, Helene Wagner 2019. vegan: Community Ecology Package.

JENNESS, J. S. 2004. Calculating Landscape Surface Area from Digital Elevation Models. *Wildlife Society Bulletin (1973-2006),* 32**,** 829-839.

JUCKER, T., ASNER, G. P., DALPONTE, M., BRODRICK, P. G., PHILIPSON, C. D., VAUGHN, N. R., TEH, Y. A., BRELSFORD, C., BURSLEM, D. F. R. P., DEERE, N. J., EWERS, R. M., KVASNICA, J., LEWIS, S. L., MALHI, Y., MILNE, S., NILUS, R., PFEIFER, M., PHILLIPS, O. L., QIE, L., RENNEBOOG, N., REYNOLDS, G., RIUTTA, T., STRUEBIG, M. J., SVÁTEK, M., TURNER, E. C. & COOMES, D. A. 2018. Estimating aboveground carbon density and its uncertainty in Borneo's structurally complex tropical forests using airborne laser scanning. *Biogeosciences,* 15**,** 3811-3830.

KARADIMOU, E. K., KALLIMANIS, A. S., TSIRIPIDIS, I. & DIMOPOULOS, P. 2016. Functional diversity exhibits a diverse relationship with area, even a decreasing one. *Scientific Reports,* 6**,** 35420-35429.

KASSAMBARA, A. 2017. *Practical Guide To Principal Component Methods in R: PCA, M(CA), FAMD, MFA, HCPC, factoextra*, CreateSpace Independent Publishing Platform.

KIKKAWA, J. 1982. Ecological association of birds and vegetation structure in wet tropical forests of Australia. *Australian Journal of Ecology,* 7**,** 325-345.

LALIBERTÉ, E. & LEGENDRE, P. 2010. A distance-based framework for measuring functional diversity from multiple traits. *Ecology,* 91**,** 299-305.

LARUE, E. A., WAGNER, F. W., FEI, S., ATKINS, J. W., FAHEY, R. T., GOUGH, C. M. & HARDIMAN, B. S. 2020. Compatibility of Aerial and Terrestrial LiDAR for Quantifying Forest Structural Diversity. *Remote Sensing,* 12**,** 1407-1421.

LEE, P. S., MACKEY, B. G. & BERRY, S. L. 2017. Modelling vegetation structure-based bird habitat resources in Australian temperate woodlands, using multi-sensors. *European Journal of Remote Sensing,* 46**,** 641-674.

LEFSKY, M. A., COHEN, W. B., PARKER, G. G. & HARDING, D. J. 2002. Lidar Remote Sensing for Ecosystem Studies. *BioScience,* 52**,** 19-30.

LESAK, A. A., RADELOFF, V. C., HAWBAKER, T. J., PIDGEON, A. M., GOBAKKEN, T. & CONTRUCCI, K. 2011. Modeling forest songbird species richness using LiDAR-derived measures of forest structure. *Remote Sensing of Environment,* 115**,** 2823-2835.

LEVICK, S. R., RICHARDS, A. E., COOK, G. D., SCHATZ, J., GUDERLE, M., WILLIAMS, R. J., SUBEDI, P., TRUMBORE, S. E. & ANDERSEN, A. N. 2019. Rapid response of habitat structure and above-ground carbon storage to altered fire regimes in tropical savanna. *Biogeosciences,* 16**,** 1493-1503.

LEVICK, S. R., WHITESIDE, T., LOEWENSTEINER, D. A., RUDGE, M. & BARTOLO, R. 2021. Leveraging TLS as a Calibration and Validation Tool for MLS and ULS Mapping of Savanna Structure and Biomass at Landscape-Scales. *Remote Sensing,* 13.

LEYEQUIEN, E., VERRELST, J., SLOT, M., SCHAEPMAN-STRUB, G., HEITKÖNIG, I. M. A. & SKIDMORE, A. 2007. Capturing the fugitive: Applying remote sensing to terrestrial animal distribution and diversity. *International Journal of Applied Earth Observation and Geoinformation,* 9**,** 1-20.

LIANG, X., KANKARE, V., HYYPPÄ, J., WANG, Y., KUKKO, A., HAGGRÉN, H., YU, X., KAARTINEN, H., JAAKKOLA, A. & GUAN, F. 2016a. Terrestrial laser scanning in forest inventories. *ISPRS Journal of Photogrammetry and Remote Sensing,* 115**,** 63-77.

LIANG, X., KANKARE, V., HYYPPÄ, J., WANG, Y., KUKKO, A., HAGGRÉN, H., YU, X., KAARTINEN, H., JAAKKOLA, A., GUAN, F., HOLOPAINEN, M. & VASTARANTA, M. 2016b. Terrestrial laser scanning in forest inventories. *ISPRS Journal of Photogrammetry and Remote Sensing,* 115**,** 63-77.

MACARTHUR, R., and J. MacArthur 1961. On bird species diversity. *Ecology,* 42**,** 594-598.

MANNING, A. D., CUNNINGHAM, R. B. & LINDENMAYER, D. B. 2013. Bringing forward the benefits of coarse woody debris in ecosystem recovery under different levels of grazing and vegetation density. *Biological Conservation,* 157**,** 204-214.

MANNING, A. D., LINDENMAYER, D. B. & BARRY, S. C. 2004a. The conservation implications of bird reproduction in the agricultural "matrix": a case study of the vulnerable superb parrot of south-eastern Australia. *Biological Conservation,* 120**,** 363-374.

MANNING, A. D., LINDENMAYER, D. B. & NIX, H. A. 2004b. Continua and Umwelt: novel perspectives on viewing landscapes. *Oikos,* 104**,** 621-628.

MANNING, A. D., WOOD, J. T., GUNNINGHAM, R. B., MCINTYRE, S., SHORTHOUSE, D. J., GORDON, I. J. & LINDENMAYER, D. B. 2011. Integrating research and restoration: the establishment of a long-term woodland experiment in south-eastern Australia. *Zoologist,* 35**,** 633-648.

MASON, N. W. H., MOUILLOT, D., LEE, W. G. & WILSON, J. B. 2005. Functional richness, functional evenness and functional divergence: the primary components of functional diversity. *Oikos,* 111**,** 112-118.

MCINTYRE, S., CUNNINGHAM, R. B., DONNELLY, C. F. & MANNING, A. D. 2014. Restoration of eucalypt grassy woodland: effects of experimental interventions on ground-layer vegetation. *Australian Journal of Botany,* 62.

MCINTYRE, S., STOL, J., HARVEY, J., NICHOLLS, A. O., CAMPBELL, A., REID, A., MANNING, A. D., LINDENMAYER, D. B. & 2010. Biomass and floristic patterns in the ground layer vegetation of box-gum grassy eucalypt woodland in Goorooyarroo and Mulligans Flat Nature Reserves, Australian Capital Territory. *Cunninghamia: a journal of plant ecology for eastern Australia,* 11**,** 319-357.

MELIN, M., HINSLEY, S. A., BROUGHTON, R. K., BELLAMY, P. & HILL, R. A. 2018. Living on the edge: utilising lidar data to assess the importance of vegetation structure for avian diversity in fragmented woodlands and their edges. *Landscape Ecology,* 33**,** 895-910.

MICHEL, P., JENKINS, J., MASON, N., DICKINSON, K. J. M. & JAMIESON, I. G. 2008. Assessing the ecological application of lasergrammetric techniques to measure fine-scale vegetation structure. *Ecological Informatics,* 3**,** 309-320.

MORRIS, E. K., CARUSO, T., BUSCOT, F., FISCHER, M., HANCOCK, C., MAIER, T. S., MEINERS, T., MÜLLER, C., OBERMAIER, E., PRATI, D., SOCHER, S. A., SONNEMANN, I., WÄSCHKE, N., WUBET, T., WURST, S. & RILLIG, M. C. 2014. Choosing and using diversity indices: insights for ecological applications from the German Biodiversity Exploratories. *Ecology and evolution,* 4**,** 3514-3524.

MUIR, J., PHINN, S., EYRE, T., SCARTH, P., PETTORELLI, N. & DISNEY, M. 2018. Measuring plot scale woodland structure using terrestrial laser scanning. *Remote Sensing in Ecology and Conservation,* 4**,** 320-338.

MÜLLER, J., STADLER, J. & BRANDL, R. 2010. Composition versus physiognomy of vegetation as predictors of bird assemblages: The role of lidar. *Remote Sensing of Environment,* 114**,** 490-495.

MUNDT, A. K. a. F. 2020. factoextra: Extract and Visualize the Results of Multivariate Data Analyses.

NAKAGAWA, S., SCHIELZETH, H. & O'HARA, R. B. 2013. A general and simple method for obtainingR2from generalized linear mixed-effects models. *Methods in Ecology and Evolution,* 4**,** 133-142.

OLSCHOFSKY, K., MUES, V. & KÖHL, M. 2016. Operational assessment of aboveground tree volume and biomass by terrestrial laser scanning. *Computers and Electronics in Agriculture,* 127**,** 699-707.

PRETZSCH, H. 2009. Description and Analysis of Stand Structures. *In:* PRETZSCH, H. (ed.) *Forest Dynamics, Growth and Yield: From Measurement to Model.* Berlin, Heidelberg: Springer Berlin Heidelberg.

RICOTTA, C. & SZEIDL, L. 2009. Diversity partitioning of Rao's quadratic entropy. *Theoretical Population Biology,* 76**,** 299-302.

ROUSE, J. W., Jr., HAAS, R. H., SCHELL, J. A. & DEERING, D. W. 1974. Monitoring Vegetation Systems in the Great Plains with Erts. *NASA Special Publication.*

ROUSSEL, J. 2017. Auty, D. lidR: Airborne LiDAR Data Manipulation and Visualization for Forestry Applications. *R package version,* 1.

ŠAŠAK, J., GALLAY, M., KAŇUK, J., HOFIERKA, J. & MINÁR, J. 2019. Combined Use of Terrestrial Laser Scanning and UAV Photogrammetry in Mapping Alpine Terrain. *Remote Sensing,* 11**,** 2154.

SASAKI, T., IMANISHI, J., FUKUI, W. & MORIMOTO, Y. 2016. Fine-scale characterization of bird habitat using airborne LiDAR in an urban park in Japan. *Urban Forestry & Urban Greening,* 17**,** 16-22.

SEAVY, N. E., VIERS, J. H. & WOOD, J. K. 2009. Riparian bird response to vegetation structure: a multiscale analysis using LiDAR measurements of canopy height. *Ecological Applications,* 19**,** 1848-1857.

SEKERCIOGLU, C. H. 2002. Effects of forestry practices on vegetation structure and bird community of Kibale National Park, Uganda. *Biological Conservation* 107**,** 229–240.

SHORTHOUSE, D. J., IGLESIAS, D., JEFFRESS, S., LANE, S., MILLS, P., WOODBRIDGE, G., MCINTYRE, S. & MANNING, A. D. 2012. The 'making of' the Mulligans Flat - Goorooyarroo experimental restoration project. *Ecological Management & Restoration,* 13**,** 112-125.

SOUDARISSANANE, S., LINDENBERGH, R., MENENTI, M. & TEUNISSEN, P. 2009. Incidence angle influence on the quality of terrestrial laser scanning points. *Proceedings ISPRS Workshop Laserscanning 2009, 1-2 Sept 2009, Paris, France,* 38.

STAGOLL, K., MANNING, A. D., KNIGHT, E., FISCHER, J. & LINDENMAYER, D. B. 2010. Using bird–habitat relationships to inform urban planning. *Landscape and Urban Planning,* 98**,** 13-25.

STANLEY, H. A. & HERMAN, H. S. J. 1974. Habitat Selection of Breeding Birds in an East Tennessee Deciduous Forest. *Ecology,* 55**,** 828-837.

SUMNALL, M. J., HILL, R. A. & HINSLEY, S. A. 2016. Comparison of small-footprint discrete return and full waveform airborne lidar data for estimating multiple forest variables. *Remote Sensing of Environment,* 173**,** 214-223.

SZ DJI TECHNOLOGY CO., L. 2018. DJI GS Pro User Manual.

TEAM, R. C. 2019. R: A Language and Environment for Statistical Computing. . Vienna, Austria: R Foundation for Statistical Computing.

TROCHTA, J., KRUCEK, M., VRSKA, T. & KRAL, K. 2017. 3D Forest: An application for descriptions of three-dimensional forest structures using terrestrial LiDAR. *PLoS One,* 12**,** e0176871.

TUCKER, C. J. 1979. Red and photographic infrared linear combinations for monitoring vegetation. *Remote Sensing of Environment,* 8**,** 127-150.

TURNER, W., SPECTOR, S., GARDINER, N., FLADELAND, M., STERLING, E. & STEININGER, M. 2003. Remote sensing for biodiversity science and conservation. *Trends in Ecology & Evolution,* 18**,** 306-314.

VAN EWIJK, K. Y., TREITZ, P. M. & SCOTT, N. A. 2011. Characterizing Forest Succession in Central Ontario using Lidar-derived Indices. *Photogrammetric Engineering & Remote Sensing,* 77**,** 261-269.

VENABLES, W. N. & RIPLEY, B. D. 2003. *Modern applied statistics with S,* New York, Springer Science & Business Media.

VERSCHUYL, J. P., HANSEN, A. J., MCWETHY, D. B., SALLABANKS, R. & HUTTO, R. L. 2008. Is the effect of forest structure on bird diversity modified by forest productivity? *Ecol Appl,* 18**,** 1155-70.

VIERLING, K. T., VIERLING, L. A., GOULD, W. A., MARTINUZZI, S. & CLAWGES, R. M. 2008. Lidar: shedding new light on habitat characterization and modeling. *Frontiers in Ecology and the Environment,* 6**,** 90-98.

WEISBERG, P. J., DILTS, T. E., BECKER, M. E., YOUNG, J. S., WONG-KONE, D. C., NEWTON, W. E. & AMMON, E. M. 2014. Guild-specific responses of avian species richness to LiDAR-derived habitat heterogeneity. *Acta Oecologica,* 59**,** 72-83.

WIENS, J. A. & ROTENBERRY, J. T. 1981. Habitat Associations and Community Structure of Birds in Shrubsteppe Environments. *Ecological Monographs,* 51**,** 21-41.

WILKES, P., LAU, A., DISNEY, M., CALDERS, K., BURT, A., GONZALEZ DE TANAGO, J., BARTHOLOMEUS, H., BREDE, B. & HEROLD, M. 2017. Data acquisition considerations for Terrestrial Laser Scanning of forest plots. *Remote Sensing of Environment,* 196**,** 140-153.

YEBRA, M., MARSELIS, S., VAN DIJK, A., CARY, G. & CHEN, Y. 2015. Using LiDAR for forest and fuel structure mapping: options, benefits, requirements and costs. Australia: Bushfire & Natural Hazards CRC.

ZEHM, A., NOBIS, M. & SCHWABE, A. 2003. Multiparameter analysis of vertical vegetation structure based on digital image processing. *Flora - Morphology, Distribution, Functional Ecology of Plants,* 198**,** 142-160.

Chapter 3. Multi-sensor approach for detecting coarse woody debris in a landscape with varied ground cover

Authors: Shukhrat Shokirov[1,2], Michael Schaefer[3], Shaun R. Levick[2], Justin Borevitz[1], Tommaso Jucker[4], Ilhom Abdurahmanov[5], Kara Youngentob[1]

[1]Research School of Biology, Australian National University, Australia

[2]Commonwealth Scientific and Industrial Research Organization, Land and Water, Australia

[3]Food Agility CRC Ltd, 81 Broadway, Ultimo, NSW, 2007, Australia

[4]School of Biological Sciences, University of Bristol, England

[5]Tashkent Institute of Irrigation and Agricultural Mechanization Engineers, Uzbekistan

Keywords: TLS, ULS, LiDAR, Coarse Woody Debris, Random Forest.

Abstract

Coarse woody debris (CWD), or fallen logs, are known to be an essential habitat element for many organisms. CWD also supports ecosystem functioning through soil formation, nutrient cycling, and carbon storage. For these reasons, accurate assessments of CWD across landscapes are of interest to many ecologists and landscape managers, but traditional field-based measurements can be time-consuming and sampling strategies may not be representative of entire landscapes. Light detection and ranging (LiDAR) technologies may be able to provide a more rapid assessment of the number and volume of CWD across wide-areas. However, most research using LiDAR for forest and woodland inventory assessment has focused on standing wood and only recently, have a few studies focused on measuring CWD. Detection accuracy of CWD with LiDAR can be impacted by the point density of LiDAR data, ground layer vegetation and sensor positioning relative to other vegetation or landscape structural features. We used high resolution terrestrial laser scanner (TLS), UAV (unoccupied aerial vehicle) laser scanner (ULS) and a combination of data from both sensors (Fusion) to estimate CWD in a grassy woodland ecosystem. The study area comprised plots with different amounts of vegetation cover and different types of CWD, both naturally occurring and introduced including dispersed, clumped or a mixture of both types. This enabled a more detailed exploration of model performance across sensor types, vegetation types and ground cover biomass. A random forest (RF) classification algorithm and noise removing operations on raster imagery were used to classify CWD. Completeness and correctness accuracy with the developed method were highly variable depending on the data and ground vegetation cover, and ranged between 20% and 86%, and 12% and 96%, respectively in comparison with field data. LiDAR derived digital surface model (DSM), surface roughness and topographic position index were important variables for CWD detection. We found that the detection accuracy of CWD varied with the type and amount of ground vegetation cover and LiDAR data. Ground cover density had a strong negative impact on accuracy, particularly for TLS and Fusion data.

Introduction

Coarse Woody Debris (CWD), or fallen dead trees, are an important structural component in forest ecosystems that provide habitat for plants and animals. CWD provides shelter, nesting areas and a foraging substrate for many bird, reptile and mammal species (Harmon et al., 2004, Manning et al., 2013). CWD also has a role in multiple aspects of ecosystem functioning including soil formation, nutrient cycling, and carbon storage (Harmon et al., 2004, Woldendorp and Keenan, 2005, Manning et al., 2013). CWD is a naturally occurring feature of forests and woodlands, but it is often removed

for firewood or lost through land-clearing or other landscape management practices (e.g., post-logging burning of forests) (West et al., 2008).

The loss of CWD from an ecosystem causes a reduction or loss of the associated biodiversity and ecological processes over short and long time periods (Manning et al., 2013). The natural accumulation rate of CWD is usually very slow and depends on a number of factors including tree genetics, stand age and anthropogenic or natural disturbance (Vandekerkhove et al., 2009). Restoring CWD is an increasingly common intervention to support biodiversity conservation and improve other ecosystem services such as carbon storage and soil improvement (Manning et al., 2004a).

Measuring the amount, volume, diameter and length of CWD is important for monitoring this resource and estimating habitat quality for a number of CWD dependent organisms (Harmon et al., 2004). Traditional field-based methods of CWD data collection are usually restricted to transects and plots, which are time-consuming and may not accurately represent the entire area from which the subsample is taken (Harmon et al., 2004, Lopes Queiroz et al., 2020). Thus, remote sensing may be a valuable tool to overcome these drawbacks and quantify CWD across wide-areas. A few studies have attempted to classify and quantify CWD using aerial multispectral imagery (Smikrud and Prakash, 2013, Windrim et al., 2019). However, shading and canopy occlusion interfere with the ability of multispectral imagery to map CWD in many environments (Blanchard et al., 2011, Richardson and Moskal, 2016).

The rapidly developing technology of Light Detection and Ranging (LiDAR) offers an alternative remote sensing technique for mapping CWD by capturing three-dimensional landscape structure and vegetation (Pasher and King, 2009, Marchi et al., 2018). LiDAR can be used from airborne or terrestrial platforms and the combined data from both platforms may help overcome occlusion issues unique to the perspective of airborne or terrestrial sensors. LiDAR uses a laser light to measure the distance between the sensor and ground features. A single pulse emitted from a LiDAR sensor can capture structural information from different layers of vegetation, including upper canopy, lower canopy and other elements near the ground (Lefsky et al., 2002, Bergen et al., 2009).

Relatively few studies have used LiDAR to quantify CWD, since most LiDAR-based measurements of forest and woodland structure have focused on standing wood. However, as this technology becomes more accessible, ecologists are increasingly interested in using LiDAR technology for investigating important below canopy structural habitat features such as CWD (Pesonen et al., 2009, Lopes Queiroz et al., 2020). A small number of studies have identified some LiDAR based metrics that may be useful for mapping CWD. For example, Pesonen et al. (2009) predicted CWD volume

from Airborne laser scanner (ALS) derived canopy height percentiles using regression analysis, and Mücke et al. (2013) utilized surface roughness features derived from full-waveform and discrete return ALS data to classify CWD. In addition, Object Based Image Analysis (OBIA) has been successfully applied using Trimble eCognition software to ALS derived raster images for automatically delineating CWD in disturbed open forest (Blanchard et al., 2011). Lopes Queiroz et al. (2019, 2020) performed geographic object based image analysis (GOBIA) with a random forest (RF) classifier in eCognition commercial software using a ALS derived digital surface model, canopy height model and aerial multispectral imagery to classify CWD. Their research is the first and only previous study that used RF models with combined ALS and multispectral imagery to detect CWD. Notably, data from unoccupied aerial vehicle laser scanners (ULS) has not been used in any prior assessments of CWD.

LiDAR-derived raster images are more often used for automatically classifying CWD (Marchi et al., 2018), but a few studies have attempted to extract CWD from high density terrestrial LiDAR point cloud data (Polewski et al., 2017, Yrttimaa et al., 2019). For instance, Polewski et al. (2017) used a statistical framework to fit a cylinder shape over a TLS data to detect CWD. Yrttimaa et al. (2019) also used a cylinder fitting algorithm on TLS point cloud data followed by raster image filtering to quantify the number and volume of CWD. Despite some successes, accurate detection of CWD below the canopy using LiDAR technology remains a challenging task and depends largely on the point density of LiDAR data cloud and surrounding vegetation height and density (Polewski et al., 2017).

All of the above mentioned studies found a negative impact of ground vegetation cover on CWD detection accuracy; however, most were conducted in optimal low groundcover conditions with a single sensor type, so it was not possible to compare model performance across different amounts of vegetation cover or with data collected from different sensors. For the first time, we look at the effects of ground vegetation cover on model performance using ULS, TLS and a combination of data from both sensors (Fusion). We utilized surface topographic variables derived solely from high resolution LiDAR datasets as inputs into RF in open source R language to test a novel approach to classify and quantify CWD.

The aim of this study was twofold:

1) To investigate the performance of Random Forest (RF) machine learning algorithms to quantify CWD from commonly used LiDAR derived topographic surface variables.

2) To test the influence of vegetation type and ground cover on CWD detection accuracy using UAV (unoccupied aerial vehicle) LiDAR (ULS), terrestrial LiDAR (TLS) and a fusion of both LiDAR datasets (Fusion).

Materials and methods

Study Area

This study was conducted in Mulligan's Flat (683 ha) and Goorooyarroo (702 ha) (MFGO) nature reserves, located in the north-eastern corner of the Australian Capital Territory (ACT), (35°09' S-149°09' E; Fig. 1). Elevation ranges between 650-700 meters with a gently undulating topography that includes low rolling hills interspersed with plains and flats (McIntyre et al., 2010). These two adjacent wildlife reserves were established in 1994 and 2006, respectively, to conserve and restore a critically endangered yellow box–Blakely's red gum grassy woodland ecosystem (Manning et al., 2011). Restoration activities include, but are not limited to, the introduction of CWD, pest exclusion fences and the reintroduction of previously locally extinct native species (Manning, Cunningham, and Lindenmayer 2013).

As part of on-going experimental restoration work at MFGO, 96×1 ha (200 m × 50 m) sites were established across both reserves in 24 clusters and include four different vegetation types: 1) high tree, high shrub cover (HTHS), 2) high tree, low shrub cover (HTLS), 3) low tree, low shrub cover (LTLS), and 4) low tree, high shrub cover (LTHS) (Manning et al. 2011) (Fig.1). In October 2007, two-thousand tonnes of CWD were distributed across 72 sites in both reserves. The remaining sites with no introduced CWD served as controls. Treatments were: (a) 20 tonnes/ha added with dispersed CWD, (b) 20 tonnes/ha added with clumped CWD, and (c) 40 tonnes/ha added with both dispersed and clumped CWD (Manning et al., 2007) (Figs. 1 and 2). Detailed information on the addition of CWD is provided in (Manning et al., 2013).

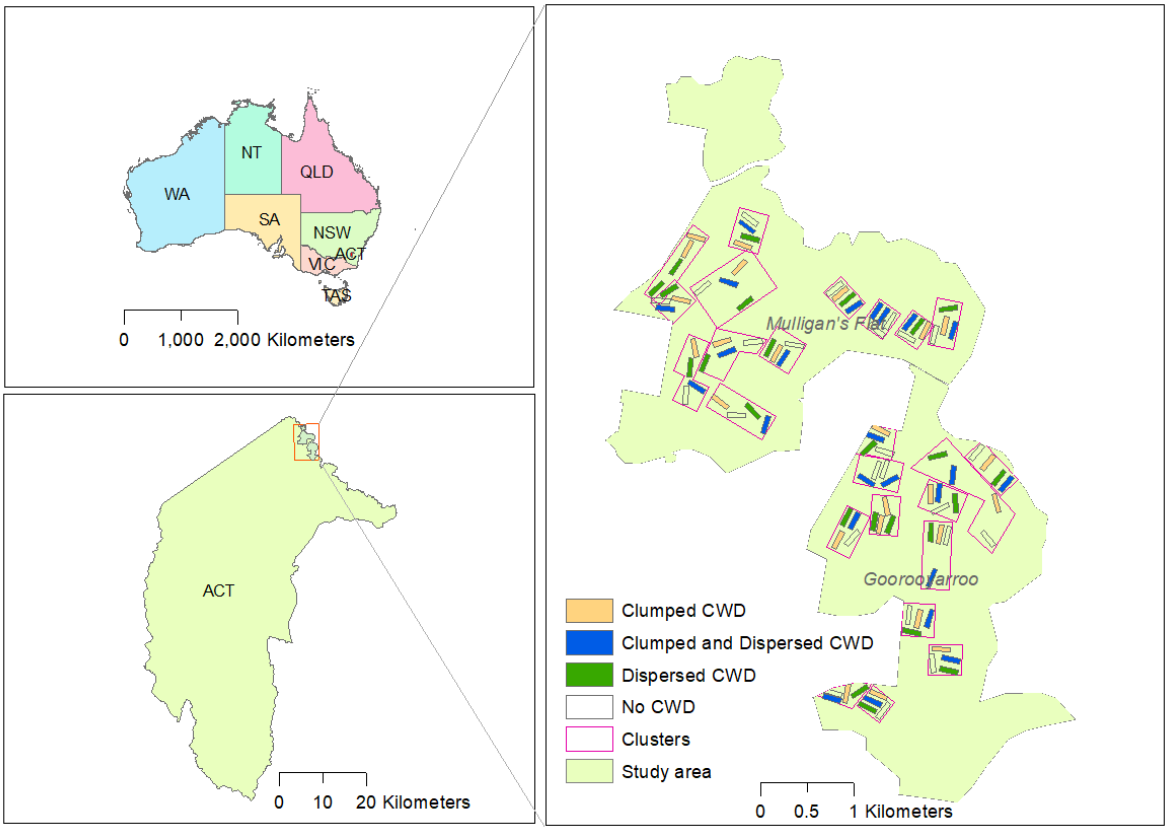

Figure 5. Map of the study area. 1) Australia, 2) Australian Capital Territory, 3) Mulligan's Flat and Goorooyarroo Nature Reserves showing experimental restoration sites with different treatments of coarse woody debris (CWD).

Figure 2. Images of dispersed (*a*) and clumped (*b*, *c*) coarse woody debris in low (*a*), medium (*c*), and high (*b*) ground vegetation cover categories.

TLS data collection and post - processing

We collected TLS data with a high-density terrestrial laser scanner (Topcon GLS2000, Topcon Corporation, Japan) that emits near-infrared light (1064 nm) laser pulses at up to 120,000 laser pulses per second. The field-of-view of the scanner is 360° horizontally and 270° vertically. A single laser pulse has a beam diameter of 4 mm at 60 m. Data was collected from 7 scan stations in each 50 m × 200 m plot in a zigzag formation with approximately equal spacing (33 m) between the stations. The number and arrangement of scan stations was determined by a pilot study to identify the optimal number and arrangement of scans to characterise all 96 sites within a one month timeframe (Shokirov et al., 2020, Shokirov, 2021). From the 1st to 31st of October 2018, TLS LiDAR data was acquired across all 96 × 1 ha sites for a total of 672 scans with 6 mm at 10 m scanning resolution and 1.7 m scanning height. The position of each scan was measured with a differential GPS (Trimble Geoexplorer 6000 series) and post-processing was performed using local base station data to improve the location accuracy to approximately 0.5 m.

Point clouds from the seven individual scan stations for each plot were co-registered using the Multi-station Adjustment (MSA) plugin in RiScan Pro software (RIEGL Laser Measurement Systems GmbH). Co-registering point clouds with MSA consists of two steps: manual and automatic registration. First, point clouds from two scans were manually coarsely aligned by using the overlapping objects (trunks, trees and shrubs) in both scans. Then, automatic registration was implemented which uses at least four identical points from overlapping areas of two scans. MSA uses the iterative closest points (ICP) algorithm that minimises the 3D distance between the identical points by translating and rotating the entire point cloud along x, y, z axes until the least minimum distance between the identical points from two dataset is achieved (Šašak et al., 2019). Then the position and orientation of the first and second scan were locked and the same procedure was performed to register the third scan to the initial two scans.

Next, the point cloud from each site was georeferenced using DGPS locations of each scan position measured in the field and clipped to the spatial extent of the 96 sites individually. Point clouds were then subsampled into 1 cm spacing to homogenize the point distributions and duplicate points were removed using Cloud Compare (CloudCompare 2.10.2).

ULS data collection and post-processing

We obtained ULS data across all of the 96 sites in fine weather conditions from the 7th until the 14th of November, 2018. The ULS LiDAR platform consisted of a hexacopter integrated with a RIEGL miniVUX-1 UAV LiDAR sensor (RIEGL Laser Measurement Systems GmbH, Austria) and an APX-15 INS/GNSS system (Trimble, USA). ULS data was acquired at approximately 80 m above the take off point at approximately 7 m s^{-1}, with up to 5 returns per pulse, 100 kHz pulse repetition rate, and up to 100,000 measurements/second. The maximum scan angle of the LiDAR sensor was approximately ±60º with swath width of approximately 100 m. On average, the four adjacent plots were covered by 500 × 500m flight area which included 11 parallel lines and one diagonal flight line on the return to landing. We used DJI ground station pro V2 to plan the flight missions (SZ DJI TECHNOLOGY CO., 2018). The ULS LiDAR sensor failed to collect data on two 1 ha sites, which were excluded from further analysis of ULS and TLS data. Data processing was done in RiPROCESS software suite from RIEGL to bring in the trajectory data of the drone flight, align the flight paths, geo-reference the point cloud and then export it in ASPRS LAS format. The trajectory data of the UAV LiDAR that was ingested into RiPROCESS was generated using POSPAC UAV (Applanix) using the IMU/GNSS data from the drone and RINEX data from the base station, which was obtained from the Gungahlin location of Smartnet global network.

The ULS LiDAR data collected over the 94 sites were clipped by corresponding polygons to create separate point clouds for each site. In general, point spacing in ULS data across 94 sites ranged from 5 cm to 17 cm with an average of 10 cm. For this reason, we homogenized the point cloud with 10 cm spacing and removed duplicate points using Cloud Compare (CloudCompare 2.10.2).

Field data

Field data collection for ground-truthing the model outputs was conducted in June, 2020. Eighteen sites were selected that included the three CWD types and four different vegetation types across both reserves. CWD in our research is defined as the downed dead wood including tree trunks and branches at least 2 m in length and 0.1 m in diameter. The minimum diameter of 0.1 m was determined based on the point spacing of ULS data (approximately 10 cm), which indicated that ULS should be able to capture CWD with at least 0.1 diameter and this aligned with the minimum size identified in other studies as well (Pesonen et al., 2009, Farnell et al., 2020). The length of 2 m is commonly used for defining of CWD for forest inventory (Grizzel et al., 2000, Edwards, 2004). The location of the centre of each individual log was recorded with a differential GPS (± 3 m accuracy). For clumped logs, a single location at the nearest midpoint of the clump was measured. Photos of each clumped and dispersed CWD were also taken.

The volume of each CWD was calculated using the cylinder volume equation:

$$V_{field} = l \times \pi \times ({}^{d}/_{2})^{2} \quad \text{Equation (1)}$$

Where, V_{field} - volume of CWD, l - length of CWD, d - diameter in the middle of the full length of CWD, π - mathematical constant.

To estimate the influence of ground cover on CWD detection accuracy, sample sites were divided into three different ground cover categories: Low (< 400 kg/ha), Medium (400 kg/ha - 800 kg/ha) and High (> 800 kg/ha) (Fig. 2). This classification was based on an earlier study (McIntyre et al., 2010), which estimated total biomass (kg/ha) of native and exotic plants across the 96 sites at MFGO. Although this previous study was conducted in 2010, the differences in ground vegetation cover were primarily driven by vegetation species and herbivore exclusion fencing at a subset of sites, which have not changed over this period, and this was confirmed through a visual comparison of sites to their earlier classification by McIntyre et al (2010).

Merging the TLS and ULS data

A fused dataset (Fusion) was created from TLS and ULS data first by manually adjusting and then automatically co-registering the data from both sensors using the Iterative Closest Point (ICP) algorithm in CloudCompare (CloudCompare 2.10.2).

Noise reduction, normalization and subsetting the point clouds

TLS, ULS and Fusion point clouds were cleaned for noise with *lasnoise* with step 0.30 (TLS and Fusion) and step 0.50 (ULS) parameters. Point clouds were classified into ground and non-ground points using the *lasground* tool in LAStools (Isenburg 2012). *Lasground* uses progressive, Triangulated Irregular Network (TIN) densification methods to classify ground points (Montealegre et al., 2015). Different settings of *lasground* were trialed and the resulting ground and non-ground points were visually assessed across different plots. This was important because improper filtering of ground points might result in incomplete or false CWD surface points. The final selected *lasground* setting were as follows: *step 2, extra_fine, not_airborne, compute_height, replace_z* for TLS and Fusion dataset and the same parameters except without *not_airborne* for ULS dataset (Isenburg 2012). Using field measurements, it was found that the height of almost all of the CWD was less than 1 m. Thus a subset of point clouds of all 94 sites was created by removing the points above 1.3 m to provide an additional height buffer.

CWD extraction workflow

Calculating DHM and other topographic variables

CWD classification involved machine learning methods with imagery data. First a 0.1 m grid-size digital surface model (DSM) was created from all returns below 1.3 m using *las2dem* (Isenburg, 2012) for all three datasets (TLS, ULS and Fusion). The *las2dem* module of LAStools first creates a Triangulated Irregular Networks (TIN) and then generates an interpolated raster image from TIN (Khosravipour et al., 2014, Stereńczak et al., 2016). After testing several parameters, “elevation” and “step 0.1” were chosen to create the DSM. In addition, a parameter of “kill 0.25” was used to avoid creating the DSM from triangles with edge longer than 0.25 m. This was done to avoid creating false planar objects in occluded areas in the plot that might have caused false positives in the RF model. To reduce the noise and generate a smoothed DSM, a Gaussian Filter algorithm in SAGA (Conrad et al., 2015) was used with the following parameters (standard deviation 1, search mode: square, search radius: 3). Subsequently, DSMs from all dataset were imported to RStudio environment and five topographical variables were calculated to characterize the shape of relief from DSM using a raster

package (Hijmans, 2020). An 8×8 moving window on the underlying DSM layer was used to compute slope and aspect variables. All six variables were stacked together to create a six band raster image. Previous studies have found these variables useful for characterizing the spatial heterogeneity of landscape surfaces (Amatulli et al., 2018). The list of variables and their descriptions are shown in Table 1. In addition, the relationship between the topographic variables derived from TLS, ULS and Fusion datasets were examined using Pearson's correlation (Appendix 1).

Table 5. Description of topographic variables.

Variable name	Description
Digital surface model (DSM)	0.1 m grid calculated from normalized points below 1.3 m using TIN interpolation method (Isenburg, 2012).
Roughness	Roughness is calculated as the largest inter-cell difference of a focal cell and its 8 neighboring pixels (Amatulli et al., 2018)
Slope	Slope expresses the degree of elevation change in the direction of the steepest descent (Amatulli et al., 2018).
Aspect	Aspect is the orientation of slope. It is measured clockwise in degrees from 0 to 360, where 0 is north-facing, 90 is east-facing, 180 is south-facing, and 270 is west-facing (Amatulli et al., 2018).
Topographic ruggedness index (TRI)	TRI is the average of the absolute differences in elevation between a focal cell and its neighboring cells. Zero values correspond to flat surfaces whereas positive values correspond to mountain areas (Amatulli et al., 2018)
Topographic position index (TPI)	TPI compares the elevation of a focal cell and the mean of its 8 neighboring cells. Positive values represent ridges, negative values correspond to valleys and zero values correspond to flat areas (Amatulli et al., 2018).

Training data preparation

To create a training dataset, CWD, shrub and grass classes were delineated based on the visual interpretation of DSM and its shaded relief data using QGIS software (QGIS, 2020). Training samples distributed across the landscape from each class (CWD, shrub, and grass) were collected from most of the 94 sites to avoid spatial autocorrelation in the training dataset (Millard and Richardson, 2015). To avoid imbalanced data, which can negatively impact classification accuracy (Maxwell et al., 2018),

approximately 300 samples per class were collected. A distance of at least 8 m between the classes was kept to avoid spatial interpolation, as recommended (Millard and Richardson, 2015).

Random forest classification

Random Forest (RF) is a widely used machine learning technique for classifying remote sensing data (Guo et al., 2011, Millard and Richardson, 2015). Many studies found that machine learning algorithms produce higher accuracy remote sensing classifications than traditional pixel based algorithms like maximum likelihood (Duro et al., 2012, Maxwell et al., 2018).

We ran RF classifications using the 'caret' package (Kuhn, 2020) in R statistical software (Team R, 2013). The caret package provides a standard syntax to execute a variety of machine-learning methods (Maxwell et al., 2018). The RF is a tree-type classification algorithm which utilizes a set of decision trees to make a prediction (Breiman, 2001, Belgiu and Drăguţ, 2016). First, training data are created by delineating small subsets of polygons as a sample of target classes on an image. Then, the algorithm trains the data by generating multiple decision trees where each tree is trained based on randomly sampling the variables in the original training data set (Belgiu and Drăguţ, 2016). Each decision tree will come up with a rule to predict a target class. Each tree produces a vote to a target class and these votes will be counted and the majority vote of trees will be used for classification (Breiman, 2001, Friedman et al., 2001).

Two parameters of the RF model can be tuned by the user: the number of decision trees (T) and the number of variables (M) randomly chosen at each split. However, multiple studies have found that tuning the number of T manually does not impact the accuracy of the results as long as the number of *T* is large enough (>300) (Probst and Boulesteix, 2017, Maxwell et al., 2018). Therefore, we selected a conservative number of 500 *T* in the caret package (Maxwell et al., 2018). The default setting of three randomly chosen variables *M* was kept at each split.

A previous study found that highly correlated predictor variables reduced the classification accuracy (Millard and Richardson, 2015). Hence, Pearson's correlation was used to calculate pair-wise correlations between the predictor variables, and variables that were highly correlated ($r > 0.9$) to any other predictor variable were removed (Millard and Richardson, 2015). To test model performance, training samples were split into training and testing datasets using proportional stratified random sampling. Approximately 70% of the samples were used to train the data using the RF algorithm and the remaining 30% of the data were reserved as a "hold-out" to test the classification accuracy (Duro et al., 2012). Model performance was examined with out-of-bag error (OOB) and confusion matrixes to estimate classification accuracy between predicted and observed data in the hold-out 30%

independent validation data (Millard and Richardson, 2015). We also evaluated the importance of predictor variables for the classification accuracy using OOB.

Post-classification refinement and shape analysis

Remote sensing data classification often requires post-classification improvement to reduce noise from classification maps (Droppova, 2011, Boz et al., 2015). We used the Majority Filter tool in ArcMAP (ESRI, 2011) for smoothing the image. Majority filter replaces cells in a raster based on the majority of their contiguous neighboring cells, and as a result, most of the isolated pixels will be assigned to a surrounding class. Then, only CWD class pixels were converted to polygon shapefiles using the Raster to Polygon conversion tool in ArcMAP. After the polygon smoothing algorithm, polygons with areas greater than 0.2 m^2 and less than 25 m^2 were selected. These thresholds were derived from the minimum area of CWD (0.1 m width and 2 m length) and visual interpretation of DSM and polygons, respectively. Elongated objects were extracted by creating a minimum bounding box for each polygon and the width and length of each box was calculated. Then, bounding boxes with lengths of less than 2 m were removed. Finally, polygons within remaining bounding boxes were selected using Select by Location tool in ArcMAP.

Calculating volume of CWD

A Zonal Statistics tool in QGIS software (QGIS, 2020) was used to calculate a volume for each detected CWD. This tool calculates several values including mean value of all pixels, number of all pixels and sum of pixels from DSM for each overlapping polygon. Volume of CWD was derived from the following equation:

$$V_{detect} = A^2 \times M \times C \quad \text{Equation (2)}$$

Where, V_{detect} − volume, A − pixel size, M − mean value of all pixels within a polygon, C − number of pixels within a polygon.

Consequently, total CWD volume for each site was calculated using the sum of all CWD volume in the site.

Classification accuracy assessment

Classification accuracy was performed by comparing the CWD vector map and field-measured coordinates of each CWD in the 18 validation sites. DSM, DSM-based shaded relief and photos from the field were also used to assist with accuracy assessments. For each of the 18 sample sites, Producer's accuracy (completeness) and User's accuracy (correctness) were estimated using Equations 3 and 4,

respectively (Mücke et al., 2013). To evaluate the accuracy of estimated CWD volume, field data of CWD volume from each plot and detected CWD volume (excluding FP), and detected total CWD volume (including FP) were compared. We excluded FP to determine the accuracy of CWD volume estimates where CWD is correctly detected. To assess the impact of FP in estimated CWD volume, we then included both TP and FP in accuracy assessment.

$$Completeness = {}^{TP}/_{(TP + FP)} \quad \text{Equation (3)}$$

$$Completeness = {}^{TP}/_{(TP + FP)} \quad \text{Equation (4)}$$

Where, a True Positive (TP) is a CWD that is detected by the method and is recorded in the field data, a False Positive (FP) is a CWD that is detected but is not recorded in the field data, and a False Negative (FN) is a CWD that is not detected but is present in the field data.

The difference between the detected and ground measured CWD volume were estimated using the coefficient of determination (R^2) and the Root Mean Square Error (RMSE, Equation 5). The CWD detection workflow is provided in Figure 3.

$$RMSE = \sqrt{[\frac{\sum(P_i - O_i)^2}{n}]} \quad \text{Equation (5)}$$

Where, Σ symbol indicates "sum", P_i is the predicted volume for the i^{th} observation, O_i is the observed volume for the i^{th} observation, n is the sample size.

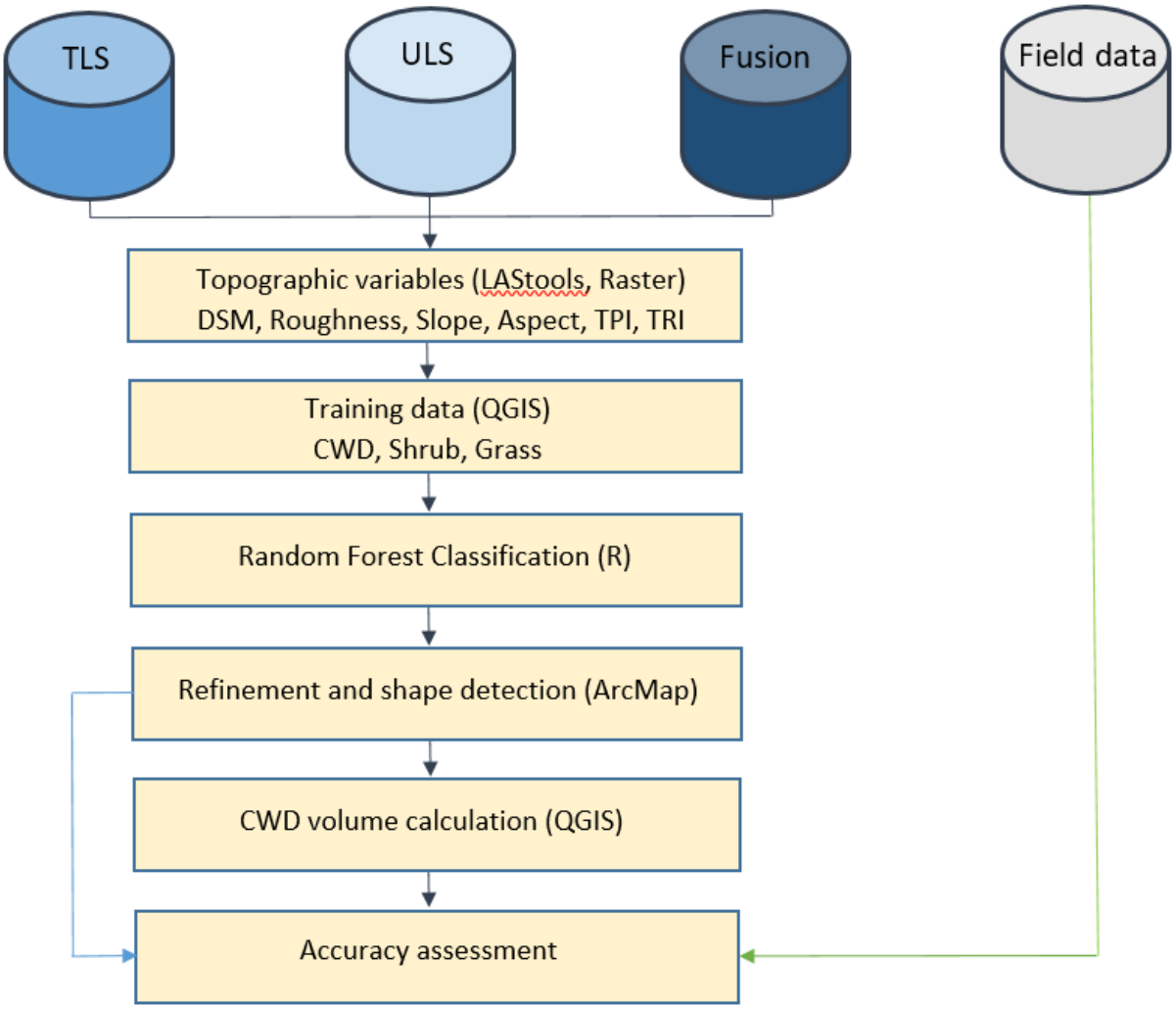

Figure 3. Workflow of coarse woody debris (CWD) extraction method, including software and packages used. Terrestrial laser scanner (TLS), an unoccupied aerial vehicle laser scanner (ULS) and fused ULS and TLS (Fusion) datasets include points below 1.3 m.

Results

CWD field data

We measured a total of 998 CWDs from 18 sites for ground-truthing. The average amount of CWD in a site was 55, the max amount was 93 and the min amount was 33. Sites with dispersed and clumped CWD had the same number on average (n = 47 and n = 46, respectively), but combined (clumped and dispersed in the same site) had a substantially higher number of CWD on average (n = 71). The length of CWD ranged from 2 m to 14 m (mean of 4.1m), and diameter in the middle of the long axis ranged from 0.1 m to 0.9 m (mean of 0.3 m). The volume of a single CWD varied from 0.02 m^3 to 3.98 m^3 (mean value of 0.37 m^3) (Appendix 2).

Variable selection and comparison across TLS, ULS and Fusion data types

Pearson's pair-wise correlations between the predictor variables indicated that surface terrain ruggedness index and slope correlated highly with other variables ($r > 0.9$) (Appendix 3). Hence, they were removed and the remaining variables, DSM, Roughness, Topographic Position Index (TPI) and Aspect raster images, were used as predictors in the RF classification.

Pearson's correlation was also used to investigate the relationship between TLS, ULS and Fusion derived surface topographic variables (Appendix 1). ULS and Fusion typically demonstrated stronger correlation among common variables than ULS and TLS but substantially less than TLS and Fusion (Appendix 1). TPI and aspect showed the weakest correlations across the data types. The highest correlation among variables was observed between TLS and Fusion, with > 0.8 correlation between the two data types for DSM, slope, TRI and roughness (Appendix 1).

Accuracy assessment of RF model

RF classification was performed on the aforementioned four predictor variables and training samples. Overall classification accuracy of the independent testing data varied between different sensors with TLS (72.5%), ULS (75.5%) and Fusion (78.2%) (Table 2). Confusion matrices, which describe correctly and incorrectly classified pixels of the predicted classes compared to the testing dataset, indicated that the model performed best in classifying grass classes (> 80.2%) but had a lower classification accuracy for CWD (> 67.9%) and shrub classes (> 66.9%) (Table 2).

Table 6. Random forest (RF) classification accuracy. Confusion matrices describe comparison between the predicted classes of pixels by RF model and independent testing data. Both predicted and testing dataset represent the number of pixels. a) Terrestrial laser scanner (TLS), b) an unoccupied aerial vehicle laser scanner (ULS), c) fused TLS and ULS (Fusion) data.

a)

Predicted data	**Hold-out testing data**				
		CWD	Shrub	Grass	**User's accuracy**
	CWD	6592	2574	541	67.9%
	Shrub	2946	6559	295	66.9%
	Grass	616	425	6346	85.9%
	Producer's accuracy	64.9%	68.6%	88.4%	
	Overall accuracy	72.5%			

b)

Predicted data	Hold-out testing data				
		CWD	Shrub	Grass	**User's accuracy**
	CWD	21941	5257	2968	72.7%
	Shrub	3194	8128	100	71.2%
	Grass	3744	859	19509	80.9%
	Producer's accuracy	76.0%	57.1%	86.4%	
	Overall accuracy	75.5%			

c)

Predicted data	Hold-out testing data				
		CWD	Shrub	Grass	**User's accuracy**
	CWD	15243	3974	2792	69.3%
	Shrub	2947	13969	497	80.2%
	Grass	3760	3185	32397	82.3%
	Producer's accuracy	69.4%	66.1%	90.8%	
	Overall accuracy	78.2%			

The OOB errors produced by RF for an accuracy assessment using the independent (hold-out) testing data as well as measures of variable importance based on the mean decrease in accuracy when a variable is not used in building a tree are presented in Figure 4. OOB error is lowest for the grass class and higher for shrub and CWD classes across different sensor data. Average OOB error is lowest for Fusion data (≈22%) and higher for ULS (≈25%) and TLS (≈28%) data. Overall, accuracy assessment by OOB error is consistent with the confusion matrix described in Table 2.

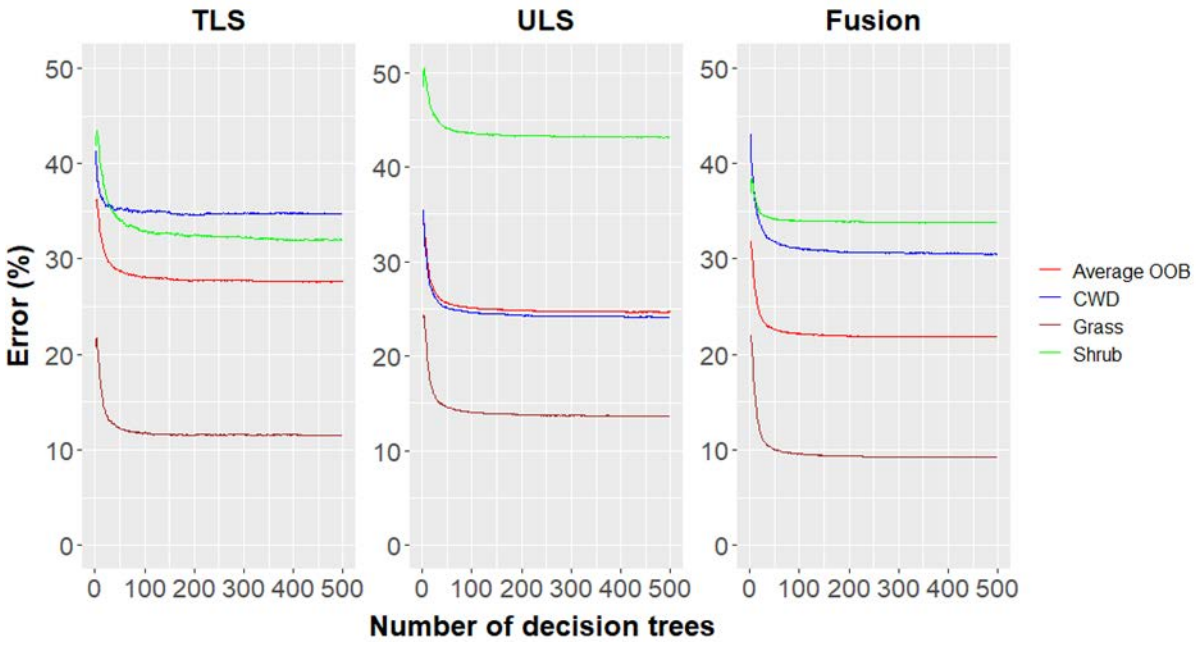

Figure 4. Random forest accuracy assessment of terrestrial laser scanner (TLS), an unoccupied aerial vehicle laser scanner (ULS), fused TLS and ULS (Fusion) data for classifying coarse woody debris (CWD), Grass and Shrubs with out-of-bag (OOB) error. OOB is calculated by comparing classified training dataset with excluded (out-of-bag) training dataset (in our case, one third of training data were left-out from training).

In general, DSM and surface roughness were the most important predictor variables in classifying CWD, shrubs and grass (Fig. 5). DSM, roughness and TPI were comparably important for identifying CWD from all three types of data. Surface aspect had the weakest prediction power for classifying all classes (Fig. 5).

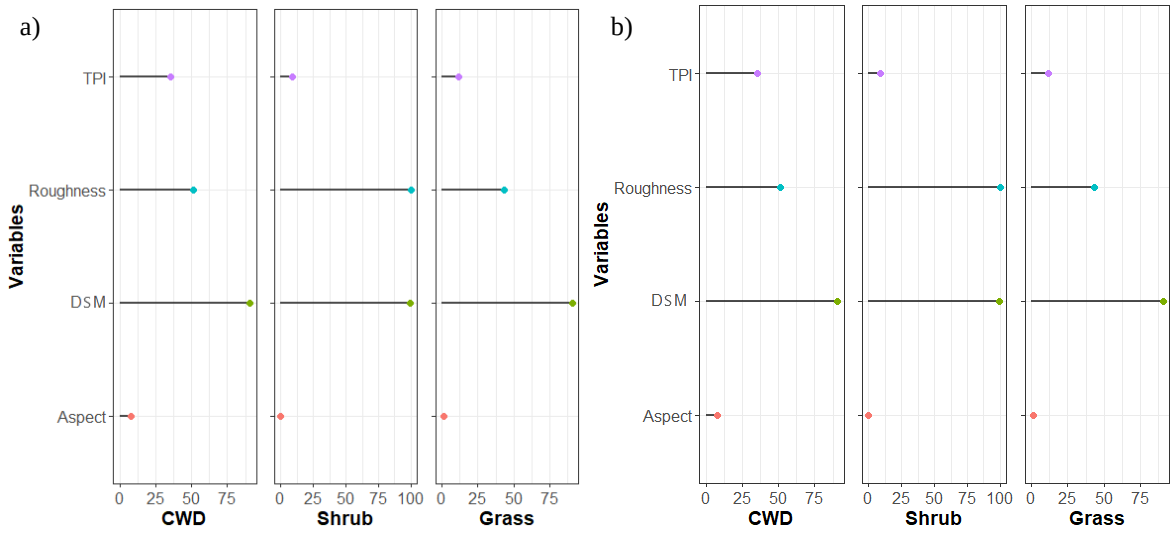

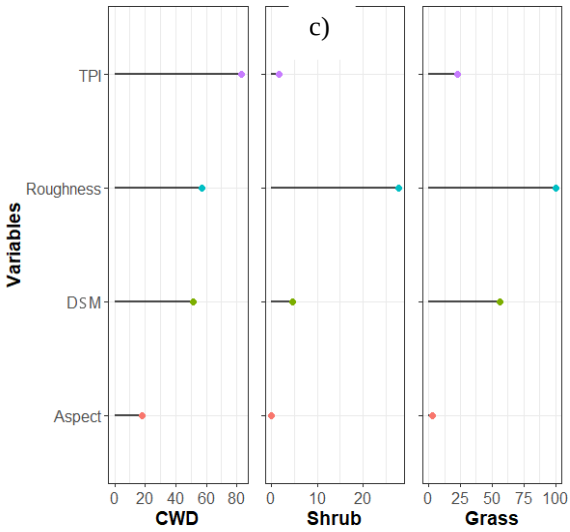

Figure 5. Predictor variable importance for random forest classification of three landscape features (coarse woody debris (CWD), shrub and grass) with LiDAR data from (a) terrestrial laser scanner (TLS), (b) an unoccupied aerial vehicle laser scanner (ULS) and (c) fused TLS and ULS data (Fusion). Digital surface model (DSM), topographic position index (TPI), topographic ruggedness index (TRI).

Accuracy assessment of CWD counts

Overall accuracy

Both sensors produced comparable completeness accuracy in counting the number of CWD and exhibited large variations in accuracy between sites (TLS = 19.6% to 75.0%, average of 57.0%, ULS = 32.8% to 82.2%, average of 57.8%) (Table 3). However, correctness accuracy for TLS was slightly higher (11.9% to 96.2%, average of 55.5%) than ULS (29.4% to 81.1% average of 51.7%). Fusion data outperformed single sensors in counting CWD for both completeness and correctness accuracy (averages = 67.0% and 55.6%, respectively), indicating that co-registering TLS and ULS sensor data improved the accuracy for this measure (Table 3).

Table 7. Overall completeness and correctness of coarse woody debris (CWD) counts in eighteen independent validation sites using data from a terrestrial laser scanner (TLS), an unoccupied aerial vehicle laser scanner (ULS), fused TLS and ULS (Fusion) data. Sites included four vegetation types (1) high tree, high shrub cover (HTHS), 2) high tree, low shrub cover (HTLS), 3) low tree, low shrub cover (LTLS), and 4) low tree, high shrub cover (LTHS)) and three ground vegetation densities (high, medium, low).

Site	Veg class	CWD type	Ground veg. type	TLS		ULS		Fusion	
				Complete-ness	Correct-ness	Complete-ness	Correct-ness	Complete-ness	Correct-ness
MF11A-4	LTHS	clumped	High	66.7	43.1	60.6	60.6	66.7	41.5
MF11A-2	LTHS	combined	Medium	66.2	41.0	46.2	81.1	64.6	50.6
MF11A-3	LTHS	dispersed	Medium	60.6	40.0	40.6	39.4	60.6	48.8
MF27A-2	LTHS	dispersed	Low	71.4	73.5	64.7	40.7	82.9	76.3
MF22A-2	HTHS	clumped	High	63.2	22.6	65.8	46.3	60.5	24.5
MF22A-3	HTHS	dispersed	High	48.7	11.9	56.4	47.8	56.4	27.2
MF22A-4	HTHS	combined	High	64.4	25.4	82.2	41.1	46.7	20.8
MF34-1	HTLS	clumped	Low	46.6	87.2	55.4	62.1	72.6	75.7
MF34-4	HTLS	combined	Medium	50.5	30.9	61.5	64.1	54.8	49.0
MF34-3	HTLS	dispersed	Low	61.3	70.8	60.5	75.4	48.6	58.1
WG150A-3	HTLS	clumped	Low	69.6	44.4	56.5	33.3	76.1	47.3
WG150A-2	HTLS	dispersed	Low	62.7	30.8	58.8	29.4	62.7	53.3
WG63A-1	LTLS	combined	Medium	75.0	94.7	72.2	71.2	86.1	72.1
WG63A-4	LTLS	combined	Low	69.9	96.2	56.8	64.6	71.6	84.1
WG148-3	LTLS	combined	Medium	38.0	85.7	58.8	58.0	75.9	81.1
WG148-4	LTLS	dispersed	Medium	55.8	78.4	39.6	30.0	69.2	65.5
WG148-2	LTLS	clumped	Medium	19.6	30.3	66.0	33.3	68.6	60.3
WG92-3	LTLS	clumped	Low	35.1	92.9	37.8	51.9	81.1	65.2
			Max	**75.0**	**96.2**	**82.2**	**81.1**	**86.1**	**84.1**
			Min	**19.6**	**11.9**	**37.8**	**29.4**	**46.7**	**20.8**
			Mean	**57.0**	**55.6**	**57.8**	**51.7**	**67.0**	**55.6**
			Median	**62.0**	**43.8**	**58.8**	**49.8**	**67.6**	**55.7**

CWD count accuracy by varied ground cover density

Ground vegetation cover had the biggest impact on CWD detection accuracy for the TLS sensor (Table 4). We found a roughly similar completeness accuracy across the sites with differing amounts of ground vegetation. However, ground vegetation had a big influence on correctness accuracy for TLS and Fusion and to a lesser extent for ULS based counts (Table 4) (Fig. 6).

Table 8. Coarse woody debris (CWD) count accuracy by low, medium and high density ground vegetation sites. Terrestrial laser scanner (TLS), an unoccupied aerial vehicle laser scanner (ULS), fused TLS and ULS (Fusion) data.

Ground vegetation density	TLS		ULS		Fusion	
	Completeness	Correctness	Completeness	Correctness	Completeness	Correctness
Low	59.5	70.8	55.8	51.1	70.8	65.7
Medium	52.2	57.3	55.0	53.9	68.6	61.1
High	60.7	25.8	66.3	49.0	57.6	28.5

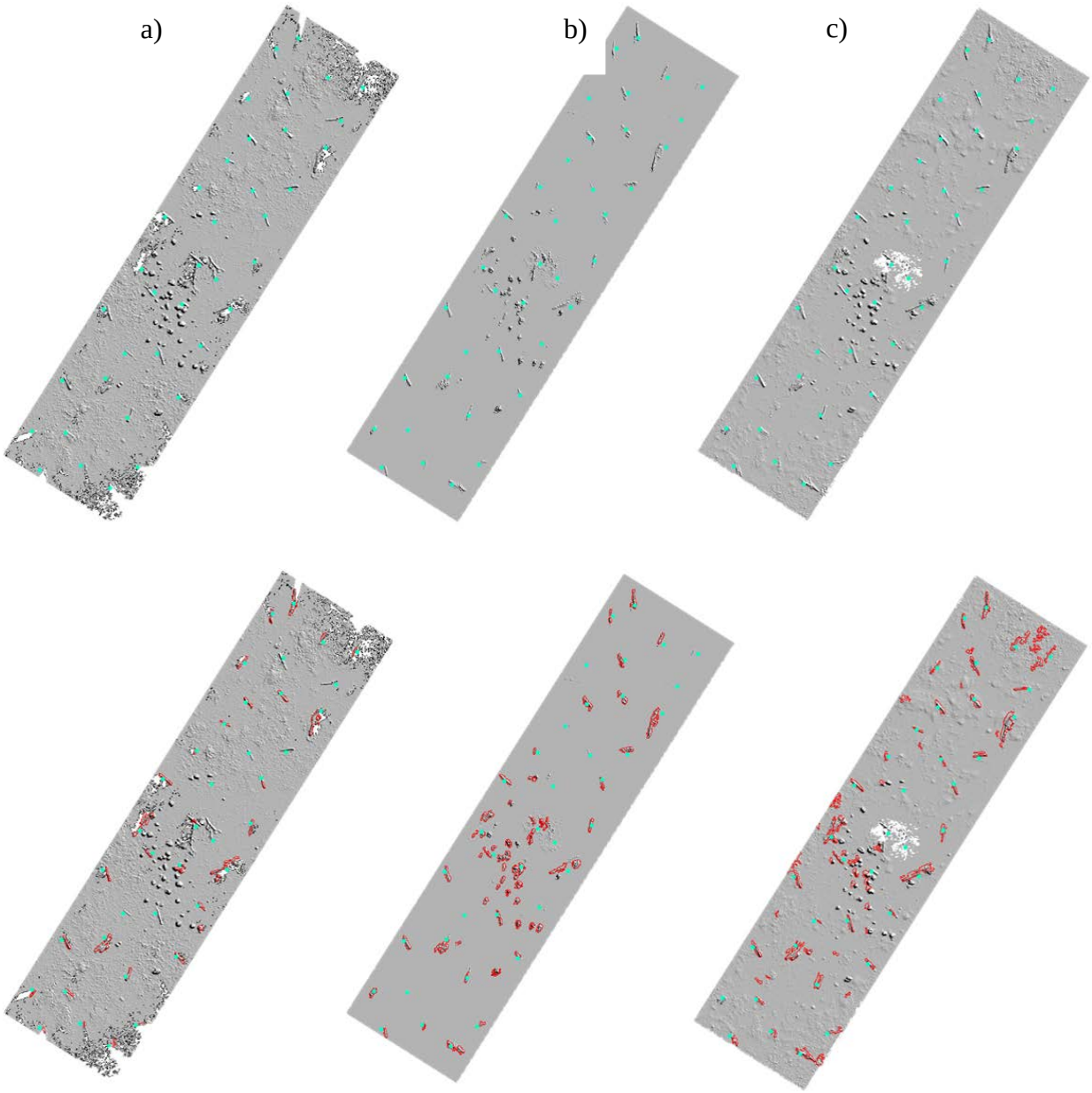

Figure 6. Shaded relief (top) and mapped coarse woody debris (CWD) (bottom) images of one sample site with combined CWD. Cyan dots indicate locations of CWD measured in the field, red polygons represent classified CWD. Images are from (a) terrestrial laser scanner (TLS), (b) an unoccupied aerial vehicle laser scanner (ULS) and (c) fused TLS and ULS (Fusion) dataset.

CWD count accuracy by vegetation cover types

Our method achieved comparable average completeness accuracy from different sensor data across LTHS, HTHS and HTLS vegetation types (Table 5). However, Fusion data provided significantly higher average completeness accuracy in plots with the LTLS vegetation type compared to the TLS and ULS data. HTHS vegetation type had a stronger negative impact on the correctness accuracy of CWD counts from TLS and Fusion data than ULS data (Table 5).

Table 9. Coarse woody debris (CWD) count accuracy by four vegetation types: low tree high shrub (LTHS), high tree high shrub (HTHS), high tree low shrub (HTLS), low tree low shrub (LTLS). Terrestrial laser scanner (TLS), an unoccupied aerial vehicle laser scanner (ULS), fused TLS and ULS (Fusion) data.

Vegetation types	TLS		ULS		Fusion	
	Completeness	Correctness	Completeness	Correctness	Completeness	Correctness
LTHS	66.2	49.4	53.0	55.5	68.7	54.3
HTHS	58.8	20.0	68.1	45.1	54.5	24.1
HTLS	58.2	52.8	58.5	52.9	63.0	56.7
LTLS	48.9	79.7	55.2	51.5	75.4	71.4

CWD volume accuracy

Using only True Positives, predictions of CWD volume was best achieved by ULS (R^2 = 0.70, RMSE = 6.9 m^3) and Fusion data (R^2 = 0.67, RMSE = 5.7 m^3). Predicted volume from TLS data with only True Positives had a relatively weak correlation with observed volume (R^2 = 0.43, RMSE 8.5 m^3) (Fig. 9, a). The predicted CWD volume was overestimated across all sensors.

When considering both True Positives and False Positives, there was a weak correlation between predicted and observed CWD volume from all types of data (Fig. 7, a_1, b_1, c_1). The relationship between predictions of CWD volume and field based CWD volume for TLS (R^2 = 0.05, p = 0.36) and Fusion (R^2 = 0.21, p = 0.059) data was not significant at the 95% confidence level. However, ULS data performed better than the other data types in predicting CWD volume with data that included True and False positives (R^2 = 0.26, p = 0.032). False Positives had a strong negative effect on calculating CWD volume (Fig. 7, a_1, b_1, c_1).

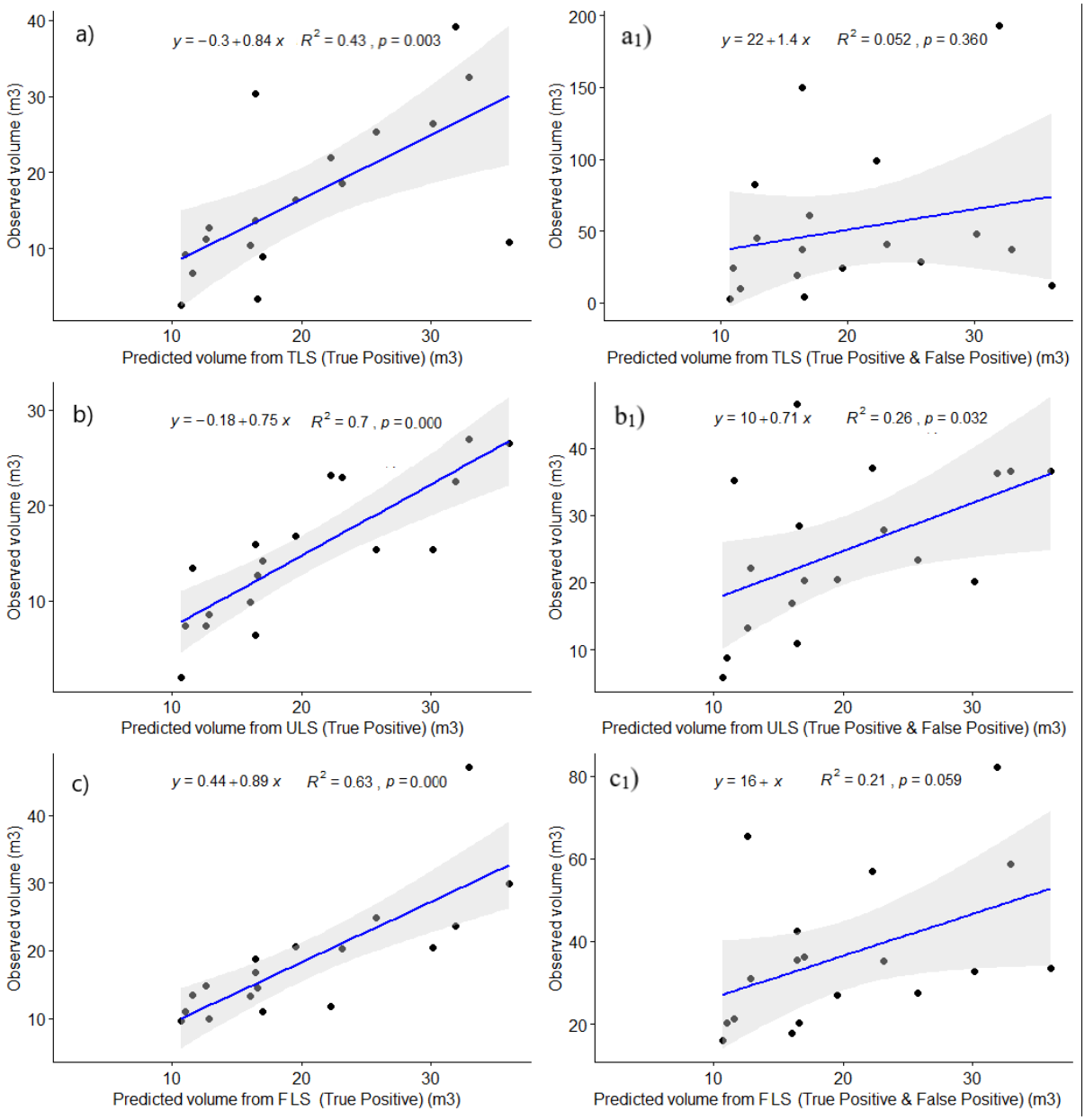

Figure 7. Relationship between observed and detected coarse woody debris (CWD) volume across the three data types; (a, a_1) terrestrial laser scanner (TLS), (b, b_1) an unoccupied aerial vehicle laser scanner (ULS), (c, c_1) fused TLS and ULS (Fusion) data. (a, b, c) are true positives only. (a_1, b_1, c_1) are true and false positives.

Discussion

To our knowledge, this is the first study that used data from TLS, ULS and a fusion of both sensors (Fusion) to classify CWD across a variety of vegetation types and different amounts of ground vegetation cover. We used a RF machine learning classification algorithm with DSM and DSM-based surface variables to extract CWD from other ground attributes including grass and shrubs. The models performed best for classifying grass cover, followed by CWD and shrubs, with significantly varied

results depending on the type of data. Our model indicated that LiDAR derived DSM, surface roughness and TPI variables contributed the most to classifying CWD. The ability to quantify CWD, in number and volume, showed variable success and large differences across sensors and landscape types.

While there are advantages of combining sensor data to obtain more complete coverage, particularly where TLS data has occlusions from ground vegetation and ULS may not be able to completely penetrate the dense canopy vegetation, in situations with high vegetation ground cover, the ULS platform outperformed TLS and Fusion data in the open woodland landscape. Against our expectations, Fusion data did not improve the model on sites with higher ground cover. However, Fusion data from sites with low tree and low shrub (LTLS) cover resulted in the most accurate CWD counts with our methodology.

A recent study classified CWD in a boreal forest using RF classifier with higher accuracy (>90%), but ground vegetation density was lower and the effects of vegetation cover were not assessed (Lopes Queiroz et al., 2019). That study utilized a combination of optical imagery and ALS LiDAR derived DSM and although model performance was good, accuracy assessments were based on cross-validation alone, rather than an independent testing dataset of field measured CWD (Lopes Queiroz et al., 2019). While ALS has shown promise in CWD assessments like these, the ability of ALS imagery to detect CWD smaller than 0.3m diameter is typically poor, due mainly to low point density and beam foot-print size (Marchi et al., 2018). In addition, although LiDAR can provide a number of surface variables, those studies used only LiDAR based DSM as an input variable (Blanchard et al., 2011, Lopes Queiroz et al., 2019). In this study, we found that, in addition to DSM, other surface variables such as roughness, aspect, topographic position index can contribute to improve CWD classification accuracy.

Effects of vegetation type and ground cover on model performance

Many previous studies have mentioned that ground cover can impact the ability of LiDAR sensors to detect and measure CWD (Polewski et al., 2017, Marchi et al., 2018). However, none have attempted to compare the accuracy of LiDAR-based CWD models across different ground cover densities. Our study examined this impact by including sites with high, medium and low ground cover biomass. As expected, high ground cover biomass resulted in more false positives in the classification and counts of CWD, which substantially decreased correctness accuracy and this effect was strongest in the TLS and Fusion data compared to ULS data (Table 4). In addition, models from ULS data performed better than TLS or Fusion models in sites with the most ground vegetation biomass, which was demonstrated

by a lower number of false positives. The ULS sensor obtained data from above the sites, and this improved the classification of CWD, which may have been obscured by dense vegetation features on the ground when LiDAR data was obtained from a sensor positioned at the ground. For this reason, with the proposed method, TLS sensors may not be appropriate for detecting CWD in a landscape with high ground vegetation cover. Notably, we collected 7 TLS scans in each site, which was the minimum number of scans required to characterize each 200 m × 50 m area (Shokirov 2021). More scans per site in a traditional grid-sampling design would likely improve the TLS performance and the reasons for these are discussed in the next section. Low and medium ground vegetation cover had less influence on completeness and correctness accuracy across all types of sensor data.

The total volume of CWD tended to be overestimated by all the sensors. This may have been a result of the interpolation techniques when creating raster imagery. When considering both true and false positives, only ULS data indicated significant prediction power of CWD volume. TLS sensor data resulted in a particularly high overestimation of site-level CWD volume, due to the high sensitivity of TLS to other ground-based objects. High ground cover sites in the study area contained dense, clumped vegetation species such as *Joycea pallida*, *Austrodanthonia* spp., and *Aristida ramose* (McIntyre et al., 2010) (Fig. 2). These types of grasses tend to create two problems for CWD detection: 1) they block the TLS laser pulses (occlusion error), which limits detection of CWD from distances over 10 m, and 2) the algorithm can have difficulty distinguishing CWD from the clumped vegetation, and consequently creates many false positives. Although fusing TLS with ULS may help overcome the first problem, the latter problem influenced the Fusion dataset as it still contains TLS data, which created false positives when the landscape is covered by substantially dense and tall grass. A discussion on how to address these issues are provided in the next section.

Similar to ground vegetation density, different vegetation cover types had variable impact on CWD classification accuracy. High tree and high shrub cover (HTHS) substantially decreased correctness accuracy in TLS and Fusion datasets by creating many false positives. This is probably due to detailed TLS data on low-lying vegetation clumps being misclassified, which contributed to false positives. Fusion data from sites with low tree and low shrub (LTLS) cover resulted in the most accurate CWD counts.

Considerations for sensor types, data collection and processing in relation to landscape context

We found a moderate relationship between TLS and ULS derived variables, but most of the TLS and Fusion based variables were strongly correlated. High correlation between the TLS and Fusion variables is likely due to the TLS being over-represented in Fusion data as TLS has higher point density, which enables it to capture more details of surface topography. As a result, the TLS data had a stronger impact on the Fusion derived DSM, which consequently produced highly correlated TLS and Fusion surface topographic variables. Conversely, ULS data is under-represented in Fusion data and therefore the relationship between the ULS and Fusion variables is weaker (Appendix 1). Future research should consider balancing the contribution of the point clouds from each sensor when fusing TLS and ULS data. The ability of the ULS sensor to collect multiple returns from above the sites allowed it to detect the ground more accurately, and as a result, it typically generated the best DSMs (Appendix 4). Conversely, the single return TLS beams did not always reach the ground as accurately as ULS data due to occlusion from dense ground vegetation and the viewing angle.

This study reported that seven TLS scans in each site could detect the majority of CWD on sites with lower or moderate ground cover; however, detection accuracy substantially decreased with increased ground cover. Based on these 7 scan, TLS data did not always capture CWD completely from all sides and experienced some occlusions due to the bigger incident angle (angle between the incoming laser pulse and surface normal) that may have prevented TLS from capturing CWD due to tall/dense vegetation blocking the laser pulse (Soudarissanane et al., 2009). Additional scans per site would improve TLS data coverage but would also require considerably more time for data collection and post-processing. Nonetheless, collecting more TLS scans per site may be necessary for sites that have high ground cover and/or increased surface variability (e.g. tall grasses or other ground objects, and/or higher topographic relief). This would decrease the incident angle of TLS scans, which would improve the accuracy of topography such as surface roughness and slope (Soudarissanane et al., 2009). Depending on the application, highly accurate surface roughness can be achieved when incident angle is $< 50^{o}$, which can significantly decrease the occlusion error (Milenković et al., 2015). In addition, multiple return TLS sensors would be more capable of detecting CWD through dense ground cover than the single return sensor that we used.

The ULS had a smaller incident angle and considering that the study area is an open woodland, this would have given the ULS an advantage for capturing CWD in more detail under the sparse canopy. The ULS sensor that we used also records up to 5 returns per laser beam, which likely factored into

performance differences between the sensors as well. The capabilities of ULS for detecting CWD could be further enhanced by increasing the point density per unit area. ULS sensors are now available with increased data acquisition flexibility and spatial resolution that can capture point density up to 2000 points per m^2, which can substantially improve the accuracy of surface topography (Levick et al., 2021). These types of sensors may be needed over more densely forested sites, where we would expect the ULS sensor to decrease in its detection accuracy due to the occlusion of the ground layer by canopy vegetation cover. The fusion of ULS and TLS data may be particularly useful in denser forests with canopy gaps where data collection from both sensors could reduce any loss of coverage. Ultimately, however, the contribution of ULS for CWD assessment would be limited by its ability to penetrate canopy vegetation. In forests with very dense canopies, it may not be possible to use ULS data for this purpose.

This study analyzed the XYZ coordinates of point clouds only. LiDAR provides intensity values for each collected point that could provide additional strong prediction power, which in turn may improve RF classification accuracy as grass and CWD might reflect significantly different intensity value (Charaniya et al., 2004). However, intensity data requires additional radiometric calibration (Yan et al., 2012) and validation tasks. Future research should consider incorporating information on the intensity of LiDAR returns as this can be useful for the classification of some land cover types and may improve the detection and quantification of CWD with LiDAR data (Yan et al., 2012, Kashani et al., 2015). In addition, future research should also trial edge-preserved smoothing interpolation techniques (Al-nasrawi et al., 2017) to create DSMs, rather than TIN raster. Edge-preserving interpolation methods may decrease the surface roughness created by grasses while retaining the strong edges of CWD, and this could help mitigate errors created by false positive CWD objects from the RF model.

Acknowledgements

We thank Paul Yeoh, Evelyn Wu, Renee Stainer, and Phoebe Hopkins for their help with data collection. This research was funded by a grant from the Australian Research Council (DE150101870) and the Commonwealth Scientific and Industrial Research Organization (Ignition Grant).

References

Al-nasrawi, M., G. Deng, and B. Thai. 2017. "Edge-Aware Smoothing through Adaptive Interpolation." *Signal, Image and Video Processing* 12 (2):347-54. doi: 10.1007/s11760-017-1164-x.

Amatulli, G., S. Domisch, M. N. Tuanmu, B. Parmentier, A. Ranipeta, J. Malczyk, and W. Jetz. 2018. "A Suite of Global, Cross-Scale Topographic Variables for Environmental and Biodiversity Modeling." *Sci Data* 5:180040. doi: 10.1038/sdata.2018.40.

Belgiu, M., and L. Drăguţ. 2016. "Random Forest in Remote Sensing: A Review of Applications and Future Directions." *ISPRS Journal of Photogrammetry and Remote Sensing* 114:24-31. doi: 10.1016/j.isprsjprs.2016.01.011.

Bergen, K. M., S. J. Goetz, R. O. Dubayah, G. M. Henebry, C. T. Hunsaker, M. L. Imhoff, R. F. Nelson, G. G. Parker, and V. C. Radeloff. 2009. "Remote Sensing of Vegetation 3-D Structure for Biodiversity and Habitat: Review and Implications for Lidar and Radar Spaceborne Missions." *Journal of Geophysical Research: Biogeosciences* 114 (G2). doi: 10.1029/2008jg000883.

Blanchard, S. D., M. K. Jakubowski, and M. Kelly. 2011. "Object-Based Image Analysis of Downed Logs in Disturbed Forested Landscapes Using Lidar." *Remote Sensing* 3 (11):2420-39. doi: 10.3390/rs3112420.

Boz, M. B., K. Calvert, and J. R. Brownson. 2015. "An Automated Model for Rooftop Pv Systems Assessment in Arcgis Using Lidar." *AIMS Energy* 3 (3):401-20.

Breiman, L. 2001. "Random Forests." *Machine Learning* 45 (1):5-32. doi: 10.1023/A:1010933404324.

Charaniya, A. P., R. Manduchi, and S. K. Lodha. 2004. Supervised Parametric Classification of Aerial Lidar Data. Paper presented at the 2004 Conference on Computer Vision and Pattern Recognition Workshop, 27 June-2 July 2004.

Conrad, O., B. Bechtel, M. Bock, H. Dietrich, E. Fischer, L. Gerlitz, J. Wehberg, V. Wichmann, and J. Böhner. 2015. "System for Automated Geoscientific Analyses (Saga) V. 2.1.4." *Geosci. Model Dev.* 8 (7):1991-2007. doi: 10.5194/gmd-8-1991-2015.

Droppova, V. 2011. "The Tools of Automated Generalization and Building Generalization in an Arcgis Environment." *Slovak Journal of Civil Engineering* 19 (1):1-7.

Duro, D. C., S. E. Franklin, and M. G. Dubé. 2012. "A Comparison of Pixel-Based and Object-Based Image Analysis with Selected Machine Learning Algorithms for the Classification of Agricultural Landscapes Using Spot-5 Hrg Imagery." *Remote Sensing of Environment* 118:259-72. doi: 10.1016/j.rse.2011.11.020.

Edwards, M. B. 2004. "Size of Coarse Woody Debris 5 Years after Girdling and Removal Treatments in 50-Year-Old Loblolly Pine Plantations." In *General Technical Reports SRS–71*, 108-13. Asheville, NC: U.S. : Department of Agriculture, Forest Service, Southern Research Station.

Author. 2011. Arcgis Desktop: Release 10.

Farnell, I., C. Elkin, E. Lilles, A.-M. Roberts, and M. Venter. 2020. "The Effects of Variable Retention Forestry on Coarse Woody Debris Dynamics and Concomitant Impacts on American Marten Habitat after 27 Years." *Canadian Journal of Forest Research* 50 (9):925-35.

Friedman, J., T. Hastie, and R. Tibshirani. 2001. *The Elements of Statistical Learning*. Vol. 1: Springer series in statistics New York.

Grizzel, J., M. McGowan, D. Smith, and T. Beechie. 2000. "Streamside Buffers and Large Woody Debris Recruitment: Evaluating the Effectiveness of Watershed Analysis."

Guo, L., N. Chehata, C. Mallet, and S. Boukir. 2011. "Relevance of Airborne Lidar and Multispectral Image Data for Urban Scene Classification Using Random Forests." *ISPRS Journal of Photogrammetry and Remote Sensing* 66 (1):56-66. doi: 10.1016/j.isprsjprs.2010.08.007.

Harmon, M. E., J. F. Franklin, F. J. Swanson, P. Sollins, S. V. Gregory, J. D. Lattin, N. H. Anderson, et al. 2004. "Ecology of Coarse Woody Debris in Temperate Ecosystems." In *Advances in Ecological Research*, 59-234. Academic Press.

Author. 2020. Raster: Geographic Data Analysis and Modeling. R package version 3.1-5. https://CRAN.R-project.org/package=raster.

Isenburg, M. 2012. "Lastools-Efficient Tools for Lidar Processing." *Available at: http: http://www.cs.unc.edu/~isenburg/lastools/*.

Kashani, A. G., M. J. Olsen, C. E. Parrish, and N. Wilson. 2015. "A Review of Lidar Radiometric Processing: From Ad Hoc Intensity Correction to Rigorous Radiometric Calibration." *Sensors (Basel)* 15 (11):28099-128. doi: 10.3390/s151128099.

Khosravipour, A., A. K. Skidmore, M. Isenburg, T. Wang, and Y. A. Hussin. 2014. "Generating Pit-Free Canopy Height Models from Airborne Lidar." *Photogrammetric Engineering & Remote Sensing* 80 (9):863-72. doi: 10.14358/pers.80.9.863.

Author. 2020. Caret: Classification and Regression Training. https://CRAN.R-project.org/package=caret.

Lefsky, M. A., W. B. Cohen, G. G. Parker, and D. J. Harding. 2002. "Lidar Remote Sensing for Ecosystem Studies." *BioScience* 52 (1):19-30. doi: 10.1641/0006-3568(2002)052[0019:lrsfes]2.0.co;2.

Levick, S. R., T. Whiteside, D. A. Loewensteiner, M. Rudge, and R. Bartolo. 2021. "Leveraging Tls as a Calibration and Validation Tool for Mls and Uls Mapping of Savanna Structure and Biomass at Landscape-Scales." *Remote Sensing* 13 (2). doi: 10.3390/rs13020257.

Lopes Queiroz, G., G. McDermid, J. Linke, C. Hopkinson, and J. Kariyeva. 2020. "Estimating Coarse Woody Debris Volume Using Image Analysis and Multispectral Lidar." *Forests* 11 (2). doi: 10.3390/f11020141.

Lopes Queiroz, G., G. J. McDermid, G. Castilla, J. Linke, and M. M. Rahman. 2019. "Mapping Coarse Woody Debris with Random Forest Classification of Centimetric Aerial Imagery." *Forests* 10 (6). doi: 10.3390/f10060471.

Manning, A. D., R. B. Cunningham, and D. B. Lindenmayer. 2013. "Bringing Forward the Benefits of Coarse Woody Debris in Ecosystem Recovery under Different Levels of Grazing and Vegetation Density." *Biological Conservation* 157:204-14. doi: 10.1016/j.biocon.2012.06.028.

Manning, A. D., D. B. Lindenmayer, and S. C. Barry. 2004. "The Conservation Implications of Bird Reproduction in the Agricultural "Matrix": A Case Study of the Vulnerable Superb Parrot of South-Eastern Australia." *Biological Conservation* 120 (3):363-74. doi: 10.1016/j.biocon.2004.03.008.

Manning, A. D., D. B. Lindenmayer, and R. B. Cunningham. 2007. "A Study of Coarse Woody Debris Volumes in Two Box-Gum Grassy Woodland Reserves in the Australian Capital Territory." *Ecological Management & Restoration* 8 (3):221-4. doi: 10.1111/j.1442-8903.2007.00371.x.

Manning, A. D., J. T. Wood, R. B. Gunningham, S. McIntyre, D. J. Shorthouse, I. J. Gordon, and D. B. Lindenmayer. 2011. "Integrating Research and Restoration: The Establishment of a Long-Term Woodland Experiment in South-Eastern Australia." *Zoologist* 35 (3):633-48.

Marchi, N., F. Pirotti, and E. Lingua. 2018. "Airborne and Terrestrial Laser Scanning Data for the Assessment of Standing and Lying Deadwood: Current Situation and New Perspectives." *Remote Sensing* 10 (9). doi: 10.3390/rs10091356.

Maxwell, A. E., T. A. Warner, and F. Fang. 2018. "Implementation of Machine-Learning Classification in Remote Sensing: An Applied Review." *International Journal of Remote Sensing* 39 (9):2784-817. doi: 10.1080/01431161.2018.1433343.

McIntyre, S., J. Stol, J. Harvey, A. O. Nicholls, A. Campbell, A. Reid, A. D. Manning, D. B. Lindenmayer, and 2010. "Biomass and Floristic Patterns in the Ground Layer Vegetation of Box-Gum Grassy Eucalypt Woodland in Goorooyarroo and Mulligans Flat Nature Reserves, Australian Capital Territory." *Cunninghamia: a journal of plant ecology for eastern Australia* 11 (3):319-57.

Milenković, M., N. Pfeifer, and P. Glira. 2015. "Applying Terrestrial Laser Scanning for Soil Surface Roughness Assessment." *Remote Sensing* 7:2007-45. doi: 10.3390/rs70202007.

Millard, K., and M. Richardson. 2015. "On the Importance of Training Data Sample Selection in Random Forest Image Classification: A Case Study in Peatland Ecosystem Mapping." *Remote Sensing* 7 (7):8489-515. doi: 10.3390/rs70708489.

Montealegre, A. L., M. T. Lamelas, and J. de la Riva. 2015. "A Comparison of Open-Source Lidar Filtering Algorithms in a Mediterranean Forest Environment." *IEEE Journal of Selected Topics in Applied Earth Observations and Remote Sensing* 8 (8):4072-85. doi: 10.1109/jstars.2015.2436974.

Mücke, W., M. Hollaus, N. Pfeifer, A. Schroiff, and B. Deák. 2013. "Comparison of Discrete and Full-Waveform Als for Dead Wood Detection." *ISPRS Annals of Photogrammetry, Remote Sensing and Spatial Information Sciences* II-5/W2:199-204. doi: 10.5194/isprsannals-II-5-W2-199-2013.

Pasher, J., and D. J. King. 2009. "Mapping Dead Wood Distribution in a Temperate Hardwood Forest Using High Resolution Airborne Imagery." *Forest Ecology and Management* 258 (7):1536-48. doi: 10.1016/j.foreco.2009.07.009.

Pesonen, A., O. Leino, M. Maltamo, and A. Kangas. 2009. "Comparison of Field Sampling Methods for Assessing Coarse Woody Debris and Use of Airborne Laser Scanning as Auxiliary Information." *Forest Ecology and Management* 257 (6):1532-41. doi: 10.1016/j.foreco.2009.01.009.

Polewski, P., W. Yao, M. Heurich, P. Krzystek, and U. Stilla. 2017. "A Voting-Based Statistical Cylinder Detection Framework Applied to Fallen Tree Mapping in Terrestrial Laser Scanning Point Clouds." *ISPRS Journal of Photogrammetry and Remote Sensing* 129:118-30. doi: 10.1016/j.isprsjprs.2017.04.023.

Probst, P., and A.-L. Boulesteix. 2017. "To Tune or Not to Tune the Number of Trees in Random Forest." *J. Mach. Learn. Res.* 18 (1):6673–90.

Author. 2020. Qgis Geographic Information System. http://qgis.org.

Author. 2013. R: A Language and Environment for Statistical Computing. http://www.R-project.org/.

Richardson, J., and L. Moskal. 2016. "An Integrated Approach for Monitoring Contemporary and Recruitable Large Woody Debris." *Remote Sensing* 8 (9). doi: 10.3390/rs8090778.

Šašak, J., M. Gallay, J. Kaňuk, J. Hofierka, and J. Minár. 2019. "Combined Use of Terrestrial Laser Scanning and Uav Photogrammetry in Mapping Alpine Terrain." *Remote Sensing* 11 (18):2154.

Shokirov, S. 2021. "Using Multi-Platform Lidar to Assess Vegetation Structure for Woodland Forest Fauna " PhD thesis, Australian National University.

Shokirov, S., S. R. Levick, T. Jucker, P. Yeoh, and K. Youngentob. 2020. "Comparison of Tls and Uls Data for Wildlife Habitat Assessments in Temperate Woodlands." In *IGARSS 2020 - 2020 IEEE International Geoscience and Remote Sensing Symposium*, 6097-100.

Smikrud, K. M., and A. Prakash. 2013. "Monitoring Large Woody Debris Dynamics in the Unuk River, Alaska Using Digital Aerial Photography." *GIScience & Remote Sensing* 43 (2):142-54. doi: 10.2747/1548-1603.43.2.142.

Soudarissanane, S., R. Lindenbergh, M. Menenti, and P. Teunissen. 2009. "Incidence Angle Influence on the Quality of Terrestrial Laser Scanning Points." *Proceedings ISPRS Workshop Laserscanning 2009, 1-2 Sept 2009, Paris, France* 38.

Stereńczak, K., M. Ciesielski, R. Balazy, and T. Zawiła-Niedźwiecki. 2016. "Comparison of Various Algorithms for Dtm Interpolation from Lidar Data in Dense Mountain Forests." *European Journal of Remote Sensing* 49 (1):599-621. doi: 10.5721/EuJRS20164932.

SZ DJI TECHNOLOGY CO., L. 2018. "Dji Gs Pro User Manual." In.

Vandekerkhove, K., L. De Keersmaeker, N. Menke, P. Meyer, and P. Verschelde. 2009. "When Nature Takes over from Man: Dead Wood Accumulation in Previously Managed Oak and Beech Woodlands in North-Western and Central Europe." *Forest Ecology and Management* 258 (4):425-35. doi: 10.1016/j.foreco.2009.01.055.

West, P. W., E. M. Cawsey, J. Stol, and D. Freudenberger. 2008. "Firewood Harvest from Forests of the Murray-Darling Basin, Australia. Part 1: Long-Term, Sustainable Supply Available from Native Forests." *Biomass and Bioenergy* 32 (12):1206-19. doi: https://doi.org/10.1016/j.biombioe.2008.02.017.

Windrim, L., M. Bryson, M. McLean, J. Randle, and C. Stone. 2019. "Automated Mapping of Woody Debris over Harvested Forest Plantations Using Uavs, High-Resolution Imagery, and Machine Learning." *Remote Sensing* 11 (6). doi: 10.3390/rs11060733.

Woldendorp, G., and R. J. Keenan. 2005. "Coarse Woody Debris in Australian Forest Ecosystems: A Review." *Austral Ecology* 30 (8):834-43. doi: 10.1111/j.1442-9993.2005.01526.x.

Yan, W. Y., A. Shaker, A. Habib, and A. P. Kersting. 2012. "Improving Classification Accuracy of Airborne Lidar Intensity Data by Geometric Calibration and Radiometric Correction." *ISPRS Journal of Photogrammetry and Remote Sensing* 67:35-44. doi: https://doi.org/10.1016/j.isprsjprs.2011.10.005.

Yrttimaa, T., N. Saarinen, V. Luoma, T. Tanhuanpää, V. Kankare, X. Liang, J. Hyyppä, M. Holopainen, and M. Vastaranta. 2019. "Detecting and Characterizing Downed Dead Wood Using Terrestrial Laser Scanning." *ISPRS Journal of Photogrammetry and Remote Sensing* 151:76-90. doi: 10.1016/j.isprsjprs.2019.03.007.

Chapter 4. Using multiplatform LiDAR to identify relationships between vegetation structure and the abundance and diversity of woodland reptiles and amphibians

Authors: Shukhrat Shokirov[1,2], Shaun R Levick[2], Tommaso Jucker[3], Adrian D. Manning[4], Kara Youngentob[1]

[1]Research School of Biology, Australian National University, Australia

[2]CSIRO Land and Water, Australia

[3]School of Biological Sciences, University of Bristol, UK

[4]Fenner School of Environment & Society Australian National University, Australia

Abstract

Remotely sensed measures of landscape and vegetation structure can help explain patterns in the occurrence and diversity of a number of different animal taxa, which can help guide management and conservation efforts. The majority of previous studies in this area have focused on birds and mammals; however, landscape-use by many reptiles and amphibians is also highly sensitive to vegetation structure. Most remote sensing studies also utilize airborne or satellite data that provides relatively rapid coverage of wide areas but may not have the resolution or viewing angle necessary to measure terrestrial features at scales that are meaningful for herpetofauna. For the first time, we collected LiDAR data from terrestrial laser scanning (TLS) and unmanned aerial vehicle laser scanning (ULS) to investigate relationships between vegetation structure and reptile and amphibian abundance, species richness and diversity in a woodland landscape. We identified relationships between the abundance and diversity of herpetofauna and a number of LiDAR derived vegetation metrics including canopy height, skewedness, vertical complexity, volume of vegetation and coarse woody debris (CWD). These relationships varied across species, groups and sensors. For example, overall reptile abundance showed a strong relationship to CWD, while amphibian abundance did not, and the relationship between CWD and reptile abundance was significant for ULS and ULS-TLS fused data ($P < 0.05$), but not TLS data alone. This reflects differences in the ability of TLS and ULS sensors to measure specific vegetation structural attributes. Overall abundance was explained slightly better by ULS data ($R^2 = 0.315$) than TLS and Fusion data ($R^2 = 0.195$, $R^2 = 0.180$, respectively), and ULS data tended to perform similarly or better than TLS data for most, but not all models. The explained variance for some individual species, such as the three-toed skink (*Chalcides striatus*), was relatively high $R^2 = 0.318$. In open woodland landscapes, ULS data has a number of benefits over TLS data for modelling relationships between herpetofauna and vegetation structure across wide areas. However, for some species, only TLS data identified significant predictor variables among the LiDAR-derived structural metrics. There were not enough individual species to determine whether this pattern related to a specific type of landscape use, but future research should investigate if and when TLS data may be more effective at identifying animal-habitat associations in woodland species. The data collected for this study was averaged over one hectare sites, but some herpetofauna primarily use landscapes at finer scales. Future research should also investigate how the scale at which LiDAR metrics are measured impacts their relationships to these animals.

Introduction

Reptiles and amphibians contribute essential ecosystem services including nutrient cycling, seed dispersal, pollination and biological pest control (Cortes et al., 2014). They serve as predators, prey and symbionts across multiple trophic levels, and influence the distribution and abundance of numerous plant and animal taxa (Halliday, 2008, Howland et al., 2014, Evans et al., 2019). Although rarely considered ecosystem engineers, the physical impact of amphibians and reptiles on aquatic and terrestrial environments through nesting and burrowing activities can affect nutrient cycling and seed germination so substantially that their absence can cause a partial or total collapse of an ecosystem (Doody et al., 2020). Reptiles can also help reduce the transmission of some zoonotic diseases such as Lyme disease (Ginsberg et al., 2021). Conversely, invasive reptile and amphibian species that have been intentionally or unintentionally introduced to new environments can cause catastrophic damage, resulting in native fauna extinction, alterations of whole ecosystems, substantial human health risks and economic losses (Shanmuganathan et al., 2010, Kraus, 2015). For these reasons, understanding the factors that influence the distribution and abundance of herpetofauna is a useful endeavor.

Modern day reptiles and amphibians tend to be relatively small in size compared to other animals and typically do not travel long distances, thereby impacting the scale at which they use landscapes for foraging, nesting, reproduction, hibernation, and shelter (McElhinny et al., 2006, Sillero and Gonçalves-Seco, 2014). As a result, habitat assessments for these animals often focus on relatively small spatial scales. At these scales, vegetation cover and coarse woody debris (CWD) are known to influence reptile and amphibian abundance, species richness and diversity (Michael et al., 2008, Owens et al., 2008, Sillero and Gonçalves-Seco, 2014, Howland et al., 2014, Mizsei et al., 2020). For example, recent studies identified strong relationships between vegetation structure, such as biomass and ground cover height, and the presence and abundance of reptiles (Howland et al., 2014, Mizsei et al., 2020). The importance of CWD as an essential habitat element for small animals, including herpetofauna, also has been demonstrated in a number of studies (Owens et al., 2008, Evans et al., 2019).

In these studies, vegetation structure and coarse woody debris were measured using traditional field based methods which can be time consuming and labor intensive and may rely on extrapolating measurements from a subset of the study areas to the larger environment, which introduces potential error and bias (Hinsley et al., 2009). Remote sensing provides a potentially cost-effective alternative that can capture more complete structural and/or spectral detail at fine scale across wide areas (Marc L. Imhoff, 1997, Leyequien et al., 2007, Sillero and Gonçalves-Seco, 2014). Many previous studies utilizing remote sensing methods for wildlife habitat assessments have relied on multispectral imagery

from satellite or airborne platforms, which provide useful information on landscape composition (Leyequien et al., 2007), however their ability to capture structural data is limited (Lefsky et al., 2002, Eldegard et al., 2014). Light Detection and Ranging (LiDAR) technologies provides accurate information on landscape structure in three dimensions, and this technology has made important contributions to habitat mapping for many species that depend on structural aspects of the landscape and/or vegetation (Lesak et al., 2011, Eldegard et al., 2014).

LiDAR sensors measure the time it takes for a laser light emitted from a sensor to hit an object and be reflected back. The distance between the sensor and objects is calculated by multiplying the measured time and speed of light and dividing by two (Newnham et al., 2015). Three-dimensional information on earth features can be collected with LiDAR from spaceborne, airborne and terrestrial platforms (Hillman et al., 2021). LiDAR has increasingly been used for forest inventories in the last two decades (White et al., 2016), and is also becoming an important tool to assess animal-habitat associations (Bradbury et al., 2005, Vierling et al., 2008, Davies and Asner, 2014).

Most research utilizing LiDAR to investigate relationships between landscape structure and animals has focused on birds and mammals (Davies and Asner, 2014). Relatively few studies have focused on herpetofauna (but for exceptions see; (Sillero and Gonçalves-Seco, 2014, Fill et al., 2015, bin Abdul Rahman, 2018). Sillero and Gonçalves-Seco (2014) used LiDAR point clouds to estimate landscape surface heterogeneity to understand microhabitat features of four lizard species. Fill et al. (2015) found a strong positive relationship between LiDAR derived ground vegetation cover and the occurrence of eastern diamondback rattlesnakes (*Crotalus adamanteus*). LiDAR data has also been used to identify potential nesting sites for flatback sea turtles (*Natator depressus*) (bin Abdul Rahman, 2018). Notably, all these studies employed airborne LiDAR to evaluate animal-habitat associations.

Airborne LiDAR is able to capture relatively rapid structural information on the mid and upper layers of vegetation; however, ground layer structural attributes can be occluded by the over-story vegetation (Cody, 1981b, Jupp and Lovell, 2007). The importance of ground layer complexity for reptile and amphibian abundance and species richness has been reported in a number of studies (Price et al., 2010, Cortes et al., 2014). Due to their lower viewing angles and typically higher resolution, terrestrial (TLS) and UAV-based (ULS) LiDAR can often see structural elements that are not visible to LiDAR sensors on high-flying airplane platforms (Loudermilk et al., 2009) and may be particularly useful for identifying low-lying vegetation structure. For the first time, we use LiDAR from TLS, ULS and the combined data from both platforms to examine the relationship between vegetation structure and woodland reptile and amphibian diversity and abundance. We expect that the ability of these sensors

to collect high details of the vegetation structure especially on the ground layer can identify important habitat structures of herpetofauna. Specific aims of this research were:

1) to utilize TLS, ULS and fusion of both dataset to determine vegetation structural metrics that are important for explaining the abundance and diversity of reptiles and amphibians in a restored box-gum grassy woodland ecosystem,

2) to evaluate the performance of three types of TLS, ULS and combination of both datasets for modelling reptile and amphibian habitat associations.

Methods

Study area

This study was conducted at Mulligan's Flat-Goorooyarroo Woodland Experiment (MFGOWE) in Canberra, Australia (35°09' S - 149°09' E, elevation 650–700 m, Fig. 1). MFGOWE consists of two joined reserves; Mulligans Flat Nature Reserve (MF) (683 ha) and Goorooyarroo Nature Reserve (GO) (702 ha), which were established in 1994 and 2006 respectively to protect and restore a critically endangered box-gum grassy woodland ecosystem (McIntyre et al., 2010). The landscape is dominated by Blakely's Red Gum (*Eucalyptus blakelyi*) and Yellow Box (*E. melliodora*), also common are Scribbly Gum (*E. rossi*), Red Stringybark (*E. macrorhyncha*) and Brittle Gum (*E. manniferia*) (McIntyre et al., 2010, Shorthouse et al., 2012). The grassy understory is most commonly comprised of *Joycea pallida*, *Austrodanthonia spp., Themeda australis* and *Aristida ramose* (McIntyre et al., 2010). The soils in the study area originated from ancient Silurian volcanoes that form the ridges and Silurian sedimentary rocks. Topography consists of low hills, undulating plains and flats (McIntyre et al., 2010). The average annual temperatures range from a minimum of 6.5 ˚C to a maximum of 19.7˚C, and average annual rainfall is 615.9 mm (McIntyre et al., 2010, Manning et al., 2011).

Mulligan's Flat and Goorooyarroo were once leasehold grazing land with areas of historical cropping and pasture improvement, before becoming nature reserves. A number of restoration activities have been undertaken since the establishment of the sanctuaries to restore and protect the native biodiversity, including but not limited to, fencing the reserves to exclude feral grazers and predators, reintroducing coarse woody debris that had been previously cleared by agricultural activities, and the reintroduction of some native mammal and bird species (Manning et al., 2011, Shorthouse et al., 2012, Manning et al., 2013). Ninety-six 1 ha sites were established across the reserve as part of the restoration and on-going monitoring activities (Manning et al., 2011). The 1 ha sites are distributed across four

types of vegetation structure: 1) high tree, high shrub cover, 2) high tree, low shrub cover, 3) low tree, low shrub cover, and 4) low tree, high shrub cover.

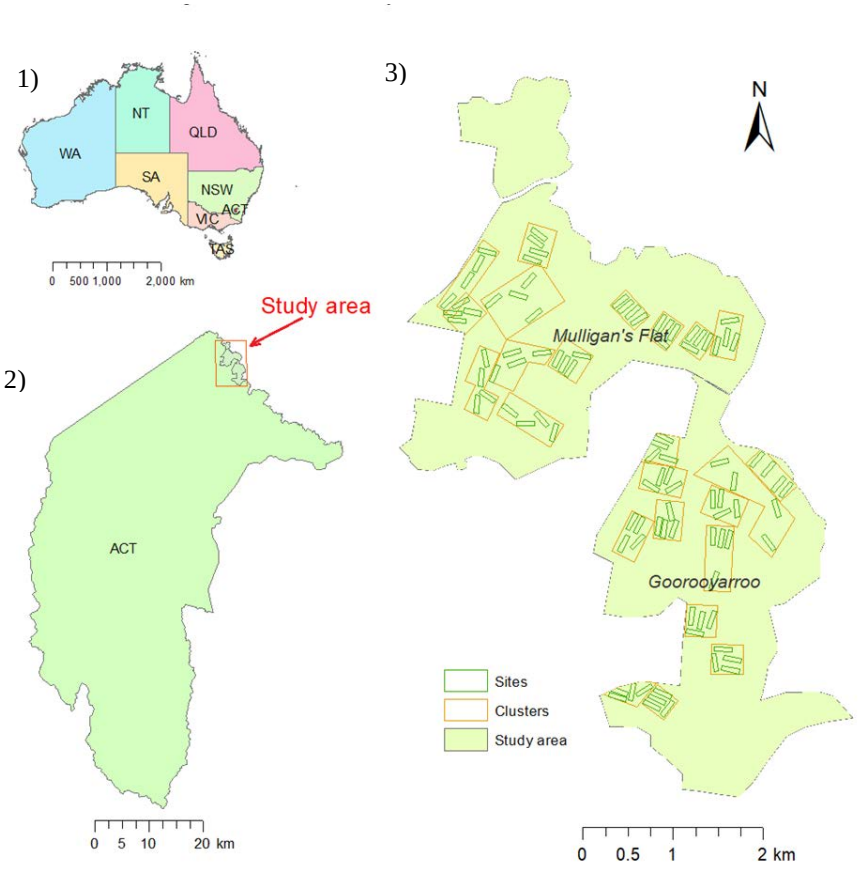

Figure 6. Map of study area. 1) Australia, 2) Australian Capital Territory, 3) Mulligan's Flat-Goorooyarroo

Animal survey data

At each of the 96 1 ha sites, reptile and amphibian surveys have been conducted yearly in March/April since 2008 (Manning et al., 2011, Evans et al., 2019). This time of year was chosen to detect adults and young from the preceding spring and summer (southern hemisphere). During each survey, every 1 ha site is searched twice by two experienced observers for 30 minutes on two different days (Evans et al., 2019). Observers visually look for reptiles and amphibians within and on top of substrates such as logs, rocks and bark, and also scanned logs for basking reptiles with binoculars. When observed, reptile and amphibian species, location and substrate are recorded (Manning et al., 2011, Evans et al., 2019). For this study, we used reptile and amphibian survey data collected from 2014 to 2019 because it was unlikely that vegetation structure or CWD had changed substantially during this time-period and multiple years of animal data were needed to achieve the statistical power necessary to identify relationships between population data and vegetation structural metrics.

TLS data collection and post - processing

We used Topcon GLS2000 equipment (Topcon, Japan) for TLS data collection over 96 sites between 1 and 31 October 2018. The Topcon GLS2000 is a laser scanner that emits near-infrared (1064 nm) laser pulses at up to 120,000 laser pulses per second. The field of view of the scanner is 360° and 270° in the horizontal and vertical direction respectfully. The beam diameter of the single pulse is 4 mm at 60 m. TLS data was collected at a scanner height of approximately 1.7 m and with a 6 mm at 10 m scanning resolution. Seven scan stations in a zigzag formation were used in the 1 ha (200 m by 50 m) sites, with each station distanced approximately 30m apart. Co-registration was performed after all the scans were collected. The position of each scan was measured with a Deferential GPS (Trimble Geoexplorer 6000 series) and post-processing was performed using local base station data to improve the location accuracy.

Point clouds from seven individual scan stations were co-registered using Multi-station Adjustment (MSA) plugins in RiScan Pro software (RIEGL Laser Measurement Systems GmbH). MSA plugins automatically search planar surfaces in the point clouds and align common points on overlapping planes from different stations. TLS data from each site was georeferenced using DGPS locations of each scan position and clipped to the spatial extent of each of the 96 polygon sites. Point clouds were subsampled into 10 mm spacing to homogenize the point distributions using Cloud Compare (CloudCompare 2.10.2) (Fig. 2).

ULS data collection and post-processing

The ULS platform consisted of a quadrocopter integrated with a RIEGL miniVUX-1UAV LiDAR sensor (RIEGL, Austria) and an APX INS/GNSS systems. ULS data with a 100 kHz pulse repetition rate and up to 100,000 measurements/second was collected across the study area from the 7^{th}-14^{th} of November, 2018 under fine weather conditions. The flight was performed at approximately 80 m above the take off point with a speed of approximately 25.2 km and up to 5 returns per pulse. DJI ground station pro V2 was utilized to plan the flight missions (SZ DJI TECHNOLOGY CO., 2018). The ULS sensor failed to collect data over two sites due a system error. These two sites were subsequently excluded from further analysis with ULS and TLS data. Sites were clipped by corresponding polygons to create separate point clouds for each site (Fig. 2).

Merging TLS and ULS point clouds

TLS and ULS LiDAR point clouds of each site were co-registered using the Iterative Closest Point (ICP) algorithm in CloudCompare (CloudCompare 2.10.2) (Fig. 2). Point clouds captured by TLS and

ULS sensors for each site were first manually adjusted and then, ICP algorithm was run to perform automatic co-registration. In ICP algorithm, the random sample limit was set to 250,000 points and RMS error difference threshold set to 1 × 10−08, following (Levick et al., 2021). Fused point clouds were subsampled into 0.01 m point spacing to make evenly distributed point clouds across the site.

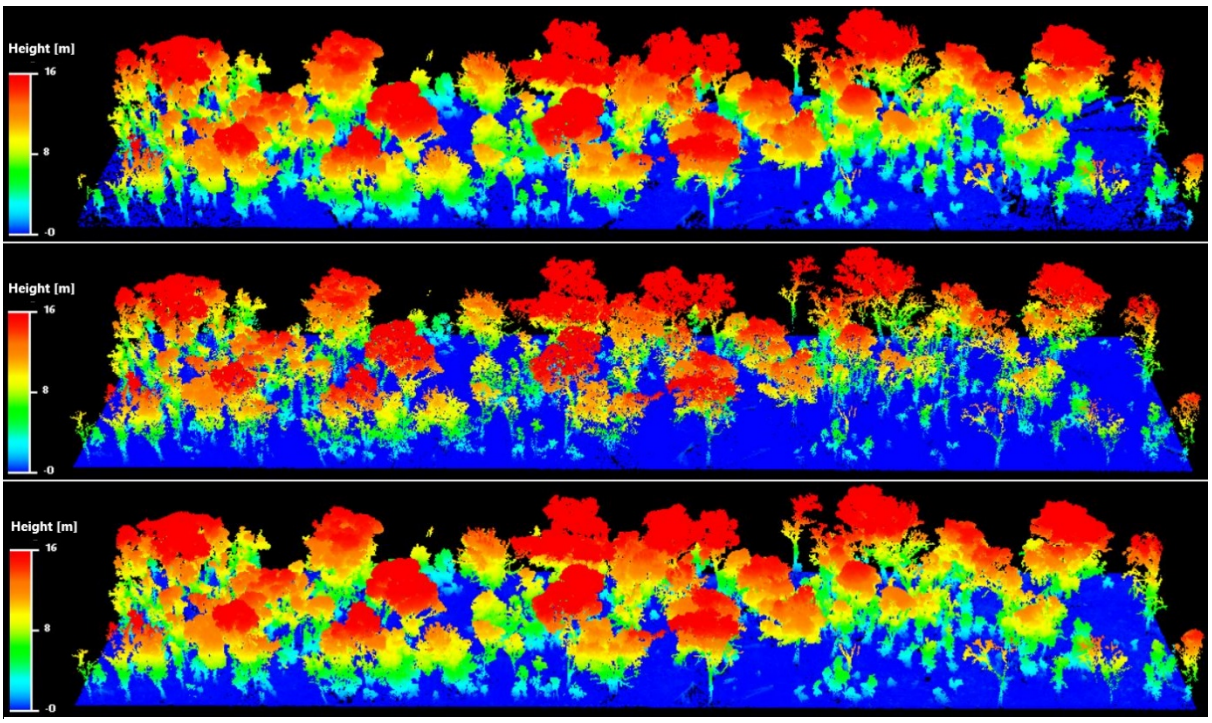

Figure 7. Normalized point cloud of site GO72A-3 colored by height. The top image is from the terrestrial laser scanner (TLS), UAV laser scanner (ULS) data is in middle, and the combination of both datasets (Fusion) is at the bottom.

Vegetation height model

Point clouds were filtered for noise and classified into ground and non-ground points using *LAStools* (Isenburg, 2012). Vegetation height models (VHM) were then created by calculating height of each above ground point relative to the ground points with *LAStools* (Isenburg, 2012) (Fig. 2). The vegetation height model represents absolute height of vegetation above the ground and is used to calculate the vegetation structural variables, which will be introduced in the following sections.

Extracting coarse woody debris

We developed a new method to identify and quantify coarse woody debris (CWD) from TLS, ULS and Fusion datasets (Shokirov et al. Chapter 3, in preparation). First, we generated a digital height model (DHM) from point clouds up to 1.3 m and calculated several topographic surface variables including roughness, topographic position index (TPI), slope and aspect. Training datasets for use with

Random Forest (RF) models were prepared by delineating CWD, shrub and grass classes on the DHM and its shaded relief. Random forest (RF) is an ensemble classifier that creates Classification and Regression Tree (CART) on training data samples where each Tree generates a voting based rule to predict a target class. The RF classification algorithm classified CWD, shrub and grass classes with accuracies over 70%. Image smoothing algorithms were run to remove noise in the classification map. Finally, CWD candidate pixels were exported as a polygon shapefile and elongated objects were extracted as CWD using GIS analysis. Additional details of this research and classification accuracies are provided in Chapter 3.

Calculating vegetation structural variables from LiDAR datasets

A number of vegetation variables were calculated from different strata of the landscape to extract as much information as possible on the vegetation structure of each site. First, canopy metrics were computed from points above 1.3 m from the ground (Table 1). Then, point clouds were stratified into three different layers, including the ground layer (≤1m), the mid-story (> 1m, ≤ 10m) and the upper story (> 10m) based on existing vegetation layer descriptions for eucalypt grassy woodlands (Department of Environment, 2013). For each vegetation layer, additional vegetation metrics were calculated (Table 1). Total vegetation volume was estimated by building 0.5 m voxels (volumetric pixels) from non-ground points, with each voxel made of one or more points. A total of 37 variables were calculated using the lidR package (Roussel, 2017). Descriptions of the 37 LiDAR –derived landscape variables, CWD volume and number are provided in Table 1.

Table 10. Descriptions of calculated vegetation structural variables from LiDAR datasets

Name of variable	**Description**
maxH	Maximum height of canopy (points > 1.3m). Higher maximum values represent bigger trees.
meanH	Mean height of canopy (points > 1.3m). If the value is higher, it means there are bigger the trees in the site, if the value is lower, more shrubs and regeneration trees abundant in the site.
stdH	Standard deviation of canopy height (points > 1.3m). It describes the height variation in the canopy.
skewH	Skewness of canopy height. Negative skewness – the distribution dominated by higher points (upper canopy is dominant) but a few extreme lower points. Positive skewness - the distribution dominated by lower points (lower canopy is dominant) but a few extreme higher points, (points > 1.3m).
kurH	Kurtosis of canopy height. Negative kurtosis – the distribution centered on mean values (mid-canopy is dominant), without much

	higher or lower canopy, positive kurtosis – the distribution heavy on tails, with more at the high and low ends and less in the center (lower and upper canopy is dominant), (points > 1.3m).
p_05, p_10, p_25, p_50, p_75, p_90, p_95, p_99	Canopy height percentiles. Canopy height percentile here was defined as the height below which a specified percentage of total point clouds were located, (points > 1.3m). For example, p_05 = 2.0 m means that 5% of vegetation points found below 2 m. Vegetation density is higher at p_05 = 2.0 m than p_05 = 3.0 m.
vci_2m, vci_5m, vci_10m, vci_15m, vci_20m	Vertical complexity indexes (VCI) at 2m, 5m, 10m, 15m, 20m height bins, (points > 1.3m). VCI was calculated by the following equation: $$VCI = (-\sum_{i=1}^{HB}[(p_i \ln(p_i)])/\ln(HB)$$ Where *VCI* in a vertical complexity index, *HB* is the total number of height bins, and p_i is the proportional abundance of LiDAR returns in height bin i. A VCI value close to one indicates that most height bins have equal amount of vegetation. VCI value decreases if the distribution of canopy in the height bin becomes more uneven (van Ewijk et al., 2011).
cov	Fraction of cover, (points > 1.3m).
height_cv	Coefficient of variation of height, (points > 1.3m). Indicates the canopy height variation.
canopy_roughness	Canopy roughness describes complexity/variability of canopy height (Herrero-Huerta et al., 2020) (points > 1.3 m). Higher variability in the canopy height provides higher roughness index and vice versa.
canopy_shannon	Normalized Shannon diversity index of canopy (Pretzsch, 2009), (points > 1.3m). Indicates canopy height diversity.
tvolume	Total vegetation volume (m^3) – number of 0.5 m^3 voxels divided by 8 (ground points excluded).
vlayer_L1	Vegetation volume (m^3) in 1st layer (points 0-1m¸ ground points excluded).
vlayer_L2	Vegetation volume (m^3) in 2st layer (points 1m-10m).
vlayer_L3	Vegetation volume (m^3) in 3st layer (points 10m and above).
meanH_L1, meanH_L2, meanH_L3	Mean height of 1st, 2nd, 3rd layer.
sdH_L1, sdH_L2, sdH_L3	Standard deviation of vegetation height in 1st, 2nd, 3rd layer.
roughness_L1, roughness_L2, roughness_L3	Roughness indexes of 1st, 2nd, 3rd layer (Jenness, 2004). Horizontal distribution of vegetation across different layers.
vci_L1, vci_L2, vci_L3	Vertical complexity indexes of 1st, 2nd, 3rd layer (van Ewijk et al., 2011). Vertical distribution of vegetation across different layers.
cwd_volume	CWD volume (Chapter 3)
numberOfCWD	Number of CWD (Chapter 3)

Statistical analyses

Reptile and amphibian data

From reptile and amphibian survey data, overall animal abundance (maximum number of individuals counted), species richness (cumulative total number of different species), and Shannon diversity index (describes both the number and the evenness of species in a dataset by accounting for the proportion of individuals that contribute to each species (Jari Oksanen, 2019)) were calculated for each site using an "FD" package (Laliberté and Legendre, 2010) in R (R Team, 2019) (Table 2). The overall species abundance data was divided into two separate groups: (1) reptile species and (2) amphibian species. The abundance value for each group was calculated by adding the number of individual animals observed within their respective group (i.e., reptile or amphibian). Individual species abundance was the sum of every individual from a species at a site.

Selecting predictor variables

Pearson correlation matrices were calculated for the TLS, ULS and Fusion datasets (Appendix 1, 2, 3) to analyze the collinearity between 37 variables. If a variable was highly correlated (0.7 maximum threshold) to another variable, the most ecologically meaningful variable with the least amount of collinearity conflicts with other variables was retained (Garden et al., 2007). Variables from ground, mid, and upper-story vegetation layers were included in the final selection as well. The same variables were selected across all three LiDAR datasets (TLS, ULS and Fusion). All the variables were standardized to ensure that the estimated coefficients were on the same scale, making it easier to compare effect sizes (Becker et al., 1988).

Modelling overall reptile and amphibian abundance, species richness and diversity

Linear mixed effects models with lmer function in the lme4 package (Bates et al., 2015) in R were used to estimate relationships between LiDAR derived landscape structural metrics and overall reptile and amphibian abundance, species richness and diversity. Linear mixed models are an extension of basic linear models, which allow fixed and random effects, and were used when the data had a grouped or nested structure (Melin et al., 2018). Random effects help account for structure within sampling. For example, due to the nested design of our study area, sites within a given cluster may be more structurally similar to one another than sites in different clusters. Therefore, we incorporated random effects (24 clusters by four vegetation classes) and fixed effects (in our case, site-level LiDAR derived variables used to predict a dependent animal population variable) in our models. The dependent

variables were overall site-level reptile and amphibian abundance, species richness and Shannon diversity.

Modelling the abundance of reptiles only, amphibians only or individual species.

The relationship between the abundance of reptiles or amphibians, as groups or individual species, and LiDAR vegetation structural characteristics were analyzed using GLMMs. The vegetation variables derived from TLS, ULS and Fusion were fixed effects and the 24 clusters were random effects that combined to make the independent variables. The abundance of each different reptile or amphibian species as well as reptile abundance overall and amphibian abundance overall were the dependent variables and were modelled separately. Unidentified skinks, defined as skinks that were observed but disappeared before observers could identify their species, were also included in the individual species modelling. Although unidentified skink category most likely does not represent an individual species, we left it in the individual species analysis to determine what vegetation structural variables were most associated with not being able to clearly identify a skink because this information may be useful for future survey design.

Examination of model fit

To examine model fit, dispersion, zero-inflation, and residual spatial and temporal autocorrelation issues, Residual Diagnostics from a HierARchical Models (DHARMa) package (Hartig, 2017) were used. For each model, marginal R^2 (R^2_{mar}) and conditional R^2 (R^2_{con}) were calculated to estimate the proportion of variance explained by fixed and mixed effects for reptile and amphibian communities and individual species (Nakagawa et al., 2013). Dependent variables had very few counts in some models, causing model convergence problems. To solve this issue, only species that had at least 10% count data across the sites were kept. Thus indicating that each species should have been observed at 10 or more sites to be valid for modelling.

Results

Reptile and amphibian observations

Observers encountered a total of 1585 individual reptiles and amphibians (571 in Mulligan's Flat and 1014 in Goorooyarroo nature reserves) from 25 species (13 lizard species, 7 frog species, 2 snake species and 1 turtle species) from dual surveys between 2014 and 2019 (Table 2). During this period,

sites had a maximum of fifty-three individuals across nine species and a minimum of one individual from one species (Table 3). Most of the sites had frogs and lizards, and a few sites had one species of snake or turtle (Table 4).

Table 11. Reptile and amphibian species that were counted between 2014 and 2019

№	Common name	Scientific name	Number of counts
	Skinks		
1	Delicate Skink	*Lampropholis delicate*	454
2	Boulenger's Skink	*Boulengeri*	501
3	Unidentified Skink	*N/A*	267
4	Three-toed Skink	*Chalcides striatus*	102
5	Shingleback	*Tiliqua rugose*	37
6	Common Dwarf Skink	*Menetia greyii*	21
7	Bearded Dragon	*Pogona*	1
8	Jacky Dragon	*Amphibolurus muricatus*	22
9	Spotted-backed Skink	*Niveoscincus ocellatus*	1
10	Olive Legless Lizard	*Delma inornata*	4
11	Common Bluetongue	*Tiliqua*	2
12	Garden Skink	*Lampropholis guichenoti*	7
13	Cunningham's Skink	*Egernia cunninghami*	3
14	Copper-tailed Skink	*Ctenotus taeniolatus*	4
	Snakes and turtles		
15	Dwyer's Snake	*Suta dwyeri*	4
16	Eastern Brown Snake	*Pseudonaja textilis*	7
17	Eastern Long-necked Turtle	*Chelodina longicollis*	1
	Frogs and toads		
18	Spotted Grass Frog	*Limnodynastes tasmaniensis*	75
19	Common Froglet	*Crinia signifera*	31
20	Peron's Tree Frog	*Litoria peronei*	2
21	Striped Marsh Frog	*Limnodynastes peronei*	1
22	Verreaux's/Whistling Tree Frog	*Litoria verreauxii*	3
23	Plains Froglet	*Crinia parinsignifera*	12
24	Smooth Toadlet	*Uperoleia laevigata*	21
25	Unidentified Frog/Toad	N/A	2

Table 12. Summary statistics for reptile and amphibian data collected from 94 sites. Abundance is total number of reptiles and amphibians, SR is species richness, and SD is Shannon diversity.

Statistics	Abundance	SR	SD
Maximum	53.0	9.0	2.0
Mean	14.3	4.6	1.2
Standard deviation	8.6	1.6	0.4
Median	13.5	5.0	1.3
Minimum	1.0	1.0	0.0
Sum	1585.0	27.0	NA

Table 13. Reptile and amphibian abundance and species richness (SR) by groups (frog and toads, lizards, snakes, and turtles) across 94 sites.

Statistics	Frog and Toads		Lizards		Snakes		Turtles	
	Abundance	SR	Abundance	SR	Abundance	SR	Abundance	SR
Maximum	43.0	5.0	41.0	7.0	1.0	1.0	1.0	1.0
Mean	3.9	1.5	15.2	3.8	1.0	1.0	1.0	1.0
Stdev	7.1	0.9	9.0	1.3	0.0	0.0	NA	NA
Median	2.0	1.0	14.0	4.0	1.0	1.0	1.0	1.0
Minimum	1.0	1.0	1.0	1.0	1.0	1.0	1.0	1.0

Selected predictor variables

Eleven of thirty-seven variables were selected for modelling based on the variable selection methods described in section 1.10 (Fig. 3). TLS and Fusion data derived variables were typically more similar in values than the ULS data as illustrated in the violin plots from Figure 3. ULS data had lower values for vegetation volume and metrics derived from under the canopy (Fig. 3).

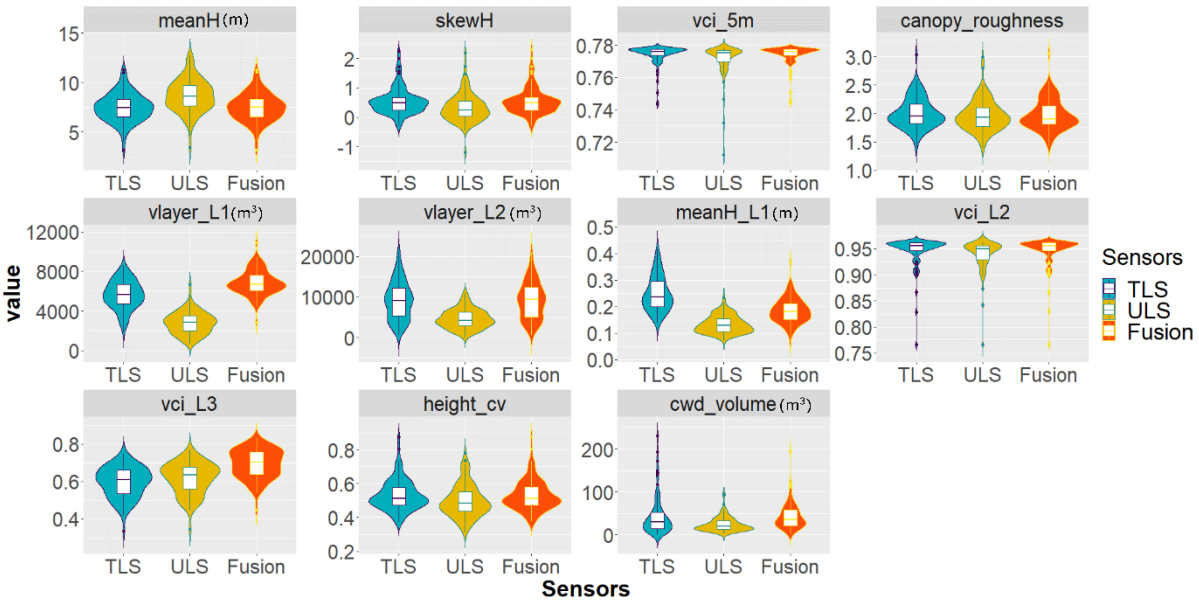

Figure 8. Violin plots illustrate the distribution of LiDAR metric values across the 11 independent variables. Boxes in the violins show median (middle line), first (bottom line) and third (top line) quartiles.

Modelling overall reptile and amphibian abundance, species richness and diversity

The lmer models showed some predictive power for overall reptile and amphibian abundance (R^2_{mar} = 19.5% (TLS), R^2_{mar} = 31.5% (ULS), R^2_{mar} = 18.0% (Fusion)) (Table 5). Reptile and amphibian abundance was positively correlated to average height of vegetation (*meanH*, $p < 0.01$), canopy height skewness (*skewH*, $p < 0.01$) and CWD volume ($p < 0.001$), and negatively correlated to second layer vegetation volume (*vlayer_L2*, $p < 0.01$), average height of first layer (*meanH_L1*, $p < 0.01$) and vegetation complexity of third layer (*vci_L3*, $p < 0.05$). Overall species richness was not significantly correlated to any of the LiDAR variables. Species diversity was positively associated with TLS and ULS derived height metrics (*meanH*, $p < 0.05$) and TLS derived canopy height skewness (*skewH*, $p < 0.05$), and negatively correlated to TLS and ULS based third layer vegetation complexity (*vci_L3*, $p < 0.05$). The explained variance for species richness and species diversity were relatively low ($R^2_{mar} \approx 10\%$) (Table 5).

Table 14. Model summary of the relationship between LiDAR derived vegetation structural metrics (independent variables) and overall reptile and amphibian abundance, species richness and diversity (dependent variables). Abundance is reptile and amphibian abundance, SR is species richness, SD is

Shannon diversity. First and second rows of independent variables show intercept and standard error of the model. Intercept of significant variables are highlighted in bold.

		Dependent variables								
		Abundance			SR			SD		
		TLS	ULS	Fusion	TLS	ULS	Fusion	TLS	ULS	Fusion
Independent variables	meanH	**0.433****	**0.411***	-0.170	0.452	1.690	0.588	**0.591****	**0.474***	0.200
		(0.165)	(0.170)	(0.112)	(0.267)	(0.929)	(0.633)	(0.228)	(0.211)	(0.143)
	skewH	**0.417****	**0.266****	-0.080	0.362	0.868	0.678	**0.437****	0.201	0.183
		(0.128)	(0.085)	(0.106)	(0.189)	(0.496)	(0.508)	(0.162)	(0.113)	(0.114)
	vci_5m	-0.046	**-0.090***	0.007	-0.052	-0.201	-0.368	-0.066	-0.039	-0.083
		(0.044)	(0.044)	(0.050)	(0.070)	(0.249)	(0.270)	(0.060)	(0.057)	(0.061)
	canopy_roughness	-0.014	-0.041	0.052	-0.003	-0.003	0.015	-0.044	-0.017	-0.028
		(0.065)	(0.057)	(0.072)	(0.079)	(0.256)	(0.284)	(0.065)	(0.058)	(0.063)
	vlayer_L1	0.089	0.172	-0.078	0.102	0.415	0.126	0.118	0.164	0.080
		(0.065)	(0.094)	(0.059)	(0.088)	(0.381)	(0.303)	(0.072)	(0.086)	(0.068)
	vlayer_L2	**-0.216*****	**-0.270*****	-0.115	-0.073	-0.560	-0.242	-0.026	-0.125	-0.029
		(0.063)	(0.081)	(0.067)	(0.075)	(0.321)	(0.283)	(0.061)	(0.072)	(0.063)
	meanH_L1	**-0.142****	-0.034	**-0.125****	0.121	0.100	-0.034	0.096	-0.002	-0.021
		(0.053)	(0.055)	(0.046)	(0.074)	(0.277)	(0.223)	(0.062)	(0.063)	(0.050)
	vci_L2	0.153	**0.153***	-0.067	0.142	0.361	0.421	0.144	0.069	0.071
		(0.079)	(0.062)	(0.083)	(0.106)	(0.309)	(0.363)	(0.089)	(0.070)	(0.081)
	vci_L3	-0.294	**-0.342***	**-0.200***	-0.319	-1.264	-0.117	**-0.422***	**-0.387***	-0.073
		(0.156)	(0.168)	(0.101)	(0.237)	(0.837)	(0.530)	(0.200)	(0.190)	(0.119)
	height_cv	-0.097	0.025	**-0.185****	0.068	0.414	-0.052	0.119	0.195	-0.003
		(0.085)	(0.115)	(0.065)	(0.136)	(0.551)	(0.372)	(0.113)	(0.125)	(0.083)
	cwd_volume	0.048	**0.139****	**0.199*****	-0.079	0.036	0.030	-0.064	-0.072	-0.015
		(0.046)	(0.053)	(0.051)	(0.072)	(0.304)	(0.298)	(0.058)	(0.069)	(0.067)
	Intercept	2.738***	2.740***	2.739***	1.557***	4.787***	4.787***	1.261***	1.261***	1.261***
		(0.080)	(0.075)	(0.092)	(0.048)	(0.172)	(0.181)	(0.039)	(0.039)	(0.039)
	Marginal (R^2_{mar})	0.195	0.315	0.180	0.080	0.123	0.082	0.120	0.118	0.089
	Conditional (R^2_{con})	0.196	0.317	0.181	0.087	0.128	0.105	0.120	0.118	0.089

Note: *p < 0.05, **p < 0.01, ***p < 0.001

Mixed effects models showed that reptile only abundance had a negative relationship to *Canopy_roughness* (p < 0.05), *vlayer_L2* (p < 0.01) and *height_cv* (p < 0.05), and a positive relationship to *skewH* (p < 0.05) and *cwd_volume* (p < 0.01). Amphibian abundance tended to increase with higher *meanH* (p < 0.001), *skewH* (p < 0.001) and *canopy_roughness* (p < 0.001), captured by different types of data. On the contrary, amphibian abundance decreased with increasing volume of layer 2 and vertical complexity of layer 3 (*vlayer_L2* = p < 0.01, and *vci_L3* = p < 0.001) (Table 6).

Table 15. Mixed effects model summary of the relationship between LiDAR derived vegetation structure and reptile abundance (lizards, snakes and turtles) and amphibian (frogs and toads) abundance. First and second rows of independent variables show intercept and standard error of the model. Intercept of significant variables is highlighted in bold.

		Dependent variables					
		Reptile			**Amphibian**		
		TLS	ULS	Fusion	TLS	ULS	Fusion
Independent variables	meanH	0.256	0.162	-0.134	**4.333*** **	**3.463*** **	0.155
		(0.172)	(0.178)	(0.118)	(0.909)	(0.852)	(0.458)
	skewH	**0.334***	0.136	-0.027	**3.063*** **	**2.022*** **	0.217
		(0.134)	(0.090)	(0.111)	(0.693)	(0.486)	(0.442)
	vci_5m	-0.057	-0.084	-0.012	0.464	-0.313	0.268
		(0.046)	(0.044)	(0.052)	(0.252)	(0.280)	(0.215)
	canopy_roughness	**-0.188***	**-0.209** **	-0.147	**1.083*** **	0.389	**1.017*** **
		(0.074)	(0.064)	(0.081)	(0.300)	(0.202)	(0.234)
	vlayer_L1	0.064	0.051	-0.121	**0.952** **	0.81	0.419
		(0.069)	(0.101)	(0.062)	(0.296)	(0.458)	(0.245)
	vlayer_L2	**-0.149***	-0.125	-0.037	**-0.714***	-0.414	**-0.671***
		(0.069)	(0.090)	(0.073)	(0.284)	(0.327)	(0.294)
	meanH_L1	**0.170** **	-0.018	-0.052	0.453	-0.239	**-0.637*** **
		(0.055)	(0.058)	(0.049)	(0.242)	(0.254)	(0.186)
	vci_L2	**0.204***	**0.130***	0.033	-0.146	**-0.793***	**-0.792***
		(0.083)	(0.064)	(0.088)	(0.391)	(0.313)	(0.358)
	vci_L3	-0.122	-0.045	0.176	**-4.067*** **	**-3.696*** **	-0.314
		(0.161)	(0.174)	(0.107)	(0.895)	(0.834)	(0.399)
	height_cv	-0.155	-0.090	**-0.161***	0.709	**1.392** **	-0.389
		(0.089)	(0.120)	(0.069)	(0.409)	(0.524)	(0.236)
	cwd_volume	0.044	**0.151** **	**0.175*** **	-0.447	0.202	0.186
		(0.049)	(0.056)	(0.053)	(0.237)	(0.233)	(0.250)
	Intercept	**2.620*** **	**2.628*** **	**2.622*** **	-0.936	-0.687	-0.618
		(0.085)	(0.082)	(0.101)	(0.498)	(0.405)	(0.376)
	Marginal (R^2_{mar})	0.213	0.221	0.169	0.266	0.280	0.277
	Conditional (R^2_{con})	0.214	0.223	0.170	0.272	0.290	0.289

Note: *p < 0.05, **p < 0.01, ***p < 0.001

Individual reptile and amphibian species abundance

Of the 27 species, eight species were observed in at least 10 sites. The abundance of these eight species and "unidentified skinks" were modelled using LiDAR structural variables. The individual species included the Boulengers Skink (*Morethia boulengeri*), Common Dwarf Skink (*Menetia greyii*), Delicate Skink (*Lampropholis delicata*), Jacky Dragon (*Agamidae*), Shingleback (*Tiliqua rugosa*),

Smooth Toadlet (*Uperoleia laevigata*), Spotted Grass Frog (*Limnodynastes tasmaniensis*), Three-toed Skink (*Saiphos equalis*) (Appendix 4). Only the Jacky Dragon did not demonstrate statistically significant relationship to any of the LiDAR derived structural metrics. The abundance of the remaining species and the "unidentified skink" group showed a significant response to one or more variables; however, these were not always consistent across sensors (Appendix 4). The predictive power of the models in explaining individual species abundance ranged from $R^2_{mar} = 0.035$ to $R^2_{mar} = 0.318$.

Discussion

In this chapter, the relationship between eleven vegetation structural variables derived from three types of LiDAR data (TLS, ULS and Fusion) and reptile and amphibian abundance, species richness and diversity were analyzed. TLS and Fusion dataset produced variables with similar values compared to the ULS dataset. This might be due to the over-representation of TLS data in Fusion dataset as TLS point cloud has much higher point density than the ULS data. As a consequence, TLS data had heavier impact on the derived structural metrics compared that of the ULS data. Our models demonstrated that woodland reptile and amphibian populations were significantly associated with a number of vegetation structural characteristics from the selected variables, the most common of which were mean canopy height, canopy skewedness, vertical complexity, volume of vegetation and CWD. Notably these relationships were not consistent across sensors, taxa groupings or species.

ULS models typically explained as much if not more variance in dependent variables as TLS data with a few exceptions. The variance in the overall abundance of reptiles and amphibians showed a stronger relationship to LiDAR derived vegetation structural variables than species richness and Shannon diversity, although this could be a function of relatively low overall diversity at any given site (maximum of 9 species). Most individual species showed a significant relationship with one or more structural variables, although model performance varied widely between species, but less so between LiDAR data types. We discuss some of the notable relationships between herpetofauna population data and vegetation structural metrics with reference to existing literature on habitat associations for these animals. We also discuss sensor performance and potential reasons why significant associations between LiDAR derived vegetation structural metrics and animal population data were not consistent across sensors.

Relationships between LiDAR derived structural metrics and the abundance and diversity of woodland herpetofauna

Overall reptile and amphibian abundance was positively associated with TLS and ULS derived mean height and skewness of canopy height (TLS and ULS), and CWD volume (ULS and Fusion) and negatively associated with mean height of vegetation from 0-1 m (TLS and Fusion) and the volume of vegetation in the middle layer from 1 to 10 meters (TLS and ULS). This suggests that the animals included in this study typically preferred habitat with a higher average canopy height with a few tall crowns but no consistent tall canopy cover. Overall abundance was associated with less vegetation biomass between the canopy and ground layer and lower average vegetation height from 0-1 m. Overall abundance was also higher in landscapes with a higher volume of CWD and this was largely driven by reptile data since amphibian abundance alone was not significantly related to CWD.

To our knowledge, only one previous study looked at LiDAR derived vegetation structural metrics and herpetofauna population data. A recent study (Fill et al., 2015) found a positive relationship between ALS LiDAR derived ground vegetation cover and the habitat selection of eastern diamondback rattlesnakes (*Crotalus adamanteus*). Contrary to their expectations, they did not find a relationship between LiDAR derived canopy metrics and snake occurrence, likely due to a lack of heterogeneity across their study sites, which meant that most sites were the preferred open-canopy habitat (Fill et al., 2015). Research using traditional field measures of vegetation structure have identified significant relationships between reptile abundance and vegetation cover, complexity and CWD (Jellinek et al., 2004, Evans et al., 2019). Howland et al. (2014) investigated many of the same reptile species as our study and found greater abundance, species richness and diversity in woodlands than in grasslands. This is thought to be the results of additional shelter and foraging substrates provided by CWD and leaf litter from scattered trees and shrubs (Evans et al., 2019). Furthermore, canopy gaps, which are also common in woodland landscapes, provide sunlit areas for reptile basking and thermoregulation (Pike et al., 2011). The negative relationship between reptile abundance and canopy roughness (TLS and ULS) suggests that landscapes with less structural variability above 1.3 m are also preferred by reptiles, although that low variability could be cause by consistently open or consistently closed cover. Notably, this relationship was significantly positive (TLS and Fusion) for amphibians, which were more abundant in areas with higher canopy variability above 1.3 m.

Numerous studies have found that frog abundance and species richness increase in areas with more tree canopy cover (Lemckert, 1999, Roznik et al., 2015). Amphibians (frogs and toads) in our study preferred greater average canopy height and shrub layer (TLS and ULS). Amphibian preference for

landscapes with a higher volume of vegetation from 0-1 m (TLS) may be explained by higher moisture levels in these areas, which supports greater vegetation density, since these animals must maintain moist skin and generally can not tolerate prolonged dry conditions (Demaynadier and Hunter, 1998). Different frog species use different landscape strata (e.g. ground vs arboreal) but too few individuals from most amphibian species were observed to robustly interrogate predictions derived from the habitat preference of specific frog genera.

Individual species abundance models also yielded interesting associations that did not always align with the existing literature. For example, an earlier study based on traditional vegetation surveys found that the presence of Boulengers Skink (*Morethia boulengeri*) was positively associated with canopy cover, so preferred woodland landscapes, but was not related to grass structure (Fischer et al., 2004, Howland et al., 2014). Similarly, another study (Fischer et al., 2004) found that the same skink preferred high vegetation cover and specifically tree cover. Our study found that the abundance of Boulengers skink was associated with higher average height in the lower layer of vegetation (e.g., grasses) (TLS) as well as vertical complexity of mid layer vegetation from 1 to 10 m (TLS and ULS) and canopy skewedness (TLS and ULS), but negatively associated with vertical complexity at 5 m (ULS) (Appendix 4). A study from 2014 (Howland et al., 2014) found that the three toed skink (*Saiphos equalis*) was strongly associated with a metric of grass vegetation structure that correlated with biomass and height, whereas our models found a significant negative relationship to the volume of vegetation from 0-1 m (TLS and Fusion) and the abundance of three toed skinks, which was also negatively associated with vertical complexity at 5 m (Appendix 4).

Performance of TLS, ULS and Fusion based models

Generally, the models from the three types of data provided similar results. For overall bird abundance, explained variance by the fixed effects (R^2_{mar}) from the ULS model was slightly higher than the TLS and Fusion models. All other models from different types of data demonstrated similar R^2_{mar}. Difference between the explained variance by the fixed effects (R^2_{mar}) and the random effects (R^2_{con}) were negligible for all the models, which implies that the clusters of sites did not have significant influence on herpetofauna abundance and species richness.

Some of the relationships between animal abundance and specific vegetation metrics derived from the different types of sensor data were unexpected. For example, overall abundance and the diversity of reptiles and amphibians combined was found to be strongly and significantly associated to both the TLS and ULS derived *meanH*. However, Fusion based *meanH* was not significantly related to any of these dependent variables (Tables 5, 6). The reason for this is unclear.

Associations between CWD volume and herpetofauna were also inconsistent across sensor types, but this is easier to explain. Overall reptile and amphibian abundance was positively associated to ULS and Fusion derived CWD but not TLS derived CWD. This is likely the result of differences in the ability of TLS and ULS sensors to detect and measure CWD. Shokirov et al (Chapter 3) found that CWD volume was measured more accurately by ULS and Fusion data than TLS data. Ground vegetation cover had strong negative impacts on CWD detection and the RF classification algorithm used to extract CWD had more difficulty differentiating CWD from dense vegetation cover (e.g. tussock grass) with TLS data than ULS and Fusion data.

ULS models performed slightly better in identifying relationships between vegetation structure and the abundance and diversity of most herpetofauna; however, ground dwelling shinglebacks (*Tiliqua rugosa*) and three-toed-skinks (*Saiphos equalis*) were an exception. This may be related to the performance of the different sensors in characterizing vegetation metrics at specific heights above the ground that are associated with particular species (Davies and Asner, 2014). TLS typically captures more detailed information below the canopy than ULS sensors, which could be why the TLS models performed better for those two species. However, TLS data may have performed better for other species if we had increased the number of scans, and therefore the coverage of points across each site (Wilkes et al., 2017, Levick et al., 2021). However, this would have substantially increased the time for TLS data collection and post-processing and made the effort of data collection between ULS and TLS less comparable.

Conclusions and directions for future research

For the first time, LiDAR derived vegetation structural metrics from TLS, ULS and a fusion of both datasets were used to model the abundance and diversity of woodland reptiles and amphibians. Our study demonstrates that LiDAR data can help identify vegetation structural features associated with a number of different herpetofauna species. In most cases, based on our LiDAR data collection methods, ULS data performed as well as, or better than TLS data for modelling overall and individual species abundance. Notably, the combined dataset showed little or no improvement in the performance of the models. However, relationships between animal populations and specific vegetation structural features were sometimes only evident with one sensor type, and that may be due to differences in the ability of the sensors or manner in which they were used, to measure particular vegetation features such as CWD and mean canopy height.

As we had multiple species of reptiles and amphibians, we calculated several height, volumetric and heterogeneity metrics across different layers of the vegetation structure to capture as much structural

variability as possible. However, there might be other vegetation metrics that are directly related to the specific species and can be calculated from LiDAR dataset, however are missing in this study. In this regard, future study should consider the prior knowledge of habitat use of individual species when calculating the landscape metrics from LiDAR dataset. In addition, some herpetofauna in the study area might select a landscape with close proximity to the water bodies (Evans et al., 2020). As our 96 experimental sites did not contain any water bodies and LiDAR data collection was limited to the boundaries of these sites, we were unable to add any metrics related to the water bodies in this study.

Future LiDAR research should incorporate metrics based on other landscape structural variables, such as rocky outcrops and hydrological features, that are also known to be important habitat features for some reptiles and amphibians (Jellinek et al., 2004). In addition, the data collected for this study was averaged over one hectare sites, but some herpetofauna primarily use landscapes at finer scales (Rotem et al., 2020). Future research should investigate how the scale at which LiDAR metrics are measured impacts their relationship to these animals.

References

BATES, D., MÄCHLER, M., BOLKER, B. & WALKER, S. 2015. Fitting Linear Mixed-Effects Models Using lme4. *Journal of Statistical Software,* 67**,** 48.

BECKER, R., CHAMBERS, M. & WILKS, A. R. 1988. *The New S Language: A Programming Environment for Data Analysis and Graphics*, Wadsworth & Brooks/Cole Advanced Books & Software.

BIN ABDUL RAHMAN, R. 2018. *Nest site selection by flatback sea turtles: Characterization of nesting beach topography with airborne LiDAR.* Honours, Murdoch University.

BRADBURY, R. B., HILL, R. A., MASON, D. C., HINSLEY, S. A., WILSON, J. D., BALZTER, H., ANDERSON, G. Q. A., MARK J. WHITTINGHAM, M. J., DAVENPORT, I. J. & BELLAMY, P. E. 2005. Modelling relationships between birds and vegetation structure using airborne LiDAR data a review with case studies from agricultural and woodland environments. *British Ornithologists' Union, IBIS,* 147**,** 443–452.

CODY, M. L. 1981. Habitat Selection in Birds: The Roles of Vegetation Structure, Competitors, and Productivity. *BioScience,* 31**,** 107-113.

CORTES, A. M., RUIZ-AGUDELO, C. A., VALENCIA-AGUILAR, A. & LADLE, R. J. 2014. Ecological functions of neotropical amphibians and reptiles: a review. *Universitas Scientiarum,* 20.

DAVIES, A. B. & ASNER, G. P. 2014. Advances in animal ecology from 3D-LiDAR ecosystem mapping. *Trends Ecol Evol,* 29**,** 681-91.

DEMAYNADIER, P. G. & HUNTER, M. L. 1998. Effects of Silvicultural Edges on the Distribution and Abundance of Amphibians in Maine. *Conservation Biology,* 12**,** 340-352.

DEPARTMENT OF ENVIRONMENT, G. o. A. 2013. Vegetation Assessment Guide.

DOODY, J. S., SOENNICHSEN, K. F., JAMES, H., MCHENRY, C. & CLULOW, S. 2020. Ecosystem engineering by deep-nesting monitor lizards. *Ecology,* n/a**,** e03271.

ELDEGARD, K., DIRKSEN, J. W., ØRKA, H. O., HALVORSEN, R., NÆSSET, E., GOBAKKEN, T. & OHLSON, M. 2014. Modelling bird richness and bird species presence in a boreal forest reserve using airborne laser-scanning and aerial images. *Bird Study,* 61**,** 204-219.

EVANS, M. J., NEWPORT, J. S. & MANNING, A. D. 2019. A long-term experiment reveals strategies for the ecological restoration of reptiles in scattered tree landscapes. *Biodiversity and Conservation,* 28**,** 2825-2843.

EVANS, M. J., SCHEELE, B. C., WESTGATE, M. J., YEBRA, M., NEWPORT, J. S. & MANNING, A. D. 2020. Beyond the pond: Terrestrial habitat use by frogs in a changing climate. *Biological Conservation,* 249**,** 108712.

FILL, J. M., WALDRON, J. L., WELCH, S. M., GIBBONS, J. W., BENNETT, S. H. & MOUSSEAU, T. A. 2015. Using multiscale spatial models to assess potential surrogate habitat for an imperiled reptile. *PLoS One,* 10**,** e0123307.

FISCHER, J., LINDENMAYER, D. B. & COWLING, A. 2004. The challenge of managing multiple species at multiple scales: reptiles in an Australian grazing landscape. *Journal of Applied Ecology,* 41**,** 32-44.

GARDEN, J. G., MCALPINE, C. A., POSSINGHAM, H. P. & JONES, D. N. 2007. Habitat structure is more important than vegetation composition for local-level management of native terrestrial reptile and small mammal species living in urban remnants: A case study from Brisbane, Australia. *Austral Ecology,* 32**,** 669-685.

GINSBERG, H. S., HICKLING, G. J., BURKE, R. L., OGDEN, N. H., BEATI, L., LEBRUN, R. A., ARSNOE, I. M., GERHOLD, R., HAN, S., JACKSON, K., MAESTAS, L., MOODY, T., PANG, G., ROSS, B., RULISON, E. L. & TSAO, J. I. 2021. Why Lyme disease is common in the northern US, but rare in the south: The roles of host choice, host-seeking behavior, and tick density. *PLOS Biology,* 19**,** e3001066.

HALLIDAY, T. R. 2008. Why amphibians are important. *International Zoo Yearbook,* 42**,** 7-14.

HARTIG, F. 2017. DHARMa: residual diagnostics for hierarchical (multi-level/mixed) regression models. *R package version 0.1,* 5.

HERRERO-HUERTA, M., BUCKSCH, A., PUTTONEN, E. & RAINEY, K. M. 2020. Canopy Roughness: A New Phenotypic Trait to Estimate Aboveground Biomass from Unmanned Aerial System. *Plant Phenomics,* 2020**,** 6735967.

HILLMAN, S., WALLACE, L., LUCIEER, A., REINKE, K., TURNER, D. & JONES, S. 2021. A comparison of terrestrial and UAS sensors for measuring fuel hazard in a dry sclerophyll forest. *International Journal of Applied Earth Observation and Geoinformation,* 95.

HINSLEY, S., HILL, R., FULLER, R., BELLAMY, P. & ROTHERY, P. 2009. Bird species distributions across woodland canopy structure gradients. *Community Ecology,* 10**,** 99-110.

HOWLAND, B., STOJANOVIC, D., GORDON, I. J., MANNING, A. D., FLETCHER, D. & LINDENMAYER, D. B. 2014. Eaten out of house and home: impacts of grazing on ground-dwelling reptiles in Australian grasslands and grassy woodlands. *PLoS One,* 9**,** e105966.

ISENBURG, M. 2012. LAStools-efficient tools for LiDAR processing. *Available at: http:* *http://www.cs.unc.edu/~isenburg/lastools/*.

JARI OKSANEN, F. G. B., Michael Friendly, Roeland Kindt, Pierre Legendre, Dan McGlinn, Peter R. Minchin, R. B. O'Hara, Gavin L. Simpson, Peter Solymos, M. Henry H. Stevens, Eduard Szoecs, Helene Wagner 2019. vegan: Community Ecology Package.

JELLINEK, S., DRISCOLL, D. A. & KIRKPATRICK, J. B. 2004. Environmental and vegetation variables have a greater influence than habitat fragmentation in structuring lizard communities in remnant urban bushland. *Austral Ecology,* 29**,** 294-304.

JENNESS, J. S. 2004. Calculating Landscape Surface Area from Digital Elevation Models. *Wildlife Society Bulletin (1973-2006),* 32**,** 829-839.

JUPP, D. L. B. & LOVELL, J. L. 2007. Airborne and Ground-Based Lidar Systems for Forest Measurement: Background and Principles. Australia: CSIRO.

KRAUS, F. 2015. Impacts from Invasive Reptiles and Amphibians. *Annual Review of Ecology, Evolution, and Systematics,* 46**,** 75-97.

LALIBERTÉ, E. & LEGENDRE, P. 2010. A distance-based framework for measuring functional diversity from multiple traits. *Ecology,* 91**,** 299-305.

LEFSKY, M. A., COHEN, W. B., PARKER, G. G. & HARDING, D. J. 2002. Lidar Remote Sensing for Ecosystem Studies. *BioScience,* 52**,** 19-30.

LEMCKERT, F. 1999. Impacts of selective logging on frogs in a forested area of northern New South Wales. *Biological Conservation,* 89**,** 321-328.

LESAK, A. A., RADELOFF, V. C., HAWBAKER, T. J., PIDGEON, A. M., GOBAKKEN, T. & CONTRUCCI, K. 2011. Modeling forest songbird species richness using LiDAR-derived measures of forest structure. *Remote Sensing of Environment,* 115**,** 2823-2835.

LEVICK, S. R., WHITESIDE, T., LOEWENSTEINER, D. A., RUDGE, M. & BARTOLO, R. 2021. Leveraging TLS as a Calibration and Validation Tool for MLS and ULS Mapping of Savanna Structure and Biomass at Landscape-Scales. *Remote Sensing,* 13.

LEYEQUIEN, E., VERRELST, J., SLOT, M., SCHAEPMAN-STRUB, G., HEITKÖNIG, I. M. A. & SKIDMORE, A. 2007. Capturing the fugitive: Applying remote sensing to terrestrial animal distribution and diversity. *International Journal of Applied Earth Observation and Geoinformation,* 9**,** 1-20.

LOUDERMILK, E. L., HIERS, J. K., O'BRIEN, J. J., MITCHELL, R. J., SINGHANIA, A., FERNANDEZ, J. C., CROPPER, W. P. & SLATTON, K. C. 2009. Ground-based LIDAR: a novel approach to quantify fine-scale fuelbed characteristics. *International Journal of Wildland Fire,* 18.

MANNING, A. D., CUNNINGHAM, R. B. & LINDENMAYER, D. B. 2013. Bringing forward the benefits of coarse woody debris in ecosystem recovery under different levels of grazing and vegetation density. *Biological Conservation,* 157**,** 204-214.

MANNING, A. D., WOOD, J. T., GUNNINGHAM, R. B., MCINTYRE, S., SHORTHOUSE, D. J., GORDON, I. J. & LINDENMAYER, D. B. 2011. Integrating research and restoration: the establishment of a long-term woodland experiment in south-eastern Australia. *Zoologist,* 35**,** 633-648.

MARC L. IMHOFF, T. D. S., Anthony Milne, Garth Morgan, and Tony Orr 1997. Remotely Sensed Indicators of Habitat Heterogeneity: Use of Synthetic Aperture Radar in Mapping Vegetation Structure and Bird Habitat. *Remote Sensing of Environment,* 60**,** 217-227.

MCELHINNY, C., GIBBONS, P., BRACK, C. & BAUHUS, J. 2006. Fauna-habitat relationships: a basis for identifying key stand structural attributes in temperate Australian eucalypt forests and woodlands. *Pacific Conservation Biology,* 12**,** 89-110.

MCINTYRE, S., STOL, J., HARVEY, J., NICHOLLS, A. O., CAMPBELL, A., REID, A., MANNING, A. D., LINDENMAYER, D. B. & 2010. Biomass and floristic patterns in the ground layer vegetation of box-gum grassy eucalypt woodland in Goorooyarroo and Mulligans Flat Nature Reserves, Australian Capital Territory. *Cunninghamia: a journal of plant ecology for eastern Australia,* 11**,** 319-357.

MELIN, M., HINSLEY, S. A., BROUGHTON, R. K., BELLAMY, P. & HILL, R. A. 2018. Living on the edge: utilising lidar data to assess the importance of vegetation structure for avian diversity in fragmented woodlands and their edges. *Landscape Ecology,* 33**,** 895-910.

MICHAEL, D. R., CUNNINGHAM, R. B. & LINDENMAYER, D. B. 2008. A forgotten habitat? Granite inselbergs conserve reptile diversity in fragmented agricultural landscapes. *Journal of Applied Ecology,* 45**,** 1742-1752.

MIZSEI, E., FEJES, Z., MALATINSZKY, Á., LENGYEL, S. & VADÁSZ, C. 2020. Reptile responses to vegetation structure in a grassland restored for an endangered snake. *Community Ecology*.

NAKAGAWA, S., SCHIELZETH, H. & O'HARA, R. B. 2013. A general and simple method for obtainingR2from generalized linear mixed-effects models. *Methods in Ecology and Evolution,* 4**,** 133-142.

NEWNHAM, G. J., ARMSTON, J. D., CALDERS, K., DISNEY, M. I., LOVELL, J. L., SCHAAF, C. B., STRAHLER, A. H. & DANSON, F. M. 2015. Terrestrial Laser Scanning for Plot-Scale Forest Measurement. *Current Forestry Reports,* 1**,** 239-251.

OWENS, A., MOSELEY, K., MCCAY, T., CASTLEBERRY, S., KILGO, J. & FORD, W. 2008. Amphibian and reptile community response to coarse woody debris manipulations in upland loblolly pine (Pinus taeda) forests. *Forest Ecology and Management,* 256**,** 2078-2083.

PIKE, D. A., WEBB, J. K. & SHINE, R. 2011. Removing forest canopy cover restores a reptile assemblage. *Ecological Applications,* 21**,** 274-280.

PRETZSCH, H. 2009. Description and Analysis of Stand Structures. *In:* PRETZSCH, H. (ed.) *Forest Dynamics, Growth and Yield: From Measurement to Model.* Berlin, Heidelberg: Springer Berlin Heidelberg.

PRICE, B., KUTT, A. S. & MCALPINE, C. A. 2010. The importance of fine-scale savanna heterogeneity for reptiles and small mammals. *Biological Conservation,* 143**,** 2504-2513.

R TEAM 2019. R: A Language and Environment for Statistical Computing. . Vienna, Austria: R Foundation for Statistical Computing.

ROTEM, G., GILADI, I., BOUSKILA, A. & ZIV, Y. 2020. Scale-dependent correlates of reptile communities in natural patches within a fragmented agroecosystem. *Landscape Ecology,* 35**,** 2339-2355.

ROUSSEL, J. 2017. Auty, D. lidR: Airborne LiDAR Data Manipulation and Visualization for Forestry Applications. *R package version,* 1.

ROZNIK, E. A., SAPSFORD, S. J., PIKE, D. A., SCHWARZKOPF, L. & ALFORD, R. A. 2015. Natural disturbance reduces disease risk in endangered rainforest frog populations. *Sci Rep,* 5**,** 13472.

SHANMUGANATHAN, T., PALLISTER, J., DOODY, S., MCCALLUM, H., ROBINSON, T., SHEPPARD, A., HARDY, C., HALLIDAY, D., VENABLES, D., VOYSEY, R., STRIVE, T., HINDS, L. & HYATT, A. 2010. Biological control of the cane toad in Australia: a review. *Animal Conservation,* 13**,** 16-23.

SHORTHOUSE, D. J., IGLESIAS, D., JEFFRESS, S., LANE, S., MILLS, P., WOODBRIDGE, G., MCINTYRE, S. & MANNING, A. D. 2012. The 'making of' the Mulligans Flat - Goorooyarroo experimental restoration project. *Ecological Management & Restoration,* 13**,** 112-125.

SILLERO, N. & GONÇALVES-SECO, L. 2014. Spatial structure analysis of a reptile community with airborne LiDAR data. *International Journal of Geographical Information Science,* 28**,** 1709-1722.

SZ DJI TECHNOLOGY CO., L. 2018. DJI GS Pro User Manual.

VAN EWIJK, K. Y., TREITZ, P. M. & SCOTT, N. A. 2011. Characterizing Forest Succession in Central Ontario using Lidar-derived Indices. *Photogrammetric Engineering & Remote Sensing,* 77**,** 261-269.

VIERLING, K. T., VIERLING, L. A., GOULD, W. A., MARTINUZZI, S. & CLAWGES, R. M. 2008. Lidar: shedding new light on habitat characterization and modeling. *Frontiers in Ecology and the Environment,* 6**,** 90-98.

WHITE, J. C., COOPS, N. C., WULDER, M. A., VASTARANTA, M., HILKER, T. & TOMPALSKI, P. 2016. Remote Sensing Technologies for Enhancing Forest Inventories: A Review. *Canadian Journal of Remote Sensing,* 42**,** 619-641.

WILKES, P., LAU, A., DISNEY, M., CALDERS, K., BURT, A., GONZALEZ DE TANAGO, J., BARTHOLOMEUS, H., BREDE, B. & HEROLD, M. 2017. Data acquisition considerations for Terrestrial Laser Scanning of forest plots. *Remote Sensing of Environment,* 196**,** 140-153.

Conclusion

Many animals are associated with elements of vegetation structure that support their particular niche (Carrasco et al. 2019). The relationship between animals and plants is often multifaceted since vegetation can provide food, shelter, influence climate, interfere with or facilitate movement, and affect interactions with sympatric species and conspecifics (McCoy and Bell 1991; Jung et al. 2012; Davies and Asner 2014). LiDAR data can be useful for classifying and quantifying vegetation structure across wide-areas, which can help ecologists recognise and understand patterns of association between animals and vegetation structure across landscapes (Bergen et al 2009). An awareness of these associations can help ecologists and landscape managers to assess habitat quality for specific species and understand how particular landscape and vegetation management practices may impact animal populations. This information can be used to target restoration activities towards achieving specific structural aims that can influence a wide variety of species, such as the reintroduction of coarse woody debris (CWD) at Mulligan's Flat-Goorooyaroo, or identify structural habitat-associations of individual species or guilds to better manage those populations and their landscapes (Freudenberger 1999; Manning et al. 2011).

LiDAR is still an emerging tool for wildlife habitat assessments and most of the existing research has utilized data from airborne platforms that can capture information across wide areas but are often limited in their ability to provide structural details below forests canopies. These sensors often have lower resolution than data from ULS or TLS as well. For the first time, we obtained both TLS and ULS data across a critically endangered woodland landscape to investigate relationships between vegetation structure and bird, reptile and amphibian diversity and abundance. We used data from both sensors individually and in combination to measure vegetation structural attributes and investigate their importance to a broad range of bird, reptile and amphibian communities and individual species. Unlike most ALS data, TLS and ULS can provide detailed information on canopy, sub-canopy and ground layer attributes of vegetation structure, which can be particularly important for animals that utilize low and mid-story vegetation cover.

Results from the first chapter showed that TLS generally measured more detailed structural information than ULS, especially in ground and mid-storey vegetation layers. This was due to the placement of the TLS on the ground and its ability to create high density point clouds. Considering this, I expected that the TLS data would outperform the ULS data in finding associations between vegetation structural variables and animal abundance, species richness and diversity.

The second chapter analysed the relationship between TLS and ULS LiDAR-derived vegetation structural variables and bird abundance, species richness and diversity. Bird communities by guilds and individual species' abundance had a stronger relationship to LiDAR derived vegetation metrics than overall bird abundance. This outcome suggested that modelling bird habitat with LiDAR data generally requires a focus on individual species or groups of birds that use similar habitat types across similar scales. In most cases ULS models performed slightly better than TLS models. However, it is important to recognise that TLS may have performed better if more ground stations were used for collecting the terrestrial LiDAR data. Although TLS captured more detail in the understory and mid-story, more data was occluded the in lower layers of vegetation by low-lying structural objects (LaRue et al. 2020), and these occlusions probably impacted the performance of the TLS data in our study. Nonetheless, our hypothesis that ULS would outperform TLS when finding association between vegetation structure and bird abundance, which was based on our sampling methods, was not supported.

In the past decade, TLS has become a popular tool for measuring vegetation structure to estimate vegetation biomass (Hackenberg et al. 2015) and forest structural diversity (LaRue et al. 2020). Depending on the landscape and the aim of the research, it is common to collect anywhere from 10 to 120 scans in a one hectare plot (Levick et al. 2021). Studies that collect a high number of scans in a 1 ha plot typically covered a relatively small total area and focused on capturing a high detail of vegetation structure at fine scales (e.g., individual tree branches) (Calders et al. 2015; Hackenberg et al. 2015). TLS can be ideal for this purpose or for ground-truthing LiDAR scans collected over wider areas in less detail from airborne sensors (Levick et al., 2012). However, a limitation of TLS is that data collected over large areas is time consuming and access can be restricted in some places due to difficult terrain and/or dense vegetation. For this research, we conducted a pilot study, which suggested that 7 TLS scans per 1 ha plot was the minimum required to characterise 1 ha (50m × 200m) grassy woodland plots within a one month time frame so that, from a subjective standpoint, the data collection timeline would be feasible to field ecologists looking to implement this methodology and somewhat comparable to our ULS data collection effort, which required a week of flight time. More TLS scans might improve the performance of TLS models; however, this would substantially increase the time required for data collection and post – processing.

In the third chapter, I developed a novel method for classifying CWD from LiDAR derived topographic surface variables by applying a random forest machine learning algorithm to ULS, TLS and Fusion datasets. CWD is an essential habitat feature that provides shelter, food and/or cover for many species (Pesonen et al. 2008; Manning, Cunningham, and Lindenmayer 2013). The estimation of CWD with

LiDAR sensors is a challenging task, because accuracy is impacted by the density of the ground vegetation, landscape topography, size of CWD, point density and sensor type (Polewski et al. 2017; Yrttimaa et al. 2019). My method revealed the contribution of several topographic and structural variables including DHM, roughness, ruggedness, slope and aspect to CWD detection accuracy. In addition, I evaluated the influence of ground cover vegetation density on model performance by examining the classification accuracy on low, medium and high density ground vegetation cover. High density ground vegetation created many false positives, which substantially decreased the classification accuracy in TLS and Fusion data. In contrast, ULS created less false positives in sites with high density ground vegetation and resulted in higher CWD classification and count accuracy. The ULS sensor was less impacted by low-lying structural occlusions than the TLS or Fusion data due to the overhead viewing angle of the sensor, and this probably explains why CWD models from ULS data performed better. Generally, medium and low density vegetation had less influence on CWD classification accuracy. CWD maps derived from this research contributed to the assessment of landscape use by reptiles and amphibians in Chapter 4.

So far, most of the studies for animal habitat modelling with LiDAR sensors are strongly biased towards avian species (Davies and Asner 2014). Thus, there is a need to investigate habitat structure with LiDAR data for other taxa, such as reptiles and amphibians (Halliday 2008; Howland et al. 2016). In Chapter 4, I used TLS, ULS, and Fusion data to investigate relationships between vegetation structure and the abundance and diversity of reptiles and amphibians in a woodland landscape. This is one of the first studies to use LiDAR derived structural metrics to model the habitat preferences of herptofauna. CWD volume, vegetation height, vegetation volume and structural diversity were the most common significant predictors from the LiDAR datasets.

The models derived from TLS, ULS and Fusion data were largely similar in performance. This was true for both herptofauna and avifauna. This suggests that ULS can capture sufficient details of vegetation structure for modelling habitat use by birds and reptiles in a woodland landscape. Given that ULS is becoming more accessible and data collection is much faster than TLS, wildlife management that requires structural information to assess habitat quality for woodland species could utilize data from ULS. In addition, ULS can be optimized for collecting information over large areas in more frequent time intervals (Levick et al. 2021). ULS also can be used for the calibration and validation of spaceborne LiDAR and SAR sensor data (Puletti et al. 2020; Levick et al. 2021), which opens the door to modelling landscape and vegetation structural variables for regional or even global scale habitat models. A recent study (Levick et al. 2021) compared the performance of TLS, ULS and mobile laser scanners (MLS) in characterizing three dimensional forest structures in savannah

ecosystem. They found that canopy structural metrics derived from these three types of sensor systems did not differ significantly, however ULS and MLS were advantageous in terms of time for data collection, which makes them more suitable for addressing many ecological problems. Significant differences were in individual tree and stem level modelling, where TLS provided high accuracy in capturing DBH and smaller stems (Levick et al. 2021). A new study by Hyyppä et al. (2021) used ULS to capture forest structure from below the canopy with flying height of 2-3 meters. Their research demonstrated that below-canopy ULS can provide more accurate measurements of height and stem volume. However, this method is still in early stages of development and may by applicable to sparse forests. Currently, flying under-canopy ULS performed manually and is more challenging in dense forests due to the obstructions from the forest structure.

Future research should investigate how different spatial scales and in particular, how matching the spatial scale of LiDAR data to the scale of landscape use by specific species, might influence our ability to identify the structural habitat associations of those animals. The one hectare plots that we used for this study may not be an appropriate representation of structure at the scale that some species experience it. Future research should also consider both a more species specific modelling approach for selecting structural variables thought to be important for specific species, and less specific machine learning approaches that do not attempt to quantify individual structural metrics from the data but instead identify relationships between animal populations and structure from the data contained within entire point-clouds. Lastly, for classifying and quantifying structural habitat elements, such as CWD, future research should incorporate LiDAR intensity values, which may improve classification accuracies (Charaniya, Manduchi, and Lodha 2004).

References

Calders, K., G. Newnham, A. Burt, S. Murphy, P. Raumonen, M. Herold, D. Culvenor, et al. 2015. "Nondestructive Estimates of above-Ground Biomass Using Terrestrial Laser Scanning." *Methods in Ecology and Evolution* 6 (2):198-208. doi: 10.1111/2041-210x.12301.

Carrasco, L., X. Giam, M. Papeş, and K. Sheldon. 2019. "Metrics of Lidar-Derived 3d Vegetation Structure Reveal Contrasting Effects of Horizontal and Vertical Forest Heterogeneity on Bird Species Richness." *Remote Sensing* 11 (7):743-62. doi: 10.3390/rs11070743.

Charaniya, A. P., R. Manduchi, and S. K. Lodha. 2004. Supervised Parametric Classification of Aerial Lidar Data. Paper presented at the 2004 Conference on Computer Vision and Pattern Recognition Workshop, 27 June-2 July 2004.

Davies, A. B., and G. P. Asner. 2014. "Advances in Animal Ecology from 3d-Lidar Ecosystem Mapping." *Trends Ecol Evol* 29 (12):681-91. doi: 10.1016/j.tree.2014.10.005.

Freudenberger, D. 1999. *Guidelines for Enhancing Grassy Woodlands for the Vegetation Investment Project*: CSIRO Wildlife and Ecology.

Hackenberg, J., M. Wassenberg, H. Spiecker, and D. Sun. 2015. "Non Destructive Method for Biomass Prediction Combining Tls Derived Tree Volume and Wood Density." *Forests* 6 (12):1274-300. doi: 10.3390/f6041274.

Halliday, T. R. 2008. "Why Amphibians Are Important." *International Zoo Yearbook* 42 (1):7-14. doi: 10.1111/j.1748-1090.2007.00037.x.

Howland, B. W. A., D. Stojanovic, I. J. Gordon, D. Fletcher, M. Snape, I. A. Stirnemann, and D. B. Lindenmayer. 2016. "Habitat Preference of the Striped Legless Lizard: Implications of Grazing by Native Herbivores and Livestock for Conservation of Grassland Biota." *Austral Ecology* 41 (4):455-64. doi: 10.1111/aec.12337.

Hyyppä, J., X. Yu, T. Hakala, H. Kaartinen, A. Kukko, H. Hyyti, J. Muhojoki, and E. Hyyppä. 2021. "Under-Canopy Uav Laser Scanning Providing Canopy Height and Stem Volume Accurately." *Forests* 12 (7). doi: 10.3390/f12070856.

Jung, K., S. Kaiser, S. Böhm, J. Nieschulze, and E. K. V. Kalko. 2012. "Moving in Three Dimensions: Effects of Structural Complexity on Occurrence and Activity of Insectivorous Bats in Managed Forest Stands." *Journal of Applied Ecology* 49 (2):523-31. doi: 10.1111/j.1365-2664.2012.02116.x.

LaRue, E. A., F. W. Wagner, S. Fei, J. W. Atkins, R. T. Fahey, C. M. Gough, and B. S. Hardiman. 2020. "Compatibility of Aerial and Terrestrial Lidar for Quantifying Forest Structural Diversity." *Remote Sensing* 12 (9):1407-21. doi: 10.3390/rs12091407.

Levick, S. R., T. Whiteside, D. A. Loewensteiner, M. Rudge, and R. Bartolo. 2021. "Leveraging Tls as a Calibration and Validation Tool for Mls and Uls Mapping of Savanna Structure and Biomass at Landscape-Scales." *Remote Sensing* 13 (2). doi: 10.3390/rs13020257.

Manning, A. D., R. B. Cunningham, and D. B. Lindenmayer. 2013. "Bringing Forward the Benefits of Coarse Woody Debris in Ecosystem Recovery under Different Levels of Grazing and Vegetation Density." *Biological Conservation* 157:204-14. doi: 10.1016/j.biocon.2012.06.028.

Manning, A. D., J. T. Wood, R. B. Gunningham, S. McIntyre, D. J. Shorthouse, I. J. Gordon, and D. B. Lindenmayer. 2011. "Integrating Research and Restoration: The Establishment of a Long-Term Woodland Experiment in South-Eastern Australia." *Zoologist* 35 (3):633-48.

McCoy, E. D., and S. S. Bell. 1991. "Habitat Structure: The Evolution and Diversification of a Complex Topic." In *Habitat Structure: The Physical Arrangement of Objects in Space*, edited by Susan S. Bell, Earl D. McCoy and Henry R. Mushinsky, 3-27. Dordrecht: Springer Netherlands.

Pesonen, A., M. Maltamo, K. Eerikäinen, and P. Packalèn. 2008. "Airborne Laser Scanning-Based Prediction of Coarse Woody Debris Volumes in a Conservation Area." *Forest Ecology and Management* 255 (8-9):3288-96. doi: 10.1016/j.foreco.2008.02.017.

Polewski, P., W. Yao, M. Heurich, P. Krzystek, and U. Stilla. 2017. "A Voting-Based Statistical Cylinder Detection Framework Applied to Fallen Tree Mapping in Terrestrial Laser Scanning Point Clouds." *ISPRS Journal of Photogrammetry and Remote Sensing* 129:118-30. doi: 10.1016/j.isprsjprs.2017.04.023.

Puletti, N., M. Grotti, C. Ferrara, and F. Chianucci. 2020. "Lidar-Based Estimates of Aboveground Biomass through Ground, Aerial, and Satellite Observation: A Case Study in a Mediterranean Forest." *Journal of Applied Remote Sensing* 14 (4):044501.

Yrttimaa, T., N. Saarinen, V. Luoma, T. Tanhuanpää, V. Kankare, X. Liang, J. Hyyppä, M. Holopainen, and M. Vastaranta. 2019. "Detecting and Characterizing Downed Dead Wood Using Terrestrial Laser Scanning." *ISPRS Journal of Photogrammetry and Remote Sensing* 151:76-90. doi: 10.1016/j.isprsjprs.2019.03.007.

Appendices Chapter 2

Chapter 2 Appendix A1. Pearson correlatio matrix of TLS variables

	maxH_t	meanH_t	stdH_t	skewH_t	kurH_t	p_05_t	p_10_t
maxH_t	1	0.574	0.761	0.008	-0.046	0.104	0.15
meanH_t	0.574	1	0.654	-0.694	-0.554	0.672	0.721
stdH_t	0.761	0.654	1	-0.118	-0.352	0.004	0.045
skewH_t	0.008	-0.694	-0.118	1	0.828	-0.604	-0.638
kurH_t	-0.046	-0.554	-0.352	0.828	1	-0.258	-0.285
p_05_t	0.104	0.672	0.004	-0.604	-0.258	1	0.992
p_10_t	0.15	0.721	0.045	-0.638	-0.285	0.992	1
p_25_t	0.264	0.838	0.173	-0.723	-0.376	0.924	0.958
p_50_t	0.41	0.951	0.412	-0.791	-0.529	0.752	0.801
p_75_t	0.588	0.966	0.732	-0.686	-0.618	0.509	0.562
p_90_t	0.71	0.83	0.946	-0.36	-0.501	0.292	0.333
p_99_t	0.873	0.652	0.896	0.017	-0.087	0.138	0.179
vci_2m_t	0.202	-0.022	0.146	-0.023	-0.09	-0.343	-0.314
vci_5m_t	0.216	0.185	0.153	-0.246	-0.328	-0.085	-0.028
vci_10m_t	0.244	0.537	0.233	-0.738	-0.738	0.314	0.344
vci_15m_t	0.655	0.601	0.739	-0.169	-0.335	0.179	0.206
vci_20m_t	0.816	0.565	0.696	-0.056	-0.105	0.164	0.201
cov_t	0.324	0.483	0.109	-0.513	-0.321	0.365	0.414
canopy_shannon_t	0.725	0.885	0.832	-0.538	-0.617	0.333	0.386
canopy_roughness_t	0.593	0.481	0.418	-0.265	-0.243	0.083	0.138
tvolume_t	0.26	0.456	0.05	-0.495	-0.262	0.387	0.43
vlayer_L1_t	-0.08	-0.143	-0.073	0.029	0.014	-0.207	-0.198
vlayer_L2_t	0.128	0.256	-0.152	-0.427	-0.194	0.313	0.344
vlayer_L3_t	0.446	0.738	0.368	-0.529	-0.326	0.525	0.575
meanH_L1_t	0.23	0.12	0.279	-0.038	-0.092	-0.207	-0.192
meanH_L2_t	0.109	0.626	-0.083	-0.761	-0.441	0.82	0.844
meanH_L3_t	0.692	0.43	0.874	0.242	0.047	-0.046	-0.022
sdH_L1_t	0.295	0.094	0.304	0.077	0.002	-0.212	-0.194
sdH_L2_t	0.332	0.622	0.397	-0.729	-0.723	0.187	0.236
sdH_L3_t	0.863	0.493	0.829	0.202	0.1	0.026	0.058
roughness_L1_t	0.139	0.059	0.065	-0.171	-0.148	-0.212	-0.18
roughness_L2_t	0.239	0.402	0.008	-0.524	-0.346	0.308	0.345
roughness_L3_t	0.695	0.435	0.76	0.124	-0.017	-0.099	-0.057
vci_L1_t	0.297	0.128	0.325	0.03	-0.041	-0.202	-0.184
vci_L2_t	0.266	0.487	0.189	-0.651	-0.649	0.238	0.281
vci_L3_t	0.828	0.587	0.905	0.079	-0.079	0.068	0.101
height_cv_t	0.289	-0.315	0.498	0.671	0.234	-0.698	-0.708

Chapter 2 Appendix A1 continued

	p_25_t	p_50_t	p_75_t	p_90_t	p_99_t	vci_2m_t	vci_5m_t
maxH_t	0.264	0.41	0.588	0.71	0.873	0.202	0.216
meanH_t	0.838	0.951	0.966	0.83	0.652	-0.022	0.185
stdH_t	0.173	0.412	0.732	0.946	0.896	0.146	0.153
skewH_t	-0.723	-0.791	-0.686	-0.36	0.017	-0.023	-0.246
kurH_t	-0.376	-0.529	-0.618	-0.501	-0.087	-0.09	-0.328
p_05_t	0.924	0.752	0.509	0.292	0.138	-0.343	-0.085
p_10_t	0.958	0.801	0.562	0.333	0.179	-0.314	-0.028
p_25_t	1	0.918	0.7	0.447	0.291	-0.19	0.113
p_50_t	0.918	1	0.886	0.631	0.449	-0.032	0.197
p_75_t	0.7	0.886	1	0.857	0.658	0.058	0.188
p_90_t	0.447	0.631	0.857	1	0.844	0.047	0.17
p_99_t	0.291	0.449	0.658	0.844	1	0.113	0.154
vci_2m_t	-0.19	-0.032	0.058	0.047	0.113	1	0.185
vci_5m_t	0.113	0.197	0.188	0.17	0.154	0.185	1
vci_10m_t	0.436	0.56	0.592	0.337	0.178	0.226	0.301
vci_15m_t	0.288	0.443	0.619	0.742	0.718	0.113	0.274
vci_20m_t	0.299	0.422	0.556	0.67	0.803	0.221	0.243
cov_t	0.527	0.557	0.439	0.233	0.205	0.576	0.423
canopy_shannon_t	0.542	0.76	0.923	0.898	0.787	0.169	0.366
canopy_roughness_t	0.302	0.464	0.499	0.43	0.448	0.548	0.397
tvolume_t	0.54	0.556	0.392	0.187	0.146	0.46	0.36
vlayer_L1_t	-0.156	-0.109	-0.133	-0.106	-0.094	0.13	0.134
vlayer_L2_t	0.416	0.386	0.19	-0.03	-0.033	0.487	0.357
vlayer_L3_t	0.703	0.763	0.683	0.52	0.425	0.289	0.247
meanH_L1_t	-0.092	0.073	0.207	0.19	0.238	0.625	0.03
meanH_L2_t	0.87	0.767	0.49	0.184	0.059	-0.127	0.312
meanH_L3_t	0.046	0.182	0.445	0.786	0.864	-0.002	0.074
sdH_L1_t	-0.116	0.014	0.177	0.206	0.27	0.573	-0.042
sdH_L2_t	0.411	0.647	0.692	0.462	0.312	0.363	0.359
sdH_L3_t	0.146	0.28	0.505	0.727	0.955	0.112	0.102
roughness_L1_t	-0.047	0.108	0.114	0.024	0.046	0.834	0.294
roughness_L2_t	0.462	0.511	0.368	0.126	0.071	0.432	0.412
roughness_L3_t	0.057	0.248	0.507	0.66	0.737	0.143	0.093
vci_L1_t	-0.096	0.054	0.214	0.231	0.282	0.608	-0.022
vci_L2_t	0.411	0.546	0.502	0.285	0.188	0.185	0.681
vci_L3_t	0.199	0.366	0.606	0.837	0.946	0.121	0.17
height_cv_t	-0.7	-0.564	-0.203	0.242	0.388	0.18	-0.083

Chapter 2 Appendix A1 continued

	vci_10m_t	vci_15m_t	vci_20m_t	cov_t	canopy_shannon_t	canopy_roughness_t
maxH_t	0.244	0.655	0.816	0.324	0.725	0.593
meanH_t	0.537	0.601	0.565	0.483	0.885	0.481
stdH_t	0.233	0.739	0.696	0.109	0.832	0.418
skewH_t	-0.738	-0.169	-0.056	-0.513	-0.538	-0.265
kurH_t	-0.738	-0.335	-0.105	-0.321	-0.617	-0.243
p_05_t	0.314	0.179	0.164	0.365	0.333	0.083
p_10_t	0.344	0.206	0.201	0.414	0.386	0.138
p_25_t	0.436	0.288	0.299	0.527	0.542	0.302
p_50_t	0.56	0.443	0.422	0.557	0.76	0.464
p_75_t	0.592	0.619	0.556	0.439	0.923	0.499
p_90_t	0.337	0.742	0.67	0.233	0.898	0.43
p_99_t	0.178	0.718	0.803	0.205	0.787	0.448
vci_2m_t	0.226	0.113	0.221	0.576	0.169	0.548
vci_5m_t	0.301	0.274	0.243	0.423	0.366	0.397
vci_10m_t	1	0.316	0.237	0.521	0.626	0.369
vci_15m_t	0.316	1	0.692	0.195	0.767	0.445
vci_20m_t	0.237	0.692	1	0.336	0.712	0.536
cov_t	0.521	0.195	0.336	1	0.448	0.631
canopy_shannon_t	0.626	0.767	0.712	0.448	1	0.578
canopy_roughness_t	0.369	0.445	0.536	0.631	0.578	1
tvolume_t	0.41	0.123	0.262	0.89	0.358	0.65
vlayer_L1_t	-0.025	-0.16	-0.143	-0.016	-0.095	0.155
vlayer_L2_t	0.407	-0.042	0.167	0.884	0.181	0.527
vlayer_L3_t	0.359	0.415	0.421	0.765	0.601	0.655
meanH_L1_t	0.176	0.252	0.298	0.32	0.265	0.307
meanH_L2_t	0.612	0.12	0.185	0.62	0.417	0.243
meanH_L3_t	-0.172	0.645	0.664	-0.103	0.561	0.255
sdH_L1_t	0.081	0.285	0.372	0.254	0.232	0.298
sdH_L2_t	0.863	0.439	0.377	0.491	0.736	0.505
sdH_L3_t	0.082	0.64	0.801	0.103	0.655	0.393
roughness_L1_t	0.273	0.067	0.195	0.634	0.188	0.632
roughness_L2_t	0.518	0.137	0.293	0.797	0.378	0.677
roughness_L3_t	0.032	0.611	0.626	0.022	0.588	0.438
vci_L1_t	0.113	0.306	0.38	0.283	0.27	0.336
vci_L2_t	0.805	0.365	0.314	0.518	0.627	0.463
vci_L3_t	0.105	0.824	0.84	0.114	0.758	0.441
height_cv_t	-0.363	0.283	0.237	-0.438	0.006	-0.044

Chapter 2 Appendix A1 continued

	tvolume_t	vlayer_L1_t	vlayer_L2_t	vlayer_L3_t	meanH_L1_t	meanH_L2_t
maxH_t	0.26	-0.08	0.128	0.446	0.23	0.109
meanH_t	0.456	-0.143	0.256	0.738	0.12	0.626
stdH_t	0.05	-0.073	-0.152	0.368	0.279	-0.083
skewH_t	-0.495	0.029	-0.427	-0.529	-0.038	-0.761
kurH_t	-0.262	0.014	-0.194	-0.326	-0.092	-0.441
p_05_t	0.387	-0.207	0.313	0.525	-0.207	0.82
p_10_t	0.43	-0.198	0.344	0.575	-0.192	0.844
p_25_t	0.54	-0.156	0.416	0.703	-0.092	0.87
p_50_t	0.556	-0.109	0.386	0.763	0.073	0.767
p_75_t	0.392	-0.133	0.19	0.683	0.207	0.49
p_90_t	0.187	-0.106	-0.03	0.52	0.19	0.184
p_99_t	0.146	-0.094	-0.033	0.425	0.238	0.059
vci_2m_t	0.46	0.13	0.487	0.289	0.625	-0.127
vci_5m_t	0.36	0.134	0.357	0.247	0.03	0.312
vci_10m_t	0.41	-0.025	0.407	0.359	0.176	0.612
vci_15m_t	0.123	-0.16	-0.042	0.415	0.252	0.12
vci_20m_t	0.262	-0.143	0.167	0.421	0.298	0.185
cov_t	0.89	-0.016	0.884	0.765	0.32	0.62
canopy_shannon_t	0.358	-0.095	0.181	0.601	0.265	0.417
canopy_roughness_t	0.65	0.155	0.527	0.655	0.307	0.243
tvolume_t	1	0.264	0.933	0.821	0.067	0.595
vlayer_L1_t	0.264	1	0.147	-0.051	-0.463	-0.072
vlayer_L2_t	0.933	0.147	1	0.623	0.13	0.594
vlayer_L3_t	0.821	-0.051	0.623	1	0.171	0.534
meanH_L1_t	0.067	-0.463	0.13	0.171	1	-0.137
meanH_L2_t	0.595	-0.072	0.594	0.534	-0.137	1
meanH_L3_t	-0.126	-0.063	-0.312	0.193	0.149	-0.26
sdH_L1_t	-0.016	-0.578	0.057	0.137	0.852	-0.213
sdH_L2_t	0.421	0.056	0.347	0.435	0.327	0.486
sdH_L3_t	0.042	-0.084	-0.104	0.284	0.224	-0.065
roughness_L1_t	0.624	0.292	0.642	0.37	0.495	0.059
roughness_L2_t	0.843	0.06	0.853	0.668	0.147	0.597
roughness_L3_t	-0.01	-0.099	-0.2	0.31	0.288	-0.206
vci_L1_t	0.017	-0.555	0.081	0.168	0.916	-0.191
vci_L2_t	0.423	0.08	0.422	0.321	0.095	0.647
vci_L3_t	0.048	-0.123	-0.136	0.362	0.266	-0.051
height_cv_t	-0.47	0.041	-0.507	-0.359	0.201	-0.821

Chapter 2 Appendix A1 continued

	meanH_L3_t	sdH_L1_t	sdH_L2_t	sdH_L3_t	roughness_L1_t	roughness_L2_t
maxH_t	0.692	0.295	0.332	0.863	0.139	0.239
meanH_t	0.43	0.094	0.622	0.493	0.059	0.402
stdH_t	0.874	0.304	0.397	0.829	0.065	0.008
skewH_t	0.242	0.077	-0.729	0.202	-0.171	-0.524
kurH_t	0.047	0.002	-0.723	0.1	-0.148	-0.346
p_05_t	-0.046	-0.212	0.187	0.026	-0.212	0.308
p_10_t	-0.022	-0.194	0.236	0.058	-0.18	0.345
p_25_t	0.046	-0.116	0.411	0.146	-0.047	0.462
p_50_t	0.182	0.014	0.647	0.28	0.108	0.511
p_75_t	0.445	0.177	0.692	0.505	0.114	0.368
p_90_t	0.786	0.206	0.462	0.727	0.024	0.126
p_99_t	0.864	0.27	0.312	0.955	0.046	0.071
vci_2m_t	-0.002	0.573	0.363	0.112	0.834	0.432
vci_5m_t	0.074	-0.042	0.359	0.102	0.294	0.412
vci_10m_t	-0.172	0.081	0.863	0.082	0.273	0.518
vci_15m_t	0.645	0.285	0.439	0.64	0.067	0.137
vci_20m_t	0.664	0.372	0.377	0.801	0.195	0.293
cov_t	-0.103	0.254	0.491	0.103	0.634	0.797
canopy_shannon_t	0.561	0.232	0.736	0.655	0.188	0.378
canopy_roughness_t	0.255	0.298	0.505	0.393	0.632	0.677
tvolume_t	-0.126	-0.016	0.421	0.042	0.624	0.843
vlayer_L1_t	-0.063	-0.578	0.056	-0.084	0.292	0.06
vlayer_L2_t	-0.312	0.057	0.347	-0.104	0.642	0.853
vlayer_L3_t	0.193	0.137	0.435	0.284	0.37	0.668
meanH_L1_t	0.149	0.852	0.327	0.224	0.495	0.147
meanH_L2_t	-0.26	-0.213	0.486	-0.065	0.059	0.597
meanH_L3_t	1	0.232	0.012	0.877	-0.103	-0.215
sdH_L1_t	0.232	1	0.2	0.292	0.329	0.115
sdH_L2_t	0.012	0.2	1	0.187	0.42	0.515
sdH_L3_t	0.877	0.292	0.187	1	0.02	-0.015
roughness_L1_t	-0.103	0.329	0.42	0.02	1	0.57
roughness_L2_t	-0.215	0.115	0.515	-0.015	0.57	1
roughness_L3_t	0.747	0.33	0.175	0.756	0.052	-0.021
vci_L1_t	0.232	0.987	0.254	0.29	0.398	0.142
vci_L2_t	-0.098	-0.016	0.815	0.089	0.307	0.579
vci_L3_t	0.92	0.333	0.269	0.939	0.029	0.01
height_cv_t	0.636	0.274	-0.249	0.485	-0.031	-0.482

Chapter 2 Appendix A1 continued

	roughness_L3_t	vci_L1_t	vci_L2_t	vci_L3_t	height_cv_t
maxH_t	0.695	0.297	0.266	0.828	0.289
meanH_t	0.435	0.128	0.487	0.587	-0.315
stdH_t	0.76	0.325	0.189	0.905	0.498
skewH_t	0.124	0.03	-0.651	0.079	0.671
kurH_t	-0.017	-0.041	-0.649	-0.079	0.234
p_05_t	-0.099	-0.202	0.238	0.068	-0.698
p_10_t	-0.057	-0.184	0.281	0.101	-0.708
p_25_t	0.057	-0.096	0.411	0.199	-0.7
p_50_t	0.248	0.054	0.546	0.366	-0.564
p_75_t	0.507	0.214	0.502	0.606	-0.203
p_90_t	0.66	0.231	0.285	0.837	0.242
p_99_t	0.737	0.282	0.188	0.946	0.388
vci_2m_t	0.143	0.608	0.185	0.121	0.18
vci_5m_t	0.093	-0.022	0.681	0.17	-0.083
vci_10m_t	0.032	0.113	0.805	0.105	-0.363
vci_15m_t	0.611	0.306	0.365	0.824	0.283
vci_20m_t	0.626	0.38	0.314	0.84	0.237
cov_t	0.022	0.283	0.518	0.114	-0.438
canopy_shannon_t	0.588	0.27	0.627	0.758	0.006
canopy_roughness_t	0.438	0.336	0.463	0.441	-0.044
tvolume_t	-0.01	0.017	0.423	0.048	-0.47
vlayer_L1_t	-0.099	-0.555	0.08	-0.123	0.041
vlayer_L2_t	-0.2	0.081	0.422	-0.136	-0.507
vlayer_L3_t	0.31	0.168	0.321	0.362	-0.359
meanH_L1_t	0.288	0.916	0.095	0.266	0.201
meanH_L2_t	-0.206	-0.191	0.647	-0.051	-0.821
meanH_L3_t	0.747	0.232	-0.098	0.92	0.636
sdH_L1_t	0.33	0.987	-0.016	0.333	0.274
sdH_L2_t	0.175	0.254	0.815	0.269	-0.249
sdH_L3_t	0.756	0.29	0.089	0.939	0.485
roughness_L1_t	0.052	0.398	0.307	0.029	-0.031
roughness_L2_t	-0.021	0.142	0.579	0.01	-0.482
roughness_L3_t	1	0.345	0.031	0.802	0.451
vci_L1_t	0.345	1	0.024	0.342	0.258
vci_L2_t	0.031	0.024	1	0.156	-0.384
vci_L3_t	0.802	0.342	0.156	1	0.488
height_cv_t	0.451	0.258	-0.384	0.488	1

Chapter 2 Appendix A2. Pearson correlation matrix of ULS variables

	maxH_u	meanH_u	stdH_u	skewH_u	kurH_u	p_05_u	p_10_u
maxH_u	1	0.632	0.771	-0.005	-0.101	0.143	0.175
meanH_u	0.632	1	0.573	-0.68	-0.418	0.602	0.676
stdH_u	0.771	0.573	1	-0.01	-0.376	-0.163	-0.105
skewH_u	-0.005	-0.68	-0.01	1	0.637	-0.568	-0.625
kurH_u	-0.101	-0.418	-0.376	0.637	1	-0.012	-0.04
p_05_u	0.143	0.602	-0.163	-0.568	-0.012	1	0.983
p_10_u	0.175	0.676	-0.105	-0.625	-0.04	0.983	1
p_25_u	0.28	0.82	0.037	-0.736	-0.151	0.889	0.942
p_50_u	0.479	0.957	0.356	-0.791	-0.389	0.652	0.726
p_75_u	0.666	0.945	0.715	-0.626	-0.53	0.376	0.453
p_90_u	0.749	0.805	0.925	-0.292	-0.468	0.18	0.245
p_99_u	0.952	0.65	0.85	0.042	-0.09	0.117	0.158
vci_2m_u	0.333	0.015	0.238	0.125	0.01	-0.262	-0.243
vci_5m_u	0.238	0.053	0.181	-0.003	-0.315	-0.215	-0.21
vci_10m_u	0.276	0.412	0.177	-0.544	-0.662	0.159	0.182
vci_15m_u	0.609	0.606	0.65	-0.325	-0.593	0.142	0.185
vci_20m_u	0.811	0.615	0.691	-0.135	-0.218	0.172	0.212
cov_u	0.393	0.327	0.077	-0.225	-0.081	0.277	0.263
canopy_shannon_u	0.806	0.789	0.829	-0.365	-0.583	0.124	0.183
canopy_roughness_u	0.608	0.557	0.395	-0.288	-0.256	0.209	0.24
tvolume_u	0.294	0.366	0.009	-0.371	-0.146	0.29	0.299
vlayer_L1_u	0.18	0.197	0.021	-0.3	-0.146	0.017	0.034
vlayer_L2_u	0.14	0.109	-0.18	-0.224	-0.055	0.2	0.175
vlayer_L3_u	0.454	0.665	0.239	-0.471	-0.211	0.468	0.512
meanH_L1_u	0.219	-0.11	0.445	0.274	-0.121	-0.566	-0.507
meanH_L2_u	0.077	0.417	-0.31	-0.576	-0.211	0.762	0.733
meanH_L3_u	0.701	0.527	0.927	0.108	-0.164	-0.057	-0.003
sdH_L1_u	0.255	-0.007	0.468	0.187	-0.213	-0.487	-0.414
sdH_L2_u	0.239	0.539	0.244	-0.699	-0.57	0.089	0.181
sdH_L3_u	0.897	0.549	0.859	0.15	-0.052	0.003	0.043
roughness_L1_u	0.22	-0.022	0.436	0.113	-0.279	-0.548	-0.482
roughness_L2_u	0.176	0.359	-0.037	-0.465	-0.364	0.27	0.314
roughness_L3_u	0.638	0.48	0.827	0.113	-0.176	-0.095	-0.029
vci_L1_u	0.262	-0.03	0.478	0.214	-0.2	-0.51	-0.443
vci_L2_u	0.328	0.341	0.297	-0.377	-0.661	-0.096	-0.059
vci_L3_u	0.866	0.668	0.926	-0.037	-0.282	0.041	0.099
height_cv_u	0.214	-0.365	0.537	0.693	0.05	-0.759	-0.761

Chapter 2 Appendix A2 continued

p_25_u	p_50_u	p_75_u	p_90_u	p_99_u	vci_2m_u	vci_5m_u	vci_10m_u	vci_15m_u
0.28	0.479	0.666	0.749	0.952	0.333	0.238	0.276	0.609
0.82	0.957	0.945	0.805	0.65	0.015	0.053	0.412	0.606
0.037	0.356	0.715	0.925	0.85	0.238	0.181	0.177	0.65
-0.736	-0.791	-0.626	-0.292	0.042	0.125	-0.003	-0.544	-0.325
-0.151	-0.389	-0.53	-0.468	-0.09	0.01	-0.315	-0.662	-0.593
0.889	0.652	0.376	0.18	0.117	-0.262	-0.215	0.159	0.142
0.942	0.726	0.453	0.245	0.158	-0.243	-0.21	0.182	0.185
1	0.884	0.619	0.378	0.268	-0.172	-0.104	0.282	0.284
0.884	1	0.871	0.62	0.47	-0.012	0.049	0.451	0.483
0.619	0.871	1	0.861	0.68	0.094	0.097	0.471	0.671
0.378	0.62	0.861	1	0.823	0.109	0.122	0.244	0.698
0.268	0.47	0.68	0.823	1	0.294	0.202	0.22	0.617
-0.172	-0.012	0.094	0.109	0.294	1	0.19	0.149	0.198
-0.104	0.049	0.097	0.122	0.202	0.19	1	0.298	0.223
0.282	0.451	0.471	0.244	0.22	0.149	0.298	1	0.608
0.284	0.483	0.671	0.698	0.617	0.198	0.223	0.608	1
0.311	0.48	0.622	0.715	0.795	0.255	0.237	0.269	0.629
0.312	0.364	0.288	0.139	0.313	0.637	0.38	0.308	0.262
0.359	0.668	0.871	0.872	0.821	0.251	0.351	0.58	0.807
0.381	0.538	0.557	0.457	0.514	0.292	0.289	0.398	0.507
0.392	0.447	0.307	0.105	0.207	0.321	0.371	0.293	0.238
0.161	0.288	0.198	0.022	0.104	0.334	0.241	0.253	0.141
0.212	0.204	0.052	-0.127	0.044	0.329	0.382	0.266	0.066
0.624	0.694	0.59	0.414	0.405	0.189	0.305	0.248	0.431
-0.445	-0.237	0.082	0.234	0.255	0.536	-0.016	0.084	0.247
0.699	0.537	0.221	-0.026	-0.003	-0.133	0.238	0.427	0.101
0.092	0.295	0.589	0.887	0.815	0.103	0.074	-0.077	0.508
-0.339	-0.135	0.172	0.3	0.288	0.375	0.124	0.152	0.337
0.397	0.616	0.579	0.323	0.211	0.22	0.115	0.739	0.489
0.141	0.352	0.612	0.787	0.961	0.281	0.195	0.207	0.586
-0.366	-0.117	0.178	0.25	0.241	0.315	0.179	0.204	0.31
0.412	0.444	0.291	0.098	0.129	0.134	0.37	0.53	0.318
0.075	0.281	0.543	0.789	0.743	0.122	0.069	0.01	0.488
-0.374	-0.163	0.157	0.297	0.291	0.455	0.107	0.137	0.33
0.115	0.368	0.405	0.298	0.291	0.205	0.574	0.778	0.535
0.225	0.468	0.736	0.906	0.929	0.243	0.199	0.274	0.762
-0.754	-0.574	-0.175	0.229	0.297	0.227	0.087	-0.255	0.145

Chapter 2 Appendix A2 continued

vci_20m_u	cov_u	canopy_shannon_u	canopy_roughness_u	tvolume_u	vlayer_L1_u	vlayer_L2_u
0.811	0.393	0.806	0.608	0.294	0.18	0.14
0.615	0.327	0.789	0.557	0.366	0.197	0.109
0.691	0.077	0.829	0.395	0.009	0.021	-0.18
-0.135	-0.225	-0.365	-0.288	-0.371	-0.3	-0.224
-0.218	-0.081	-0.583	-0.256	-0.146	-0.146	-0.055
0.172	0.277	0.124	0.209	0.29	0.017	0.2
0.212	0.263	0.183	0.24	0.299	0.034	0.175
0.311	0.312	0.359	0.381	0.392	0.161	0.212
0.48	0.364	0.668	0.538	0.447	0.288	0.204
0.622	0.288	0.871	0.557	0.307	0.198	0.052
0.715	0.139	0.872	0.457	0.105	0.022	-0.127
0.795	0.313	0.821	0.514	0.207	0.104	0.044
0.255	0.637	0.251	0.292	0.321	0.334	0.329
0.237	0.38	0.351	0.289	0.371	0.241	0.382
0.269	0.308	0.58	0.398	0.293	0.253	0.266
0.629	0.262	0.807	0.507	0.238	0.141	0.066
1	0.316	0.768	0.529	0.322	0.239	0.179
0.316	1	0.333	0.5	0.792	0.514	0.779
0.768	0.333	1	0.612	0.303	0.216	0.105
0.529	0.5	0.612	1	0.521	0.448	0.339
0.322	0.792	0.303	0.521	1	0.815	0.925
0.239	0.514	0.216	0.448	0.815	1	0.698
0.179	0.779	0.105	0.339	0.925	0.698	1
0.439	0.695	0.501	0.612	0.852	0.563	0.637
0.132	-0.002	0.234	-0.077	-0.202	-0.089	-0.184
0.146	0.435	0.171	0.228	0.47	0.218	0.477
0.646	-0.041	0.667	0.293	-0.109	-0.116	-0.294
0.224	-0.029	0.333	-0.002	-0.134	-0.159	-0.116
0.336	0.254	0.556	0.386	0.368	0.452	0.247
0.773	0.217	0.782	0.435	0.104	0.042	-0.037
0.231	-0.043	0.339	0.018	0.044	0.159	0.039
0.249	0.397	0.38	0.306	0.49	0.281	0.475
0.598	-0.07	0.666	0.299	-0.146	-0.17	-0.325
0.223	0.008	0.321	0	-0.143	-0.14	-0.125
0.354	0.274	0.657	0.437	0.288	0.285	0.252
0.839	0.196	0.882	0.517	0.134	0.072	-0.065
0.158	-0.275	0.093	-0.126	-0.379	-0.195	-0.349

Chapter 2 Appendix A2 continued

vlayer_L3_u	meanH_L1_u	meanH_L2_u	meanH_L3_u	sdH_L1_u	sdH_L2_u	sdH_L3_u	roughness_L1_u
0.454	0.219	0.077	0.701	0.255	0.239	0.897	0.22
0.665	-0.11	0.417	0.527	-0.007	0.539	0.549	-0.022
0.239	0.445	-0.31	0.927	0.468	0.244	0.859	0.436
-0.471	0.274	-0.576	0.108	0.187	-0.699	0.15	0.113
-0.211	-0.121	-0.211	-0.164	-0.213	-0.57	-0.052	-0.279
0.468	-0.566	0.762	-0.057	-0.487	0.089	0.003	-0.548
0.512	-0.507	0.733	-0.003	-0.414	0.181	0.043	-0.482
0.624	-0.445	0.699	0.092	-0.339	0.397	0.141	-0.366
0.694	-0.237	0.537	0.295	-0.135	0.616	0.352	-0.117
0.59	0.082	0.221	0.589	0.172	0.579	0.612	0.178
0.414	0.234	-0.026	0.887	0.3	0.323	0.787	0.25
0.405	0.255	-0.003	0.815	0.288	0.211	0.961	0.241
0.189	0.536	-0.133	0.103	0.375	0.22	0.281	0.315
0.305	-0.016	0.238	0.074	0.124	0.115	0.195	0.179
0.248	0.084	0.427	-0.077	0.152	0.739	0.207	0.204
0.431	0.247	0.101	0.508	0.337	0.489	0.586	0.31
0.439	0.132	0.146	0.646	0.224	0.336	0.773	0.231
0.695	-0.002	0.435	-0.041	-0.029	0.254	0.217	-0.043
0.501	0.234	0.171	0.667	0.333	0.556	0.782	0.339
0.612	-0.077	0.228	0.293	-0.002	0.386	0.435	0.018
0.852	-0.202	0.47	-0.109	-0.134	0.368	0.104	0.044
0.563	-0.089	0.218	-0.116	-0.159	0.452	0.042	0.159
0.637	-0.184	0.477	-0.294	-0.116	0.247	-0.037	0.039
1	-0.221	0.446	0.17	-0.093	0.341	0.285	-0.034
-0.221	1	-0.558	0.341	0.904	0.125	0.343	0.804
0.446	-0.558	1	-0.329	-0.442	0.241	-0.109	-0.419
0.17	0.341	-0.329	1	0.363	0.029	0.828	0.28
-0.093	0.904	-0.442	0.363	1	0.168	0.376	0.873
0.341	0.125	0.241	0.029	0.168	1	0.171	0.265
0.285	0.343	-0.109	0.828	0.376	0.171	1	0.314
-0.034	0.804	-0.419	0.28	0.873	0.265	0.314	1
0.461	-0.097	0.583	-0.182	0.047	0.502	0.044	0.128
0.149	0.36	-0.283	0.855	0.405	0.08	0.75	0.298
-0.116	0.945	-0.475	0.37	0.99	0.15	0.381	0.86
0.233	0.13	0.328	0.099	0.234	0.664	0.267	0.295
0.379	0.334	-0.107	0.883	0.401	0.291	0.935	0.354
-0.393	0.608	-0.818	0.536	0.522	-0.277	0.409	0.489

Chapter 2 Appendix A2 continued

roughness_L2_u	roughness_L3_u	vci_L1_u	vci_L2_u	vci_L3_u	height_cv_u
0.176	0.638	0.262	0.328	0.866	0.214
0.359	0.48	-0.03	0.341	0.668	-0.365
-0.037	0.827	0.478	0.297	0.926	0.537
-0.465	0.113	0.214	-0.377	-0.037	0.693
-0.364	-0.176	-0.2	-0.661	-0.282	0.05
0.27	-0.095	-0.51	-0.096	0.041	-0.759
0.314	-0.029	-0.443	-0.059	0.099	-0.761
0.412	0.075	-0.374	0.115	0.225	-0.754
0.444	0.281	-0.163	0.368	0.468	-0.574
0.291	0.543	0.157	0.405	0.736	-0.175
0.098	0.789	0.297	0.298	0.906	0.229
0.129	0.743	0.291	0.291	0.929	0.297
0.134	0.122	0.455	0.205	0.243	0.227
0.37	0.069	0.107	0.574	0.199	0.087
0.53	0.01	0.137	0.778	0.274	-0.255
0.318	0.488	0.33	0.535	0.762	0.145
0.249	0.598	0.223	0.354	0.839	0.158
0.397	-0.07	0.008	0.274	0.196	-0.275
0.38	0.666	0.321	0.657	0.882	0.093
0.306	0.299	0	0.437	0.517	-0.126
0.49	-0.146	-0.143	0.288	0.134	-0.379
0.281	-0.17	-0.14	0.285	0.072	-0.195
0.475	-0.325	-0.125	0.252	-0.065	-0.349
0.461	0.149	-0.116	0.233	0.379	-0.393
-0.097	0.36	0.945	0.13	0.334	0.608
0.583	-0.283	-0.475	0.328	-0.107	-0.818
-0.182	0.855	0.37	0.099	0.883	0.536
0.047	0.405	0.99	0.234	0.401	0.522
0.502	0.08	0.15	0.664	0.291	-0.277
0.044	0.75	0.381	0.267	0.935	0.409
0.128	0.298	0.86	0.295	0.354	0.489
1	0.025	0	0.579	0.101	-0.446
0.025	1	0.403	0.185	0.817	0.461
0	0.403	1	0.209	0.401	0.558
0.579	0.185	0.209	1	0.355	-0.086
0.101	0.817	0.401	0.355	1	0.38
-0.446	0.461	0.558	-0.086	0.38	1

Chapter 2 Appendix A3. Linear mixed effects model of bird abundance (Abundance), species richness (SR), bird Shannon diversity index (Bird_shannon), functional richness (FRic), functional evenness (FEve), functional divergence (FDiv), functional dispersion (FDis), Rao's quadratic entropy (RaoQ) in relation to vegetation structural metrics – PCA1, PCA2, PCA3, PCA4 calculated from all the LiDAR variables

Explanatory Varibles	Response variables							
	Abundance		SR		Bird_shannon		FEve	
	TLS	ULS	TLS	ULS	TLS	ULS	TLS	ULS
PCA1	-6.085	-8.385*	-0.942	-1.385**	-0.06	-0.085**	-0.003	0.001
	(4.251)	(4.076)	(0.535)	(0.502)	(0.032)	(0.029)	(0.007)	(0.007)
PCA2	5.469	1.414	0.442	-0.316	0.033	0.003	-0.004	-0.001
	(4.882)	(4.923)	(0.638)	(0.657)	(0.038)	(0.038)	(0.008)	(0.008)
PCA3	5.917	7.530	0.719	-0.465	0.008	-0.054	-0.014	-0.013
	(4.414)	(4.512)	(0.561)	(0.578)	(0.033)	(0.033)	(0.007)	(0.007)
PCA4	-2.241	-0.640	-0.332	0.894	-0.015	0.063*	0.002	
	(3.695)	(3.938)	(0.451)	(0.491)	(0.027)	(0.028)	(0.007)	
Intercept	126.864***	126.935***	22.142***	22.111***	2.629***	2.627***	0.672***	0.6715146
	(6.777)	(6.424)	(1.091)	(1.057)	(0.065)	(0.064)	(0.008)	0.008
Log Likelihood	-457.502	-457.036	-273.980	-273.001	-22.814	-19.436	103.288	103.964
Akaike Inf. Crit.	929.004	928.073	561.959	560.001	59.628	52.872	-192.576	-193.928
Bayesian Inf. Crit.	946.807	945.876	579.762	577.804	77.431	70.675	-174.773	-176.125
Marginal R2	0.057	0.071	0.043	0.078	0.036	0.100	0.044	0.039
Conditional R2	0.516	0.485	0.681	0.679	0.677	0.710	0.173	0.153

Note: *p < 0.05, **p < 0.01, ***p < 0.001

Explanatory Varibles	FDiv		FDis		RaoQ	
	TLS	ULS	TLS	ULS	TLS	ULS
PCA1	0.002	-0.001	0.000	-0.002	0.000	-0.001
	(0.004)	(0.004)	(0.002)	(0.002)	(0.001)	(0.001)
PCA2	0.005	0.006	0.005	0.005	0.002	0.002
	(0.004)	(0.004)	(0.003)	(0.003)	(0.001)	(0.001)
PCA3	0.006	0.004	0.001	-0.002	0.001	-0.001
	(0.004)	(0.004)	(0.002)	(0.002)	(0.001)	(0.001)
PCA4		-0.003	0.000	0.000	0.000	0.000
		(0.004)	(0.002)	(0.002)	(0.001)	(0.001)
Intercept	0.874***	0.874***	0.242***	0.242***	0.065***	0.065***
	(0.004)	(0.004)	(0.003)	(0.003)	(0.001)	(0.001)
Log Likelihood	166.213	161.460	208.105	208.639	276.918	277.400
Akaike Inf. Crit.	-320.427	-308.920	-402.211	-403.278	-539.836	-540.801
Bayesian Inf. Crit.	-305.167	-291.117	-384.408	-385.475	-522.033	-522.998
Marginal R2	0.050	0.048	0.049	0.062	0.047	0.061
Conditional R2	0.067	0.073	0.274	0.306	0.293	0.364

Chapter 2 Appendix A4. Linear mixed effects model of bird abundance (Abundance), species richness (SR), bird diversity index (Bird_shannon), functional richness (FRic), functional evennes (FEve), functional divergence (FDiv), functional dispersion (FDis), Rao's quadratic entropy (RaoQ) in relation to vegetation structural metrics.

Explanatory variables	**Response variables**					
	Abundance		SR		Bird_shannon	
	TLS	ULS	TLS	ULS	TLS	ULS
maxH	2.240 (8.549)	4.623 (9.801)	0.542 (0.985)	0.836 (1.120)	0.053 (0.057)	0.043 (0.064)
meanH	-15.029 (22.545)	-24.253 (23.796)	**7.733**** (2.596)	5.031 (2.714)	**0.414**** (0.150)	**0.333*** (0.156)
skewH	-11.727 (14.444)	-8.657 (11.348)	**3.969*** (1.665)	2.366 (1.281)	**0.205*** (0.096)	0.143 (0.073)
vci_2m	2.729 (8.689)	-3.565 (4.833)	-1.089 (1.008)	-0.476 (0.548)	-0.101 (0.058)	-0.025 (0.031)
vci_5m	-2.202 (6.710)	-2.314 (5.545)	0.960 (0.778)	-0.457 (0.650)	0.062 (0.045)	0.029 (0.037)
vci_15m	8.823 (6.738)	8.734 (7.040)	-0.896 (0.781)	-0.317 (0.819)	-0.086 (0.045)	-0.029 (0.047)
canopy_roughness	-8.506 (7.779)	2.341 (6.393)	-1.467 (0.917)	-0.827 (0.788)	**-0.123*** (0.053)	-0.062 (0.045)
tvolume	10.178 (9.706)	3.584 (6.278)	1.899 (1.152)	**1.672*** (0.765)	**0.157*** (0.066)	**0.092*** (0.044)
meanH_L3	20.177 (16.514)	28.138 (17.502)	**-5.966**** (1.905)	-3.749 (2.041)	**-0.354**** (0.110)	**-0.252*** (0.117)
vci_L1	-2.318 (6.533)	10.831 (6.295)	0.165 (0.762)	0.720 (0.786)	0.053 (0.044)	0.051 (0.045)
vci_L2	-6.992 (9.407)	-10.257 (7.134)	-0.070 (1.099)	0.440 (0.860)	0.034 (0.063)	0.013 (0.049)
height_cv	-7.699 (13.531)	-24.2 (16.528)	**4.761**** (1.564)	2.776 (1.957)	**0.334***** (0.090)	0.195 (0.112)
Intercept	126.918*** (7.206)	126.949*** (6.161)	22.072*** (0.988)	22.088*** (1.102)	2.625*** (0.055)	2.626*** (0.065)
Log Likelihood	-430.240	-430.281	-257.983	-261.017	-26.362	-30.058
Akaike Inf. Crit.	890.480	890.561	545.966	552.035	82.724	90.117
Bayesian Inf. Crit.	928.630	928.711	584.116	590.184	120.874	128.266
Marginal R2	0.097	0.164	0.139	0.141	0.171	0.161
Conditional R2	0.576	0.502	0.690	0.737	0.684	0.757

Note: *p < 0.05, **p < 0.01, ***p < 0.001

Chapter 2 Appendix A4 continued

Explanatory variables	Response variables							
	FEve		FDiv		FDis		RaoQ	
	TLS	ULS	TLS	ULS	TLS	ULS	TLS	ULS
maxH	0.016 (0.016)	0.019 (0.018)	0.006 (0.008)	0.009 (0.009)	-0.001 (0.005)	0.002 (0.005)	-0.001 (0.002)	-0.001 (0.002)
meanH	-0.042 (0.042)	-0.020 (0.044)	-0.028 (0.021)	-0.036 (0.022)	0.006 (0.013)	-0.010 (0.013)	0.006 (0.006)	-0.001 (0.006)
skewH	-0.04 (0.027)	-0.035 (0.021)	-0.023 (0.014)	-0.012 (0.011)	0.002 (0.008)	0.003 (0.006)	0.003 (0.004)	0.003 (0.003)
vci_2m	-0.021 (0.016)	0.013 (0.009)	-0.009 (0.008)	-0.002 (0.005)	**-0.010*** (0.005)	-0.004 (0.003)	**-0.005*** (0.002)	-0.002 (0.001)
vci_5m	-0.023 (0.012)	0.004 (0.010)	-0.005 (0.006)	-0.009 (0.005)	0.001 (0.004)	0.001 (0.003)	0.001 (0.002)	0.0005 (0.001)
vci_15m	**-0.026*** (0.012)	-0.019 (0.013)	**-0.016**** (0.006)	**-0.013*** (0.006)	**-0.009*** (0.004)	-0.003 (0.004)	**-0.004*** (0.002)	-0.001 (0.002)
canopy_roughness	0.007 (0.013)	0.004 (0.011)	**0.018**** (0.007)	0.005 (0.005)	0.005 (0.004)	0.001 (0.003)	0.002 (0.002)	0.001 (0.002)
tvolume	0.028 (0.017)	0.007 (0.011)	-0.011 (0.008)	-0.003 (0.005)	-0.00002 (0.005)	0.002 (0.003)	0.0005 (0.002)	0.001 (0.002)
meanH_L3	0.013 (0.031)	-0.007 (0.031)	0.026 (0.016)	**0.034*** (0.016)	-0.003 (0.009)	0.013 (0.010)	-0.004 (0.004)	0.004 (0.004)
vci_L1	0.014 (0.012)	-0.010 (0.011)	-0.001 (0.006)	0.007 (0.005)	0.005 (0.004)	**0.010**** (0.003)	0.002 (0.002)	**0.005**** (0.002)
vci_L2	0.017 (0.017)	-0.008 (0.012)	0.005 (0.008)	0.010 (0.006)	0.005 (0.005)	0.004 (0.004)	0.002 (0.002)	0.002 (0.002)
height_cv	0.028 (0.025)	0.026 (0.029)	-0.004 (0.013)	-0.023 (0.015)	0.012 (0.008)	-0.013 (0.009)	**0.008*** (0.004)	-0.004 (0.004)
Intercept	0.671*** (0.009)	0.671*** (0.008)	0.874*** (0.004)	0.874*** (0.004)	0.242*** (0.003)	0.242*** (0.003)	0.065*** (0.001)	0.065*** (0.001)
Log Likelihood	83.110	80.863	138.186	136.399	178.161	178.534	241.139	240.941
Akaike Inf. Crit.	-136.220	-131.727	-246.373	-242.798	-326.323	-327.067	-452.278	-451.883
Bayesian Inf. Crit.	-98.071	-93.577	-208.223	-204.648	-288.173	-288.918	-414.129	-413.733
Marginal R2	0.158	0.137	0.207	0.187	0.149	0.181	0.153	0.171
Conditional R2	0.315	0.228	0.347	0.271	0.358	0.347	0.388	0.436

Chapter 2 Appendix A5. Model summary of the relationship between LiDAR derived vegetation structural metrics (independent variables) and bird abundance by guilds (dependent variables).

Dependent variables	Independent variables					
	GS.HC		WB.HC		WG.HC	
	TLS	ULS	TLS	ULS	TLS	ULS
maxH	-0.355	**-0.619****	**-1.097***	0.102	**0.143****	**0.189****
	(0.208)	(0.231)	(0.524)	(0.507)	(0.055)	(0.059)
meanH	0.527	0.815	**4.053***	-0.781	**-0.386****	-0.218
	(0.502)	(0.524)	(1.711)	(1.479)	(0.138)	(0.142)
skewH	0.249	0.413	**2.719***	1.057	**-0.210***	-0.098
	(0.325)	(0.245)	(1.082)	(0.722)	(0.090)	(0.065)
vci_2m	0.073	-0.003	0.083	-0.582	-0.061	**-0.099****
	(0.218)	(0.099)	(0.445)	(0.329)	(0.057)	(0.034)
vci_5m	0.015	0.049	**1.523****	**1.704****	**-0.115****	**-0.198*****
	(0.135)	(0.110)	(0.550)	(0.599)	(0.039)	(0.030)
vci_15m	-0.008	-0.070	0.849	**1.801****	0.022	**-0.124***
	(0.178)	(0.182)	(0.472)	(0.562)	(0.049)	(0.049)
canopy_roughness	**0.501****	**0.476****	0.120	0.191	-0.08	**-0.106***
	(0.160)	(0.146)	(0.381)	(0.328)	(0.054)	(0.046)
tvolume	-0.439	-0.274	-0.019	0.401	-0.113	0.037
	(0.287)	(0.156)	(0.596)	(0.348)	(0.073)	(0.049)
meanH_L3	-0.231	-0.277	**-3.019***	0.396	**0.292****	0.201
	(0.367)	(0.390)	(1.264)	(1.237)	(0.102)	(0.107)
vci_L1	0.103	0.169	-0.264	**0.724***	0.032	**0.256*****
	(0.169)	(0.156)	(0.292)	(0.299)	(0.047)	(0.050)
vci_L2	-0.112	-0.010	-0.212	-0.411	-0.037	0.054
	(0.220)	(0.169)	(0.679)	(0.491)	(0.063)	(0.046)
height_cv	0.274	0.324	1.740	-1.622	-0.102	-0.014
	(0.321)	(0.377)	(0.906)	(1.187)	(0.093)	(0.111)
Intercept	**0.484***	**0.463***	**-1.986****	**-2.322*****	**3.238*****	**3.229*****
	-0.19	-0.207	-0.618	-0.686	-0.103	-0.099
Log Likelihood	-182.568	-182.448	-101.284	-96.176	-397.457	-373.766
Akaike Inf. Crit.	393.135	392.896	230.567	220.351	822.914	775.531
Bayesian Inf. Crit.	428.741	428.502	266.173	255.957	858.52	811.137
Marginal R2	0.238	0.150	0.399	0.408	0.249	0.370
Conditional R2	0.488	0.552	0.649	0.597	0.711	0.756

Note: *p < 0.05, **p < 0.01, ***p < 0.001

Chapter 2 Appendix A5 continued

Dependent variables	Independent variables					
	WS.HC		Arb.Nest		Grnd.Nest	
	TLS	ULS	TLS	ULS	TLS	ULS
maxH	-0.011	-0.009	**-0.109****	**-0.203*****	**-4.057****	**-2.918****
	(0.033)	(0.035)	(0.039)	(0.042)	(1.489)	(1.193)
meanH	-0.041	-0.014	**0.320****	**0.277****	**4.365**	**4.090****
	(0.082)	(0.087)	(0.099)	(0.103)	(2.700)	(2.065)
skewH	-0.046	-0.050	**0.180****	**0.164*****	**4.509***	**2.635****
	(0.052)	(0.040)	(0.062)	(0.048)	(2.085)	(1.103)
vci_2m	**0.096****	0.011	**0.125****	0.006	-0.311	-0.599
	(0.032)	(0.017)	(0.039)	(0.020)	(0.598)	(0.563)
vci_5m	0.017	0.020	0.060	0.009	-0.745	-0.725
	(0.026)	(0.021)	(0.034)	(0.028)	(0.474)	(0.472)
vci_15m	**0.092*****	**0.069****	-0.027	-0.015	0.358	-0.090
	(0.028)	(0.028)	(0.033)	(0.032)	(0.506)	(0.521)
canopy_roughness	**-0.128*****	-0.03	**-0.075***	0.046	-0.513	0.278
	(0.031)	(0.026)	(0.035)	(0.030)	(0.693)	(0.456)
tvolume	**0.108****	0.030	**0.120***	**0.088****	**2.007***	1.107
	(0.040)	(0.025)	(0.047)	(0.029)	(0.796)	(0.626)
meanH_L3	0.114	0.091	-0.107	-0.016	-0.562	-0.886
	(0.064)	(0.069)	(0.078)	(0.081)	(1.066)	(1.202)
vci_L1	**-0.073****	0.025	**-0.063***	0.009	0.159	-0.088
	(0.024)	(0.027)	(0.029)	(0.032)	(0.322)	(0.471)
vci_L2	-0.040	-0.056	-0.061	-0.007	**1.891***	1.084
	(0.038)	(0.029)	(0.045)	(0.035)	(0.936)	(0.630)
height_cv	-0.049	-0.014	**0.150***	0.120	1.555	1.977
	(0.057)	(0.067)	(0.069)	(0.079)	(0.992)	(1.245)
Intercept	**4.488*****	**4.493*****	**4.120*****	**4.126*****	**-3.299*****	**-3.016*****
	-0.062	-0.062	-0.071	-0.074	-0.943	-0.865
Log Likelihood	-526.675	-551.886	-496.938	-517.229	-56.296	-59.607
Akaike Inf. Crit.	1 081.349	1 131.772	1 021.876	1 062.459	140.592	147.215
Bayesian Inf. Crit.	1 116.956	1 167.379	1 057.482	1 098.065	176.198	182.821
Marginal R2	0.203	0.194	0.216	0.179	0.338	0.355
Conditional R2	0.598	0.508	0.592	0.534	0.566	0.443

Chapter 2 Appendix A5 continued

Dependent variables	Independent variables					
	Hol.Nest		Opp.Nest		Usty.Nest	
	TLS	ULS	TLS	ULS	TLS	ULS
maxH	**0.211*****	**0.323*****	0.173	0.090	-0.072	-0.239
	(0.046)	(0.048)	(0.109)	(0.116)	(0.194)	(0.199)
meanH	**-0.605*****	**-0.583*****	0.027	0.571	**-1.514****	-0.390
	(0.114)	(0.119)	(0.274)	(0.292)	(0.502)	(0.461)
skewH	**-0.375*****	**-0.319*****	0.011	0.173	**-1.095*****	-0.091
	(0.072)	(0.054)	(0.172)	(0.145)	(0.318)	(0.246)
vci_2m	-0.015	-0.048	0.003	0.077	-0.168	-0.242
	(0.044)	(0.025)	(0.111)	(0.081)	(0.219)	(0.141)
vci_5m	**-0.082****	**-0.073****	0.019	0.078	-0.126	**-0.371****
	(0.030)	(0.024)	(0.093)	(0.080)	(0.168)	(0.119)
vci_15m	**0.223*****	**0.118****	0.012	-0.041	**0.729*****	**0.407***
	(0.042)	(0.041)	(0.097)	(0.099)	(0.205)	(0.191)
canopy_roughness	**-0.154*****	**-0.115****	**-0.316****	**-0.295****	-0.047	0.047
	(0.044)	(0.037)	(0.109)	(0.094)	(0.200)	(0.158)
tvolume	-0.060	-0.036	**0.343***	0.001	0.151	0.100
	(0.059)	(0.038)	(0.138)	(0.086)	(0.265)	(0.150)
meanH_L3	**0.373*****	**0.333*****	0.004	-0.266	**0.945***	0.529
	(0.084)	(0.093)	(0.209)	(0.224)	(0.385)	(0.345)
vci_L1	-0.002	**0.177*****	-0.068	-0.096	-0.236	-0.111
	(0.037)	(0.040)	(0.077)	(0.089)	(0.154)	(0.155)
vci_L2	-0.031	**-0.078***	0.093	0.156	-0.042	**0.392***
	(0.052)	(0.039)	(0.132)	(0.100)	(0.279)	(0.179)
height_cv	**-0.237****	**-0.246****	0.244	**0.448***	-0.420	0.045
	(0.074)	(0.094)	(0.194)	(0.227)	(0.397)	(0.385)
Intercept	**3.734*****	**3.731*****	**1.643*****	**1.635*****	0.284	0.290
	-0.105	-0.095	-0.222	-0.247	-0.334	-0.343
Log Likelihood	-440.019	-415.733	-313.209	-316.977	-220.378	-225.865
Akaike Inf. Crit.	908.038	859.467	654.418	661.954	468.755	479.729
Bayesian Inf. Crit.	943.644	895.073	690.024	697.56	504.362	515.336
Marginal R2	0.196	0.287	0.137	0.090	0.085	0.068
Conditional R2	0.777	0.799	0.662	0.706	0.588	0.565

Chapter 2 Appendix A5 continued

Dependent variables	Independent variables					
	Air.Forage		Aqu.Forage		Arb.Forage	
	TLS	ULS	TLS	ULS	TLS	ULS
maxH	0.042	0.246	**-1.097***	0.102	**0.093***	**0.140*****
	(0.337)	(0.380)	(0.524)	(0.507)	(0.037)	(0.040)
meanH	-0.608	**-2.176***	**4.053***	-0.781	-0.067	-0.168
	(0.703)	(0.891)	(1.711)	(1.479)	(0.094)	(0.098)
skewH	-0.094	-0.546	**2.719***	1.057	-0.099	**-0.151*****
	(0.446)	(0.458)	(1.082)	(0.722)	(0.060)	(0.046)
vci_2m	0.245	0.357	0.083	-0.582	0.025	0.008
	(0.235)	(0.198)	(0.445)	(0.329)	(0.036)	(0.020)
vci_5m	0.045	-0.055	**1.523****	**1.704****	0.039	**0.047***
	(0.269)	(0.165)	(0.550)	(0.599)	(0.028)	(0.024)
vci_15m	-0.106	0.049	0.849	**1.801****	**0.070***	0.061
	(0.234)	(0.246)	(0.472)	(0.562)	(0.032)	(0.032)
canopy_roughness	-0.469	-0.064	0.120	0.191	**-0.152*****	**-0.059***
	(0.244)	(0.233)	(0.381)	(0.328)	(0.035)	(0.030)
tvolume	**1.247*****	**0.660****	-0.019	0.401	0.081	0.009
	(0.364)	(0.227)	(0.596)	(0.348)	(0.045)	(0.028)
meanH_L3	**1.276***	**2.305****	**-3.019***	0.396	0.084	**0.156***
	(0.620)	(0.832)	(1.264)	(1.237)	(0.072)	(0.077)
vci_L1	0.051	-0.259	-0.264	**0.724***	**-0.061***	**0.071***
	(0.181)	(0.256)	(0.292)	(0.299)	(0.028)	(0.030)
vci_L2	-0.359	-0.310	-0.212	-0.411	-0.027	**-0.082***
	(0.323)	(0.264)	(0.679)	(0.491)	(0.043)	(0.033)
height_cv	-0.202	-0.864	1.740	-1.622	0.0003	-0.101
	(0.561)	(0.677)	(0.906)	(1.187)	(0.064)	(0.076)
Intercept	-0.895	-0.94	**-1.986****	**-2.322*****	**4.210*****	**4.212*****
	-0.463	-0.513	-0.618	-0.686	-0.062	-0.058
Log Likelihood	-149	-155.902	-101.284	-96.176	-483.271	-488.543
Akaike Inf. Crit.	325.999	339.804	230.567	220.351	994.542	1 005.087
Bayesian Inf. Crit.	361.605	375.41	266.173	255.957	1 030.148	1 040.693
Marginal R2	0.204	0.161	0.399	0.408	0.185	0.238
Conditional R2	0.424	0.427	0.649	0.597	0.576	0.547

Chapter 2 Appendix A5 continued

Dependent variables	Independent variables					
	Grnd.Forage		Opp.Forage		Low.Disp	
	TLS	ULS	TLS	ULS	TLS	ULS
maxH	-0.045	-0.062	**-0.171***	**-0.190***	0.011	0.014
	(0.058)	(0.060)	(0.070)	(0.074)	(0.034)	(0.036)
meanH	-0.102	0.144	**-0.412***	-0.212	**-0.244****	-0.132
	(0.138)	(0.138)	(0.175)	(0.194)	(0.083)	(0.086)
skewH	0.054	0.123	**-0.254***	-0.086	**-0.152****	**-0.084***
	(0.088)	(0.063)	(0.109)	(0.086)	(0.053)	(0.039)
vci_2m	0.052	**-0.078***	0.116	0.011	**0.121*****	-0.008
	(0.056)	(0.037)	(0.066)	(0.030)	(0.033)	(0.018)
vci_5m	**-0.144*****	**-0.214*****	-0.009	-0.007	**-0.062***	**-0.079*****
	(0.040)	(0.030)	(0.055)	(0.044)	(0.025)	(0.020)
vci_15m	**0.096***	-0.026	0.045	0.018	**0.134*****	0.053
	(0.048)	(0.047)	(0.056)	(0.057)	(0.029)	(0.029)
canopy_roughness	**-0.237*****	**-0.152****	**0.209*****	**0.209*****	**-0.073***	-0.021
	(0.056)	(0.047)	(0.053)	(0.047)	(0.032)	(0.027)
tvolume	-0.003	0.063	0.048	0.023	-0.022	-0.020
	(0.071)	(0.046)	(0.078)	(0.049)	(0.043)	(0.027)
meanH_L3	0.133	0.009	**0.569*****	**0.324***	**0.235*****	**0.150***
	(0.103)	(0.104)	(0.142)	(0.158)	(0.062)	(0.067)
vci_L1	0.004	**0.167*****	-0.045	-0.025	**-0.097*****	0.036
	(0.046)	(0.049)	(0.051)	(0.053)	(0.027)	(0.028)
vci_L2	0.058	0.082	-0.049	0.019	-0.070	-0.036
	(0.064)	(0.045)	(0.081)	(0.060)	(0.038)	(0.028)
height_cv	-0.029	0.139	**-0.390*****	-0.21	**-0.136***	-0.006
	(0.095)	(0.108)	(0.114)	(0.143)	(0.055)	(0.067)
Intercept	**3.283*****	**3.280*****	**3.023*****	**3.030*****	**4.413*****	**4.415*****
	-0.111	-0.107	-0.076	-0.08	-0.067	-0.063
Log Likelihood	-420.465	-399.967	-377.264	-390.686	-497.613	-505.083
Akaike Inf. Crit.	868.93	827.934	782.528	809.372	1 023.227	1 038.166
Bayesian Inf. Crit.	904.536	863.541	818.134	844.978	1 058.833	1 073.772
Marginal R2	0.144	0.210	0.310	0.223	0.110	0.147
Conditional R2	0.695	0.699	0.549	0.489	0.672	0.591

Chapter 2 Appendix A5 continued

Dependent variables	Independent variables Partial.Disp TLS	ULS
maxH	0.011 (0.051)	0.049 (0.055)
meanH	0.190 (0.129)	0.040 (0.135)
skewH	0.059 (0.082)	-0.010 (0.064)
vci_2m	-0.089 (0.049)	-0.044 (0.030)
vci_5m	**0.081*** (0.040)	**0.072*** (0.034)
vci_15m	-0.026 (0.044)	0.013 (0.043)
canopy_roughness	**-0.169***** (0.046)	-0.061 (0.040)
tvolume	**0.228***** (0.060)	**0.110**** (0.037)
meanH_L3	-0.034 (0.103)	0.119 (0.107)
vci_L1	0.040 (0.035)	**0.149***** (0.041)
vci_L2	0.024 (0.059)	-0.042 (0.045)
height_cv	0.183 (0.094)	-0.063 (0.104)
Intercept	**3.560*****	**3.563*****
	-0.096	-0.104
Log Likelihood	-495.84	-499.214
Akaike Inf. Crit.	1 019.679	1 026.428
Bayesian Inf. Crit.	1 055.285	1 062.034
Marginal R2	0.208	0.187
Conditional R2	0.572	0.639

Chapter 2 Appendix A6. Model summary of the relationship between LiDAR derived vegetation structural metrics (independent variables) and abundance of individual species (dependent variables).

	Independent variables					
Dependent variables	Australian_Magpie		Australian_Raven		Black_faced_Cuckoo_shrike	
	TLS	ULS	TLS	ULS	TLS	ULS
maxH	-0.090	-0.124	-0.508	-0.469	0.239	0.152
	(0.110)	(0.120)	(0.317)	(0.356)	(0.206)	(0.253)
meanH	0.540	0.445	1.202	1.341	0.093	-0.459
	(0.284)	(0.294)	(0.807)	(0.837)	(0.611)	(0.629)
skewH	0.248	0.119	0.488	0.784	-0.244	-0.009
	(0.177)	(0.133)	(0.520)	(0.426)	(0.375)	(0.298)
vci_2m	0.098	-0.073	0.084	**-0.506***	**-0.492***	-0.142
	(0.111)	(0.064)	(0.303)	(0.218)	(0.207)	(0.136)
vci_5m	-0.051	-0.094	0.021	-0.029	**0.670****	0.197
	(0.093)	(0.071)	(0.254)	(0.180)	(0.220)	(0.185)
vci_15m	**-0.240****	**-0.255****	-0.031	-0.083	-0.074	0.059
	(0.090)	(0.089)	(0.233)	(0.241)	(0.185)	(0.173)
canopy_roughness	-0.054	-0.036	**0.639****	**0.653*****	-0.293	0.047
	(0.098)	(0.085)	(0.234)	(0.183)	(0.206)	(0.158)
tvolume	-0.167	0.014	-0.471	0.030	**0.591****	**0.332***
	(0.133)	(0.087)	(0.347)	(0.206)	(0.191)	(0.147)
meanH_L3	-0.117	-0.036	-0.638	-0.949	-0.432	0.326
	(0.228)	(0.229)	(0.622)	(0.662)	(0.472)	(0.473)
vci_L1	-0.027	0.169	-0.195	**0.651****	**0.303***	0.113
	(0.092)	(0.095)	(0.232)	(0.214)	(0.127)	(0.155)
vci_L2	0.058	0.049	-0.123	0.021	**-0.557***	-0.195
	(0.126)	(0.091)	(0.327)	(0.218)	(0.248)	(0.184)
height_cv	0.219	0.187	0.607	0.460	0.418	-0.380
	(0.197)	(0.221)	(0.526)	(0.570)	(0.397)	(0.439)
Intercept	**1.856*****	**1.860*****	-0.369	**-0.415***	**0.300***	0.295
	(0.138)	(0.137)	(0.210)	(0.188)	(0.133)	(0.174)
Log Likelihood	-255.100	-254.925	-123.470	-117.020	-156.353	-166.995
Akaike Inf. Crit.	538.201	537.851	274.940	262.039	340.706	361.989
Bayesian Inf. Crit.	573.807	573.457	310.546	297.645	376.312	397.595
Marginal R2	0.105	0.120	0.085	0.249	0.378	0.150
Conditional R2	0.748	0.756	0.195	0.313	0.396	0.354

Note: *p < 0.05, **p < 0.01, ***p < 0.001

Chapter 2 Appendix A6 continued

	Independent variables							
Dependent variables	Brown_headed_Honeyeater		Brown_Thornbill		Buff_rumped_Thornbill		Common_Bronzewing	
	TLS	ULS	TLS	ULS	TLS	ULS	TLS	ULS
maxH	0.244	0.056	-0.037	0.159	-0.074	-0.256	0.127	-0.223
	(0.441)	(0.494)	(0.529)	(0.521)	(0.135)	(0.158)	(0.484)	(0.531)
meanH	1.205	0.618	**-4.002***	-1.829	0.141	**0.961***	1.750	4.180
	(1.264)	(1.310)	(1.631)	(1.520)	(0.356)	(0.423)	(2.031)	(2.635)
skewH	0.105	0.139	-1.137	-1.291	0.420	**0.481***	0.444	2.141
	(0.692)	(0.587)	(0.809)	(0.717)	(0.222)	(0.200)	(1.158)	(1.251)
vci_2m	-0.500	0.185	0.923	**0.743***	0.237	**0.214***	**-2.616****	-2.029
	(0.334)	(0.240)	(0.497)	(0.372)	(0.146)	(0.095)	(0.860)	(1.077)
vci_5m	0.577	0.036	1.131	-0.433	0.013	-0.015	-0.516	-0.697
	(0.447)	(0.382)	(0.936)	(0.450)	(0.146)	(0.153)	(0.535)	(0.633)
vci_15m	0.366	0.534	**2.730*****	**1.062***	0.234	-0.083	-0.154	0.160
	(0.323)	(0.335)	(0.601)	(0.493)	(0.129)	(0.125)	(0.686)	(1.029)
canopy_roughness	0.472	**0.618***	**-1.502****	**-0.931***	**-0.384****	-0.223	0.875	-0.225
	(0.347)	(0.279)	(0.485)	(0.449)	(0.141)	(0.118)	(0.464)	(0.570)
tvolume	**1.004***	0.416	1.004	-0.355	**0.474****	0.034	0.481	0.641
	(0.451)	(0.291)	(0.787)	(0.363)	(0.172)	(0.106)	(0.654)	(0.625)
meanH_L3	-1.237	-0.377	2.861	1.186	0.090	-0.231	-2.990	-3.059
	(1.173)	(1.238)	(1.750)	(1.557)	(0.292)	(0.346)	(1.793)	(2.243)
vci_L1	0.298	0.037	-0.417	-0.416	-0.130	**-0.227***	**2.006****	1.606
	(0.197)	(0.293)	(0.365)	(0.454)	(0.090)	(0.114)	(0.645)	(0.851)
vci_L2	-1.072	-0.709	0.248	**1.260***	0.308	**0.457****	1.216	1.543
	(0.566)	(0.417)	(1.375)	(0.542)	(0.191)	(0.144)	(0.864)	(0.814)
height_cv	0.476	-0.062	**-3.671****	-0.796	-0.396	0.156	**2.989***	1.873
	(0.830)	(0.952)	(1.265)	(1.158)	(0.275)	(0.319)	(1.301)	(1.812)
Intercept	**-1.924****	**-1.947***	**-3.985****	**-3.707***	0.66	0.623	**-3.084*****	**-3.770****
	(0.692)	(0.766)	(1.323)	(1.783)	(0.365)	(0.403)	(0.651)	(1.191)
Log Likelihood	-109.254	-112.360	-78.480	-92.429	-241.967	-245.903	-42.615	-47.579
Akaike Inf. Crit.	246.508	252.720	184.959	212.857	511.933	519.806	113.230	123.158
Bayesian Inf. Crit.	282.114	288.326	220.565	248.464	547.539	555.412	148.836	158.764
Marginal R2	0.299	0.343	0.372	0.405	0.189	0.131	0.532	0.415
Conditional R2	0.582	0.512	0.823	0.594	0.767	0.759	0.616	0.735

Chapter 2 Appendix A6 continued

	Independent variables					
Dependent variables	Common_Starling		Crested_Pigeon		Crimson_Rosella	
	TLS	ULS	TLS	ULS	TLS	ULS
maxH	**0.341***	**0.285***	-0.200	-0.513	**0.349*****	**0.496*****
	(0.146)	(0.143)	(0.263)	(0.323)	(0.086)	(0.091)
meanH	**-1.840*****	**-0.901****	-1.022	-0.414	**-1.030*****	**-0.887*****
	(0.327)	(0.331)	(0.718)	(0.780)	(0.227)	(0.229)
skewH	**-0.856*****	**-0.353***	-0.295	-0.097	**-0.747*****	**-0.559*****
	(0.221)	(0.163)	(0.438)	(0.358)	(0.143)	(0.108)
vci_2m	-0.094	0.075	**0.535***	0.099	0.093	-0.055
	(0.129)	(0.099)	(0.271)	(0.104)	(0.088)	(0.048)
vci_5m	**-0.287*****	**-0.341*****	**-0.465***	-0.120	**-0.138***	0.031
	(0.080)	(0.057)	(0.192)	(0.160)	(0.064)	(0.050)
vci_15m	**0.768*****	0.218	0.133	0.026	**0.169***	0.135
	(0.153)	(0.130)	(0.226)	(0.237)	(0.074)	(0.074)
canopy_roughness	-0.062	**-0.339****	0.360	**0.461****	-0.035	-0.004
	(0.139)	(0.122)	(0.189)	(0.175)	(0.079)	(0.064)
tvolume	-0.110	-0.008	-0.251	0.114	-0.064	-0.081
	(0.187)	(0.139)	(0.349)	(0.187)	(0.101)	(0.063)
meanH_L3	**1.108*****	**0.592***	**1.376***	**0.995**	**0.677*****	**0.401***
	(0.217)	(0.241)	(0.577)	(0.623)	(0.172)	(0.177)
vci_L1	-0.021	-0.039	-0.136	0.102	-0.023	**0.151***
	(0.111)	(0.131)	(0.221)	(0.196)	(0.070)	(0.066)
vci_L2	-0.210	0.122	0.501	0.033	-0.159	**-0.296*****
	(0.151)	(0.120)	(0.336)	(0.272)	(0.098)	(0.068)
height_cv	**-0.904*****	-0.203	**-0.883***	-0.501	**-0.516*****	**-0.452****
	(0.203)	(0.270)	(0.410)	(0.531)	(0.147)	(0.171)
Intercept	0.361	0.354	-0.072	-0.071	**2.344*****	**2.338*****
	(0.419)	(0.442)	(0.228)	(0.253)	(0.079)	(0.067)
Log Likelihood	-231.988	-229.368	-154.924	-158.974	-285.809	-276.577
Akaike Inf. Crit.	491.977	486.736	337.848	345.949	599.618	581.155
Bayesian Inf. Crit.	527.583	522.342	373.454	381.555	635.224	616.761
Marginal R2	0.313	0.195	0.206	0.097	0.182	0.316
Conditional R2	0.769	0.774	0.428	0.442	0.488	0.527

Chapter 2 Appendix A6 continued

	Independent variables					
Dependent variables	Eastern_Rosella		Galah		Golden_Whistler	
	TLS	ULS	TLS	ULS	TLS	ULS
maxH	0.191	**0.359*****	**0.302***	0.285	-0.283	-0.281
	(0.099)	(0.106)	(0.143)	(0.161)	(0.799)	(0.527)
meanH	-0.387	**-0.877*****	-0.370	-0.276	0.956	
	(0.249)	(0.255)	(0.370)	(0.391)	(1.487)	
skewH	**-0.424****	**-0.448*****	-0.279	-0.168		
	(0.158)	(0.124)	(0.238)	(0.178)		
vci_2m	0.009	-0.081	0.123	0.006		
	(0.098)	(0.050)	(0.147)	(0.067)		
vci_5m	**0.150***	0.005	0.104	0.055	0.979	
	(0.070)	(0.055)	(0.103)	(0.085)	(0.970)	
vci_15m	**0.371*****	**0.310****	0.143	-0.040	0.653	1.007
	(0.102)	(0.101)	(0.124)	(0.129)	(0.723)	(0.608)
canopy_roughness	-0.169	-0.120	0.164	0.153	**1.215****	0.579
	(0.100)	(0.078)	(0.129)	(0.108)	(0.471)	0.389
tvolume	**-0.369****	**-0.282*****	**-0.482****	**-0.240***		
	(0.130)	(0.084)	(0.176)	(0.113)		
meanH_L3	0.265	**0.608****	0.143	0.024	-2.680	-1.567
	(0.175)	(0.190)	(0.268)	(0.301)	(1.893)	(0.853)
vci_L1	-0.045	**0.175***	0.089	**0.253***	**-0.708***	**-1.014****
	(0.087)	(0.089)	(0.119)	(0.115)	(0.342)	(0.389)
vci_L2	-0.232	-0.059	**-0.411****	**-0.286***	-0.876	0.123
	(0.119)	(0.090)	(0.157)	(0.115)	(1.233)	(0.515)
height_cv	-0.157	**-0.428***	-0.258	-0.048	-0.422	
	(0.155)	(0.201)	(0.223)	(0.294)	(1.640)	
Intercept	**1.980*****	**1.978*****	**1.188*****	**1.186*****	**-3.638*****	**-0.2806*****
	(0.146)	(0.139)	(0.123)	(0.131)	(0.799)	(0.527)
Log Likelihood	-293.257	-293.902	-221.612	-222.414	-33.200	-33.200
Akaike Inf. Crit.	614.513	615.803	471.224	472.828	88.300	88.300
Bayesian Inf. Crit.	650.120	651.409	506.830	508.434	116.300	116.300
Marginal R2	0.324	0.351	0.269	0.228	0.674	0.565
Conditional R2	0.748	0.732	0.452	0.431	0.694	0.590

Chapter 2 Appendix A6 continued

	Independent variables							
Dependent variables	Grey_Butcherbird		Grey_Fantail		Grey_Shrike_thrush		Laughing_Kookaburra	
	TLS	ULS	TLS	ULS	TLS	ULS	TLS	ULS
maxH	0.107	0.093	-0.203	-0.251	0.588	0.995	-0.180	0.571
	(0.364)	(0.425)	(0.161)	(0.178)	(0.612)	(0.732)	(0.597)	(0.581)
meanH	1.720	1.059	0.024	0.103	0.019	-0.267	-2.052	-0.684
	(1.290)	(1.212)	(0.387)	(0.387)	(1.372)	(1.519)	(1.756)	(2.035)
skewH	-0.059	-0.159	0.351	0.388	-0.464	-0.673	0.138	-0.921
	(0.709)	(0.604)	(0.247)	(0.220)	(0.815)	(1.628)	(1.329)	(0.893)
vci_2m	**1.365*****	0.178	0.072	0.181	-0.354	-1.080	**0.994***	-0.841
	(0.389)	(0.142)	(0.162)	(0.121)	(1.131)	(1.441)	(0.482)	(0.499)
vci_5m	0.255	0.044	0.114	0.030	0.405	0.592	0.214	-0.312
	(0.283)	(0.201)	(0.140)	(0.148)	(0.685)	(0.737)	(0.731)	(0.307)
vci_15m	0.277	0.016	**0.529****	**0.384***	-0.040	0.385	0.650	-0.100
	(0.360)	(0.384)	(0.167)	(0.166)	(0.667)	(1.200)	(0.562)	(0.414)
canopy_roughness	-0.321	-0.204	-0.275	-0.110	-1.177	-0.956	-0.651	-0.170
	(0.337)	(0.257)	(0.145)	(0.118)	(0.930)	(0.933)	(0.510)	(0.308)
tvolume	**-0.876***	-0.092	**0.411***	0.066	0.138	-0.391	0.214	0.506
	(0.432)	(0.248)	(0.205)	(0.130)	(1.101)	(0.825)	(0.583)	(0.404)
meanH_L3	-1.477	-1.397	0.153	0.366	-0.229	0.001	2.236	-0.327
	(1.092)	(0.978)	(0.306)	(0.317)	(1.279)	(1.330)	(1.747)	(1.678)
vci_L1	**-1.022****	0.124	-0.106	**-0.317***	1.249	1.874	0.514	-0.591
	(0.357)	(0.301)	(0.111)	(0.147)	(0.814)	(1.513)	(0.600)	(0.350)
vci_L2	-0.580	0.089	0.188	0.274	-0.442	-0.866	2.762	0.922
	(0.492)	(0.310)	(0.217)	(0.173)	(0.915)	(0.848)	(1.830)	(0.540)
height_cv	0.774	1.156	-0.345	-0.332	0.470	-0.666	-3.084	0.393
	(0.854)	(0.805)	(0.315)	(0.343)	(1.615)	(1.820)	(1.595)	(1.183)
Intercept	**-1.278****	**-1.110***	**0.662***	**0.670***	**-4.936***	-6.475	**-3.116****	**-1.921*****
	(0.493)	(0.455)	(0.286)	(0.289)	(2.307)	(3.957)	(1.174)	(0.415)
Log Likelihood	-113.669	-118.213	-234.062	-236.202	-45.893	-46.280	-66.879	-68.335
Akaike Inf. Crit.	255.337	264.426	496.124	500.404	119.787	120.561	161.758	164.671
Bayesian Inf. Crit.	290.943	300.032	531.731	536.010	155.393	156.167	197.365	200.277
Marginal R2	0.155	0.106	0.095	0.089	0.087	0.103	0.484	0.364
Conditional R2	0.670	0.577	0.639	0.665	0.757	0.832	0.484	0.364

Chapter 2 Appendix A6 continued

	Independent variables							
Dependent variables	Leaden_Flycatcher		Little_Corella		Magpie_lark		Masked_Lapwing	
	TLS	ULS	TLS	ULS	TLS	ULS	TLS	ULS
maxH	-0.116	-0.153	**2.850****	**1.792****	0.075	-0.232	0.072	-0.247
	(0.353)	(0.430)	(1.068)	(0.682)	(0.272)	(0.329)	(0.490)	(0.611)
meanH	1.769	1.390	6.250	6.606	-0.528	0.974	0.977	1.646
	(0.916)	(1.090)	(3.296)	(4.416)	(0.785)	(0.798)	(1.907)	(1.762)
skewH	0.600	0.430	0.299	0.702	-0.419	0.196	-1.594	-1.333
	(0.507)	(0.520)	(1.139)	(1.034)	(0.565)	(0.395)	(1.333)	(1.345)
vci_2m	-0.040	0.345	0.407	-1.321	-0.267	-0.088	-1.759	-1.284
	(0.316)	(0.186)	(0.992)	(0.683)	(0.252)	(0.152)	(1.099)	(1.129)
vci_5m	0.370	**1.129***	**2.636*****	0.595	-0.397	0.029	-0.128	0.062
	(0.340)	(0.501)	(0.790)	(0.504)	(0.234)	(0.160)	(0.630)	(0.443)
vci_15m	-0.380	-0.094	**-2.267***	-1.110	0.392	0.357	-1.042	-0.621
	(0.295)	(0.292)	(0.893)	(0.812)	(0.217)	(0.219)	(0.708)	(0.942)
canopy_roughness	-0.074	0.368	-1.118	**0.931***	**-0.943****	**-0.701****	0.667	0.408
	(0.273)	(0.212)	(1.205)	(0.468)	(0.322)	(0.268)	(0.580)	(0.553)
tvolume	**1.110*****	0.362	-0.986	**-1.037***	0.348	0.038	-0.232	-1.830
	(0.331)	(0.219)	(1.152)	(0.501)	(0.272)	(0.207)	(1.042)	(1.270)
meanH_L3	-1.419	-1.344	**-7.150***	-6.615	0.264	-0.476	-1.751	-1.828
	(0.833)	(0.997)	(3.436)	(4.082)	(0.598)	(0.631)	(1.521)	(1.250)
vci_L1	-0.079	-0.319	0.789	**2.577****	**0.449***	**0.534***	0.667	-0.422
	(0.190)	(0.253)	(0.907)	(0.813)	(0.199)	(0.242)	(0.687)	(0.726)
vci_L2	-0.488	**-0.730***	**-2.261***	**-1.404****	0.696	-0.044	-0.446	0.475
	(0.383)	(0.357)	(1.080)	(0.515)	(0.375)	(0.247)	(0.880)	(0.685)
height_cv	1.165	0.855	5.064	3.556	0.437	0.340	**2.789***	**2.908***
	(0.710)	(0.835)	(2.720)	(3.254)	(0.547)	(0.529)	(1.333)	(1.476)
Intercept	**-1.045*****	**-1.159*****	**-5.644***	**-4.206****	-0.619	-0.591	**-3.347*****	**-4.259***
	(0.295)	(0.310)	(2.216)	(1.498)	(0.409)	(0.407)	(0.921)	(1.654)
Log Likelihood	-102.792	-101.055	-55.479	-46.525	-141.357	-142.172	-45.837	-46.860
Akaike Inf. Crit.	233.583	230.110	138.957	121.051	310.714	312.344	119.674	121.720
Bayesian Inf. Crit.	269.189	265.716	174.563	156.657	346.320	347.950	155.280	157.327
Marginal R2	0.391	0.451	0.314	0.581	0.186	0.167	0.289	0.398
Conditional R2	0.391	0.505	0.716	0.743	0.740	0.722	0.515	0.741

Chapter 2 Appendix A6 continued

	Independent variables							
Dependent variables	Mistletoebird		Nankeen_Kestrel		Noisy_Friarbird		Noisy_Miner	
	TLS	ULS	TLS	ULS	TLS	ULS	TLS	ULS
maxH	0.022	0.020	-1.032	-0.368	0.145	0.125	**-0.586*****	**-0.754*****
	(0.265)	(0.304)	(0.733)	(0.812)	(0.211)	(0.243)	(0.119)	(0.150)
meanH	1.205	1.486	**-4.290***	1.367	-0.740	-0.589	0.350	-0.232
	(0.872)	(0.935)	(2.184)	(2.715)	(0.597)	(0.619)	(0.327)	(0.413)
skewH	0.850	0.604	-3.798	0.498	**-0.922***	**-0.654***	0.066	-0.081
	(0.483)	(0.431)	(2.044)	(1.270)	(0.390)	(0.275)	(0.205)	(0.193)
vci_2m	0.269	-0.373		-0.433	0.044	0.151	**0.285****	-0.027
	(0.297)	(0.242)		(0.551)	(0.212)	(0.102)	(0.103)	(0.042)
vci_5m	0.617	0.359		-0.199	0.114	0.209	0.003	0.055
	(0.317)	(0.265)		(0.306)	(0.181)	(0.131)	(0.076)	(0.064)
vci_15m	0.017	-0.256	**2.778***	0.959	0.010	0.112	-0.073	-0.031
	(0.255)	(0.259)	(1.160)	(1.159)	(0.169)	(0.167)	(0.102)	(0.101)
canopy_roughness	-0.512	-0.362	**1.671***	0.837	-0.009	0.072	**0.482*****	**0.398*****
	(0.292)	(0.231)	(0.822)	(0.504)	(0.232)	(0.195)	(0.082)	(0.072)
tvolume	-0.211	0.030	**-4.234*****	**-2.130****	0.036	-0.238	**-0.301***	-0.168
	(0.340)	(0.230)	(1.251)	(0.756)	(0.236)	(0.162)	(0.134)	(0.090)
meanH_L3	-0.722	-0.912	**2.843***	-0.982	0.431	0.183	0.286	**0.772***
	(0.785)	(0.795)	(1.347)	(2.289)	(0.510)	(0.504)	(0.259)	(0.342)
vci_L1	-0.199	-0.054	-0.337	1.146	0.023	-0.075	-0.140	-0.096
	(0.202)	(0.201)	(0.367)	(0.607)	(0.152)	(0.170)	(0.100)	(0.100)
vci_L2	0.901	**0.720***	**1.978***	0.775	-0.369	**-0.429***	**-0.551*****	**-0.439*****
	(0.516)	(0.332)	(0.811)	(0.659)	(0.262)	(0.174)	(0.147)	(0.115)
height_cv	-0.020	0.449		0.470	-0.220	-0.200	-0.264	-0.352
	(0.647)	(0.722)		(1.772)	(0.429)	(0.439)	(0.165)	(0.255)
Intercept	**-0.534***	-0.465	-5.663	**-4.018*****	0.208	0.2	0.691	0.661
	(0.263)	(0.257)	(1.608)	(1.010)	(0.222)	(0.216)	(0.605)	(0.633)
Log Likelihood	-126.882	-127.686	-29.200	-33.000	-157.465	-154.465	-281.398	-285.794
Akaike Inf. Crit.	281.763	283.373	80.400	94.001	342.930	336.930	590.796	599.588
Bayesian Inf. Crit.	317.369	318.979	108.400	129.607	378.536	372.537	626.402	635.194
Marginal R2	0.436	0.319	0.817	0.609	0.083	0.100	0.042	0.049
Conditional R2	0.621	0.573	0.824	0.672	0.600	0.609	0.921	0.916

Chapter 2 Appendix A6 continued

	Independent variables					
Dependent variables	Olive_backed_Oriole		Pallid_Cuckoo		Pied_Currawong	
	TLS	ULS	TLS	ULS	TLS	ULS
maxH	-1.209	**-1.602***	0.041	-0.042	0.430	0.433
	(0.640)	(0.697)	(0.466)	(0.466)	(0.484)	(0.599)
meanH	3.485	3.307	-0.807	0.748	-1.949	-1.654
	(1.843)	(2.020)	(1.174)	(1.170)	(1.548)	(1.436)
skewH	1.946	0.850	-0.193	0.036	-1.538	-0.811
	(1.069)	(0.862)	(0.724)	(0.549)	(1.024)	(0.737)
vci_2m	-0.372	0.181	-0.011	-0.145	-0.534	0.157
	(0.528)	(0.347)	(0.439)	(0.320)	(0.431)	(0.279)
vci_5m	0.047	-0.439	-0.328	-0.194	1.191	**1.363***
	(0.512)	(0.396)	(0.296)	(0.237)	(0.672)	(0.681)
vci_15m	-0.437	-0.441	0.207	-0.541	-0.264	-0.129
	(0.470)	(0.453)	(0.400)	(0.321)	(0.432)	(0.392)
canopy_roughness	-0.266	0.199	-0.008	-0.296	0.142	0.189
	(0.515)	(0.418)	(0.443)	(0.342)	(0.463)	(0.335)
tvolume	1.020	**1.102***	-0.408	-0.367	0.834	0.290
	(0.630)	(0.485)	(0.576)	(0.341)	(0.426)	(0.287)
meanH_L3	-2.814	-2.182	0.242	-0.437	1.366	1.206
	(1.590)	(1.488)	(0.794)	(0.845)	(1.213)	(1.093)
vci_L1	**0.971****	-0.166	0.090	0.032	-0.021	-0.025
	(0.362)	(0.398)	(0.350)	(0.269)	(0.269)	(0.333)
vci_L2	0.479	0.111	0.590	0.566	-0.933	-0.851
	(0.664)	(0.446)	(0.474)	(0.334)	(0.749)	(0.502)
height_cv	1.436	2.166	0.344	1.051	-0.947	-1.207
	(1.006)	(1.185)	(0.622)	(0.761)	(0.967)	(0.997)
Intercept	**-2.558*****	**-2.323*****	**-1.522*****	**-1.353*****	**-1.996*****	**-1.937*****
	(0.777)	(0.698)	(0.373)	(0.321)	(0.462)	(0.438)
Log Likelihood	-68.613	-68.868	-72.542	-73.281	-73.269	-73.814
Akaike Inf. Crit.	165.225	165.735	173.084	174.563	174.537	175.628
Bayesian Inf. Crit.	200.831	201.341	208.690	210.169	210.143	211.234
Marginal R2	0.309	0.324	0.250	0.291	0.442	0.307
Conditional R2	0.694	0.577	0.510	0.449	0.560	0.488

Chapter 2 Appendix A6 continued

	Independent variables					
Dependent variables	Red_rumped_Parrot		Red_Wattlebird		Rufous_Whistler	
	TLS	ULS	TLS	ULS	TLS	ULS
maxH	0.533	**0.850***	-0.035	-0.145	0.014	-0.172
	(0.465)	(0.428)	(0.351)	(0.462)	(0.227)	(0.237)
meanH	-1.281	-1.571	1.965	**3.563****	0.437	0.126
	(1.339)	(1.021)	(1.078)	(1.368)	(0.485)	(0.545)
skewH	-1.586	**-1.072***	0.535	0.845	0.510	0.535
	(0.832)	(0.529)	(0.772)	(0.660)	(0.307)	(0.290)
vci_2m	-0.526	**-0.944***	0.232	**-0.554****	0.169	0.208
	(0.404)	(0.381)	(0.297)	(0.209)	(0.214)	(0.142)
vci_5m	-0.483	-0.119	**0.677***	**0.838***	0.315	-0.097
	(0.276)	(0.180)	(0.322)	(0.346)	(0.217)	(0.202)
vci_15m	**1.374****	**1.006***	-0.188	**-0.579***	-0.038	0.018
	(0.503)	(0.441)	(0.260)	(0.262)	(0.175)	(0.182)
canopy_roughness	-0.558	-0.006	-0.358	0.393	-0.202	0.012
	(0.389)	(0.273)	(0.364)	(0.252)	(0.183)	(0.144)
tvolume	0.101	-0.116	-0.060	-0.024	0.502	0.198
	(0.495)	(0.309)	(0.286)	(0.217)	(0.259)	(0.163)
meanH_L3	-0.479	0.179	-1.008	**-2.627****	-0.202	0.246
	(1.025)	(0.841)	(0.815)	(1.009)	(0.419)	(0.451)
vci_L1	0.089	**0.804***	-0.110	0.386	-0.244	**-0.431****
	(0.327)	(0.313)	(0.170)	(0.273)	(0.142)	(0.167)
vci_L2	**1.168***	-0.037	-0.670	-0.569	-0.307	0.158
	(0.544)	(0.329)	(0.388)	(0.297)	(0.249)	(0.201)
height_cv	1.823	-0.112	0.562	**1.808***	0.025	-0.079
	(1.073)	(0.857)	(0.658)	(0.801)	(0.374)	(0.445)
Intercept	**-1.683****	**-1.244****	**-0.926***	-1.124*	-0.031	-0.046
	(0.614)	(0.453)	(0.415)	(0.470)	(0.330)	(0.365)
Log Likelihood	-108.826	-108.849	-128.382	-122.011	-167.184	-173.749
Akaike Inf. Crit.	245.652	245.698	284.763	272.022	362.368	375.498
Bayesian Inf. Crit.	281.258	281.304	320.369	307.628	397.974	411.104
Marginal R2	0.339	0.349	0.113	0.223	0.139	0.067
Conditional R2	0.339	0.349	0.611	0.730	0.693	0.712

Chapter 2 Appendix A6 continued

	Independent variables					
Dependent variables	Sacred_Kingfisher		Silvereye		Spotted_Pardalote	
	TLS	ULS	TLS	ULS	TLS	ULS
maxH	-1.536	**-2.539****	-0.173	-0.390	**-1.618****	-0.924
	(0.784)	(0.887)	(0.725)	(0.706)	(0.568)	(0.652)
meanH	**8.132*****	**7.809****	-3.112	-3.571	**4.309***	2.479
	(2.193)	(2.505)	(2.270)	(2.339)	(1.795)	(1.747)
skewH	**4.580****	**4.188****	-2.001	-2.038	**4.001*****	**3.141****
	(1.487)	(1.381)	(1.338)	(1.115)	(1.078)	(1.084)
vci_2m	-0.839	-0.050	0.243	0.020	-0.396	0.000
	(0.490)	(0.300)	(0.677)	(0.283)	(0.399)	(0.261)
vci_5m	0.727	0.331	**1.813***	**-0.608***	0.840	**1.450***
	(0.815)	(0.533)	(0.838)	(0.303)	(0.579)	(0.703)
vci_15m	0.068	0.179	**1.891****	0.821	0.698	**1.154***
	(0.552)	(0.428)	(0.667)	(0.637)	(0.439)	(0.509)
canopy_roughness	**1.119***	0.672	0.663	0.488	**0.883***	**0.739***
	(0.512)	(0.401)	(0.653)	(0.445)	(0.409)	(0.333)
tvolume	-0.197	0.389	0.221	0.762	0.706	0.344
	(0.594)	(0.357)	(0.805)	(0.419)	(0.424)	(0.283)
meanH_L3	**-8.784*****	**-6.706****	2.117	2.986	-3.213	-2.136
	(2.265)	(2.118)	(1.927)	(2.062)	(1.740)	(1.743)
vci_L1	**0.789***	**0.744***	-0.115	0.412	0.165	0.258
	(0.324)	(0.346)	(0.336)	(0.611)	(0.231)	(0.342)
vci_L2	0.685	0.728	-1.284	1.344	1.045	1.074
	(0.981)	(0.533)	(1.057)	(0.813)	(1.063)	(0.876)
height_cv	**3.324****	**2.185***	**-3.280***	-2.773	-0.713	-2.477
	(1.164)	(1.109)	(1.414)	(1.600)	(1.270)	(1.697)
Intercept	**-3.183*****	**-2.566*****	**-3.308****	**-3.123****	**-2.722*****	**-3.203*****
	(0.830)	(0.600)	(1.073)	(1.046)	(0.626)	(0.773)
Log Likelihood	-64.285	-68.809	-83.346	-86.216	-70.451	-72.207
Akaike Inf. Crit.	156.570	165.618	194.693	200.431	168.903	172.413
Bayesian Inf. Crit.	192.177	201.224	230.299	236.037	204.509	208.019
Marginal R2	0.735	0.762	0.127	0.200	0.772	0.800
Conditional R2	0.786	0.762	0.133	0.209	0.803	0.821

Chapter 2 Appendix A6 continued

	Independent variables					
Dependent variables	Striated_Pardalote		Striated_Thornbill		Sulphur_crested_Cockatoo	
	TLS	ULS	TLS	ULS	TLS	ULS
maxH	0.112	0.187	**-0.468***	**-0.815****	-0.170	0.049
	(0.118)	(0.122)	(0.220)	(0.268)	(0.174)	(0.189)
meanH	-0.175	-0.175	**1.686****	0.314	0.895	-0.176
	(0.304)	(0.318)	(0.627)	(0.571)	(0.504)	(0.479)
skewH	-0.035	-0.082	**1.361*****	**0.943****	0.137	-0.210
	(0.189)	(0.145)	(0.405)	(0.316)	(0.294)	(0.234)
vci_2m	-0.216*	-0.019	0.084	**0.583*****	-0.040	**-0.225***
	(0.102)	(0.061)	(0.180)	(0.129)	(0.184)	(0.098)
vci_5m	-0.139	0.085	**1.356*****	-0.413	0.061	-0.007
	(0.078)	(0.064)	(0.304)	(0.269)	(0.131)	(0.107)
vci_15m	0.086	0.144	**0.560****	0.162	-0.039	-0.007
	(0.100)	(0.098)	(0.175)	(0.183)	(0.179)	(0.176)
canopy_roughness	**-0.287****	**-0.178***	-0.276	**-0.363***	0.059	0.168
	(0.100)	(0.081)	(0.208)	(0.172)	(0.139)	(0.116)
tvolume	**0.298***	0.050	**0.490***	**0.603*****	0.051	**0.305***
	(0.122)	(0.078)	(0.228)	(0.147)	(0.211)	(0.130)
meanH_L3	0.120	0.187	**-1.268****	0.550	-0.425	0.469
	(0.227)	(0.248)	(0.454)	(0.422)	(0.375)	(0.355)
vci_L1	0.150	**0.233****	**-0.215***	**-1.015*****	-0.007	**0.564*****
	(0.078)	(0.084)	(0.107)	(0.190)	(0.144)	(0.133)
vci_L2	**0.295***	-0.094	**-0.803****	**1.095*****	0.311	0.041
	(0.131)	(0.091)	(0.303)	(0.233)	(0.224)	(0.153)
height_cv	0.049	-0.367	0.454	-0.002	**0.891***	-0.163
	(0.191)	(0.228)	(0.373)	(0.412)	(0.368)	(0.373)
Intercept	**1.913*****	**1.920*****	-0.372	-0.323	**0.773*****	**0.768*****
	(0.102)	(0.095)	(0.514)	(0.492)	(0.161)	(0.140)
Log Likelihood	-284.684	-281.591	-200.843	-200.226	-222.368	-215.093
Akaike Inf. Crit.	597.368	591.181	429.686	428.452	472.737	458.185
Bayesian Inf. Crit.	632.974	626.787	465.292	464.058	508.343	493.791
Marginal R2	0.207	0.250	0.359	0.354	0.276	0.376
Conditional R2	0.388	0.411	0.680	0.698	0.276	0.376

Chapter 2 Appendix A6 continued

	Independent variables					
Dependent variables	Superb_Parrot		Varied_Sittella		Weebill	
	TLS	ULS	TLS	ULS	TLS	ULS
maxH	**1.210****	**1.092***	-5.454	**-4.311***	-0.060	-0.286
	(0.415)	(0.489)	(3.332)	(1.782)	(0.137)	(0.154)
meanH	-1.795	1.053	**19.735***	**17.259***	**1.110****	**1.103****
	(1.235)	(1.413)	(9.043)	(6.793)	(0.354)	(0.350)
skewH	-1.247	-0.093	**17.375***	**7.280****	**0.500***	**0.386***
	(0.766)	(0.671)	(7.469)	(2.772)	(0.217)	(0.180)
vci_2m	0.000	-0.517	**0.343***	0.652	**0.347***	0.032
	(0.324)	(0.276)	(0.918)	(0.403)	(0.155)	(0.083)
vci_5m	0.496	-0.248	-2.783	-0.603	0.022	-0.061
	(0.389)	(0.250)	(1.802)	(0.593)	(0.112)	(0.110)
vci_15m	0.374	-0.326	**10.859***	0.478	-0.161	-0.116
	(0.411)	(0.338)	(5.065)	(1.023)	(0.123)	(0.121)
canopy_roughness	-0.565	**-0.914****	0.574	0.183	**-0.396****	-0.092
	(0.366)	(0.310)	(1.295)	(0.592)	(0.147)	(0.117)
tvolume	-0.131	-0.338	-0.596	0.525	-0.038	-0.140
	(0.490)	(0.349)	(1.526)	(0.490)	(0.183)	(0.116)
meanH_L3	0.577	-1.579	**-15.032***	**-11.284***	**-0.655***	-0.482
	(0.921)	(1.186)	(6.704)	(5.233)	(0.276)	(0.265)
vci_L1	-0.237	**0.998***	0.554	-0.114	**-0.340****	-0.198
	(0.350)	(0.429)	(0.727)	(0.477)	(0.106)	(0.112)
vci_L2	-0.284	0.380	2.452	1.194	0.286	0.242
	(0.506)	(0.304)	(2.450)	(1.147)	(0.172)	(0.137)
height_cv	-0.293	1.433	2.030	5.477	**0.963*****	**0.943*****
	(0.721)	(0.978)	(2.904)	(3.217)	(0.285)	(0.270)
Intercept	**-1.632****	**-1.998****	**-14.1039***	**-4.711****	**1.210*****	**1.244*****
	(0.610)	(0.750)	(5.538)	(1.684)	(0.217)	(0.220)
Log Likelihood	-117.643	-115.437	-61.100	-61.580	-302.015	-308.123
Akaike Inf. Crit.	263.286	258.875	150.100	151.161	632.031	644.246
Bayesian Inf. Crit.	298.892	294.481	185.700	186.767	667.637	679.852
Marginal R2	0.169	0.186	0.704	0.834	0.124	0.094
Conditional R2	0.508	0.603	0.704	0.834	0.443	0.399

Chapter 2 Appendix A6 continued

	Independent variables					
Dependent variables	Western_Gerygone		White_eared_Honeyeater		White_throated_Gerygone	
	TLS	ULS	TLS	ULS	TLS	ULS
maxH	0.275	0.140	-0.025	-0.023	-0.349	**-1.044****
	(0.291)	(0.326)	(1.176)	(1.276)	(0.294)	(0.368)
meanH	-0.495	-0.594	4.863	**5.170***	**3.112*****	**3.885*****
	(0.771)	(0.747)	(2.556)	(2.499)	(0.854)	(1.059)
skewH	0.103	0.089	2.578	1.341	**2.378*****	**2.632*****
	(0.458)	(0.430)	(1.639)	(1.958)	(0.569)	(0.568)
vci_2m	0.045	-0.450	0.930	-1.093	-0.048	0.209
	(0.364)	(0.310)	(1.670)	(1.580)	(0.254)	(0.167)
vci_5m	0.073	-0.105	1.237	2.382	0.660	0.062
	(0.305)	(0.322)	(1.662)	(2.069)	(0.346)	(0.218)
vci_15m	0.467	0.489	0.522	1.099	0.414	0.473
	(0.321)	(0.329)	(1.204)	(1.831)	(0.269)	(0.295)
canopy_roughness	**-1.079*****	**-0.557***	-0.457	-0.029	-0.166	-0.080
	(0.326)	(0.251)	(1.365)	(0.944)	(0.265)	(0.221)
tvolume	0.816	0.239	0.065	1.143	0.312	0.196
	(0.426)	(0.271)	(1.681)	(1.442)	(0.278)	(0.186)
meanH_L3	-0.357	0.558	-4.312	-4.237	**-3.137*****	**-3.244*****
	(0.628)	(0.600)	(2.363)	(2.259)	(0.762)	(0.898)
vci_L1	0.236	0.315	-1.244	0.174	0.050	**-0.429***
	(0.229)	(0.255)	(1.217)	(0.965)	(0.157)	(0.196)
vci_L2	**0.906***	**0.702***	-0.478	-0.898	0.369	**1.181*****
	(0.460)	(0.353)	(1.867)	(1.495)	(0.450)	(0.340)
height_cv	1.180	0.147	3.674	4.840	0.943	1.217
	(0.654)	(0.675)	(2.409)	(2.739)	(0.512)	(0.632)
Intercept	**-1.023***	-0.967	**-7.723****	**-10.267****	-0.531	**-0.728***
	(0.471)	(0.494)	(2.861)	(3.430)	(0.324)	(0.357)
Log Likelihood	-126.940	-131.884	-31.538	-32.722	-139.763	-138.238
Akaike Inf. Crit.	281.879	291.769	91.077	93.444	307.526	304.476
Bayesian Inf. Crit.	317.486	327.375	126.683	129.050	343.132	340.082
Marginal R2	0.301	0.155	0.097	0.163	0.506	0.574
Conditional R2	0.500	0.543	0.820	0.888	0.732	0.781

Chapter 2 Appendix A6 continued

	Independent variables					
Dependent variables	White_throated_Treecreeper		White_winged_Chough		White_winged_Triller	
	TLS	ULS	TLS	ULS	TLS	ULS
maxH	**-2.020****	-0.673	**-0.704*****	**-0.977*****	0.402	-0.074
	(0.769)	(0.669)	(0.192)	(0.162)	(0.646)	(0.513)
meanH	2.477	**5.038***	**1.876*****	**2.150*****	-2.525	-0.314
	(1.543)	(2.008)	(0.454)	(0.498)	(1.950)	(1.489)
skewH	**3.990*****	**2.715****	**1.485*****	**1.291*****	-1.130	0.517
	(1.148)	(0.962)	(0.247)	(0.208)	(1.125)	(0.754)
vci_2m	0.592	-0.152	**0.793*****	-0.096	**-2.615****	**-1.657***
	(0.631)	(0.235)	(0.158)	(0.099)	(0.875)	(0.717)
vci_5m	**-1.365***	0.868	0.020	0.003	0.056	-0.182
	(0.545)	(0.600)	(0.156)	(0.122)	(0.537)	(0.303)
vci_15m	**1.077***	0.800	0.137	**0.252***	-0.615	-1.026
	(0.546)	(0.479)	(0.136)	(0.122)	(0.647)	(0.545)
canopy_roughness	0.301	**1.200*****	**-0.424****	**0.447*****	**1.339***	0.438
	(0.549)	(0.314)	(0.150)	(0.116)	(0.562)	(0.396)
tvolume	**1.518***	0.040	0.413	0.132	0.640	0.451
	(0.658)	(0.244)	(0.214)	(0.112)	(0.801)	(0.534)
meanH_L3	-2.111	**-6.399****	**-1.200****	**-1.438*****	2.337	1.486
	(1.705)	(2.022)	(0.407)	(0.433)	(1.618)	(1.225)
vci_L1	0.519	**-0.913****	0.162	0.263	**2.236****	**1.465****
	(0.386)	(0.347)	(0.112)	(0.139)	(0.795)	(0.519)
vci_L2	**2.390***	-0.408	0.103	**-0.262***	-0.346	0.549
	(1.167)	(0.458)	(0.199)	(0.124)	(0.856)	(0.470)
height_cv	-1.663	1.712	0.439	0.638	-1.175	-1.551
	(1.219)	(1.207)	(0.316)	(0.331)	(1.487)	(1.402)
Intercept	**-3.579*****	**-3.234*****	0.48	0.578	**-3.729****	**-2.913*****
	(0.868)	(0.589)	(0.385)	(0.378)	(1.372)	(0.823)
Log Likelihood	-52.653	-54.619	-307.917	-331.057	-62.554	-72.476
Akaike Inf. Crit.	133.306	137.239	643.833	690.113	153.108	172.951
Bayesian Inf. Crit.	168.912	172.845	679.439	725.720	188.714	208.557
Marginal R2	0.739	0.777	0.272	0.196	0.271	0.242
Conditional R2	0.803	0.777	0.504	0.487	0.637	0.269

Chapter 2 Appendix A6 continued

	Independent variables					
Dependent variables	Willie_Wagtail		Wood_Duck		Yellow_faced_Honeyeater	
	TLS	ULS	TLS	ULS	TLS	ULS
maxH	0.400	0.358	-0.819	0.489	0.631	0.662
	(0.376)	(0.363)	(0.648)	(0.591)	(0.564)	(0.551)
meanH	-0.008	1.248	**4.807***	0.099	**-7.654*****	-1.926
	(0.948)	(0.869)	(2.066)	(1.658)	(1.897)	(1.607)
skewH	-0.090	0.551	**3.181***	1.466	**-3.631*****	0.482
	(0.607)	(0.443)	(1.313)	(0.826)	(1.046)	(0.725)
vci_2m	**-1.754*****	-0.520	0.840	**-0.995***	**-2.620*****	**-1.476*****
	(0.487)	(0.330)	(0.547)	(0.399)	(0.688)	(0.434)
vci_5m	-0.374	-0.225	**1.507***	**1.922****	**-1.571****	**-0.743****
	(0.280)	(0.187)	(0.600)	(0.716)	(0.533)	(0.263)
vci_15m	-0.448	-0.412	**1.244***	**1.883****	**1.856****	0.688
	(0.336)	(0.330)	(0.577)	(0.674)	(0.632)	(0.493)
canopy_roughness	0.652	0.368	0.260	0.263	0.316	0.075
	(0.344)	(0.249)	(0.503)	(0.377)	(0.531)	(0.404)
tvolume	0.140	**-0.637***	-0.849	-0.134	**1.606***	**0.727***
	(0.439)	(0.300)	(0.779)	(0.393)	(0.659)	(0.348)
meanH_L3	0.025	-0.612	**-3.608***	-0.531	**4.625*****	1.485
	(0.762)	(0.686)	(1.535)	(1.422)	(1.279)	(1.314)
vci_L1	**1.204****	0.412	-0.446	**0.798***	**1.389*****	**1.385****
	(0.401)	(0.308)	(0.356)	(0.363)	(0.416)	(0.425)
vci_L2	-0.014	-0.014	-0.573	-0.738	1.463	0.663
	(0.426)	(0.285)	(0.780)	(0.543)	(0.805)	(0.450)
height_cv	0.718	0.583	1.294	-1.473	**-2.309***	**-2.297***
	(0.683)	(0.702)	(1.012)	(1.391)	(1.069)	(1.059)
Intercept	**-1.675*****	**-1.338*****	**-2.665*****	**-2.796*****	**-2.937****	**-2.199****
	(0.391)	(0.313)	(0.808)	(0.777)	(1.017)	(0.681)
Log Likelihood	-88.446	-101.011	-84.209	-79.745	-116.755	-107.056
Akaike Inf. Crit.	204.892	230.021	196.417	187.490	261.510	242.113
Bayesian Inf. Crit.	240.498	265.627	232.024	223.096	297.117	277.719
Marginal R2	0.273	0.224	0.181	0.322	0.045	0.131
Conditional R2	0.273	0.224	0.222	0.322	0.045	0.131

Chapter 2 Appendix A6 continued

Independent variables				
Dependent variables	Yellow_rumped_Thornbill		Yellow_Thornbill	
	TLS	ULS	TLS	ULS
maxH	**0.725*****	**0.631*****	1.674	-0.882
	(0.148)	(0.161)	(1.525)	(1.090)
meanH	-0.532	-0.282	6.741	5.595
	(0.555)	(0.453)	(3.986)	(3.349)
skewH	0.381	**0.592***	3.648	1.038
	(0.318)	(0.249)	(2.662)	(1.724)
vci_2m	-0.083	-0.207	**4.088****	-0.757
	(0.210)	(0.133)	(1.404)	(0.677)
vci_5m	0.114	-0.152	2.247	-0.007
	(0.192)	(0.178)	(1.467)	(0.724)
vci_15m	-0.008	0.028	-1.036	**-2.150****
	(0.183)	(0.156)	(0.969)	(0.737)
canopy_roughness	**-1.068*****	**-0.907*****	**-5.081*****	**-1.914****
	(0.200)	(0.175)	(1.461)	(0.728)
tvolume	0.438	**0.368***	**-3.995***	-0.645
	(0.246)	(0.168)	(1.758)	(0.734)
meanH_L3	-0.125	0.092	-4.897	-2.894
	(0.384)	(0.300)	(3.294)	(2.888)
vci_L1	0.057	**0.386***	**-2.558***	0.081
	(0.143)	(0.153)	(1.081)	(1.094)
vci_L2	0.284	**0.472****	0.326	**1.835***
	(0.218)	(0.167)	(1.315)	(0.932)
height_cv	0.054	-0.158	2.362	3.147
	(0.371)	(0.333)	(1.583)	(1.753)
Intercept	0.200	0.175	**-13.287*****	**-9.507*****
	(0.388)	(0.391)	(3.365)	(2.791)
Log Likelihood	-221.600	-222.728	-52.623	-56.752
Akaike Inf. Crit.	471.201	473.457	133.246	141.505
Bayesian Inf. Crit.	506.807	509.063	168.852	177.111
Marginal R2	0.245	0.153	0.109	0.068
Conditional R2	0.553	0.609	0.945	0.905

Appendices Chapter 3

Chapter 3. Appendix 1. Pearson's correlation indexes between the surface topographic variables derived from the (a) Terrestrial laser scanner (TLS) and an unoccupied aerial vehicle laser scanner (ULS), (b) a TLS and fused laser scanner (Fusion), (c) Fusion and ULS. Digital surface model (DSM), topographic position index (TPI), topographic ruggedness index (TRI).

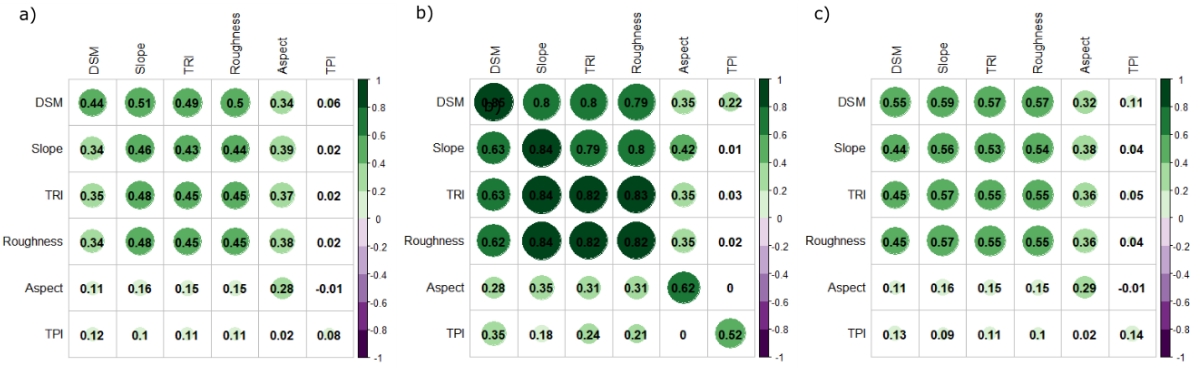

Chapter 3. Appendix 2. Boxplots show the distribution of measured coarse woody debris (CWD) data. Upper, mid and lower horizontal lines of the box indicate 1th, median and 3rd quartiles. Red dots inside a boxplot are mean values. Whiskers extend to the highest and lowest extreme of observations, and the dots on the whiskers are outliers.

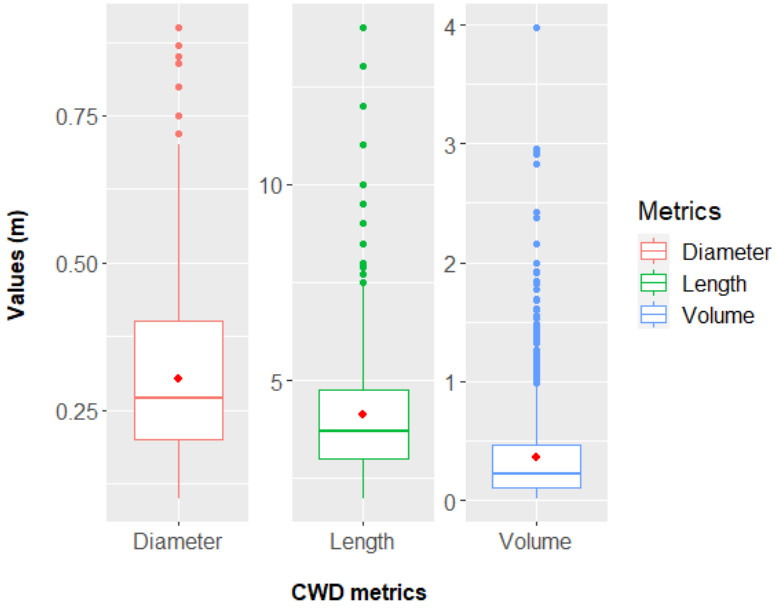

Chapter 3. Appendix 3. Pearson's pairwise correlations between the variables calculated from (a) Terrestrial laser scanner (TLS), (b) an unoccupied aerial vehicle laser scanner (ULS) and (c) a fused TLS and ULS (Fusion) data. Digital surface model (DSM), topographic position index (TPI), topographic ruggedness index (TRI).

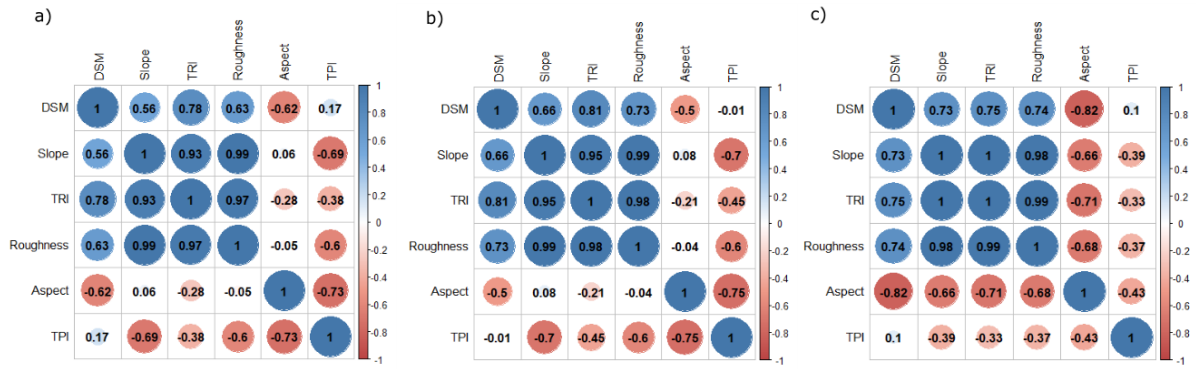

Chapter 3. Appendix 4. The digital surface model (DSM) samples from (a) Terrestrial laser scanner (TLS) (b) an unoccupied aerial vehicle laser scanner (ULS), (c) a TLS and fused laser scanner (Fusion).

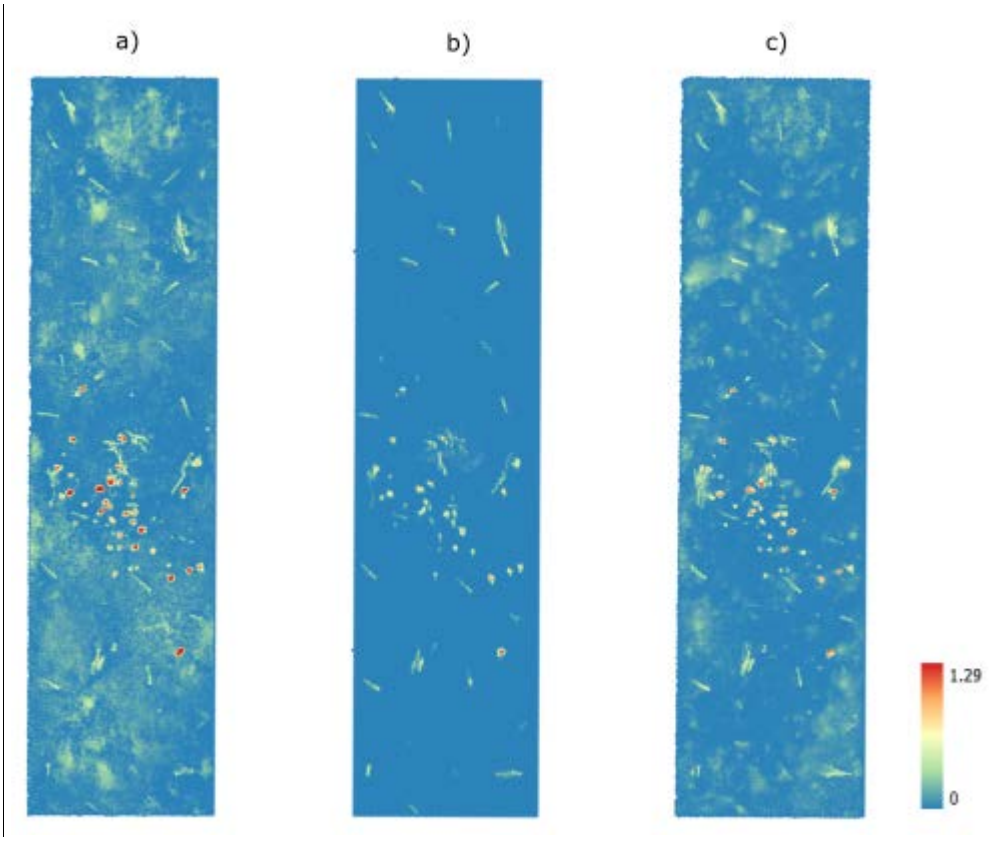

Appendices Chapter 4

Chapter 4 Appendix B1. Pearson correlation matrix of TLS derived vegetation structural variables

	maxH_t	meanH_t	stdH_t	skewH_t	kurH_t	p_05_t	p_10_t	p_25_t	p_50_t
maxH_t	1.000	0.574	0.761	0.008	-0.046	0.104	0.150	0.264	0.410
meanH_t	0.574	1.000	0.654	-0.694	-0.554	0.672	0.721	0.838	0.951
stdH_t	0.761	0.654	1.000	-0.118	-0.352	0.004	0.045	0.173	0.412
skewH_t	0.008	-0.694	-0.118	1.000	0.828	-0.604	-0.638	-0.723	-0.791
kurH_t	-0.046	-0.554	-0.352	0.828	1.000	-0.258	-0.285	-0.376	-0.529
p_05_t	0.104	0.672	0.004	-0.604	-0.258	1.000	0.992	0.924	0.752
p_10_t	0.150	0.721	0.045	-0.638	-0.285	0.992	1.000	0.958	0.801
p_25_t	0.264	0.838	0.173	-0.723	-0.376	0.924	0.958	1.000	0.918
p_50_t	0.410	0.951	0.412	-0.791	-0.529	0.752	0.801	0.918	1.000
p_75_t	0.588	0.966	0.732	-0.686	-0.618	0.509	0.562	0.700	0.886
p_90_t	0.710	0.830	0.946	-0.360	-0.501	0.292	0.333	0.447	0.631
p_99_t	0.873	0.652	0.896	0.017	-0.087	0.138	0.179	0.291	0.449
vci_2m_t	0.202	-0.022	0.146	-0.023	-0.090	-0.343	-0.314	-0.190	-0.032
vci_5m_t	0.216	0.185	0.153	-0.246	-0.328	-0.085	-0.028	0.113	0.197
vci_10m_t	0.244	0.537	0.233	-0.738	-0.738	0.314	0.344	0.436	0.560
vci_15m_t	0.655	0.601	0.739	-0.169	-0.335	0.179	0.206	0.288	0.443
vci_20m_t	0.816	0.565	0.696	-0.056	-0.105	0.164	0.201	0.299	0.422
cov_t	0.324	0.483	0.109	-0.513	-0.321	0.365	0.414	0.527	0.557
canopy_shannon_t	0.725	0.885	0.832	-0.538	-0.617	0.333	0.386	0.542	0.760
canopy_roughness_t	0.593	0.481	0.418	-0.265	-0.243	0.083	0.138	0.302	0.464
tvolume_t	0.260	0.456	0.050	-0.495	-0.262	0.387	0.430	0.540	0.556
vlayer_L1_t	-0.080	-0.143	-0.073	0.029	0.014	-0.207	-0.198	-0.156	-0.109
vlayer_L2_t	0.128	0.256	-0.152	-0.427	-0.194	0.313	0.344	0.416	0.386
vlayer_L3_t	0.446	0.738	0.368	-0.529	-0.326	0.525	0.575	0.703	0.763
meanH_L1_t	0.230	0.120	0.279	-0.038	-0.092	-0.207	-0.192	-0.092	0.073
meanH_L2_t	0.109	0.626	-0.083	-0.761	-0.441	0.820	0.844	0.870	0.767
meanH_L3_t	0.692	0.430	0.874	0.242	0.047	-0.046	-0.022	0.046	0.182
sdH_L1_t	0.295	0.094	0.304	0.077	0.002	-0.212	-0.194	-0.116	0.014
sdH_L2_t	0.332	0.622	0.397	-0.729	-0.723	0.187	0.236	0.411	0.647
sdH_L3_t	0.863	0.493	0.829	0.202	0.100	0.026	0.058	0.146	0.280
roughness_L1_t	0.139	0.059	0.065	-0.171	-0.148	-0.212	-0.180	-0.047	0.108
roughness_L2_t	0.239	0.402	0.008	-0.524	-0.346	0.308	0.345	0.462	0.511
roughness_L3_t	0.695	0.435	0.760	0.124	-0.017	-0.099	-0.057	0.057	0.248
vci_L1_t	0.297	0.128	0.325	0.030	-0.041	-0.202	-0.184	-0.096	0.054
vci_L2_t	0.266	0.487	0.189	-0.651	-0.649	0.238	0.281	0.411	0.546
vci_L3_t	0.828	0.587	0.905	0.079	-0.079	0.068	0.101	0.199	0.366
height_cv_t	0.289	-0.315	0.498	0.671	0.234	-0.698	-0.708	-0.700	-0.564
cwd_volume_t	-0.051	0.039	-0.016	-0.144	-0.100	-0.058	-0.050	0.016	0.095
numberOfCWD_t	-0.059	0.025	-0.068	-0.154	-0.086	-0.018	-0.011	0.040	0.091

Chapter 4 Appendix B1 continued

	p_75_t	p_90_t	p_99_t	vci_2m_t	vci_5m_t	vci_10m_t	vci_15m_t	vci_20m_t
maxH_t	0.588	0.710	0.873	0.202	0.216	0.244	0.655	0.816
meanH_t	0.966	0.830	0.652	-0.022	0.185	0.537	0.601	0.565
stdH_t	0.732	0.946	0.896	0.146	0.153	0.233	0.739	0.696
skewH_t	-0.686	-0.360	0.017	-0.023	-0.246	-0.738	-0.169	-0.056
kurH_t	-0.618	-0.501	-0.087	-0.090	-0.328	-0.738	-0.335	-0.105
p_05_t	0.509	0.292	0.138	-0.343	-0.085	0.314	0.179	0.164
p_10_t	0.562	0.333	0.179	-0.314	-0.028	0.344	0.206	0.201
p_25_t	0.700	0.447	0.291	-0.190	0.113	0.436	0.288	0.299
p_50_t	0.886	0.631	0.449	-0.032	0.197	0.560	0.443	0.422
p_75_t	1.000	0.857	0.658	0.058	0.188	0.592	0.619	0.556
p_90_t	0.857	1.000	0.844	0.047	0.170	0.337	0.742	0.670
p_99_t	0.658	0.844	1.000	0.113	0.154	0.178	0.718	0.803
vci_2m_t	0.058	0.047	0.113	1.000	0.185	0.226	0.113	0.221
vci_5m_t	0.188	0.170	0.154	0.185	1.000	0.301	0.274	0.243
vci_10m_t	0.592	0.337	0.178	0.226	0.301	1.000	0.316	0.237
vci_15m_t	0.619	0.742	0.718	0.113	0.274	0.316	1.000	0.692
vci_20m_t	0.556	0.670	0.803	0.221	0.243	0.237	0.692	1.000
cov_t	0.439	0.233	0.205	0.576	0.423	0.521	0.195	0.336
canopy_shannon_t	0.923	0.898	0.787	0.169	0.366	0.626	0.767	0.712
canopy_roughness_t	0.499	0.430	0.448	0.548	0.397	0.369	0.445	0.536
tvolume_t	0.392	0.187	0.146	0.460	0.360	0.410	0.123	0.262
vlayer_L1_t	-0.133	-0.106	-0.094	0.130	0.134	-0.025	-0.160	-0.143
vlayer_L2_t	0.190	-0.030	-0.033	0.487	0.357	0.407	-0.042	0.167
vlayer_L3_t	0.683	0.520	0.425	0.289	0.247	0.359	0.415	0.421
meanH_L1_t	0.207	0.190	0.238	0.625	0.030	0.176	0.252	0.298
meanH_L2_t	0.490	0.184	0.059	-0.127	0.312	0.612	0.120	0.185
meanH_L3_t	0.445	0.786	0.864	-0.002	0.074	-0.172	0.645	0.664
sdH_L1_t	0.177	0.206	0.270	0.573	-0.042	0.081	0.285	0.372
sdH_L2_t	0.692	0.462	0.312	0.363	0.359	0.863	0.439	0.377
sdH_L3_t	0.505	0.727	0.955	0.112	0.102	0.082	0.640	0.801
roughness_L1_t	0.114	0.024	0.046	0.834	0.294	0.273	0.067	0.195
roughness_L2_t	0.368	0.126	0.071	0.432	0.412	0.518	0.137	0.293
roughness_L3_t	0.507	0.660	0.737	0.143	0.093	0.032	0.611	0.626
vci_L1_t	0.214	0.231	0.282	0.608	-0.022	0.113	0.306	0.380
vci_L2_t	0.502	0.285	0.188	0.185	0.681	0.805	0.365	0.314
vci_L3_t	0.606	0.837	0.946	0.121	0.170	0.105	0.824	0.840
height_cv_t	-0.203	0.242	0.388	0.180	-0.083	-0.363	0.283	0.237
cwd_volume_t	0.049	-0.011	-0.029	0.230	0.131	0.155	-0.064	-0.115
numberOfCWD_t	0.020	-0.056	-0.035	0.186	0.129	0.183	-0.122	-0.151

Chapter 4 Appendix B1 continued

	cov_t	canopy_shannon_t	canopy_roughness_t	tvolume_t	vlayer_L1_t
maxH_t	0.324	0.725	0.593	0.260	-0.080
meanH_t	0.483	0.885	0.481	0.456	-0.143
stdH_t	0.109	0.832	0.418	0.050	-0.073
skewH_t	-0.513	-0.538	-0.265	-0.495	0.029
kurH_t	-0.321	-0.617	-0.243	-0.262	0.014
p_05_t	0.365	0.333	0.083	0.387	-0.207
p_10_t	0.414	0.386	0.138	0.430	-0.198
p_25_t	0.527	0.542	0.302	0.540	-0.156
p_50_t	0.557	0.760	0.464	0.556	-0.109
p_75_t	0.439	0.923	0.499	0.392	-0.133
p_90_t	0.233	0.898	0.430	0.187	-0.106
p_99_t	0.205	0.787	0.448	0.146	-0.094
vci_2m_t	0.576	0.169	0.548	0.460	0.130
vci_5m_t	0.423	0.366	0.397	0.360	0.134
vci_10m_t	0.521	0.626	0.369	0.410	-0.025
vci_15m_t	0.195	0.767	0.445	0.123	-0.160
vci_20m_t	0.336	0.712	0.536	0.262	-0.143
cov_t	1.000	0.448	0.631	0.890	-0.016
canopy_shannon_t	0.448	1.000	0.578	0.358	-0.095
canopy_roughness_t	0.631	0.578	1.000	0.650	0.155
tvolume_t	0.890	0.358	0.650	1.000	0.264
vlayer_L1_t	-0.016	-0.095	0.155	0.264	1.000
vlayer_L2_t	0.884	0.181	0.527	0.933	0.147
vlayer_L3_t	0.765	0.601	0.655	0.821	-0.051
meanH_L1_t	0.320	0.265	0.307	0.067	-0.463
meanH_L2_t	0.620	0.417	0.243	0.595	-0.072
meanH_L3_t	-0.103	0.561	0.255	-0.126	-0.063
sdH_L1_t	0.254	0.232	0.298	-0.016	-0.578
sdH_L2_t	0.491	0.736	0.505	0.421	0.056
sdH_L3_t	0.103	0.655	0.393	0.042	-0.084
roughness_L1_t	0.634	0.188	0.632	0.624	0.292
roughness_L2_t	0.797	0.378	0.677	0.843	0.060
roughness_L3_t	0.022	0.588	0.438	-0.010	-0.099
vci_L1_t	0.283	0.270	0.336	0.017	-0.555
vci_L2_t	0.518	0.627	0.463	0.423	0.080
vci_L3_t	0.114	0.758	0.441	0.048	-0.123
height_cv_t	-0.438	0.006	-0.044	-0.470	0.041
cwd_volume_t	0.154	0.061	0.280	0.303	0.633
numberOfCWD_t	0.185	0.033	0.161	0.319	0.637

Chapter 4 Appendix B1 continued

	vlayer_L2_t	vlayer_L3_t	meanH_L1_t	meanH_L2_t	meanH_L3_t	sdH_L1_t
maxH_t	0.128	0.446	0.230	0.109	0.692	0.295
meanH_t	0.256	0.738	0.120	0.626	0.430	0.094
stdH_t	-0.152	0.368	0.279	-0.083	0.874	0.304
skewH_t	-0.427	-0.529	-0.038	-0.761	0.242	0.077
kurH_t	-0.194	-0.326	-0.092	-0.441	0.047	0.002
p_05_t	0.313	0.525	-0.207	0.820	-0.046	-0.212
p_10_t	0.344	0.575	-0.192	0.844	-0.022	-0.194
p_25_t	0.416	0.703	-0.092	0.870	0.046	-0.116
p_50_t	0.386	0.763	0.073	0.767	0.182	0.014
p_75_t	0.190	0.683	0.207	0.490	0.445	0.177
p_90_t	-0.030	0.520	0.190	0.184	0.786	0.206
p_99_t	-0.033	0.425	0.238	0.059	0.864	0.270
vci_2m_t	0.487	0.289	0.625	-0.127	-0.002	0.573
vci_5m_t	0.357	0.247	0.030	0.312	0.074	-0.042
vci_10m_t	0.407	0.359	0.176	0.612	-0.172	0.081
vci_15m_t	-0.042	0.415	0.252	0.120	0.645	0.285
vci_20m_t	0.167	0.421	0.298	0.185	0.664	0.372
cov_t	0.884	0.765	0.320	0.620	-0.103	0.254
canopy_shannon_t	0.181	0.601	0.265	0.417	0.561	0.232
canopy_roughness_t	0.527	0.655	0.307	0.243	0.255	0.298
tvolume_t	0.933	0.821	0.067	0.595	-0.126	-0.016
vlayer_L1_t	0.147	-0.051	-0.463	-0.072	-0.063	-0.578
vlayer_L2_t	1.000	0.623	0.130	0.594	-0.312	0.057
vlayer_L3_t	0.623	1.000	0.171	0.534	0.193	0.137
meanH_L1_t	0.130	0.171	1.000	-0.137	0.149	0.852
meanH_L2_t	0.594	0.534	-0.137	1.000	-0.260	-0.213
meanH_L3_t	-0.312	0.193	0.149	-0.260	1.000	0.232
sdH_L1_t	0.057	0.137	0.852	-0.213	0.232	1.000
sdH_L2_t	0.347	0.435	0.327	0.486	0.012	0.200
sdH_L3_t	-0.104	0.284	0.224	-0.065	0.877	0.292
roughness_L1_t	0.642	0.370	0.495	0.059	-0.103	0.329
roughness_L2_t	0.853	0.668	0.147	0.597	-0.215	0.115
roughness_L3_t	-0.200	0.310	0.288	-0.206	0.747	0.330
vci_L1_t	0.081	0.168	0.916	-0.191	0.232	0.987
vci_L2_t	0.422	0.321	0.095	0.647	-0.098	-0.016
vci_L3_t	-0.136	0.362	0.266	-0.051	0.920	0.333
height_cv_t	-0.507	-0.359	0.201	-0.821	0.636	0.274
cwd_volume_t	0.201	0.122	-0.035	0.076	-0.094	-0.342
numberOfCWD_t	0.242	0.097	-0.086	0.147	-0.151	-0.427

Chapter 4 Appendix B1 continued

	sdH_L2_t	sdH_L3_t	roughness_L1_t	roughness_L2_t	roughness_L3_t	vci_L1_t
maxH_t	0.332	0.863	0.139	0.239	0.695	0.297
meanH_t	0.622	0.493	0.059	0.402	0.435	0.128
stdH_t	0.397	0.829	0.065	0.008	0.760	0.325
skewH_t	-0.729	0.202	-0.171	-0.524	0.124	0.030
kurH_t	-0.723	0.100	-0.148	-0.346	-0.017	-0.041
p_05_t	0.187	0.026	-0.212	0.308	-0.099	-0.202
p_10_t	0.236	0.058	-0.180	0.345	-0.057	-0.184
p_25_t	0.411	0.146	-0.047	0.462	0.057	-0.096
p_50_t	0.647	0.280	0.108	0.511	0.248	0.054
p_75_t	0.692	0.505	0.114	0.368	0.507	0.214
p_90_t	0.462	0.727	0.024	0.126	0.660	0.231
p_99_t	0.312	0.955	0.046	0.071	0.737	0.282
vci_2m_t	0.363	0.112	0.834	0.432	0.143	0.608
vci_5m_t	0.359	0.102	0.294	0.412	0.093	-0.022
vci_10m_t	0.863	0.082	0.273	0.518	0.032	0.113
vci_15m_t	0.439	0.640	0.067	0.137	0.611	0.306
vci_20m_t	0.377	0.801	0.195	0.293	0.626	0.380
cov_t	0.491	0.103	0.634	0.797	0.022	0.283
canopy_shannon_t	0.736	0.655	0.188	0.378	0.588	0.270
canopy_roughness_t	0.505	0.393	0.632	0.677	0.438	0.336
tvolume_t	0.421	0.042	0.624	0.843	-0.010	0.017
vlayer_L1_t	0.056	-0.084	0.292	0.060	-0.099	-0.555
vlayer_L2_t	0.347	-0.104	0.642	0.853	-0.200	0.081
vlayer_L3_t	0.435	0.284	0.370	0.668	0.310	0.168
meanH_L1_t	0.327	0.224	0.495	0.147	0.288	0.916
meanH_L2_t	0.486	-0.065	0.059	0.597	-0.206	-0.191
meanH_L3_t	0.012	0.877	-0.103	-0.215	0.747	0.232
sdH_L1_t	0.200	0.292	0.329	0.115	0.330	0.987
sdH_L2_t	1.000	0.187	0.420	0.515	0.175	0.254
sdH_L3_t	0.187	1.000	0.020	-0.015	0.756	0.290
roughness_L1_t	0.420	0.020	1.000	0.570	0.052	0.398
roughness_L2_t	0.515	-0.015	0.570	1.000	-0.021	0.142
roughness_L3_t	0.175	0.756	0.052	-0.021	1.000	0.345
vci_L1_t	0.254	0.290	0.398	0.142	0.345	1.000
vci_L2_t	0.815	0.089	0.307	0.579	0.031	0.024
vci_L3_t	0.269	0.939	0.029	0.010	0.802	0.342
height_cv_t	-0.249	0.485	-0.031	-0.482	0.451	0.258
cwd_volume_t	0.226	-0.068	0.456	0.152	-0.005	-0.259
numberOfCWD_t	0.210	-0.089	0.394	0.121	-0.117	-0.347

Chapter 4 Appendix B1 continued

	vci_L2_t	vci_L3_t	height_cv_t	cwd_volume_t	numberOfCWD_t
maxH_t	0.266	0.828	0.289	-0.051	-0.059
meanH_t	0.487	0.587	-0.315	0.039	0.025
stdH_t	0.189	0.905	0.498	-0.016	-0.068
skewH_t	-0.651	0.079	0.671	-0.144	-0.154
kurH_t	-0.649	-0.079	0.234	-0.100	-0.086
p_05_t	0.238	0.068	-0.698	-0.058	-0.018
p_10_t	0.281	0.101	-0.708	-0.050	-0.011
p_25_t	0.411	0.199	-0.700	0.016	0.040
p_50_t	0.546	0.366	-0.564	0.095	0.091
p_75_t	0.502	0.606	-0.203	0.049	0.020
p_90_t	0.285	0.837	0.242	-0.011	-0.056
p_99_t	0.188	0.946	0.388	-0.029	-0.035
vci_2m_t	0.185	0.121	0.180	0.230	0.186
vci_5m_t	0.681	0.170	-0.083	0.131	0.129
vci_10m_t	0.805	0.105	-0.363	0.155	0.183
vci_15m_t	0.365	0.824	0.283	-0.064	-0.122
vci_20m_t	0.314	0.840	0.237	-0.115	-0.151
cov_t	0.518	0.114	-0.438	0.154	0.185
canopy_shannon_t	0.627	0.758	0.006	0.061	0.033
canopy_roughness_t	0.463	0.441	-0.044	0.280	0.161
tvolume_t	0.423	0.048	-0.470	0.303	0.319
vlayer_L1_t	0.080	-0.123	0.041	0.633	0.637
vlayer_L2_t	0.422	-0.136	-0.507	0.201	0.242
vlayer_L3_t	0.321	0.362	-0.359	0.122	0.097
meanH_L1_t	0.095	0.266	0.201	-0.035	-0.086
meanH_L2_t	0.647	-0.051	-0.821	0.076	0.147
meanH_L3_t	-0.098	0.920	0.636	-0.094	-0.151
sdH_L1_t	-0.016	0.333	0.274	-0.342	-0.427
sdH_L2_t	0.815	0.269	-0.249	0.226	0.210
sdH_L3_t	0.089	0.939	0.485	-0.068	-0.089
roughness_L1_t	0.307	0.029	-0.031	0.456	0.394
roughness_L2_t	0.579	0.010	-0.482	0.152	0.121
roughness_L3_t	0.031	0.802	0.451	-0.005	-0.117
vci_L1_t	0.024	0.342	0.258	-0.259	-0.347
vci_L2_t	1.000	0.156	-0.384	0.188	0.202
vci_L3_t	0.156	1.000	0.488	-0.080	-0.136
height_cv_t	-0.384	0.488	1.000	-0.086	-0.139
cwd_volume_t	0.188	-0.080	-0.086	1.000	0.933
numberOfCWD_t	0.202	-0.136	-0.139	0.933	1.000

Chapter 4 Appendix B2. Pearson correlation matrix of ULS derived vegetation structural variables

	maxH_u	meanH_u	stdH_u	skewH_u	kurH_u	p_05_u	p_10_u	p_25_u	p_50_u
maxH_u	1.000	0.632	0.771	-0.005	-0.101	0.143	0.175	0.280	0.479
meanH_u	0.632	1.000	0.573	-0.680	-0.418	0.602	0.676	0.820	0.957
stdH_u	0.771	0.573	1.000	-0.010	-0.376	-0.163	-0.105	0.037	0.356
skewH_u	-0.005	-0.680	-0.010	1.000	0.637	-0.568	-0.625	-0.736	-0.791
kurH_u	-0.101	-0.418	-0.376	0.637	1.000	-0.012	-0.040	-0.151	-0.389
p_05_u	0.143	0.602	-0.163	-0.568	-0.012	1.000	0.983	0.889	0.652
p_10_u	0.175	0.676	-0.105	-0.625	-0.040	0.983	1.000	0.942	0.726
p_25_u	0.280	0.820	0.037	-0.736	-0.151	0.889	0.942	1.000	0.884
p_50_u	0.479	0.957	0.356	-0.791	-0.389	0.652	0.726	0.884	1.000
p_75_u	0.666	0.945	0.715	-0.626	-0.530	0.376	0.453	0.619	0.871
p_90_u	0.749	0.805	0.925	-0.292	-0.468	0.180	0.245	0.378	0.620
p_99_u	0.952	0.650	0.850	0.042	-0.090	0.117	0.158	0.268	0.470
vci_2m_u	0.333	0.015	0.238	0.125	0.010	-0.262	-0.243	-0.172	-0.012
vci_5m_u	0.238	0.053	0.181	-0.003	-0.315	-0.215	-0.210	-0.104	0.049
vci_10m_u	0.276	0.412	0.177	-0.544	-0.662	0.159	0.182	0.282	0.451
vci_15m_u	0.609	0.606	0.650	-0.325	-0.593	0.142	0.185	0.284	0.483
vci_20m_u	0.682	0.480	0.581	0.039	0.021	0.110	0.146	0.227	0.360
cov_u	0.393	0.327	0.077	-0.225	-0.081	0.277	0.263	0.312	0.364
canopy_shannon_u	0.806	0.789	0.829	-0.365	-0.583	0.124	0.183	0.359	0.668
canopy_roughness_u	0.608	0.557	0.395	-0.288	-0.256	0.209	0.240	0.381	0.538
tvolume_u	0.294	0.366	0.009	-0.371	-0.146	0.290	0.299	0.392	0.447
vlayer_L1_u	0.180	0.197	0.021	-0.300	-0.146	0.017	0.034	0.161	0.288
vlayer_L2_u	0.140	0.109	-0.180	-0.224	-0.055	0.200	0.175	0.212	0.204
vlayer_L3_u	0.454	0.665	0.239	-0.471	-0.211	0.468	0.512	0.624	0.694
meanH_L1_u	0.219	-0.110	0.445	0.274	-0.121	-0.566	-0.507	-0.445	-0.237
meanH_L2_u	0.077	0.417	-0.310	-0.576	-0.211	0.762	0.733	0.699	0.537
meanH_L3_u	0.701	0.527	0.927	0.108	-0.164	-0.057	-0.003	0.092	0.295
sdH_L1_u	0.255	-0.007	0.468	0.187	-0.213	-0.487	-0.414	-0.339	-0.135
sdH_L2_u	0.239	0.539	0.244	-0.699	-0.570	0.089	0.181	0.397	0.616
sdH_L3_u	0.897	0.549	0.859	0.150	-0.052	0.003	0.043	0.141	0.352
roughness_L1_u	0.220	-0.022	0.436	0.113	-0.279	-0.548	-0.482	-0.366	-0.117
roughness_L2_u	0.176	0.359	-0.037	-0.465	-0.364	0.270	0.314	0.412	0.444
roughness_L3_u	0.638	0.480	0.827	0.113	-0.176	-0.095	-0.029	0.075	0.281
vci_L1_u	0.262	-0.030	0.478	0.214	-0.200	-0.510	-0.443	-0.374	-0.163
vci_L2_u	0.328	0.341	0.297	-0.377	-0.661	-0.096	-0.059	0.115	0.368
vci_L3_u	0.866	0.668	0.926	-0.037	-0.282	0.041	0.099	0.225	0.468
height_cv_u	0.214	-0.365	0.537	0.693	0.050	-0.759	-0.761	-0.754	-0.574
cwd_volume_u	0.203	0.168	0.323	-0.114	-0.162	-0.287	-0.210	-0.042	0.158
numberOfCWD_u	0.149	0.056	0.263	-0.059	-0.190	-0.383	-0.314	-0.158	0.058

Chapter 4 Appendix B2 continued

	p_75_u	p_90_u	p_99_u	vci_2m_u	vci_5m_u	vci_10m_u	vci_15m_u	vci_20m_u
maxH_u	0.666	0.749	0.952	0.333	0.238	0.276	0.609	0.682
meanH_u	0.945	0.805	0.650	0.015	0.053	0.412	0.606	0.480
stdH_u	0.715	0.925	0.850	0.238	0.181	0.177	0.650	0.581
skewH_u	-0.626	-0.292	0.042	0.125	-0.003	-0.544	-0.325	0.039
kurH_u	-0.530	-0.468	-0.090	0.010	-0.315	-0.662	-0.593	0.021
p_05_u	0.376	0.180	0.117	-0.262	-0.215	0.159	0.142	0.110
p_10_u	0.453	0.245	0.158	-0.243	-0.210	0.182	0.185	0.146
p_25_u	0.619	0.378	0.268	-0.172	-0.104	0.282	0.284	0.227
p_50_u	0.871	0.620	0.470	-0.012	0.049	0.451	0.483	0.360
p_75_u	1.000	0.861	0.680	0.094	0.097	0.471	0.671	0.483
p_90_u	0.861	1.000	0.823	0.109	0.122	0.244	0.698	0.574
p_99_u	0.680	0.823	1.000	0.294	0.202	0.220	0.617	0.694
vci_2m_u	0.094	0.109	0.294	1.000	0.190	0.149	0.198	0.221
vci_5m_u	0.097	0.122	0.202	0.190	1.000	0.298	0.223	0.174
vci_10m_u	0.471	0.244	0.220	0.149	0.298	1.000	0.608	0.000
vci_15m_u	0.671	0.698	0.617	0.198	0.223	0.608	1.000	0.329
vci_20m_u	0.483	0.574	0.694	0.221	0.174	0.000	0.329	1.000
cov_u	0.288	0.139	0.313	0.637	0.380	0.308	0.262	0.275
canopy_shannon_u	0.871	0.872	0.821	0.251	0.351	0.580	0.807	0.587
canopy_roughness_u	0.557	0.457	0.514	0.292	0.289	0.398	0.507	0.429
tvolume_u	0.307	0.105	0.207	0.321	0.371	0.293	0.238	0.271
vlayer_L1_u	0.198	0.022	0.104	0.334	0.241	0.253	0.141	0.200
vlayer_L2_u	0.052	-0.127	0.044	0.329	0.382	0.266	0.066	0.150
vlayer_L3_u	0.590	0.414	0.405	0.189	0.305	0.248	0.431	0.373
meanH_L1_u	0.082	0.234	0.255	0.536	-0.016	0.084	0.247	0.082
meanH_L2_u	0.221	-0.026	-0.003	-0.133	0.238	0.427	0.101	0.028
meanH_L3_u	0.589	0.887	0.815	0.103	0.074	-0.077	0.508	0.606
sdH_L1_u	0.172	0.300	0.288	0.375	0.124	0.152	0.337	0.159
sdH_L2_u	0.579	0.323	0.211	0.220	0.115	0.739	0.489	0.112
sdH_L3_u	0.612	0.787	0.961	0.281	0.195	0.207	0.586	0.686
roughness_L1_u	0.178	0.250	0.241	0.315	0.179	0.204	0.310	0.171
roughness_L2_u	0.291	0.098	0.129	0.134	0.370	0.530	0.318	0.095
roughness_L3_u	0.543	0.789	0.743	0.122	0.069	0.010	0.488	0.554
vci_L1_u	0.157	0.297	0.291	0.455	0.107	0.137	0.330	0.159
vci_L2_u	0.405	0.298	0.291	0.205	0.574	0.778	0.535	0.191
vci_L3_u	0.736	0.906	0.929	0.243	0.199	0.274	0.762	0.695
height_cv_u	-0.175	0.229	0.297	0.227	0.087	-0.255	0.145	0.147
cwd_volume_u	0.246	0.240	0.222	0.380	0.044	0.140	0.257	0.184
numberOfCWD_u	0.153	0.152	0.146	0.428	0.083	0.172	0.226	0.167

Chapter 4 Appendix B2 continued

	cov_u	canopy_shannon_u	canopy_roughness_u	tvolume_u	vlayer_L1_u
maxH_u	0.393	0.806	0.608	0.294	0.180
meanH_u	0.327	0.789	0.557	0.366	0.197
stdH_u	0.077	0.829	0.395	0.009	0.021
skewH_u	-0.225	-0.365	-0.288	-0.371	-0.300
kurH_u	-0.081	-0.583	-0.256	-0.146	-0.146
p_05_u	0.277	0.124	0.209	0.290	0.017
p_10_u	0.263	0.183	0.240	0.299	0.034
p_25_u	0.312	0.359	0.381	0.392	0.161
p_50_u	0.364	0.668	0.538	0.447	0.288
p_75_u	0.288	0.871	0.557	0.307	0.198
p_90_u	0.139	0.872	0.457	0.105	0.022
p_99_u	0.313	0.821	0.514	0.207	0.104
vci_2m_u	0.637	0.251	0.292	0.321	0.334
vci_5m_u	0.380	0.351	0.289	0.371	0.241
vci_10m_u	0.308	0.580	0.398	0.293	0.253
vci_15m_u	0.262	0.807	0.507	0.238	0.141
vci_20m_u	0.275	0.587	0.429	0.271	0.200
cov_u	1.000	0.333	0.500	0.792	0.514
canopy_shannon_u	0.333	1.000	0.612	0.303	0.216
canopy_roughness_u	0.500	0.612	1.000	0.521	0.448
tvolume_u	0.792	0.303	0.521	1.000	0.815
vlayer_L1_u	0.514	0.216	0.448	0.815	1.000
vlayer_L2_u	0.779	0.105	0.339	0.925	0.698
vlayer_L3_u	0.695	0.501	0.612	0.852	0.563
meanH_L1_u	-0.002	0.234	-0.077	-0.202	-0.089
meanH_L2_u	0.435	0.171	0.228	0.470	0.218
meanH_L3_u	-0.041	0.667	0.293	-0.109	-0.116
sdH_L1_u	-0.029	0.333	-0.002	-0.134	-0.159
sdH_L2_u	0.254	0.556	0.386	0.368	0.452
sdH_L3_u	0.217	0.782	0.435	0.104	0.042
roughness_L1_u	-0.043	0.339	0.018	0.044	0.159
roughness_L2_u	0.397	0.380	0.306	0.490	0.281
roughness_L3_u	-0.070	0.666	0.299	-0.146	-0.170
vci_L1_u	0.008	0.321	0.000	-0.143	-0.140
vci_L2_u	0.274	0.657	0.437	0.288	0.285
vci_L3_u	0.196	0.882	0.517	0.134	0.072
height_cv_u	-0.275	0.093	-0.126	-0.379	-0.195
cwd_volume_u	0.118	0.287	0.322	0.283	0.584
numberOfCWD_u	0.103	0.251	0.302	0.296	0.626

Chapter 4 Appendix B2 continued

	vlayer_L2_u	vlayer_L3_u	meanH_L1_u	meanH_L2_u	meanH_L3_u	sdH_L1_u
maxH_u	0.140	0.454	0.219	0.077	0.701	0.255
meanH_u	0.109	0.665	-0.110	0.417	0.527	-0.007
stdH_u	-0.180	0.239	0.445	-0.310	0.927	0.468
skewH_u	-0.224	-0.471	0.274	-0.576	0.108	0.187
kurH_u	-0.055	-0.211	-0.121	-0.211	-0.164	-0.213
p_05_u	0.200	0.468	-0.566	0.762	-0.057	-0.487
p_10_u	0.175	0.512	-0.507	0.733	-0.003	-0.414
p_25_u	0.212	0.624	-0.445	0.699	0.092	-0.339
p_50_u	0.204	0.694	-0.237	0.537	0.295	-0.135
p_75_u	0.052	0.590	0.082	0.221	0.589	0.172
p_90_u	-0.127	0.414	0.234	-0.026	0.887	0.300
p_99_u	0.044	0.405	0.255	-0.003	0.815	0.288
vci_2m_u	0.329	0.189	0.536	-0.133	0.103	0.375
vci_5m_u	0.382	0.305	-0.016	0.238	0.074	0.124
vci_10m_u	0.266	0.248	0.084	0.427	-0.077	0.152
vci_15m_u	0.066	0.431	0.247	0.101	0.508	0.337
vci_20m_u	0.150	0.373	0.082	0.028	0.606	0.159
cov_u	0.779	0.695	-0.002	0.435	-0.041	-0.029
canopy_shannon_u	0.105	0.501	0.234	0.171	0.667	0.333
canopy_roughness_u	0.339	0.612	-0.077	0.228	0.293	-0.002
tvolume_u	0.925	0.852	-0.202	0.470	-0.109	-0.134
vlayer_L1_u	0.698	0.563	-0.089	0.218	-0.116	-0.159
vlayer_L2_u	1.000	0.637	-0.184	0.477	-0.294	-0.116
vlayer_L3_u	0.637	1.000	-0.221	0.446	0.170	-0.093
meanH_L1_u	-0.184	-0.221	1.000	-0.558	0.341	0.904
meanH_L2_u	0.477	0.446	-0.558	1.000	-0.329	-0.442
meanH_L3_u	-0.294	0.170	0.341	-0.329	1.000	0.363
sdH_L1_u	-0.116	-0.093	0.904	-0.442	0.363	1.000
sdH_L2_u	0.247	0.341	0.125	0.241	0.029	0.168
sdH_L3_u	-0.037	0.285	0.343	-0.109	0.828	0.376
roughness_L1_u	0.039	-0.034	0.804	-0.419	0.280	0.873
roughness_L2_u	0.475	0.461	-0.097	0.583	-0.182	0.047
roughness_L3_u	-0.325	0.149	0.360	-0.283	0.855	0.405
vci_L1_u	-0.125	-0.116	0.945	-0.475	0.370	0.990
vci_L2_u	0.252	0.233	0.130	0.328	0.099	0.234
vci_L3_u	-0.065	0.379	0.334	-0.107	0.883	0.401
height_cv_u	-0.349	-0.393	0.608	-0.818	0.536	0.522
cwd_volume_u	0.131	0.193	0.426	-0.262	0.236	0.329
numberOfCWD_u	0.183	0.134	0.452	-0.268	0.145	0.366

Chapter 4 Appendix B2 continued

	sdH_L2_u	sdH_L3_u	roughness_L1_u	roughness_L2_u	roughness_L3_u	vci_L1_u
maxH_u	0.239	0.897	0.220	0.176	0.638	0.262
meanH_u	0.539	0.549	-0.022	0.359	0.480	-0.030
stdH_u	0.244	0.859	0.436	-0.037	0.827	0.478
skewH_u	-0.699	0.150	0.113	-0.465	0.113	0.214
kurH_u	-0.570	-0.052	-0.279	-0.364	-0.176	-0.200
p_05_u	0.089	0.003	-0.548	0.270	-0.095	-0.510
p_10_u	0.181	0.043	-0.482	0.314	-0.029	-0.443
p_25_u	0.397	0.141	-0.366	0.412	0.075	-0.374
p_50_u	0.616	0.352	-0.117	0.444	0.281	-0.163
p_75_u	0.579	0.612	0.178	0.291	0.543	0.157
p_90_u	0.323	0.787	0.250	0.098	0.789	0.297
p_99_u	0.211	0.961	0.241	0.129	0.743	0.291
vci_2m_u	0.220	0.281	0.315	0.134	0.122	0.455
vci_5m_u	0.115	0.195	0.179	0.370	0.069	0.107
vci_10m_u	0.739	0.207	0.204	0.530	0.010	0.137
vci_15m_u	0.489	0.586	0.310	0.318	0.488	0.330
vci_20m_u	0.112	0.686	0.171	0.095	0.554	0.159
cov_u	0.254	0.217	-0.043	0.397	-0.070	0.008
canopy_shannon_u	0.556	0.782	0.339	0.380	0.666	0.321
canopy_roughness_u	0.386	0.435	0.018	0.306	0.299	0.000
tvolume_u	0.368	0.104	0.044	0.490	-0.146	-0.143
vlayer_L1_u	0.452	0.042	0.159	0.281	-0.170	-0.140
vlayer_L2_u	0.247	-0.037	0.039	0.475	-0.325	-0.125
vlayer_L3_u	0.341	0.285	-0.034	0.461	0.149	-0.116
meanH_L1_u	0.125	0.343	0.804	-0.097	0.360	0.945
meanH_L2_u	0.241	-0.109	-0.419	0.583	-0.283	-0.475
meanH_L3_u	0.029	0.828	0.280	-0.182	0.855	0.370
sdH_L1_u	0.168	0.376	0.873	0.047	0.405	0.990
sdH_L2_u	1.000	0.171	0.265	0.502	0.080	0.150
sdH_L3_u	0.171	1.000	0.314	0.044	0.750	0.381
roughness_L1_u	0.265	0.314	1.000	0.128	0.298	0.860
roughness_L2_u	0.502	0.044	0.128	1.000	0.025	0.000
roughness_L3_u	0.080	0.750	0.298	0.025	1.000	0.403
vci_L1_u	0.150	0.381	0.860	0.000	0.403	1.000
vci_L2_u	0.664	0.267	0.295	0.579	0.185	0.209
vci_L3_u	0.291	0.935	0.354	0.101	0.817	0.401
height_cv_u	-0.277	0.409	0.489	-0.446	0.461	0.558
cwd_volume_u	0.406	0.218	0.538	0.126	0.228	0.353
numberOfCWD_u	0.408	0.158	0.564	0.123	0.172	0.389

Chapter 4 Appendix B2 continued

	vci_L2_u	vci_L3_u	height_cv_u	cwd_volume_u	numberOfCWD_u
maxH_u	0.328	0.866	0.214	0.203	0.149
meanH_u	0.341	0.668	-0.365	0.168	0.056
stdH_u	0.297	0.926	0.537	0.323	0.263
skewH_u	-0.377	-0.037	0.693	-0.114	-0.059
kurH_u	-0.661	-0.282	0.050	-0.162	-0.190
p_05_u	-0.096	0.041	-0.759	-0.287	-0.383
p_10_u	-0.059	0.099	-0.761	-0.210	-0.314
p_25_u	0.115	0.225	-0.754	-0.042	-0.158
p_50_u	0.368	0.468	-0.574	0.158	0.058
p_75_u	0.405	0.736	-0.175	0.246	0.153
p_90_u	0.298	0.906	0.229	0.240	0.152
p_99_u	0.291	0.929	0.297	0.222	0.146
vci_2m_u	0.205	0.243	0.227	0.380	0.428
vci_5m_u	0.574	0.199	0.087	0.044	0.083
vci_10m_u	0.778	0.274	-0.255	0.140	0.172
vci_15m_u	0.535	0.762	0.145	0.257	0.226
vci_20m_u	0.191	0.695	0.147	0.184	0.167
cov_u	0.274	0.196	-0.275	0.118	0.103
canopy_shannon_u	0.657	0.882	0.093	0.287	0.251
canopy_roughness_u	0.437	0.517	-0.126	0.322	0.302
tvolume_u	0.288	0.134	-0.379	0.283	0.296
vlayer_L1_u	0.285	0.072	-0.195	0.584	0.626
vlayer_L2_u	0.252	-0.065	-0.349	0.131	0.183
vlayer_L3_u	0.233	0.379	-0.393	0.193	0.134
meanH_L1_u	0.130	0.334	0.608	0.426	0.452
meanH_L2_u	0.328	-0.107	-0.818	-0.262	-0.268
meanH_L3_u	0.099	0.883	0.536	0.236	0.145
sdH_L1_u	0.234	0.401	0.522	0.329	0.366
sdH_L2_u	0.664	0.291	-0.277	0.406	0.408
sdH_L3_u	0.267	0.935	0.409	0.218	0.158
roughness_L1_u	0.295	0.354	0.489	0.538	0.564
roughness_L2_u	0.579	0.101	-0.446	0.126	0.123
roughness_L3_u	0.185	0.817	0.461	0.228	0.172
vci_L1_u	0.209	0.401	0.558	0.353	0.389
vci_L2_u	1.000	0.355	-0.086	0.221	0.270
vci_L3_u	0.355	1.000	0.380	0.288	0.222
height_cv_u	-0.086	0.380	1.000	0.207	0.237
cwd_volume_u	0.221	0.288	0.207	1.000	0.929
numberOfCWD_u	0.270	0.222	0.237	0.929	1.000

Chapter 4 Appendix B3. Pearson correlation matrix of TLS derived vegetation structural variables

	maxH_m	meanH_m	stdH_m	skewH_m	kurH_m	p_05_m	p_10_m	p_25_m
maxH_m	1.000	0.445	0.577	-0.014	-0.047	0.085	0.116	0.222
meanH_m	0.445	1.000	0.652	-0.691	-0.546	0.674	0.720	0.837
stdH_m	0.577	0.652	1.000	-0.115	-0.347	0.002	0.041	0.169
skewH_m	-0.014	-0.691	-0.115	1.000	0.826	-0.606	-0.636	-0.720
kurH_m	-0.047	-0.546	-0.347	0.826	1.000	-0.255	-0.279	-0.368
p_05_m	0.085	0.674	0.002	-0.606	-0.255	1.000	0.993	0.928
p_10_m	0.116	0.720	0.041	-0.636	-0.279	0.993	1.000	0.959
p_25_m	0.222	0.837	0.169	-0.720	-0.368	0.928	0.959	1.000
p_50_m	0.332	0.950	0.407	-0.788	-0.521	0.756	0.801	0.918
p_75_m	0.428	0.966	0.731	-0.682	-0.610	0.511	0.560	0.698
p_95_m	0.572	0.760	0.963	-0.218	-0.402	0.216	0.253	0.362
p_99_m	0.680	0.651	0.895	0.023	-0.076	0.137	0.175	0.288
vci_2m_m	0.222	-0.038	0.228	0.059	-0.004	-0.451	-0.416	-0.279
vci_5m_m	0.226	0.193	0.149	-0.250	-0.323	-0.054	-0.008	0.128
vci_10m_m	0.181	0.537	0.229	-0.737	-0.730	0.318	0.345	0.436
vci_15m_m	0.497	0.602	0.738	-0.171	-0.332	0.181	0.206	0.288
vci_20m_m	0.526	0.439	0.582	0.082	0.070	0.101	0.135	0.216
cov_m	0.299	0.485	0.104	-0.515	-0.318	0.379	0.420	0.529
canopy_shannon_m	0.561	0.885	0.831	-0.535	-0.608	0.335	0.384	0.539
canopy_roughness_m	0.445	0.468	0.402	-0.254	-0.227	0.077	0.130	0.296
tvolume_m	0.277	0.443	0.035	-0.507	-0.272	0.384	0.418	0.526
vlayer_1_m	-0.058	-0.192	-0.120	0.042	0.049	-0.236	-0.235	-0.196
vlayer_2_m	0.183	0.171	-0.200	-0.380	-0.175	0.255	0.276	0.336
vlayer_3_m	0.355	0.749	0.346	-0.566	-0.350	0.569	0.610	0.729
meanH_L1_m	0.174	0.057	0.289	-0.013	-0.110	-0.304	-0.276	-0.179
meanH_L2_m	0.143	0.622	-0.090	-0.756	-0.431	0.826	0.844	0.868
meanH_L3_m	0.530	0.429	0.874	0.246	0.055	-0.051	-0.025	0.043
sdH_L1_m	0.216	0.091	0.295	-0.007	-0.092	-0.266	-0.231	-0.135
sdH_L2_m	0.295	0.624	0.394	-0.730	-0.715	0.194	0.241	0.414
sdH_L3_m	0.667	0.489	0.826	0.212	0.116	0.023	0.053	0.140
roughness_L1_m	0.149	0.010	0.056	-0.122	-0.123	-0.250	-0.220	-0.103
roughness_L2_m	0.229	0.399	0.021	-0.498	-0.328	0.301	0.332	0.450
roughness_L3_m	0.406	0.382	0.718	0.160	0.010	-0.131	-0.093	0.016
vci_L1_m	0.194	0.109	0.296	-0.058	-0.117	-0.265	-0.231	-0.121
vci_L2_m	0.230	0.484	0.183	-0.645	-0.635	0.243	0.280	0.409
vci_L3_m	0.393	0.533	0.860	0.105	-0.069	0.053	0.078	0.154
height_cv_m	0.209	-0.312	0.503	0.667	0.229	-0.703	-0.709	-0.700
cwd_volume_m	0.151	0.113	0.038	-0.153	-0.106	0.038	0.047	0.088
numberOfCWD_m	0.054	0.029	-0.079	-0.148	-0.090	0.043	0.051	0.071

Chapter 4 Appendix B3 continued

	p_50_m	p_75_m	p_95_m	p_99_m	vci_2m_m	vci_5m_m	vci_10m_m
maxH_m	0.332	0.428	0.572	0.680	0.222	0.226	0.181
meanH_m	0.950	0.966	0.760	0.651	-0.038	0.193	0.537
stdH_m	0.407	0.731	0.963	0.895	0.228	0.149	0.229
skewH_m	-0.788	-0.682	-0.218	0.023	0.059	-0.250	-0.737
kurH_m	-0.521	-0.610	-0.402	-0.076	-0.004	-0.323	-0.730
p_05_m	0.756	0.511	0.216	0.137	-0.451	-0.054	0.318
p_10_m	0.801	0.560	0.253	0.175	-0.416	-0.008	0.345
p_25_m	0.918	0.698	0.362	0.288	-0.279	0.128	0.436
p_50_m	1.000	0.884	0.539	0.446	-0.075	0.206	0.562
p_75_m	0.884	1.000	0.782	0.657	0.081	0.191	0.591
p_95_m	0.539	0.782	1.000	0.895	0.076	0.158	0.258
p_99_m	0.446	0.657	0.895	1.000	0.173	0.156	0.175
vci_2m_m	-0.075	0.081	0.076	0.173	1.000	0.175	0.139
vci_5m_m	0.206	0.191	0.158	0.156	0.175	1.000	0.315
vci_10m_m	0.562	0.591	0.258	0.175	0.139	0.315	1.000
vci_15m_m	0.444	0.621	0.766	0.716	0.159	0.274	0.323
vci_20m_m	0.312	0.429	0.585	0.704	0.289	0.155	-0.005
cov_m	0.560	0.440	0.162	0.200	0.444	0.423	0.519
canopy_shannon_m	0.759	0.924	0.866	0.786	0.175	0.369	0.626
canopy_roughness_m	0.456	0.485	0.393	0.434	0.549	0.407	0.357
tvolume_m	0.545	0.383	0.093	0.132	0.355	0.373	0.426
vlayer_1_m	-0.144	-0.173	-0.178	-0.163	0.130	0.021	-0.076
vlayer_2_m	0.299	0.113	-0.160	-0.073	0.388	0.401	0.416
vlayer_3_m	0.778	0.689	0.442	0.412	0.183	0.257	0.391
meanH_L1_m	-0.016	0.165	0.176	0.228	0.698	0.291	0.188
meanH_L2_m	0.766	0.486	0.094	0.054	-0.262	0.329	0.613
meanH_L3_m	0.178	0.445	0.853	0.865	0.115	0.074	-0.174
sdH_L1_m	0.026	0.184	0.199	0.243	0.731	0.217	0.171
sdH_L2_m	0.650	0.693	0.392	0.308	0.330	0.359	0.864
sdH_L3_m	0.273	0.502	0.799	0.954	0.198	0.102	0.074
roughness_L1_m	0.048	0.071	-0.033	0.031	0.795	0.257	0.256
roughness_L2_m	0.504	0.365	0.069	0.078	0.342	0.418	0.482
roughness_L3_m	0.195	0.461	0.669	0.678	0.264	0.072	-0.029
vci_L1_m	0.051	0.209	0.188	0.245	0.714	0.294	0.221
vci_L2_m	0.545	0.499	0.225	0.184	0.127	0.690	0.811
vci_L3_m	0.310	0.561	0.860	0.874	0.157	0.118	0.061
height_cv_m	-0.564	-0.199	0.355	0.391	0.291	-0.091	-0.364
cwd_volume_m	0.142	0.114	0.035	0.048	0.156	0.070	0.137
numberOfCWD_m	0.086	0.004	-0.076	-0.036	0.130	0.109	0.142

Chapter 4 Appendix B3 continued

	vci_15m_m	vci_20m_m	cov_m	canopy_shannon_m	canopy_roughness_m
maxH_m	0.497	0.526	0.299	0.561	0.445
meanH_m	0.602	0.439	0.485	0.885	0.468
stdH_m	0.738	0.582	0.104	0.831	0.402
skewH_m	-0.171	0.082	-0.515	-0.535	-0.254
kurH_m	-0.332	0.070	-0.318	-0.608	-0.227
p_05_m	0.181	0.101	0.379	0.335	0.077
p_10_m	0.206	0.135	0.420	0.384	0.130
p_25_m	0.288	0.216	0.529	0.539	0.296
p_50_m	0.444	0.312	0.560	0.759	0.456
p_75_m	0.621	0.429	0.440	0.924	0.485
p_95_m	0.766	0.585	0.162	0.866	0.393
p_99_m	0.716	0.704	0.200	0.786	0.434
vci_2m_m	0.159	0.289	0.444	0.175	0.549
vci_5m_m	0.274	0.155	0.423	0.369	0.407
vci_10m_m	0.323	-0.005	0.519	0.626	0.357
vci_15m_m	1.000	0.423	0.192	0.768	0.430
vci_20m_m	0.423	1.000	0.289	0.533	0.442
cov_m	0.192	0.289	1.000	0.445	0.629
canopy_shannon_m	0.768	0.533	0.445	1.000	0.562
canopy_roughness_m	0.430	0.442	0.629	0.562	1.000
tvolume_m	0.115	0.192	0.877	0.351	0.576
vlayer_1_m	-0.190	-0.160	-0.174	-0.168	-0.015
vlayer_2_m	-0.084	0.095	0.875	0.133	0.460
vlayer_3_m	0.408	0.341	0.795	0.604	0.596
meanH_L1_m	0.193	0.240	0.255	0.262	0.396
meanH_L2_m	0.118	0.053	0.621	0.412	0.236
meanH_L3_m	0.642	0.619	-0.107	0.560	0.245
sdH_L1_m	0.264	0.340	0.396	0.275	0.453
sdH_L2_m	0.441	0.157	0.484	0.734	0.488
sdH_L3_m	0.634	0.711	0.093	0.649	0.376
roughness_L1_m	0.028	0.157	0.549	0.149	0.622
roughness_L2_m	0.167	0.210	0.786	0.379	0.687
roughness_L3_m	0.563	0.505	-0.053	0.529	0.428
vci_L1_m	0.217	0.260	0.330	0.293	0.443
vci_L2_m	0.365	0.119	0.514	0.624	0.454
vci_L3_m	0.810	0.638	0.013	0.694	0.336
height_cv_m	0.283	0.216	-0.443	0.009	-0.048
cwd_volume_m	-0.014	-0.010	0.037	0.112	0.169
numberOfCWD_m	-0.129	-0.070	0.137	0.015	0.148

Chapter 4 Appendix B3 continued

	tvolume_m	vlayer_1_m	vlayer_2_m	vlayer_3_m	meanH_L1_m	meanH_L2_m
maxH_m	0.277	-0.058	0.183	0.355	0.174	0.143
meanH_m	0.443	-0.192	0.171	0.749	0.057	0.622
stdH_m	0.035	-0.120	-0.200	0.346	0.289	-0.090
skewH_m	-0.507	0.042	-0.380	-0.566	-0.013	-0.756
kurH_m	-0.272	0.049	-0.175	-0.350	-0.110	-0.431
p_05_m	0.384	-0.236	0.255	0.569	-0.304	0.826
p_10_m	0.418	-0.235	0.276	0.610	-0.276	0.844
p_25_m	0.526	-0.196	0.336	0.729	-0.179	0.868
p_50_m	0.545	-0.144	0.299	0.778	-0.016	0.766
p_75_m	0.383	-0.173	0.113	0.689	0.165	0.486
p_95_m	0.093	-0.178	-0.160	0.442	0.176	0.094
p_99_m	0.132	-0.163	-0.073	0.412	0.228	0.054
vci_2m_m	0.355	0.130	0.388	0.183	0.698	-0.262
vci_5m_m	0.373	0.021	0.401	0.257	0.291	0.329
vci_10m_m	0.426	-0.076	0.416	0.391	0.188	0.613
vci_15m_m	0.115	-0.190	-0.084	0.408	0.193	0.118
vci_20m_m	0.192	-0.160	0.095	0.341	0.240	0.053
cov_m	0.877	-0.174	0.875	0.795	0.255	0.621
canopy_shannon_m	0.351	-0.168	0.133	0.604	0.262	0.412
canopy_roughness_m	0.576	-0.015	0.460	0.596	0.396	0.236
tvolume_m	1.000	0.221	0.879	0.816	0.111	0.599
vlayer_1_m	0.221	1.000	0.025	-0.131	-0.014	-0.139
vlayer_2_m	0.879	0.025	1.000	0.559	0.187	0.569
vlayer_3_m	0.816	-0.131	0.559	1.000	0.015	0.582
meanH_L1_m	0.111	-0.014	0.187	0.015	1.000	-0.134
meanH_L2_m	0.599	-0.139	0.569	0.582	-0.134	1.000
meanH_L3_m	-0.146	-0.095	-0.351	0.155	0.183	-0.265
sdH_L1_m	0.099	-0.405	0.240	0.139	0.706	-0.144
sdH_L2_m	0.440	0.059	0.324	0.448	0.282	0.484
sdH_L3_m	0.018	-0.141	-0.134	0.253	0.242	-0.071
roughness_L1_m	0.573	0.296	0.609	0.267	0.573	0.004
roughness_L2_m	0.778	-0.035	0.758	0.663	0.104	0.566
roughness_L3_m	-0.129	-0.145	-0.316	0.175	0.321	-0.258
vci_L1_m	0.154	-0.089	0.231	0.089	0.969	-0.091
vci_L2_m	0.436	-0.003	0.447	0.339	0.232	0.645
vci_L3_m	-0.076	-0.183	-0.286	0.262	0.217	-0.116
height_cv_m	-0.472	0.055	-0.479	-0.398	0.241	-0.822
cwd_volume_m	0.253	0.636	0.078	0.062	0.280	0.114
numberOfCWD_m	0.381	0.677	0.250	0.095	0.227	0.166

Chapter 4 Appendix B3 continued

	meanH_L3_m	sdH_L1_m	sdH_L2_m	sdH_L3_m	roughness_L1_m
maxH_m	0.530	0.216	0.295	0.667	0.149
meanH_m	0.429	0.091	0.624	0.489	0.010
stdH_m	0.874	0.295	0.394	0.826	0.056
skewH_m	0.246	-0.007	-0.730	0.212	-0.122
kurH_m	0.055	-0.092	-0.715	0.116	-0.123
p_05_m	-0.051	-0.266	0.194	0.023	-0.250
p_10_m	-0.025	-0.231	0.241	0.053	-0.220
p_25_m	0.043	-0.135	0.414	0.140	-0.103
p_50_m	0.178	0.026	0.650	0.273	0.048
p_75_m	0.445	0.184	0.693	0.502	0.071
p_95_m	0.853	0.199	0.392	0.799	-0.033
p_99_m	0.865	0.243	0.308	0.954	0.031
vci_2m_m	0.115	0.731	0.330	0.198	0.795
vci_5m_m	0.074	0.217	0.359	0.102	0.257
vci_10m_m	-0.174	0.171	0.864	0.074	0.256
vci_15m_m	0.642	0.264	0.441	0.634	0.028
vci_20m_m	0.619	0.340	0.157	0.711	0.157
cov_m	-0.107	0.396	0.484	0.093	0.549
canopy_shannon_m	0.560	0.275	0.734	0.649	0.149
canopy_roughness_m	0.245	0.453	0.488	0.376	0.622
tvolume_m	-0.146	0.099	0.440	0.018	0.573
vlayer_1_m	-0.095	-0.405	0.059	-0.141	0.296
vlayer_2_m	-0.351	0.240	0.324	-0.134	0.609
vlayer_3_m	0.155	0.139	0.448	0.253	0.267
meanH_L1_m	0.183	0.706	0.282	0.242	0.573
meanH_L2_m	-0.265	-0.144	0.484	-0.071	0.004
meanH_L3_m	1.000	0.197	0.011	0.878	-0.103
sdH_L1_m	0.197	1.000	0.291	0.252	0.519
sdH_L2_m	0.011	0.291	1.000	0.180	0.382
sdH_L3_m	0.878	0.252	0.180	1.000	0.013
roughness_L1_m	-0.103	0.519	0.382	0.013	1.000
roughness_L2_m	-0.186	0.202	0.499	-0.009	0.503
roughness_L3_m	0.721	0.271	0.121	0.704	0.013
vci_L1_m	0.183	0.802	0.331	0.250	0.596
vci_L2_m	-0.101	0.181	0.812	0.083	0.276
vci_L3_m	0.898	0.264	0.212	0.868	-0.052
height_cv_m	0.639	0.234	-0.251	0.488	0.014
cwd_volume_m	-0.023	-0.137	0.201	0.003	0.315
numberOfCWD_m	-0.134	-0.189	0.151	-0.090	0.404

Chapter 4 Appendix B3 continued

	roughness_L2_m	roughness_L3_m	vci_L1_m	vci_L2_m	vci_L3_m	height_cv_m
maxH_m	0.229	0.406	0.194	0.230	0.393	0.209
meanH_m	0.399	0.382	0.109	0.484	0.533	-0.312
stdH_m	0.021	0.718	0.296	0.183	0.860	0.503
skewH_m	-0.498	0.160	-0.058	-0.645	0.105	0.667
kurH_m	-0.328	0.010	-0.117	-0.635	-0.069	0.229
p_05_m	0.301	-0.131	-0.265	0.243	0.053	-0.703
p_10_m	0.332	-0.093	-0.231	0.280	0.078	-0.709
p_25_m	0.450	0.016	-0.121	0.409	0.154	-0.700
p_50_m	0.504	0.195	0.051	0.545	0.310	-0.564
p_75_m	0.365	0.461	0.209	0.499	0.561	-0.199
p_95_m	0.069	0.669	0.188	0.225	0.860	0.355
p_99_m	0.078	0.678	0.245	0.184	0.874	0.391
vci_2m_m	0.342	0.264	0.714	0.127	0.157	0.291
vci_5m_m	0.418	0.072	0.294	0.690	0.118	-0.091
vci_10m_m	0.482	-0.029	0.221	0.811	0.061	-0.364
vci_15m_m	0.167	0.563	0.217	0.365	0.810	0.283
vci_20m_m	0.210	0.505	0.260	0.119	0.638	0.216
cov_m	0.786	-0.053	0.330	0.514	0.013	-0.443
canopy_shannon_m	0.379	0.529	0.293	0.624	0.694	0.009
canopy_roughness_m	0.687	0.428	0.443	0.454	0.336	-0.048
tvolume_m	0.778	-0.129	0.154	0.436	-0.076	-0.472
vlayer_1_m	-0.035	-0.145	-0.089	-0.003	-0.183	0.055
vlayer_2_m	0.758	-0.316	0.231	0.447	-0.286	-0.479
vlayer_3_m	0.663	0.175	0.089	0.339	0.262	-0.398
meanH_L1_m	0.104	0.321	0.969	0.232	0.217	0.241
meanH_L2_m	0.566	-0.258	-0.091	0.645	-0.116	-0.822
meanH_L3_m	-0.186	0.721	0.183	-0.101	0.898	0.639
sdH_L1_m	0.202	0.271	0.802	0.181	0.264	0.234
sdH_L2_m	0.499	0.121	0.331	0.812	0.212	-0.251
sdH_L3_m	-0.009	0.704	0.250	0.083	0.868	0.488
roughness_L1_m	0.503	0.013	0.596	0.276	-0.052	0.014
roughness_L2_m	1.000	-0.032	0.163	0.560	-0.049	-0.454
roughness_L3_m	-0.032	1.000	0.299	-0.016	0.744	0.460
vci_L1_m	0.163	0.299	1.000	0.256	0.227	0.196
vci_L2_m	0.560	-0.016	0.256	1.000	0.101	-0.384
vci_L3_m	-0.049	0.744	0.227	0.101	1.000	0.507
height_cv_m	-0.454	0.460	0.196	-0.384	0.507	1.000
cwd_volume_m	0.065	0.043	0.234	0.173	-0.069	-0.103
numberOfCWD_m	0.132	-0.148	0.191	0.179	-0.185	-0.156

Chapter 4 Appendix B3 continued

	cwd_volume_m	numberOfCWD_m
maxH_m	0.151	0.054
meanH_m	0.113	0.029
stdH_m	0.038	-0.079
skewH_m	-0.153	-0.148
kurH_m	-0.106	-0.090
p_05_m	0.038	0.043
p_10_m	0.047	0.051
p_25_m	0.088	0.071
p_50_m	0.142	0.086
p_75_m	0.114	0.004
p_95_m	0.035	-0.076
p_99_m	0.048	-0.036
vci_2m_m	0.156	0.130
vci_5m_m	0.070	0.109
vci_10m_m	0.137	0.142
vci_15m_m	-0.014	-0.129
vci_20m_m	-0.010	-0.070
cov_m	0.037	0.137
canopy_shannon_m	0.112	0.015
canopy_roughness_m	0.169	0.148
tvolume_m	0.253	0.381
vlayer_1_m	0.636	0.677
vlayer_2_m	0.078	0.250
vlayer_3_m	0.062	0.095
meanH_L1_m	0.280	0.227
meanH_L2_m	0.114	0.166
meanH_L3_m	-0.023	-0.134
sdH_L1_m	-0.137	-0.189
sdH_L2_m	0.201	0.151
sdH_L3_m	0.003	-0.090
roughness_L1_m	0.315	0.404
roughness_L2_m	0.065	0.132
roughness_L3_m	0.043	-0.148
vci_L1_m	0.234	0.191
vci_L2_m	0.173	0.179
vci_L3_m	-0.069	-0.185
height_cv_m	-0.103	-0.156
cwd_volume_m	1.000	0.900
numberOfCWD_m	0.900	1.000

Chapter 4 Appendix B4. Model summary of the relationship between LiDAR derived vegetation structural metrics (independent variables) and individual species of reptile and amphibian abundance(dependent variables).

Independent variables	Dependent variables								
	Boulengers_Skink			Common_Dwarf_Skink			Delicate_Skink		
	TLS	ULS	Fusion	TLS	ULS	Fusion	TLS	ULS	Fusion
meanH	0.286	0.135	-0.043	0.543	-0.173	0.113	0.212	0.064	-0.328
	(0.290)	(0.301)	(0.193)	(1.554)	(1.442)	(0.867)	(0.304)	(0.303)	(0.211)
skewH	0.551*	0.305*	0.243	0.481	-0.268	0.111	0.195	0.005	-0.269
	(0.225)	(0.153)	(0.180)	(1.198)	(0.973)	(0.744)	(0.226)	(0.161)	(0.191)
vci_5m	-0.108	-0.205**	-0.084	0.734	0.793	0.429	-0.066	-0.045	0.014
	(0.081)	(0.072)	(0.091)	(0.518)	(0.674)	(0.478)	(0.076)	(0.078)	(0.088)
canopy_roughness	-0.137	-0.194	-0.098	-0.218	-0.414	-0.359	-0.255*	-0.352***	-0.205
	(0.134)	(0.113)	(0.143)	(0.425)	(0.372)	(0.386)	(0.118)	(0.102)	(0.128)
vlayer_L1	0.215	-0.176	-0.132	0.13	0.082	-0.153	0.02	0.131	-0.045
	(0.122)	(0.183)	(0.106)	(0.449)	(0.533)	(0.399)	(0.112)	(0.142)	(0.106)
vlayer_L2	-0.276*	0.021	-0.137	-0.655	0.042	-0.141	-0.03	-0.082	0.077
	(0.119)	(0.167)	(0.126)	(0.439)	(0.541)	(0.422)	(0.105)	(0.127)	(0.113)
meanH_L1	0.253**	-0.019	-0.018	0.783*	0.388	0.227	0.141	-0.015	-0.180*
	(0.091)	(0.093)	(0.080)	(0.381)	(0.384)	(0.260)	(0.094)	(0.094)	(0.085)
vci_L2	0.291*	0.237*	0.181	0.426	0.339	0.825	0.202	0.12	-0.009
	(0.140)	(0.111)	(0.147)	(0.654)	(0.600)	(0.676)	(0.135)	(0.108)	(0.143)
vci_L3	-0.133	0.037	0.077	0.141	0.66	0.44	-0.066	0.092	0.392*
	(0.279)	(0.301)	(0.182)	(1.414)	(1.418)	(0.806)	(0.276)	(0.286)	(0.185)
height_cv	-0.284	-0.15	-0.19	-0.322	-0.197	0.189	-0.018	-0.06	-0.094
	(0.154)	(0.214)	(0.120)	(0.745)	(0.988)	(0.557)	(0.155)	(0.192)	(0.118)
cwd_volume	-0.08	0.256**	0.177*	-0.05	0.215	0.264	0.05	0.141	0.142
	(0.089)	(0.097)	(0.088)	(0.404)	(0.344)	(0.387)	(0.082)	(0.090)	(0.091)
Intercept	1.375***	1.387***	1.374***	-2.078***	-2.095***	-1.913***	1.485***	1.482***	1.475***
	(0.148)	(0.142)	(0.162)	(0.358)	(0.462)	(0.319)	(0.092)	(0.087)	(0.110)
Marginal R2	0.162	0.152	0.113	0.264	0.286	0.264	0.122	0.218	0.158
Conditional R2	0.166	0.156	0.115	0.483	0.500	0.483	0.128	0.228	0.164
Notifications	*p < 0.05, **p < 0.01, ***p < 0.001								

Chapter 4 Appendix B4 continued

Independent variables	Jacky_Dragon			Shingleback			Smooth_Toadlet		
	TLS	ULS	Fusion	TLS	ULS	Fusion	TLS	ULS	Fusion
meanH	1.209	0.78	-0.225	2.480*	1.728	1.024	2.744	-0.217	-0.106
	(1.428)	(1.129)	(0.773)	(1.020)	(1.049)	(0.653)	(1.953)	(1.704)	(0.965)
skewH	0.665	0.252	-0.291	2.554***	0.991*	1.396**	1.09	-0.749	-0.794
	(0.988)	(0.558)	(0.622)	(0.732)	(0.484)	(0.512)	(1.302)	(0.854)	(0.934)
vci_5m	-0.151	-0.261	-0.081	-0.41	-0.136	-0.591*	-0.15	0.464	0.083
	(0.295)	(0.259)	(0.280)	(0.284)	(0.271)	(0.267)	(0.408)	(0.425)	(0.396)
canopy_roughness	-0.166	-0.226	-0.213	-0.121	-0.483	-0.004	-0.161	0.166	-0.109
	(0.440)	(0.331)	(0.369)	(0.427)	(0.389)	(0.361)	(0.602)	(0.422)	(0.559)
vlayer_L1	0.034	0.289	-0.153	0.507	0.441	0.189	0.308	-0.6	-0.141
	(0.431)	(0.463)	(0.423)	(0.402)	(0.526)	(0.348)	(0.593)	(0.670)	(0.539)
vlayer_L2	0.238	0.069	0.441	-0.394	-0.023	-0.317	0.291	-0.008	0.273
	(0.368)	(0.396)	(0.331)	(0.359)	(0.440)	(0.337)	(0.495)	(0.529)	(0.444)
meanH_L1	-0.025	-0.324	-0.354	1.012**	0.379	0.228	-0.293	0.057	-1.109*
	(0.361)	(0.381)	(0.304)	(0.367)	(0.332)	(0.269)	(0.508)	(0.390)	(0.439)
vci_L2	0.225	0.029	-0.214	1.264**	0.319	0.921*	0.369	-0.715	-0.377
	(0.595)	(0.360)	(0.399)	(0.489)	(0.358)	(0.426)	(0.715)	(0.477)	(0.588)
vci_L3	-0.75	-0.409	0.642	-1.943*	-0.951	-0.58	-2.733	-0.168	-0.296
	(1.334)	(1.040)	(0.655)	(0.932)	(1.023)	(0.544)	(1.767)	(1.506)	(0.806)
height_cv	0.435	0.448	0.005	-0.199	-0.069	-0.4	1.6	0.244	0.828
	(0.744)	(0.668)	(0.439)	(0.603)	(0.694)	(0.436)	(0.916)	(0.857)	(0.519)
cwd_volume	-0.245	0.019	0.339	-0.478	-0.307	-0.431	-0.648	0.313	0.554
	(0.404)	(0.391)	(0.373)	(0.346)	(0.392)	(0.346)	(0.622)	(0.461)	(0.468)
Intercept	-1.703***	-1.562***	-1.595***	1.619***	-1.436***	-1.404***	-2.516***	-2.038***	-2.441***
	(0.371)	(0.236)	(0.242)	(0.362)	(0.346)	(0.318)	(0.589)	(0.379)	(0.522)
Marginal R2	0.035	0.048	0.062	0.235	0.110	0.130	0.133	0.086	0.196
Conditional R2	0.079	0.116	0.144	0.330	0.164	0.197	0.219	0.180	0.338
Notifications	*p < 0.05,	**p < 0.01,	***p < 0.001						

Chapter 4 Appendix B4 continued

Independent variables	Spotted_Grass_Frog			Three_toed_Skink			Unidentified_Skink		
	TLS	ULS	Fusion	TLS	ULS	Fusion	TLS	ULS	Fusion
meanH	1.807	2.233*	0.134	0.969	-0.033	0.188	-0.407	-0.03	-0.102
	(0.972)	(0.998)	(0.552)	(0.608)	(0.680)	(0.405)	(0.371)	(0.358)	(0.236)
skewH	1.698*	1.508**	0.615	0.775	-0.209	0.136	-0.181	0.13	0.031
	(0.755)	(0.546)	(0.506)	(0.443)	(0.328)	(0.322)	(0.291)	(0.196)	(0.214)
vci_5m	0.186	-0.198	0.056	-0.357*	0.174	-0.453**	0.018	-0.104	0.017
	(0.263)	(0.306)	(0.247)	(0.156)	(0.159)	(0.165)	(0.100)	(0.085)	(0.105)
canopy_roughness	0.660*	0.215	0.609*	0.104	0.211	0.259	-0.064	-0.155	-0.025
	(0.291)	(0.244)	(0.256)	(0.190)	(0.180)	(0.184)	(0.123)	(0.107)	(0.121)
vlayer_L1	0.791*	0.636	0.679*	-0.578**	-0.398	-0.527**	0.232	0.294	0.08
	(0.368)	(0.486)	(0.303)	(0.205)	(0.319)	(0.202)	(0.135)	(0.154)	(0.122)
vlayer_L2	-0.548	-0.356	-0.478	-0.14	-0.253	-0.167	-0.216	-0.384**	-0.162
	(0.334)	(0.357)	(0.336)	(0.188)	(0.263)	(0.186)	(0.122)	(0.140)	(0.122)
meanH_L1	0.357	-0.189	-0.3	0.25	0.06	0.175	0.057	-0.071	-0.017
	(0.302)	(0.314)	(0.225)	(0.171)	(0.213)	(0.137)	(0.117)	(0.118)	(0.092)
vci_L2	-0.073	0.678	-0.275	0.44	-0.389	0.288	-0.115	0.131	-0.027
	(0.412)	(0.358)	(0.379)	(0.256)	(0.224)	(0.237)	(0.173)	(0.124)	(0.161)
vci_L3	-1.801	-2.660**	-0.208	-0.957	0.021	-0.327	0.518	0.092	0.165
	(0.944)	(0.991)	(0.494)	(0.550)	(0.631)	(0.351)	(0.337)	(0.328)	(0.205)
height_cv	-0.272	0.794	-0.713*	0.23	-0.162	0.06	-0.475**	-0.222	-0.253
	(0.482)	(0.632)	(0.319)	(0.333)	(0.426)	(0.274)	(0.183)	(0.223)	(0.137)
cwd_volume	-0.272	0.183	-0.173	0.318	0.126	0.041	0.078	0.14	0.195
	(0.243)	(0.282)	(0.299)	(0.175)	(0.220)	(0.225)	(0.092)	(0.117)	(0.104)
Intercept	-1.062**	-0.998**	-0.960**	-0.277	-0.202	-0.197	0.954***	0.955***	0.959***
	(0.400)	(0.369)	(0.352)	(0.168)	(0.182)	(0.159)	(0.093)	(0.083)	(0.088)
Marginal R2	0.217	0.242	0.216	0.318	0.190	0.244	0.163	0.239	0.167
Conditional R2	0.243	0.273	0.249	0.381	0.230	0.300	0.180	0.263	0.185
Notifications	*p < 0.05, **p < 0.01, ***p < 0.001								